The Dissertation Committee for Rong Jiao Certifies that this is the approved version of the following dissertation:

RATCHETING, WRINKLING AND COLLAPSE OF TUBES DUE TO AXIAL CYCLING

Committee:

Kyriakides, Stelios, Supervisor

Landis, Chad

Liechti, Kenneth M.

Ravi-Chandar, K.

Tassoulas, John L.

RATCHETING, WRINKLING AND COLLAPSE OF TUBES DUE TO AXIAL CYCLING

by

Rong Jiao, B.S.; M.S.

Dissertation

Presented to the Faculty of the Graduate School of
The University of Texas at Austin
in Partial Fulfillment
of the Requirements
for the Degree of

Doctor of Philosophy

The University of Texas at Austin
December 2011

Dedication

To my wife Ping Sun, my parents Zhonghua Jiao and Mei Kong, and my daughter Caroline Jiao.

Acknowledgements

I would like to express my deep appreciation to my advisor, Professor Stelios Kyriakides, whom I consider one of my greatest intellectual benefactors up to now. Over the past five years, his continuous guidance and support helped me throughout my studies and research. His enthusiasm and dedication to research, his method of work and insistence on excellence, and his solid work ethics have been influenced me dramatically and will attend me in the rest of my career.

I would also like to express my gratitude to Professors Kenneth M. Liechti, K. Ravi-Chandar, Chad Landis and John Tassoulas served as members of my committee, reviewing my dissertation and offering me their constructive comments. I also appreciate the excellent and informative teaching from Professors Eric Becker, Jeffrey K. Bennighof, Clint N. Dawson, Rui Huang, Thomas J.R. Hughes, Mark E. Mear, J. Tinsley Oden and Gregory J. Rodin.

Special appreciations go to Dr. Edmundo Corona and Dr. Francois Bardi for their detailed explanations of custom programs CYPRUS and shell compression that I am using in my research. Also, Professor Ali Limam, Dr. Liang-Hai Lee and Professor Yannis Korkolis are appreciated for their helps in my experiments.

Many thanks are also given to staff members Travis Crooks, David Gray, Pablo Cortez and Jim Williams for their technical support. Without their supports, my experiments could not have been performed.

In my years in UT-Austin, I was very lucky to have met and worked with a large number of talented and dedicated fellow graduate students and the list of their names is

too long to show here. However, they are really thanked for not only the scientific but also the social interactions we have had.

I am also truly grateful for the support of my parents, Zhonghua Jiao and Mei Kong. Their unconditional love is always my faith and motivation to continue in my career and persuades me never to give up.

Lastly many thanks are reserved for my wife, Ping Sun, as I could not have finished my degree without her support and love.

Ratcheting, Wrinkling and Collapse of Tubes Due to Axial Cycling

Rong Jiao, PhD

The University of Texas at Austin, 2011

Supervisor: Stelios Kyriakides

The first instability of circular tubes compressed into the plastic range is axisymmetric wrinkling, which is stable. Compressed further the wrinkle amplitude grows, leading to a limit load instability followed by collapse. The two instabilities can be separated by strain levels of a few percent. This work investigates whether a tube that develops small amplitude wrinkles can be subsequently collapsed by persistent cycling. The problem was first investigated experimentally using SAF 2507 super-duplex steel tubes with D/t of 28.5. The tubes are first compressed to strain levels high enough for mild wrinkles to form and then cycled axially under stress control about a compressive mean stress. This type of cycling usually results in accumulation of compressive strain; here it is accompanied by growth of the amplitude of the initial wrinkles. The tube average strain initially grows nearly linearly with the number of cycles, but as a critical value of wrinkle amplitude is approached, wrinkling localizes, the rate of ratcheting grows exponentially and the tube collapses.

Similar experiments were then performed for tubes involving axial cycling under internal pressure and the combined loads cause simultaneous ratcheting in the hoop and axial directions as well as a gradual growth of the wrinkles. The rate of ratcheting and the number of cycles to collapse depend on the initial compressive pre-strain, the internal pressure, and the stress cycle parameters all of which were varied sufficiently to generate a sufficient data base. Interestingly, in both the pressurized and unpressurized cases collapse was found to occur when the accumulated average strain reaches the value at which the tube localizes under monotonic compression.

A custom shell model of the tube with initial axisymmetric imperfections, coupled to the Dafalias-Popov two-surface nonlinear kinematic hardening model, are presented and used to simulate the experiments performed. It is demonstrated that when suitably calibrated this modeling framework reproduces the prevalent ratcheting deformations and the evolution of wrinkling including the conditions at collapse accurately for all experiments. The calibrated model is then used to evaluate the ratcheting behavior of pipes under thermal-pressure cyclic loading histories experienced by axially restrained pipelines.

Table of Contents

Nomenclature

a	Material constant in plastic modulus calculation
$\mathbf{a}$	Deviatoric part of back stress $\boldsymbol{\alpha}$
a_i	Axisymmetric coefficients of discretized radial displacement
A_i	Transverse internal area of tube
b	Material constant in plastic modulus calculation
$\mathbf{b}$	Deviatoric part of center of bound surface $\boldsymbol{\beta}$
b_i	Axisymmetric coefficients of discretized axial displacement
C_{ij}	Instantaneous moduli of the material constitutive matrix
C_r	Stress relaxation coefficient in Dafalias-Popov two-surface model
dM	Scalar in calculation of translation of $\boldsymbol{\beta}$
D	Outer diameter of tube
E	Young's modulus
E_o^p	Initial modulus of the bound surface
E_b^p	Current modulus of the bound surface
E_s	Secant modulus
E_t	Tangent modulus
F	Axial force
h	Material parameter in plastic modulus calculation
H	Plastic modulus
$\mathbf{I}$	Identity tensor
I_x	Integration number in Gauss's integration along axial direction
I_z	Integration number in Gauss's integration in thickness
k	Constant in Armstrong-Frederick hardening rule

k_0, k_1	Constant in calculation of k
L	Half-length of tube in analysis
$\boldsymbol{m}$	Direction from the current stress to its corresponding stress on the bound surface
M_{ij}	Bending moment intensity
M_{xx}	Bending moment intensity in axial direction
$M_{\theta\theta}$	Bending moment intensity in circumferential direction
$\boldsymbol{n}$	Unit normal to the yield surface
N	Number of half-wavelength considered in analysis
N_C	Total number of cycles applied
N_{ij}	Force intensity
N_{xx}	Force intensity in axial direction
$N_{\theta\theta}$	Force intensity in circumferential direction
N_u	Number of terms in the discretized axial displacement
N_w	Number of terms in the discretized radial displacement
P	Internal pressure
P_o	Yield pressure
$\boldsymbol{q}$	Vector containing coefficients of discretized displacements
R	Mean radius of tube
$\boldsymbol{s}$	Deviatoric part of $\boldsymbol{\sigma}$
$\bar{\boldsymbol{s}}$	Deviatoric part of $\bar{\boldsymbol{\sigma}}$
S_r	Ratio of the radial yield stress over the axial yield stress
S_θ	Ratio of the hoop yield stress over the axial yield stress
t	Wall thickness of tube
$t_{\max}$	Maximum measured wall thickness of tube
$t_{\min}$	Minimum measured wall thickness of tube

t_o	Average wall thickness of tube
Δt	Amplitude of wall thickness variation
u	Axial displacement
$\tilde{u}$	Axial buckling mode
v	Poisson’s Ratio
w	Radial displacement
$w_{\max}$	Maximum radial displacement
$\tilde{w}$	Radial buckling mode
$\overline{w}$	Initial imperfection
W	External work
W^P	Plastic work
x	Axial coordinate
z	Radial coordinate
$d\boldsymbol{\alpha}$	Increment of $\boldsymbol{\alpha}$
$d\boldsymbol{\beta}$	Increment of $\boldsymbol{\beta}$
$d\boldsymbol{\varepsilon}$	Increment strain tensor
$d\boldsymbol{\varepsilon}^e$	Elastic part in incremental strain tensor
$d\boldsymbol{\varepsilon}^p$	Plastic part in incremental strain tensor
$d\varepsilon_e^p$	Incremental plastic equivalent strain
$d\varepsilon_x$	Strain increment in axial direction
$d\varepsilon_x^p$	Plastic strain increment in axial direction
$d\varepsilon_\theta$	Strain increment in circumferential direction
$d\varepsilon_\theta^p$	Plastic strain increment in circumferential direction
$d\mu$	Scalar defining the amplitude of translation of $d\boldsymbol{\alpha}$
$d\boldsymbol{\sigma}$	Incremental stress tensor

$d\sigma_{ij}$	Components of stress increment
$d\sigma_x$	Stress increment in axial direction
$d\sigma_\theta$	Stress increment in circumferential direction
a	Thermal coefficient of expansion
$\boldsymbol{\alpha}$	Back stress tensor
α_x	Back stress in axial direction
α_θ	Back stress in circumferential direction
$\boldsymbol{\beta}$	Stress tensor for the center of the bound surface
β_x	Axial component in $\boldsymbol{\beta}$
β_θ	Circumferential component in $\boldsymbol{\beta}$
γ	Material constant in plastic modulus calculation
δ	Distance from the current stress to its corresponding stress on the bound surface
δ_{in}	Initial value of δ for the last elastic state
δ_x	Axial displacement
δ_x^p	Peak value of axial displacement in each cycle
δW	Virtual external work
δW_F	Virtual external work by axial force
ΔT	Change of temperature
Δw	Difference between the maximum and minimum radial displacements of the most deformed wrinkle
$\Delta\varepsilon_x$	Change of axial strain
ε_C	Critical strain at bifurcation
ε_e^p	Plastic equivalent strain
$\bar{\varepsilon}_f$	Peak average strain at the end of cyclic loading

ε_{ij}	Total strain
ε_{ij}^{e}	Elastic strain
ε_{ij}^{p}	Plastic strain
$\bar{\varepsilon}_{Lmom}$	Average limit strain at monotonic compression
ε_{x}	Axial strain
ε_{xp}	Peak value of axial strain in each cycle
$\bar{\varepsilon}_{x}$	Average axial strain
$\bar{\varepsilon}_{xmon}$	Average axial strain at the end of monotonic loading
ε_{θ}	Circumferential strain
$\bar{\varepsilon}_{\theta}$	Average circumferential strain
$\varepsilon_{\theta p}$	Peak value of circumferential strain in each cycle
ε_{ij}^{o}	Membrane strain
ε_{xx}^{o}	Membrane strain in axial direction
$\varepsilon_{\theta\theta}^{o}$	Membrane strain in circumferential direction
θ	Circumferential coordinate
κ_{ij}	Curvature
κ_{xx}	Curvature in axial direction
$\kappa_{\theta\theta}$	Curvature in circumferential direction
λ	Half-wavelength of axisymmetric wrinkles
$\boldsymbol{\nu}$	Direction of translation of $d\boldsymbol{\alpha}$
Ξ_{o}	Wall eccentricities
$\boldsymbol{\sigma}$	Stress tensor
σ_{a}	Amplitude in axial stress cycle
σ_{b}	Radius of bound surface
σ_{C}	Critical stress at first bifurcation

σ_e	Equivalent stress
σ_{ij}	Stress components
σ_L	Limit stress
σ_m	Mean stress in axial stress cycle
σ_o	Radius of yield surface
σ_{ox}	Yield stress in axial direction
σ_{or}	Yield stress in radial direction
$\sigma_{o\theta}$	Yield stress in hoop direction
σ_r	Stress in radial direction
σ_x	Stress in axial direction
σ_{xmon}	Axial stress at the end of monotonic loading
σ_θ	Stress in hoop direction
$\bar{\boldsymbol{\sigma}}$	Congruent stress tensor on the bound surface to $\boldsymbol{\sigma}$ on the yield surface
$\bar{\sigma}_x$	Axial component in $\bar{\boldsymbol{\sigma}}$
$\bar{\sigma}_\theta$	Circumferential component in $\bar{\boldsymbol{\sigma}}$
τ	Normalized amplitude of wall thickness variation
ω_o	Axisymmetric imperfection amplitude
ω_1	Bias imperfection amplitude
ζ	Constant in calculation of k

CHAPTER 1

INTRODUCTION

1.1 BACKGROUND

Pipelines constitute the preferred means of gathering and transporting gas and liquids such as oil, water, chemicals or sewage. They are being installed world wide on land as well as offshore. Land pipelines often traverse long distances in many cases crossing environmentally sensitive areas. Offshore lines include shorter flowlines for gathering hydrocarbons to a local point such as a platform, and transport pipelines that take processed products to shore or to an offloading station.

Often both land based and offshore pipelines are buried in trenches and covered with soil for protection. In such cases geological instabilities such as landslides, fault movement, slope instability, or soil liquefaction caused by an earthquake can result in large ground movements that can damage the pipelines including buckling failures (Yun and Kyriakides, 1990). Subsidence due to melting of permafrost and slope instability (Murray, 1997; Wilkie *et al.*, 2000; Yoosef-Ghodsi *et al.*, 2000) and compression due to thermal expansion caused by the passage of hot hydrocarbons (Ju and Kyriakides, 1988) are other causes of buckling.

Compression of buried pipelines results in either of two main types of buckling: relatively stiff pipes buried in relatively shallow trenches behave as beam columns, bending vertically out of the ground—*upheaval buckling*—or laterally on the foundation surface—*lateral buckling* (Hobbs, 1984); shell-type localized buckling, involving either axisymmetric lobes (Fig. 1.1) or non-axisymmetric modes consisting of a number of circumferential waves (Fig. 1.2), occurs mainly for larger diameter pipelines buried in relatively deep trenches.

Another scenario that can lead to shell-type buckling occurs in pipelines that are trenched, buried (Fig. 1.3) or anchored where the soil cover can axially constrain the line. Because of the restrain the passage of hot hydrocarbons at a high pressure can plastically deform the pipe (see Klever *et al.*, 1994; Di Vito *et al.*, 2010). In some cases the compression is high enough to exceed the critical buckling stress causing the line to wrinkle (Paquette and Kyriakides, 2006; Kyriakides and Corona, 2007). Mild wrinkling is benign, but at higher strain levels the amplitude grows leading eventually to collapse by localization of the wrinkles. Imperfections due to small misalignments at girth welds, heat-affected regions around the welds, hard spots at connections with other equipment, etc., can all enhance the onset of wrinkling. During a lifetime of 20 to 30 years, pipelines experience several startup and shutdown cycles (~ hundreds), which basically heat and cool the line. A question arises as to whether wrinkles formed as a result of such stress risers can grow (ratchet) from the shutdown and startup cycles and if so what are the consequences. Thus, the main objective of the present work is to understand and model the effects of such startup and shutdown cycles on the structural integrity of such pipelines. Cycling of solids that result in yielding is complicated by strain ratcheting phenomena. Thus ratcheting can interact with structural nonlinearities such as wrinkling in a complex manner and lead to hitherto unknown limit states.

1.2 MATERIAL RATCHETING

Ratcheting in the context of material behavior is defined as the accumulation of plastic strain or deformation under unsymmetrical stress cycles. It can develop under uniaxial as well as multiaxial cyclic loadings when at least one stress component is prescribed. Although ratcheting under uniaxial stress cycling was known since the early works of Morrow (1965), Landgraf (1970) and others, the first systematic effort to understand and quantify the major parameters that influence the rate of ratcheting is due to Hassan and Kyriakides (1992, 1994a)—see these references for a more complete historical perspective. An example of uniaxial ratcheting is shown in Figs. 1.4 for a particular stainless steel. A bar is cycled axially using the saw-tooth stress history shown in Fig. 1.4a. The cycle has a mean stress σ_m and an amplitude σ_a. The cycling results in the gradual accumulation of axial strain in the direction of the mean stress. The maximum strain recorded in each cycle, ε_{xp}, is plotted in Fig. 1.4c as a function of the number of cycles (*N*). The rate of ratcheting exhibits an initial transient and then becomes nearly constant. At higher values of strain the rate of ratcheting accelerates leading to failure (see Fig. 1 in Hassan and Kyriakides, 1994a).

Biaxial ratcheting was more widely investigated in particular using cyclic torsion of thin walled tubes under prescribed tension (Moyar and Sinclair, 1963; Benham, 1965; Shiratori *et al.*, 1979 among others). Hassan *et al.* (1992) and Hassan and Kyriakides (1994b) expanded on the subject and extended it by conducting some of the earliest biaxial ratcheting results. An example of biaxial ratcheting is shown in Figs. 1.5. A tube is pressurized to a certain level and the pressure is then kept constant. The tube is then cycled axially using the saw-tooth stress history shown in Fig. 1.5a with cycle parameters of σ_m and σ_a. The cycling results in the gradual accumulation of axial strain in the direction of the mean stress and simultaneous expansion of the diameter of the tube. Figure 1.5c shows the induced hoop strain plotted against the axial strain. Both are seen to grow with the number of cycles applied. Once more, the rate of ratcheting depends on the pressure (hoop stress) and the two axial stress cycle parameters. Again, persistent cycling leads to failure due to the two accumulated strains. The mode of failure depends on the relative amplitudes of the pressure and the axial stress cycle parameters.

Two families of cyclic plasticity models capable of predicting ratcheting have been developed during the last twenty years: *uncoupled* and *coupled* (Bari and Hassan, 2000). In the uncoupled modeling schemes, the hardening rule and the flow rule are decoupled so that the kinematic hardening rule can be freely selected for best performance in the application at hand. Uncoupled models include the Dafalias and Popov two-surface model (Dafalias and Popov, 1975, 1976) along with modifications proposed in the series of papers by Hassan-Kyriakides and co-workers (Hassan *et al.*, 1992; Hassan and Kyriakides, 1992, 1994a, b; Corona *et al.*, 1996; Bari and Hassan, 2001; Jiao and Kyriakides, 2009). This framework was used to successfully predict uniaxial ratcheting for the first time in Hassan and Kyriakides (1992, 1994a). The models were also shown to yield good predictions to multiaxial ratcheting for a variety of cyclic loading paths. This was achieved using appropriate choices of nonlinear kinematic hardening rules and careful calibration.

In the coupled modeling schemes, the plastic modulus calculation is coupled to the kinematic hardening rule through the consistency condition. Coupled models include those of Chaboche (Chaboche, 1986, 1991), Ohno-Wang (Ohno and Wang, 1993a, b) and their modified versions (McDowell, 1995; Jiang and Sehitoglu, 1996a, b; Abdel Karim and Ohno, 2000; Bari and Hassan, 2002; Chen and Jiao, 2004; Chen *et al.*, 2005). With careful calibration to uniaxial ratcheting experiments, the Chaboche and Ohno-Wang models can both give reasonable predictions of uniaxial ratcheting. However, they over-predict multiaxial ratcheting for all loading paths (see Bari and Hassan, 2000). This weakness was alleviated by modifications proposed by Bari and Hassan (2002) for the Chaboche model and by Chen and Jiao (2004) and Chen *et al.* (2005) for the Ohno-Wang model.

1.3 STRUCTURAL RATCHETING

Structural degradation under cyclic loadings has received some attention in the literature. For example, motivated by pipeline applications, Shaw and Kyriakides (1985) and Kyriakides and Shaw (1987) showed that cyclically bending tubes into the plastic range results in accumulation of ovalization. Ovalization degrades the bending rigidity of tubes and leads to buckling and collapse when a critical value is reached. Corona and Kyriakides (1991) expanded on this finding and extended the work by cyclically bending tubes in the presence of external pressure. Kim and Park (2006), Rahman *et al.* (2008), and Chang and Pan (2009) conducted similar cyclic bending experiments using bending facilities that were based on the concept of the cyclic bending machine of Shaw and Kyriakides (1987).

Oh *et al.* (2008) and Hassan and Rahman (2009) motivated by nuclear reactor tubular components reported ratcheting of pipe elbows that are cyclically bent in the presence of internal pressure. Cycling leads to simultaneous expansion and ovalization of the elbow corner.

Corona and co-workers investigated the cyclic bending behavior of beam structures of different cross sectional geometries. For square tubes Vaze and Corona (1998) showed that cycling leads to degradation caused by the growth of axial wrinkles in the flanges. The wrinkles eventually localize leading to collapse. Ellison and Corona (1998) reported that when cycled relatively short T-beams degrade mainly by wrinkling of the web. Eventually the wrinkles develop into a local buckle. For relative long T-beams, the web again wrinkles while simultaneously it buckles laterally (lateral-torsional buckling) and significant cross-sectional rolling occurs causing a rapid drop in bending rigidity. Yin *et al.* (2004) reported gradual degradation and localized collapse of aluminum I-beams under fully reversed curvature controlled cycles. Cycling leads to degradation mainly caused by wrinkling and rotation of the cross section.

What is common in these problems is interaction between geometric nonlinearities with cyclic plasticity and ratcheting. The prediction of structural ratcheting requires structural modeling, usually finite element models, coupled with material constitutive models capable of simulating material behavior under cyclic loading histories. This requires calibration and evaluation of the cyclic plasticity model, an effort which usually requires dedicated cyclic material experiments.

1.4 OUTLINE OF PRESENT STUDY

In Section 1.1 we outlined a potential interaction between ratcheting and axial wrinkling in buried pipelines brought by repeating startup and shutdown thermomechanical cycles. The aim of the present study is to use experiments and analyses to investigate some of the most favorable loading histories that involve axial cycling of pressurized and unpressurized tubes that can bring to fore the interaction between material ratcheting and wrinkling and any other potential limit states. To this end, rather than cycling a pressurized or unpressurized pipe by heat and cool cycles, we will cycle the axial load in a way that induces ratcheting with and without internal pressure.

As inferred above, ratcheting is a complex material behavior whose modeling is rather demanding. So to achieve the goals of this study it will be necessary to conduct the necessary material ratcheting experiments required to calibrate the cyclic plasticity models adopted.

Once the structural and material models are shown to capture the main phenomena uncovered in the structural experiments, the models will be used to study the thermomechanical cycling problem of buried pipelines. The break up of this dissertation is as follows:

Chapter 2 presents the experimental set-ups and procedure used for the structural and material tests.

Chapter 3 discuses the simplest of the problem examined that involves stress-controlled axial cycling of pre-wrinkled tubes. Here the objective is to see how the accumulated strain interacts with the wrinkles.

Chapter 4 presents experimental results from the second problem considered, which involves axial cycling of pre-wrinkled tubes in the presence of constant internal pressure.

In Chapter 5 we investigate whether wrinkling can be initiated directly by ratcheting. Experiments under pure compression and compression combined with internal pressure will be reported.

In Chapter 6, a custom shell model with initial axisymmetric imperfections, coupled to a cyclic plasticity model is formulated. The chapter also includes description of the calibration procedure required for optimal performance of this constitutive model.

Chapter 7 presents numerical simulations of the experiments under pure axial cyclic loading described in Chapter 3. A sensitivity study of the formulation to the imperfections and to key constitutive model parameters is then performed.

Chapter 8 presents numerical simulations of the experiments under axial cyclic loading and internal pressure described in Chapter 4.

The problem of the onset of wrinkling by material compressive strain induced by ratcheting is analyzed in Chapter 9.

In Chapter 10, the calibrated model is first used to simulate the ratcheting behavior of pipes under thermal-pressure cycles and then used to evaluate the behavior of pipes under strain-pressure cyclic loading histories experienced by axially restrained pipelines.

Chapter 11 contains a summary of the work along with major conclusions.

CHAPTER 2

EXPERIMENTAL SET-UPS AND PROCEDURES

It is well known that stress-controlled axial cycling leads to accumulation of axial strain or strain ratcheting. Similar cycling in the presence of second stress component leads to ratcheting of two strains. At the same time tubes compressed into the plastic range tend to develop axisymmetric wrinkles. The aim of this study is to understand how axial compressive strain induced by ratcheting interacts with wrinkling and to investigate if it can lead to collapse. The problem was first investigated through systematic experiments performed on SAF2507 super-duplex tubes. This chapter describes the experimental set-ups and procedures used in this study.

2.1 EXPERIMENTS UNDER PURE AXIAL LOADING

All experiments were performed on super-duplex SAF2507 stainless-steel tubes. This is a two-phase (ferritic-austenitic) stainless steel used in highly corrosive applications. The Sandvik SAF2507 has the following composition (Sandvik, 2008).

Table 2.1 Alloy Chemical Composition (%) of the SAF 2507 tubes

C	Cr	Mo	Mn	N	Ni	P	S	Si
0.030	25	4	1.2	0.3	7	0.035	0.02	0.8

2.1.1 Test Specimens

The tube stock came in lengths of about 20 ft (6.096m), and had a nominal diameter of 2.375 (60.32 mm) in and a nominal wall thickness of 0.154 in (3.91 mm). Tubular specimens typically 11 in (279.4 mm) long with the geometry shown in Fig. 2.1 were machined out of the tubular stock. The specimens were designed as follows (see also Bardi and Kyriakides, 2006). Axial buckling can be influenced by initial geometric imperfections (Gellin, 1979) and by stress concentrations such as those generated by clamped ends (Lee, 1962) or other end constraints (Batterman, 1965). Thus, the test specimens had to be designed in a way that reduced the influence of these effects. Specimens were first machined and reamed on the inside to the desired dimension. The outer profile of the tube was produced on a CNC lathe with the tube being placed on centers true to the ID to ensure that the inner and outer surfaces of the test section were concentric (a tolerance of about ±0.001 in (0.0254 mm) was prescribed). Special attention was given to cutting speeds and depth as well as to cooling using coolant so as to avoid hardening of the material and to produce a smooth surface (Bardi, 2006). The test section has an OD of approximately 2.25 in (57.15 mm), a length of 3.0 in (76.2 mm) and a wall thickness of about 0.078 in (1.98 mm). Linear tapers connect the test section to thicker end segments that are left in the as-received diameter (see Fig. 2.1). This choice of specimen geometry implies that the onset and growth of wrinkling was approaching that expected of a long uniform tube.

The length of the tapers was selected through finite element calculations so as to minimize the effect of the thickness discontinuities on the axial stress. The FE model reproduced the axisymmetric setup and simultaneously took advantage of the symmetry about the mid-span. The domain was discretized with four-node, linear, axisymmetric solid elements CAX4. Four elements through the thickness were used for the whole domain. In the axial direction the test section has 50 elements, 40 elements in the linear taper and 20 elements for the thicker end segment (see Fig. 2.2).

The SAF2507 super-duplex stainless steel was modeled as a rate-independent, finitely deforming, elastic-plastic solid that hardens isotropically. The material model was calibrated using the true stress-logarithmic strain version of the measured uniaxial stress-strain response. The boundary conditions applied reproduced those of the experiments as (see Fig. 2.2). The tube was compressed by prescribing the axial displacement δ_x of the thicker end. The axial force was evaluated from the sum of reaction forces at all the nodes on the symmetry plane.

Figure 2.3 shows the stress concentration $\sigma_x / \overline{\sigma}_x$ ($\overline{\sigma}_x$ is the average axial stress at the mid-span of the specimen) vs. axial position measured from the point of thickness discontinuity (see Fig. 2.2). Included are results for the inner --$z = -t/2$-- and outer surfaces --$z = t/2$-- of the test section. The stress concentrations shown correspond to the beginning of compression for $\overline{\sigma}_x / \sigma_{ox} = 0.15$ and just after yielding for $\overline{\sigma}_x / \sigma_{ox} = 1.01$. The stress concentration of the inner surface varies between 0.96 and 1.01, and the one of the outer varies between 0.99 and 1.04. Included in the figure is also the corresponding axial profile of the mid-surface for $\overline{\sigma}_x / \sigma_{ox} = 1.01$. The radial displacement *w/R* varies between 0.36% and 0.59%. Thus we can conclude that the tapering of the specimen reduces significantly stress concentrations at the discontinuity.

2.1.2 Experimental Set-up for Axial Cycling of Tubes

The monotonic and cyclic experiments were performed in a universal servo-hydraulic testing machine with a 225 kips (10MN) capacity that can be operated in displacement or load control. The specimen was mounted into two 10 in (254 mm) solid steel, custom made axisymmetric grips which also serve as the mounts for various experimental accessories. The specimen was sealed with solid brass end-plugs as shown in Fig. 2.4. The ends of the specimen were secured in place with *Ringfeder* ring locking assemblies (3.54 in--89.92 mm ID) and suitable spacers. The arrangement provided a stiff testing conditions required for stability experiments. The load cell was calibrated to a 10V output at full scale.

An extensometer with a customized extension that enabled spanning the whole test section (Fig. 2.4) was used to monitor its change in length (range ±0.2 in--5.08 mm or 6.67% average strain). The extensometer was calibrated to a 10V output at full scale.

2.1.3 Axial Scanning of Tube Surface

A scanning device was used to periodically scan the surface of the test section during the tests. The device consists of a miniature LVDT mounted on a 12 in (304.8 mm) long linear encoder that allows monitoring the axial position of the transducer with a 10^{-4} in (2.54×10^{-3} mm) accuracy (see Fig. 2.4). The LVDT had a range of ±0.050 in (±1.27 mm) and was calibrated to a 10V full-scale output using a precise micrometer. The LVDT was gradually moved from one end of the test section to the other using a fishing line connected to small reel.

The axial scans were recorded using a separate data acquisition system developed in LabVIEW (see Fig. 2.5b). The linear encoder communicates with the data acquisition though an RS232 interface connected to a serial port of the computer. Each time a digital value of axial position arrives, the A/D records a corresponding value from the LVDT output. The measured radial deflection scan was modified by subtracting a linear trend to cancel any initial non-parallelism existing between the tube test section wall and the linear encoder (Bardi, 2006).

For monotonic loading, the tube was first scanned in the axial direction at zero axial displacement, and then at regular strain intervals as compression progressed. For cyclic experiments, the tube is scanned axially at zero load, at the end of the monotonic part of the loading, and subsequently during cyclic loading every 10 to 15 cycles.

2.1.4 Data Acquisition

During the experiment, voltage outputs from the testing machine corresponding to the axial load (F) and axial displacement, and from extensometer (δ_x) were recorded on a common time base using a digital data acquisition system operating in the LabVIEW environment (8 channel converter board with a 16 bit resolution) (see Fig. 2.5a). Data was recorded whenever the displacement of the machine changed by 0.001 in (0.0254 mm), the loading changed by 0.5 kips (2.224KN), the extensometer by 0.1% strain or every second (10 seconds while performing an axial scan of the test section of the tube). At the end of the experiment, the data was stored as text files which were transferred to PC computers for further analysis.

2.1.5 Experimental Procedure

2.1.5.1 Monotonic Compression

Before testing, brass plugs were inserted in the ends of the tubes. The tubes were then placed in the testing machine and the *Ringfeder* clamps were tightened. The clamps were tightened in a specific sequence to minimize any induced bending or shearing of the specimen. The specimen was then compressed at a prescribed displacement rate of 0.015 in/min (0.381 mm/min) which resulted in an axial strain rate of about 2×10^{-5} s^{-1}. Soon after the specimen started deforming plastically, the compression was paused and an axial scan was performed. Loading was then resumed and paused periodically for a series of scans. These scans were subsequently used to identify the onset of axisymmetric buckling. One or two of the wrinkles tended to localize and eventually a load maximum was reached, indicating the collapse of the specimen. After this the test was terminated, the tube was unloaded, and the experimental data was saved to a text file in the LabVIEW program.

2.1.5.2 Axial Cyclic Loading

For the cyclic experiments, the specimen was first preloaded to a compressive strain of $\varepsilon_C < \bar{\varepsilon}_{xmon} < \bar{\varepsilon}_L$ (see Fig. 2.6a and throughout this dissertation compressive axial strain and stress are positive) at a strain rate of approximately 2×10^{-5} s^{-1} under displacement control, so that wrinkles of small but finite amplitude appear on its surface. Then the shell was cyclically loaded under stress (load) control using the axial stress history shown in Fig. 2.6b with an amplitude of σ_a about a compressive mean stress of σ_m with periods of two minutes. These two stress values will be chosen such that the maximum compressive stress in the cycle corresponds to the value at which the specimen was unloaded from during the initial monotonic phase of the loading history.

Axial scans were performed at zero load, at the end of the monotonic part of the loading (i.e., at $\bar{\varepsilon}_{xmon}$), and subsequently during cyclic loading every 10 to 15 cycles.

2.2 EXPERIMENTS UNDER AXIAL CYCLIC LOADING WITH INTERNAL PRESSURE

2.2.1 Test Specimens

The tube specimens for the experiments under axial cycling with internal pressure were similar to those used in the experiments under pure axial loading (see Fig. 2.7). However, the test section was increased to 4.0 in (101.6 mm) in order to accommodate the longer wrinkle wavelength that develops for compression under internal pressure (Paquette and Kyriakides 2006).

A stress concentration occurs at the interface of the taper and the test section. The specimen was analyzed again using finite elements in order to evaluate the effect of the thickness discontinuities. The geometry used in the finite element model is similar to that in Fig. 2.2 except that the length of the test section was 4 in (101.6 mm) long. The domain was also discretized by four-nodes, linear, axisymmetric elements CAX4. The mesh, material model, boundary conditions and the prescribed loading increments were the same as before. The specimen was compressed at an internal pressure of $P/P_o = 0.59$.

Figure 2.8 shows the stress concentration along the length of the test section for a tube with $D/t = 28.38$. Included are results for the inner --$z = -t/2$-- and outer surfaces --$z = t/2$-- of the test section. The stress concentrations shown correspond to the beginning of compression for $\bar{\sigma}_x/\sigma_o = 0.15$ and just after yielding for $\bar{\sigma}_x/\sigma_o = 1.01$. The stress concentration of the inner surface varies between 0.93 and 1.05, and the one of the outer varies between 0.90 and 1.04. Included in the figure is also the corresponding axial profile of the mid-surface for $\bar{\sigma}_x/\sigma_o = 1.01$. The radial displacement *w/R* varies between 1.01% and 1.08%. Thus we can conclude that the tapering of the specimen reduces adequately stress concentrations at the discontinuity for this loading also.

2.2.2 Experimental Set-up for Axial Cycling of Tubes with Internal Pressure

The experimental set-up was similar to the one used in the experiments under pure axial loading described above except that an independent closed loop control pressurization system was used to pressurize the specimens (see Fig. 2.9). It consists of a 10,000 psi (68.95 MPa) pressure intensifier, which operates on standard 3,000 psi (20.68 MPa) hydraulic power. The pressure is monitored by a pressure transducer attached to the upper grip as shown in the figure. The transducer was calibrated to a 10V output at 10,000 psi (68.95 MPa). The system was run under pressure control in these experiments. Strain gages were used to measure the circumferential strains at usually two locations in the test section of specimens.

2.2.3 Axial Scanning of Tube Surface

A new scanning device was used to periodically scan the surface of the test section for experiments under axial cycling with internal pressure. The device consists of a non-contact laser displacement transducer mounted on a lead screw-driven slide. The slide is equipped with a rotary encoder that allows monitoring the axial position of the transducer (see Fig. 2.9). The transducer (Keyance LK-G82) sends a beam to the surface of the specimen; the reflection passes through a lens system and is received by a Li-CCD that is at some distance from the source of the emitted beam. The displacement of the reflecting surface is then evaluated by triangulation. The specific transducer used has a range of 3.15 ± 0.59 in (80 ± 15 mm) and was operated at a resolution of 3.94×10^{-5} in (1 μm) with a spot size of about 2.76×10^{-3} in (70 μm). The transducer is operated by an LK-G controller and operated by software LK-Navigator in PC to set up input and output signals. The analog output must be turned on and the corresponding calibration was 1V for 0.0394 in (1 mm) radial displacement. The instrument operates at 50 kHz.

The surface is scanned axially along a generator by manually rotating the slide lead screw causing translation of the transducer. The lead screw thread (20 TPI) combined with the encoder (HEDS5500-A06 with 500 CPR) provides an axial resolution of 10^{-4} in-- 2.54×10^{-3} mm (10000 counts per inch). The count is performed using a PCI-QUAD04 PC card that operates in conjunction with a LabVIEW subroutine. The resultant displacement is recorded in the data acquisition system on a common time base with the laser transducer output (flowchart of the data acquisition system shown in Fig. 2.10b).

In monotonic compression tests the specimen was first scanned at zero load, and at regular intervals during the loading. In the cyclic experiments the specimen was scanned several times during the monotonic part of the loading, and every 10 to 15 cycles during cycling. The high resolution of the transducer makes it sensitive to surface roughness and vibrations. The noise was reduced by mounting the instrument and the slide on a stiff support structure (only shown partially in Fig. 2.9). Despite this improvement, the signals still exhibited some high frequency noise that had to be filtered out. The radial deflection output was modified by subtracting a linear trend to cancel any non-parallelism existing between the tube test section wall and the lead screw-driven slide.

2.2.4 Data Acquisition

An extensometer with a customized extension that enabled spanning the whole test section (Fig. 2.9) was used to monitor its change in length (range $\pm 0.2\,\text{in}$--5.08 mm or ±5.0% average strain). The extensometer was calibrated to a 10V output at full scale.

The signals from the load, displacement, strain, and pressure transducer were all recorded on a common time base using a digital data acquisition system operating in the LabVIEW environment (8 channel converter board with a 16 bit resolution) (see Fig. 2.10a).

2.2.5 Experimental Procedure

2.2.5.1 Monotonic Compression

The testing procedure used for the pressurized specimens was similar to the one for pure monotonic compression except that the specimens were first pressurized to a pre-chosen level and then compressed monotonically at a constant displacement rate of rate of 0.015 in/min--3.81 mm/min (corresponds to an average strain rate of about 2×10^{-5} s^{-1}).

2.2.5.2 Axial Cyclic Loading under Constant Internal Pressure

The testing procedure was similar to that of the pure axial loading cyclic experiments except that the tubes were first pressurized to a pre-chosen level and kept constant. Then the tubes were compressed under displacement control to $\bar{\varepsilon}_{xmon}$, a strain that lies between the critical wrinkling strain ε_C and the limit strain, $\bar{\varepsilon}_L$, corresponding to this pressure as shown in Fig. 2.11a; in other words, ensuring that wrinkles of small but finite amplitude appear on their surfaces. The tubes were subsequently cycled under stress (load) control using the axial stress history shown in Fig. 2.11b, with an amplitude σ_a and a compressive mean stress σ_m (Fig. 2.11b). The two stress levels were selected such that the maximum compressive stress in the cycle corresponded to the value at which the specimen was unloaded from during the initial monotonic phase of the loading history (i.e., $\sigma_m + \sigma_a = \sigma_x(\bar{\varepsilon}_{xmon})$). Although the two strains are coupled, one can say that the ratcheting in the axial direction depends mainly on the amplitude and mean stress of the axial stress cycles while the pressure affects mainly the ratcheting in the hoop direction. The test was terminated before a sign that the structure was close to collapse.

CHAPTER 3

WRINKLING DUE TO AXIAL CYCLING: EXPERIMENTAL RESULTS

This Chapter presents results from experiments involving tubes cycled axially under stress control about a compressive mean stress. This type of cycling can result in material ratcheting or accumulation of compressive strain. Since the tubes tested were pre-wrinkled, the main objective of the experiments was to understand and quantify how material ratcheting interacts with wrinkling. To set the stage for the cyclic experiments, plastic buckling of tubes under monotonic compression is reviewed first.

3.1 REVIEW OF MONOTONIC COMPRESSION

The problem of plastic buckling of tubes due to compression was studied extensively by Bardi and Kyriakides (2006). They conducted compression experiments of SAF2507 tubes with D/t values in the range of 23-52. Similar experiments were also performed in the present study for the tube geometry and material properties of the specimens that were cycled. Figure 3.1 shows one of the recorded nominal stress (σ_x)-shortening (δ_x / L, $L \equiv$ gage length) response for a tube with D/t = 28.71. It exhibits a linear elastic regime following by yielding typical of a hardening material. Under persistent compression the response modulus gradually decreases and attains a limit load at an average strain of 4.5%.

Figure 3.2a shows a 3-D rendering of a set of axial scans of the radial displacement (w/R) of the surface of the test section along a generator at different average strain levels ($\bar{\varepsilon}_x \equiv \delta_x / L$). The scans correspond to the locations marked with solid bullets on the response in Fig. 3.1. The results are similar to those reported in Bardi and Kyriakides (2006). Initially, the test section deforms uniformly and the axial displacement scans change very little. Signs of gradual growth of small initial imperfections can be seen in the scan at $\bar{\varepsilon}_x = 1.0\%$. By an average strain of 1.15%, the scan starts to show a wavy pattern that becomes even clearer at $\bar{\varepsilon}_x = 1.45\%$. At even higher average strains, the wavy patterns become fully developed with clear peaks and valleys as the tube has wrinkled in a nearly axisymmetric manner. The amplitude of the wrinkles grows with compression, and in the process the axial stiffness of the tube gradually reduces. At the same time, the amplitudes of the wrinkles at the ends of the test section start to grow faster (see selected scans in Fig. 3.2b). At an average strain of 4.5% a load maximum develops, causing deformation to localize further this time on the LHS of the specimen. The experiment was interrupted at $\bar{\varepsilon}_x = 5.2\%$ and unloaded. The last scan included in Fig. 3.2b was recorded just prior to unloading.

As in Bardi and Kyriakides (2006), we will associate the first signs of wrinkling with the value yielded by a plastic bifurcation analysis associated with an axisymmetric buckling mode (i.e., the mathematical idealization of buckling; see Kyriakides *et al.*, 2005). In this case our best estimate of the onset of wrinkling is bounded between strains of 1.15% and 1.45%, marked with arrows (↓) on the response in Fig. 3.1. The corresponding stresses are included in Table 3.1 under σ_C. The bounds for ε_C are included in Fig. 3.3 (using ◆◇), where similar experimental results from Bardi and Kyriakides (2006) are plotted vs. D/t on log-log scales. The corresponding calculated critical strain is drawn with a solid line. The two sets of new results are seen to follow the trend of the previous results.

The recorded stress maximum and the corresponding strain ($\bar{\varepsilon}_{Lmon}$) are associated with the onset of collapse. The data from the five experiments are also included in Fig. 3.3 (using ▼), where again they are seen to be in reasonable agreement with the results of Bardi and Kyriakides (2006). Thus, in this case the onset of wrinkling is separated from collapse by an average strain of about 3%. The wavelengths of the wrinkles (2λ) were measured and found to also vary within a range partly influenced by the finiteness of the test section (see Table 3.1). The wavelengths are again in line with those reported in Bardi and Kyriakides (2006). A total of five monotonic compression tests were performed and the specimen parameters and critical variables measured are summarized in Table 3.1.

3.2 REPRESENTATIVE CYCLIC LOADING EXPERIMENTAL RESULTS

Results from Exp. CWR6 are now used to describe the main features of experiments under axial cyclic loading. The main geometric parameters of the test specimen are listed in Table 3.2. The mechanical properties of the mother tube from which the specimens were extracted were measured in independent experiments and the main parameters are given in Table 3.3. Figure 3.4a shows the stress-displacement response recorded. This tube was compressed to $\bar{\varepsilon}_{xmon}$ = 2.24% and then unloaded. The maximum stress reached during this part of the test was σ_{xmon} = 108.5 ksi (748.5 MPa). Figure 3.4b shows axial scans of the initial unloaded tube surface and one following plastic deformation from monotonic compression (N = 0). By the time the compression level reached $\bar{\varepsilon}_{xmon}$, several wrinkles are seen to have formed in the test section. The specimen was then cycled axially in compression under load control about a mean stress σ_m = 37.71 ksi (260.1 MPa) and an amplitude σ_a = 70.82 ksi (488.4 MPa) (see Fig. 3.4a); in other words, the maximum stress in each cycle corresponds to the monotonic unloading stress σ_{xmon}. The specimen immediately starts to ratchet axially as evidenced by the stress-displacement response in Fig. 3.4a. Figure 3.4c shows a plot of the peak displacement (δ_x^p / L) in each cycle vs. the number of the cycle N. Following an initial transient that in this case lasts a few cycles, ratcheting settles to a nearly constant rate. In the neighborhood of cycle 150 (corresponds to an average strain of about 3.4%), ratcheting starts to accelerate eventually growing exponentially. The width of the stress loops in Fig. 3.4a progressively increases, the peaks of the cycles become rounder and in the last cycle recorded (N = 182) the stress is seen to reach a peak and then to decrease before unloading commences. This is a sign that the structure is close to collapse and control was lost for part of the cycle.

Table 3.3 Mechanical properties of SAF 2507 tubes used in the experiments

Mat.	E Msi (GPa)	σ_{ox} ksi (MPa)	S_θ †	S_r †
SAW6	28.2 (195)	88.0 (607)	1.15	0.85

† From Table 2 in Bardi and Kyriakides (2006)

Figure 3.4b shows axial scans taken initially every 30 cycles and in the later parts of the test more often (see cycle numbers in the inset). Wrinkling is seen to localize at an increasing rate at one of the ends of the test section. Indeed we know from experience that this specimen would not be able to survive even one more load cycle, as this most pronounced wrinkle would collapse in the manner shown in Fig. 12 of Bardi and Kyriakides (2006). The test was thus terminated after cycle 182. Figure 3.4d shows a photograph of the specimen after the test. The localization of the wrinkle in the upper part of the test section is quite obvious. Included in Fig. 3.4c is the amplitude of this dominant wrinkle ($w_{\max}/R$) vs. N. The trend of the growth of this variable is similar to that of δ_x^p. Clearly the recorded ratcheting in δ_x is partly due to accumulation of material strain and partly due to shortening caused by the growth of the amplitude of the wrinkles, which can be viewed as a structural "damage". In the early stages of the cyclic history, material ratcheting is the main contributor while in the later parts, during the exponential growth of δ_x^p and $w_{\max}$, the contribution of wrinkling dominates (note that under compression there is no reason for material ratcheting to accelerate).

The nature of $\delta_x^p - N$ plot in Fig. 3.4c is of course reminiscent of a constant load creep curve with N replacing time. Indeed, the results exhibit the instantaneous deformation of a creep curve followed by a *primary (or transient)*, a *secondary* (or *steady state*) and a *tertiary* regime that here ends with collapse as opposed to rupture in creep. As in creep, the present phenomenon has two mechanism, material ratcheting and structural degradation in the form of wrinkle growth. But unlike creep where strain hardening and recovery are competing, here the two mechanisms cooperate. The tertiary creep regime is more complex in which it can involve additional mechanisms such as grain boundary separation, internal formation of cracks and voids. In the present phenomenon the wrinkle growth becomes more dominant in the tertiary regime.

In search of a simple measure of the life expectancy of a tube cycled in this manner, we compare collapse under monotonic and under cyclic loads. Thus the horizontal dashed line drawn in Fig. 3.4c corresponds to the average of the strains ($\bar{\varepsilon}_{Lmon} = 4.33\%$) at the limit loads recorded in the five monotonic experiments. Clearly, in this case the onset of collapse under the cyclic loading history applied occurs very close to the average collapse strain recorded in the monotonic experiments. This important conclusion will be further scrutinized in the light of additional experiments.

Detailed results from a second cyclic experiment are shown in Fig. 3.5 in order to illustrate the influence of some of the main parameters of the problem on the induced ratcheting and localization. In this case (Exp. CWR4) the specimen was preloaded to the slightly smaller average compressive strain of $\bar{\varepsilon}_{xmon} = 2.18\%$ reaching a corresponding stress of 107.21 ksi (739.4 MPa). The specimen was then cycled axially with an amplitude of $\sigma_a = 70.33$ ksi (485 MPa) about a mean stress of $\sigma_m = 36.88$ ksi (254.3

MPa) (see Fig. 3.5a). The maximum stress of the cycles is again very close to the value reached during monotonic compression. Although σ_a is about the same as the value in the previous experiment, the peak-to-peak stress level of the cycles is somewhat smaller. Figure 3.5b shows that the initial compression wrinkled the tube rather uniformly, but the wrinkles had smaller amplitude than those of CWR6 in Fig. 3.4b (as will be illustrated using analysis, the amplitude of the initial wrinkles is also influenced by initial imperfections in the tube). This and the somewhat milder stress cycles induce a slower rate of ratcheting as is illustrated in the recorded stress-displacement response in Fig. 3.5a and in the plot of the cycle peak displacement vs. the number of the cycle in Fig. 3.5c. The same can be said for the rate of growth of the wrinkle amplitude as illustrated by the $w_{\max}/R - N$ plot included in Fig. 3.5c. Following a small initial transient, the rate of ratcheting settles to a nearly constant value that is maintained for about 250 cycles. By this time the amplitude of all wrinkles has grown significantly albeit quite uniformly. Subsequently the rate of ratcheting starts to accelerate and the loops traced become increasingly wider. The rate of growth of the amplitude of the wrinkles also accelerates while simultaneously the deformation localized in one of the ends (see Fig. 3.5c). The experiment was terminated after cycle 340. Included in Fig. 3.5c is the average strain at the limit load of the monotonic tests ($\bar{\varepsilon}_{Lmon}$). Once more this value is seen to correspond quite well to the cyclic displacement at which the rate of ratcheting and localization are accelerating significantly.

3.3 SUMMARY OF CYCLIC LOADING EXPERIMENTAL RESULTS

A total of 10 cyclic experiments like the two described in Section 3.2 were performed in which the main parameters influencing the rate of ratcheting were further evaluated (see Table 3.2). In the interest of brevity we will mainly report and compare the rate of ratcheting recorded as represented by the net shortening per cycle ($\delta_x^p - N$) response. The stress-shortening responses and the evolution of wrinkles for the balance of this set of experiments appear in Appendix C. In Fig. 3.6a we compare the ratcheting results from 6 experiments, which had approximately the same average compressive pre-strain of $\bar{\varepsilon}_{xmon} \approx 2.3\%$ but different cycle amplitudes, σ_a, given in the inset. In each case σ_m was chosen so that the maximum stress of the first cycle matched the maximum stress reached during the initial monotonic loading (see Table 3.2 for details). All trajectories have the characteristic shape of creep curves differing mainly in the extent of the initial transient and that of the steady state. As expected, the effect of σ_a on the rate of ratcheting, represented by the slope of the nearly linear parts of the trajectories, is very significant. Furthermore, in all cases at some point the rate of growth of δ_x^p starts to accelerate becoming exponential. All specimens were cycled up to the point when collapse was eminent at which time the test was terminated.

Included in Fig. 3.6a is the average strain at the limit loads of the five monotonic loading tests ($\bar{\varepsilon}_{Lmon} = 4.33\%$). This strain level is seen to fall in the part of each trajectory where the rate of ratcheting is in the accelerated rate regime albeit in some cases in the earlier parts and in some in the latter parts of these regimes. This trend confirms the observation made earlier that under cyclic loading the specimens tend to collapse at average strain levels that approximately correspond to that at collapse under monotonic loading. Thus, the average strain under monotonic loading seems to be the maximum strain that the structure can undergo irrespective of how this strain is developed (accumulated). This is a very strong result indeed as it provides a simple means of estimating the life expectancy of such structures under cyclic loads. This observation is reminiscent of a similar one reported in Kyriakides and Shaw (1987) and Corona and Kyriakides (1991) regarding the life span of Al-alloy tubes cyclically bent plastically. This type of cycling causes accumulation of ovalization that eventually leads to collapse. The cycled structure collapses when the accumulated ovalization reaches the value at which it collapses under monotonic bending (similar results were reported recently by Chang and Pan (2009) for stainless steel tubes). Figure 3.6b shows the initial wrinkles of CWR2, CWR6 and CWR7 at the end of monotonic loading. The amplitudes of the different initial wrinkles are approximately the same, which indicates that the initial imperfections of these specimens are very similar. (The same initial imperfections will be adopted in the simulations of CWR2, CWR6 and CWR7 in Chapter 6.)

Figure 3.7a shows a second set of ratcheting results from experiments in which the specimens were loaded to different levels of strain during monotonic loading while the cycle amplitude was kept constant (σ_a = 70.33 ksi – 485 MPa). In each case the mean stress had to be adjusted slightly in order to match the maximum stress of the cycle with the maximum stress level achieved during monotonic loading (see values in figure inset). Increasing $\bar{\varepsilon}_{xmon}$ increases the amplitude of the initial wrinkles as illustrated in Fig. 3.7b. The $\delta_x^p - N$ results in Fig. 3.7a show that larger initial wrinkles tend to increase the rate of ratcheting and decrease the number of cycles to collapse. Thus, Exp. CWR4 with $\bar{\varepsilon}_{xmon}$ = 2.18% collapsed after 340 cycles while CWR8 with $\bar{\varepsilon}_{xmon}$ = 3.0% reached a critical state after 130 cycles. Once more the rate of ratcheting is seen to accelerate when the accumulated deformation approaches $\bar{\varepsilon}_{Lmon}$.

As pointed out earlier, each tube has unique, small initial geometric imperfections that influence the onset of collapse both under monotonic and cyclic loadings. The test specimens were first bored and rimmed on the inside and the outer surface, including the linear tapers, was turned last in an NC lathe. The two-step process ends up with very round inner and outer surfaces but minor misalignments in the two setups can result in a small amount of wall eccentricity and misalignment of the axes of the two surfaces.

These imperfections were measured manually and their extent manifests in the thickness variations reported in Table 3.2. A wall thickness variation of about 0.0015 in (38 μm) and a wall eccentricity of about 2% are typical ($\Xi_o = (t_{\max} - t_{\min})/(t_{\max} + t_{\min})$). Figure 3.8 shows the repercussions of variation of imperfections on the rate of ratcheting. Chosen are results from tubes with extreme differences in their imperfections. Figure 3.8a shows ratcheting results from three experiments that were compressed to the same average strain of $\bar{\varepsilon}_{xmon}$ = 2.6% and then cycled with the same cyclic stress parameters. Two of the specimens, CWR9 and CWR13, have similar ratcheting responses and a life span of 271 and 235 cycles respectively. Both of these tubes sustained average strains that are somewhat higher than the 4.33% level of the monotonic loading tests.

The third experiment included in Fig. 3.8a, CWR11, ratcheted at a much faster rate and lasted only 83 cycles and sustained an average strain that is very close to the level of the monotonic tests. The cause of this difference can be seen in Fig. 3.8b which shows axial profiles of the wrinkles developed in each tube from the 2.6% shortening induced by monotonic loading. First, the wrinkle profiles are distinctly different in the three cases, and second their amplitudes differ. CWR9 has the smallest amplitude, CWR13 somewhat larger while the amplitude of CWR11 is essentially double that of CWR9. The cause of this difference is a somewhat larger eccentricity and inner/outer surface axis misalignment recorded for CWR11.

The influence of initial imperfections on the evolution of wrinkles is further illustrated in Figs. 3.9a and 3.9b. Figure 3.9a shows a set of wrinkle profiles recorded during the cyclic history of CWR9. In this case, the amplitude of wrinkles caused by monotonic loading is relatively small while the wrinkles are uniformly distributed in the test section. At small cycle counts they grow nearly uniformly. At a relatively high cycle count ($N > 250$) deformation localizes close to one end of the test section. By contrast, in the case of CWR11, monotonic compression results in wrinkles of much larger amplitude. Consequently they grow faster with N and localize at a significantly smaller cycle count.

CHAPTER 4

WRINKLING DUE TO AXIAL CYCLING AND INTERNAL PRESSURE: EXPERIMENTAL RESULTS

This Chapter presents results from experiments involving pressurized tubes cycled axially under stress control about a compressive mean stress. This type of loading can result in material ratcheting, or accumulation of compressive strain, both on the axial and circumferential direction, or in other words this is biaxial ratcheting. Since the tubes tested were pre-wrinkled and pressurized, the main objective of the experiments was to understand and quantify how biaxial ratcheting interacts with wrinkling. To set the stage for the cyclic experiments, plastic buckling of tubes under monotonic compression with internal pressure is reviewed first.

4.1 EXPERIMENTAL RESULTS-MONOTONIC COMPRESSION WITH INTERNAL PRESSURE

In the way of setting the problem up let us first review plastic buckling under compression and internal pressure. Paquette and Kyriakides (2006) investigated the problem is detail by conducting compression experiments on pressurized super-duplex 2507 tubes with D/t values of 39.8 and 28.3. They showed that the general features of plastic buckling under combined axial compression and internal pressure are similar to those of pure axial loading reported in Bardi and Kyriakides (2006) and Bardi *et al.* (2006). Their findings are summarized and confirmed for the present material and geometry in Fig. 4.1 where monotonic compressive responses for an un-pressurized and a pressurized tube are compared. The tubes were machined out of SAF 2507 super-duplex stainless steel and had $D/t = 28.5$.

Starting with the zero pressure case, compression yields the tube, which initially deforms uniformly. Point a at a strain of 1.25% represents the onset of wrinkling, which can be evaluated straight forwardly using a plastic bifurcation algorithm as described in Appendix B (see also Lee, 1962; Batterman, 1965; Kyriakides *et al.*, 2005; Kyriakides and Corona, 2007). The wrinkle amplitude starts very small but grows as the compression increases. This leads to a gradual reduction in the axial rigidity of the structure and the eventual development of a limit load instability at point b at the much higher average strain of 3.85%. Beyond this point the structure starts to collapse by localization of usually one of the wrinkles. Thus, the average strain at b constitutes a limit state.

Compression in the presence of internal pressure leads to a similar response but with a lower stress trajectory represented by o'a'b'c' in Fig. 4.1. (Test conducted under displacement control. The initial tensile stress is caused by the pressure that is applied before compression commences). However, the significant difference in strain between the onset of wrinkling and collapse remains. Figures 4.2, taken from Paquette and Kyriakides (2006), show how the critical variables are influenced by the level of internal pressure at which the test was conducted. The limit stress (σ_L) decreases with P, the average limit strain ($\bar{\varepsilon}_{Lmon}$) increases slightly and the bifurcation strain (ε_C) remains essentially constant. (In Fig. 4.1 the pressurized case has a somewhat lower $\bar{\varepsilon}_{Lmon}$ than the unpressurized response. This is mainly due to differences in small initial imperfections between the two tubes that tend to affect the onset of collapse.)

4.2 RESULTS FROM A TYPICAL AXIAL CYCLING UNDER PRESSURE EXPERIMENT

Results from Exp. CWR34 are now used to describe the main features of the ratcheting behavior in the presence of pressure. The main geometric parameters of the test specimen are listed in Table 4.1. The mechanical properties of the two mother tubes from which the specimens were extracted were measured in independent experiments and the main parameters are given in Table 4.2. Included are the yield anisotropy parameters

(S_r,S_θ) measured as described in Appendix A. The pressure was first ramped up to 4000 psi (276 bar = $0.59P_o$). The specimen was then compressed under displacement control to $\bar{\varepsilon}_{xmon}$ = 2.04% when the axial load was removed. Figure 4.3a shows the stress-displacement response recorded. The maximum stress reached during this part of the test was σ_{xmon} = 86.8 ksi (599 MPa). Figure 4.4a shows axial scans of the normal displacement of the surface, *w*, in the initial unloaded state and following plastic deformation from monotonic compression (*N* = 0). The initial surface of the tube shows minimal imperfections. By the time the compression level reached $\bar{\varepsilon}_{xmon}$, three wrinkles have formed in the test section. The half wavelength of the wrinkles, λ, listed in Table 4.1 is 0.548*R* a value that is close to that predicted by plastic bifurcation analysis (see Appendix B).

Table 4.2 Mechanical properties of SAF 2507 tubes used in the experiments

Mat.	*E* Msi (GPa)	σ_{ox} ksi (MPa)	S_θ	S_r
SAW7	28.2 (195)	84.5 (583)	1.15	0.85
SAW8	28.2 (195)	92.8 (640)	1.09	0.88

The specimen was subsequently cycled axially under load control about a mean stress σ_m = 18.8 ksi (129 MPa) and an amplitude σ_a = 68.0 ksi (469 MPa) (Fig. 4.3a); in other words, the maximum compressive stress of each cycle corresponds to the monotonic unloading stress σ_{xmon}. The specimen immediately starts to ratchet axially as evidenced by the stress-displacement response in Fig. 4.3a. Figure 4.3b shows a plot of the peak displacement (δ_x^p/L) in each cycle vs. the number of the cycle *N*. Following an initial transient that lasts a few cycles (~20), ratcheting settles to a nearly constant rate. Simultaneously, because of the internal pressure the tube ratchets in the circumferential direction. This is illustrated in Fig. 4.4a where the axial scans of w are seen to gradually shift towards larger values as N increases indicating that the diameter of the tube is gradually growing. The ratcheting in the hoop strain is also recorded by the two strain gages, one located close to the central wrinkle peak (SG1) and the second in one of the valleys (SG2) as shown in Fig. 4.4a. The peak values recorded by the two gages every fourth cycle are plotted against N in Fig. 4.4b. Both show a healthy rate of ratcheting with SG1 growing much faster than SG2 due to its more favorable location. A more complete picture of the biaxial ratcheting is shown in Fig. 4.5 where the average axial strain is plotted against the hoop strain measured by SG1. Clearly, the interaction of the two strains is rather complex and evolves with N. However, it can be seen that the axial strain is accumulated at nearly twice the rate of the hoop strain. The early part of this response is reminiscent of biaxial ratcheting results reported in the material tests of Hassan *et al.* (1992) conducted on heat-treated carbon steel 1026.

As the cycling progresses, the amplitudes of the three waves in the test section grow while simultaneously a tendency for the two outer ones to grow faster than the central one develops. Despite the linear tapers that were built into the ends of the specimens, some small stress concentrations still remain at the discontinuities causing this amplified growth. Figure 4.3b includes a plot of the amplitude of the LHS wave ($w_{\max}/R$) vs. N. $w_{\max}$ experiences also an initial transient followed by a nearly linear rate of growth. However, in the neighborhood of cycle 190 ($\delta_x^p/L \approx 2.87\%$) the axial ratcheting starts to accelerate (Fig. 4.3b) while the circumferential one starts to decelerate somewhat (Fig. 4.4b). Concurrently, deformation starts to localize in the wave on the LHS whose amplitude is seen in Fig. 4.3b to grow at an increasing rate. In fact both δ_x^p and $w_{\max}$ grow exponentially after cycle 250. During this growth the width of the stress loops in Fig. 4.3a progressively increases, the peaks of the cycles become rounder and in the last cycle recorded (N = 284), the stress is seen to reach a peak and then to decrease before unloading commences. This is a sign that the structure is close to collapse and control was lost for part of the cycle. The test was terminated at this point as experience taught that collapse was eminent. Figure 4.6a shows a photograph of a specimen tested under similar conditions (CWR39) after the test. The three axisymmetric waves that developed are clearly visible as is also the more pronounced growth of the top wrinkle.

In summary, cycling the tube axially under constant pressure leads to material ratcheting in both the hoop and axial directions. For the particular load parameters of the present problem the rate of the axial ratcheting is nearly double that in the hoop direction. The axial strain accumulation promotes growth of the wrinkles formed during the pre-compression. At some stage wrinkling localizes in one of the wrinkles and subsequent cycling contributes mainly to its growth. This growth of the amplitude of this wrinkle becomes exponential and this in turn makes the growth of the average axial strain (δ_x^p / L) also exponential as this variable reflects partly accumulation of material strain and partly the shortening caused by the growth of the amplitude of the wrinkles.

Following the trends of the purely axial cyclic experimental results in Chapter 3, we include in Fig. 4.3b the average strain corresponding to the limit load recorded in a monotonic compression experiment ($\bar{\varepsilon}_{Lmon}$) conducted at the same pressure level (Exp. CRW45 in Table 4.3). Clearly, here too the exponential growth of the wrinkle that leads to collapse coincides with the average strain at the onset of collapse under monotonic compression.

4.3 SUMMARY OF EXPERIMENTAL RESULTS

The experimental program involved a total of 13 experiments similar to the one described in Section 4.2 in which the main parameters that influence ratcheting that is the internal pressure, the amplitude and mean stress of the axial cycles, and the pre-strain are further evaluated. The geometric and loading parameters of the experiments are listed in Table 4.1. In the interest of brevity here we will report and compare the measured shortening (δ_x^p) and the circumferential strain ($\varepsilon_{\theta p}$) vs. N responses. The stress-shortening responses and the evolution of wrinkles for the balance of this set of experiments appear in Appendix D. The experiments are grouped based on the main loading parameter varied.

4.3.1 Variation of Internal Pressure

Figures 4.7 and 4.8 present results from four experiments that were tested at four different levels of pressure (0, 0.22, 0.49, 0.60) P_o. They were all pre-compressed to the same strain level of 2.5% and cycled axially with the same stress amplitude of σ_a = 56 ksi (386 MPa). Once again, in order to satisfy the requirement that $(\sigma_m + \sigma_a) = \sigma_x(\bar{\varepsilon}_{xmon})$, σ_m had to be changed for each case because internal pressure tends to lower the axial stress-strain response of the tube (see Fig. 4.1 and Table 4.1). Figure 4.7 shows the recorded $\delta_x^p / L - N$ results and Fig. 4.8a the hoop peak strains vs. N ($\varepsilon_{\theta p} - N$) at two locations in the test section of each of the three pressurized tubes. Figure 4.8b shows the wrinkle profiles of the four tubes at the completion of the initial monotonic compression. The locations of the two strain gages are marked as SG1 and SG2 with solid bullets on the profiles. Typically SG1 is closer to a wrinkle peak and SG2 to a valley. The locations dictate the difference in the two values of $\varepsilon_{\theta p}$ (Fig. 4.8a).

Before continuing with the evaluation of the ratcheting results it is worth taking a closer look at the wrinkle profiles. As pointed in Paquette and Kyriakides (2006), internal pressure tends to increase the wrinkle wavelength and this is observed in the results in Fig. 4.8b as well as in the measured λs listed in Table 4.1. Furthermore, as reported in earlier, each tube has unique, small initial geometric imperfections that influence to some degree the onset of collapse both under monotonic and cyclic loadings. The fabrication of the specimens (see Sections 2.1.1 and 3.3) results in circular inner and outer surfaces but minor misalignments in the two setups can produce a small amount of wall eccentricity and misalignment of the axes of the two surfaces. The extents of these imperfections are quantified in Table 4.1. A wall thickness variation of about 0.001 in (25 μm) and a wall eccentricity of less than 1% are typical. Although these variations are small, they can still influence the development of wrinkles and the onset of collapse. Thus, two seemingly identical specimens tested under the same conditions can produce somewhat different wrinkle patterns. The influence of such imperfections will be further scrutinized in the results that follow.

Returning to the ratcheting results in Figs. 4.7 and 4.8a, it can be seen that pressure decreases the number of cycles and average strain at collapse, and increases the ratcheting rate of circumferential strain. Included in Fig. 4.7 are the average strains at the onset of collapse under monotonic compression at the same pressure level (see also Table 4.3; it is noted that two of these results come from experiments and two from analysis along the lines of that of Paquette and Kyriakides, 2006). For Exps. 40, 41 and 44 the exponential growth parts of the $\delta_x^p / L - N$ plot agree well with $\bar{\varepsilon}_{Lmon}$ whereas for Exp. 42 the specimen collapsed at a lower strain level after only 38 cycles. This specimen developed a larger amplitude wrinkle away from the ends, during the initial monotonic compression (Fig. 4.8b). This is presumably caused by initial imperfections (observe that the wall eccentricity and thickness variation of this tube are larger than the average values of the rest of the specimens—Table 4.1). Figure 4.9a shows a set of wrinkle profiles recorded during the cyclic history of Exp. 42. Clearly, the central wrinkle dominated the deformation behavior as the remainder of the test section changed only modestly. The localization of this wrinkle can also be seen in the photograph of this specimen in Fig. 4.6b taken at the end of the experiment.

Experiment 44, cycled without internal pressure, illustrates the opposite behavior. In this case the initial imperfections were smaller than usual (see Table 4.1) and so a very small amount of wrinkling was recorded after the monotonic compression. As a result, both the ratcheting of δ_x and the wrinkles amplitudes (Fig. 4.9b) grew rather slowly with *N*. Wrinkling localized eventually at one of the ends but collapse took 1441 cycles. Furthermore, the average strain at collapse was close to 5% as opposed to values of 4.33% reported in similar experiments in Chapter 3. The value of $\bar{\varepsilon}_{Lmon}$ of 4.92% was calculated using unusually small initial imperfections (see Table 4.3).

4.3.2 Variation of σ_a

Next we consider a set of three experiments that were tested at a common pressure of $0.59\,P_o$. They were pre-compressed to the same level of $\bar{\varepsilon}_{xmon}$ = 2.0% but were cycled with a different stress amplitude. Results for σ_a = (60, 64, 68) ksi or (414, 441, 469) MPa are summarized in Figs. 4.10 and 4.11. Figure 4.10 shows the measured peak shortenings as a function of *N* and Fig. 4.11a the peak hoop strains at two locations. Clearly, increasing σ_a tends to increase somewhat the axial ratcheting but more importantly causes the tube to collapse in fewer cycles. The wrinkle profiles after the initial monotonic compression plotted in Fig. 4.11b are seen to be very similar. Consequently the final exponential growth in δ_x^p that is associated with collapse is seen to occur at the same strain level. This strain level is also in good agreement with the average strain at the limit load ($\bar{\varepsilon}_{Lmon}$) measured in a monotonic loading experiment (CWR45 in Table 4.3). The pairs of hoop strain plots in Fig. 4.11a measured at the two locations marked on the wrinkle profiles in Fig. 4.11b do not show any significant difference indicating a relative insensitivity to σ_a.

Figures 4.12 and 4.13 show results from three similar experiments that were tested at a pressure of $0.49\,P_o$. The three tubes were also pre-compressed to the same $\bar{\varepsilon}_{xmon}$ = 2.0% and were cycled at σ_a = (54, 56, 58) ksi or (372, 386, 400) MPa. The $\delta_x^p - N$ results in Fig. 4.12 show a reduction in the number of cycles to collapse with increasing σ_a that is even more pronounced than that in Fig. 4.10. Furthermore, the average strain levels at collapse are quite different with CWR31 failing at a higher strain than CWR24 and CWR25. This different behavior can be traced to differences in initial imperfections resulting in the quite different wrinkle patterns after pre-compression seen in Fig. 4.13b. CWR24 and CWR25 have initial wrinkles with significantly larger amplitude than CWR31. Included in Fig. 4.12 is the measured average strain at the onset of collapse in a monotonic compression experiment tested at the same internal pressure (CWR30 in Table 4.3). The average strain level of $\bar{\varepsilon}_{Lmon}$= 3.17% is close to the strain levels measured just before collapse in CWR24 and CWR25 but lower than that of CWR31 again presumably for the same reason. Indeed a comparison of the wrinkle profiles in the two monotonic compression experiments tested at $P = 0.49\,P_o$ and $0.59\,P_o$ (Table 4.3) revealed that at $\bar{\varepsilon}_{xmon}$ = 2.0% the former developed larger amplitude wrinkles than the latter. This lead to the difference observed in the average strains at the onset of collapse between the two (3.17% vs. 3.44%). The points raised here point out that in addition to the loading parameters the collapse of our specimens is also influenced by small geometric imperfections that are somewhat random and difficult to quantify.

4.3.3 Variation of $\bar{\varepsilon}_{xmon}$

In Chapter 3, it was shown that the level to which the specimen is pre-compressed, represented by $\bar{\varepsilon}_{xmon}$, influenced the number of axial cycles to collapse in the pure axial cycling experiments. As might be expected, the same is true for cyclic compression under internal pressure. Figures 4.14 and 4.15 compare ratcheting results CWR34 and CWR39 tested at a pressure of $0.59\,P_o$ with a cycle amplitude of $\sigma_a = 68$ ksi (469 MPa). The first was pre-compressed to an average strain of about 2.0% and the second to 2.5%. Monotonic compression to a larger average strain results in initial wrinkles of larger amplitude as is clearly seen in Fig. 4.15b. This in turn results in a faster rate of ratcheting in δ_x and to a smaller number of cycles to collapse as evidenced in Fig. 4.14. Both tubes were approaching collapse at an average strain level of about 3.5% that coincides well with the monotonic compression value at the same pressure (CWR45 in Table 4.3). Unfortunately, the hoop strain gages ended at rather different locations in the wrinkle patterns that developed and thus comparison of their results is inconclusive.

A second pair of similar results appears in Figs. 4.16 and 4.17. CWR35 and CWR40 were tested at a pressure of $0.22\,P_o$ with a cycle amplitude of $\sigma_a = 56$ ksi (386 MPa). The first was pre-compressed to an average strain of about 2.5% and the second to 2.0%. Consequently CWR40 developed wrinkles with larger amplitude (Fig. 4.17b) and this led again to a faster rate of ratcheting in δ_x and a smaller number of cycles to collapse than CWR35. Once more, the tubes approached collapse at average strain levels that are close to those expected for monotonic compression loading at this pressure ($\bar{\varepsilon}_{Lmon}$ calculated with parameters listed in Table 4.3).

4.3.4 Wrinkle Wavelength and Limit Strain

The wavelengths of the wrinkles (2λ) in all cyclic loading experiments were measured (see Table 4.1) and λ / R are plotted against P / P_o in Fig. 4.18a (using ■).

Included are similar measurements for approximately the same tube D/t taken from Paquette and Kyriakides (2006). The λs from the cyclic experiments follow the same trend as those from the monotonic compression results; pressure tends to increase the wavelength. This happens even though the stress levels of the cyclic experiments are smaller than those of the monotonic ones. Included in the same figure are predictions from plastic bifurcation analysis (see Appendix B—red line corresponds to present material properties that are somewhat different from those of Paquette and Kyriakides, 2006; see Table 4.4). The predictions are in good agreement with the measurements.

Table 4.4 Mechanical Properties of SAF 2507 tubes

Mat.	E Msi (GPa)	σ_{ox} ksi (MPa)	S_θ	S_r	D/t
SAF4[1]	28.5 (197)	81.34 (561)	1.15	0.85	28.29
SAW8[2]	28.2 (195)	92.8 (640)	1.09	0.88	28.38

1. Paquette and Kyriakides (2006). 2. Present work.

The final average strains, $\bar{\varepsilon}_f$, at the end of cycling from the present experiments (see Table 4.1) are plotted against P/P_o in Fig. 4.18b (using ■). Included in the same plot are the limit strains $\bar{\varepsilon}_{Lmon}$ from the monotonic compression experiments (using ●) of Paquette and Kyriakides (2006). Although the cyclic strain results exhibit more scatter than the monotonic limit strains the agreement between the two sets of results can be described as reasonable confirming the trend pointed out earlier in this chapter. Included in the figure are limit strains predicted for monotonic compression under pressure from the analysis (red line corresponds to present material properties that are somewhat different from those of Paquette and Kyriakides, 2006; see Table 4.4). The predictions are in reasonable agreement with the experimental values.

CHAPTER 5

EXPERIMENTAL RESULTS FROM TUBES THAT WERE CYCLED WITHOUT PRE-WRINKLING

For the experiments reported in Chapters 3 and 4 the tubes were first wrinkled to a certain extent by compression. The tubes were then cycled about a compressive mean stress causing simultaneous material ratcheting and growth of the wrinkles. In this chapter we examine whether wrinkling can be initiated directly by ratcheting. Thus here the initial compression is terminated well before the critical wrinkling strain and the tubes are subsequently cycled. Experiments under pure axial cycling compression and axial cycling combined with internal pressure will be reported.

5.1 PURE AXIAL CYCLING

The question asked in these experiments is whether a tube can be wrinkled by strain accumulated by ratcheting. This was achieved as follows: the tube was first compressed monotonically into the plastic range under displacement control to a strain ($\bar{\varepsilon}_{xmon}$) that was significantly smaller than the strain level at which the tube showed the first signs of wrinkling under monotonic loading (ε_C in Table 3.1); in other words, ensuring that the tube was free of wrinkles. The machine was then switched to load control and the tube was cycled axially with an amplitude of σ_a about a compressive mean stress σ_m, following the triangular history shown in Fig. 2.6b. Three such experiments were performed (CWR 15, 18 and 19) each having the major parameters listed in Table 5.1.

A representative stress-displacement response recorded in Exp. CWR19 is shown in Fig. 5.1a. In this case $(\bar{\varepsilon}_{xmon}, \sigma_{xmon})$ = (0.99%, 100.2 ksi—691 MPa) and the loading parameters of the first 410 cycles were (σ_a, σ_m) = (74.0, 26.2) ksi--(511, 180) MPa. The ratcheting induced by cycling is clearly visible in the figure, where the average strain ($\delta_x / L \equiv \bar{\varepsilon}_x$) at the end of 410 cycles is seen to reach a value of 2.29%. The cycling was interrupted every 10 or 15 cycles in order to perform an axial scan of the test section, as described in Section 2.2.3. Figure 5.1b shows a select number of the axial scans plotted in the same manner as in the monotonic experiment shown in Fig. 3.2a. Here the scans are identified by the average strain of the cycle ($\bar{\varepsilon}_x$) and the number of the cycle (N). Included are scans taken before the test at zero load (0:0) and ones at strains of 0.7% and 0.99% before the cycling commenced, identified by (0.7:0) and (0.99:0) respectively. These scans show the presence of very small initial imperfections that get slightly, if at all, amplified by the accumulated compressive deformation. In the first scan during the cycling, taken after 10 cycles (1.08:10), the surface profile has changed little. In the next scan shown, (1.30:40), the first signs of a wavy pattern are starting to emerge and the wrinkles become fully developed by cycle 110, when $\bar{\varepsilon}_x$ reached a value of 1.60%. Thus, the onset of wrinkling is bounded by strain levels of 1.30% and 1.60%. Subsequently, as the tube is further compressed by the ratcheting, the wrinkle amplitude is seen to grow. This phase of the test was terminated at (2.29:410).

It is useful to compare the strain at the onset of wrinkling with the corresponding critical strains measured under monotonic loading. The two bounds of (1.30, 1.60)% are included in Table 5.1 under ε_C. If we compare the two bounds to the corresponding ones recorded under monotonic compression bounds for the two monotonic tests CWR20 and CWR21 in Table 3.1. The two bounding strains are also included in Fig. 5.3a, where they are seen to fall in line with other data for this tube *D/t*. The wrinkle wavelengths of CWR19 were found to be in the range of $\lambda / R \in (0.262, 0.368)$ (see Table 5.1). Once more these values are in reasonable agreement with the corresponding values from the monotonic tests CWR20 and CWR21 in Table 3.1. In other words, the tube buckles into an axisymmetric mode at about the same strain and with about the same wavelength as it does under monotonic loading. This happens despite the fact that the stress level at the onset of wrinkling is 100.2 ksi (691 MPa), whereas under monotonic loading it was between about 102 and 104 ksi (707-717 MPa). It would thus seem that this type of plastic buckling is strain-driven, which goes against the conventional understanding that it is stress-driven.

Once the wrinkles are fully developed, the test becomes similar to the ones described in Section 3.3 where the effect of ratcheting on pre-wrinkled tubes was examined. Stress-controlled cycling of pre-wrinkled tubes causes the amplitude of the wrinkles to grow, and eventually leads to localization of wrinkling and collapse. In the present test, the initial rate of ratcheting is relatively slow, and in view of this the cycle mean stress was increased to 33.94 ksi (234 MPa) in order to reach collapse in a fewer number of cycles. This choice resulted in a maximum cycle stress of 107.9 ksi (744 MPa), a value that corresponds to the monotonic loading stress at the current strain of 2.29% (see Fig. 5.1a). 197 additional cycles were performed with the new cycle parameters. The higher mean stress increased the rate of ratcheting considerably, reflected by the wider stress-“strain” loops traced. When the average strain reached approximately 4%, wrinkling localized initially at the two ends and subsequently at the end on the LHS of the specimen (Fig. 5.1b). The test was terminated on cycle 607, when the localized wrinkle was deemed to be close to collapsing.

The rate of ratcheting is also depicted in Fig. 5.1c, where the peak displacement (δ_x^p / L) in each cycle is plotted against the number of the cycle *N*. Following an initial transient that lasts about 75 cycles, the rate of ratcheting settles to a nearly constant rate (it actually gradually slows down slightly). During the first 100 or so cycles when the test section is essentially free of wrinkles, δ_x^p / L corresponds to the ratcheting in the axial strain. Subsequently, δ_x^p is partly due to accumulated material strain and partly due to shortening caused by the growth of the amplitude of the wrinkles.

Included in Fig. 5.1c is the radial displacement ($w_{\max}$) experienced at the location of the dominant wrinkle (i.e., on the left hand end in Fig. 5.1b) vs. *N*. The trend of the growth of this variable is similar to that of δ_x^p. Once more, before the initiation of wrinkles, $w_{\max}/R$ corresponds to the hoop strain, which is approximately $0.5\varepsilon_x$. When the wrinkles develop, the radial displacement is partly due to the material ratcheting and partly due to the wrinkle amplitude. The higher mean stress of the second part of the test is seen to increase both the rate of δ_x^p and $w_{\max}$ considerably. Both variables exhibit an initial transient, then settle to a constant rate of growth, and around cycle 530 start to grow at a faster rate that becomes exponential during the last 50 or so cycles. The test was terminated when the average strain reached a value of 5.23% (depicted as $\bar{\varepsilon}_f$ in Table 5.1).

Included in Fig. 5.1c with a horizontal dashed line is the average strain at which the tubes collapsed under monotonic loading ($\bar{\varepsilon}_{Lmon}$). We can see that this strain level corresponds to the strain at which the cycled tube is experiencing exponential growth in both δ_x^p and $w_{\max}$. In other words, under this type of cycling loading the tube tends to collapse at approximately the same average strain as it does under monotonic loading. This occurs despite the stress level in the cyclic test being 107.9 ksi (744 MPa) versus about 116 ksi (800 MPa) for monotonic tests. This conclusion is in concert with a similar one in Section 3.3 and once more points to the onset of localization being a strain-driven instability. It is also reminiscent of experimental results in Corona and Kyriakides (1991) involving moment-controlled cyclic bending of Al-alloy tubes that induces ratcheting of curvature and simultaneous accumulation of ovalization. It was found that the cycled tubes collapsed when the curvature at which they collapsed under monotonic bending was reached.

Two additional cyclic experiments were conducted (CWR15, CWR18) with approximately the same geometric and loading parameters (see Table 5.1). CWR15 was compressed monotonically to a strain of 0.80%. It was then cycled with an amplitude and mean stress of 74.0 ksi and 24.3 ksi (510, 168 MPa) respectively for 410 cycles. The recorded maximum displacement in each cycle is plotted against N in Fig. 5.2 along with the results for the other two experiments. The somewhat smaller $\bar{\varepsilon}_{xmon}$ and σ_m result in slightly lower rate of ratcheting. Wrinkles became discernible between strain levels of 1.30% and 1.45%, in other words in the same neighborhood as they did for CWR19 and for the monotonic loading experiments. After cycle 410, at $\delta_x^p / L = 1.90\%$, the mean stress was increased to 31.89 ksi (222 MPa) and 199 additional cycles were applied. The results in Fig. 5.2 show that after about cycle 550 the rate of ratcheting accelerated and showed clear signs of approaching collapse when δ_x^p / L reached a value of 4.33%, which again corresponds to the onset of collapse under monotonic loading. The third experiment (CWR18) had slightly different values of $\bar{\varepsilon}_{xmon}$ and σ_m (Table 5.1), and consequently the rate of ratcheting is somewhat higher than that of CWR15. The first phase of the test involved 490 cycles reaching an average strain of 2.14%. The specimen showed signs of wrinkling between strains of 1.28% and 1.55%. The second phase of the test had $\sigma_m =$ 31.90 ksi (222 MPa) and lasted for 142 cycles. Once more, around an average strain of 4.33% the specimen showed signs of approaching collapse. The test was terminated at an average strain of 5.23%.

The bounds for ε_C from the three experiments are included in Fig. 5.3a (using ■□), where experimental results from the pure monotonic compression tests from Bardi and Kyriakides (2006) are plotted vs. D/t on log-log scales. The corresponding calculated critical strain is drawn with a solid line. The three sets of new results are seen to follow the trend of the previous results. The half-wavelengths of the wrinkles (λ) were also measured (see Table 5.1) and plotted in Fig. 5.3b (using ■□) together with the monotonic compression results from Bardi and Kyriakides (2006). The wavelengths are again in line with those reported previously.

Thus is summary, all three cyclic experiments show similar tends. Compressive strain induced by ratcheting causes axisymmetric wrinkling at approximately the same strain that wrinkles tend to appear under monotonic compression. Furthermore, the wrinkle wavelengths under cyclic loading are of the same order of magnitude as those measured in monotonic loading tests. These events take place despite the fact that the stress in the cyclic experiments was consistently lower than the critical stress under monotonic loading. This indicates that the onset of plastic wrinkling is deformation rather than stress driven. Shells always have small initial imperfections, which in the present case can be considered to have a somewhat random distribution. These imperfections get accentuated by compression. It appears that as the critical strain is approached the minimum energy wavelengths get excited and grow faster than other wavelengths. The dominant wrinkles tend to grow with further straining by ratcheting. At an average strain that is again similar to the value at which the shell tends to localize and collapse under monotonic loading, wrinkling localizes and the shell collapses very much as if it was loaded monotonically.

5.2 AXIAL CYCLING UNDER INTERNAL PRESSURE

Similar experiments were performed in order to investigate if compression induced by ratcheting can wrinkle tubes that are internally pressurized. To this end specimen CWR47 (see Table 5.1) was tested as follows. The tube was first pressurized to

$0.59 P_o$ and then was compressed monotonically into the plastic range under displacement control to a strain of $\bar{\varepsilon}_{xmon}$ = 0.92%. Axial scans taken at strains of 0.70% and 0.92% (see Fig. 5.5) show the formation of small bulges at the ends of the test section while the central part remains relatively undisturbed. The machine was then switched to load control and the tube was cycled axially with an amplitude of $\sigma_a = 56.0$ ksi (386 MPa) about a compressive mean stress $\sigma_m = 21.8$ ksi (151 MPa). The recorded stress-shortening response shown in Fig. 5.4a shows the ensuing axial ratcheting. The rate of shortening can be seen in the $\delta_x^p / L - N$ plot in Fig. 5.4b to exhibit an initial transient followed by a nearly steady-state. As the tube gets shorter the two end-wrinkles are seen to grow and in the profile for $\bar{\varepsilon}_x$ = 1.09% after 40 cycles the first signs of a central wrinkle appear. In the next profile, at N = 70, the average strain has reached 1.30% and the central wrinkle is now fully developed. We thus consider the tube to be wrinkled by ratcheting at a strain between 1.09% and 1.30%.

Subsequent cycling leads to the growth of the amplitude of the three wrinkles at a rate that is quantified in the $w_{\max} / R - N$ plot in Fig. 5.4b ($w_{\max}$ is the amplitude of the most deformed wrinkle -- RHS of Fig. 5.5). This phase of the experiment (part ①) was terminated after 310 cycles when the strain had reached a level of 1.67%. Beyond this point the results are similar to the ones reported in Section 4.2. At this stage in order to accelerate the rate of ratcheting the mean stress of the cycles was increased to σ_m = 28.6 ksi (198 MPa) and cycling was continued for 30 more cycles (part ②). As expected the rate of ratcheting as well as the rate of growth of the wrinkles increased as clearly seen in Figs. 5.4a and 5.4b. The test was terminated at cycle 340 before reaching its critical collapse state.

In order to compare the initiation and evolution of wrinkling under cyclic loading and monotonic loading, a monotonic compression test was performed on a tube pressurized to the same pressure level (CWR45 in Table 4.3). The recorded axial stress-shortening response is included in Fig. 5.4a. Axial scans of the surface were taken at pre-selected values of strain during brief interruptions of the compression. The profiles recorded at different values of the average axial strain are shown in Fig. 5.6 (note that the $\bar{\varepsilon}_x$ axis is truncated). The initial profile taken in the unloaded condition shows the test section to be essentially straight. In the second profile at $\bar{\varepsilon}_x = 0.60\%$ two small bulges just start to appear at the ends of the test section while the central section remains straight. In other words, behavior is overall similar to that in Fig. 5.5 except that the amplitudes of the two end-bulges are somewhat smaller than the ones under cyclic loading at the same strain levels. At somewhat higher levels of $\bar{\varepsilon}_x$, the shapes of the profiles remain relatively unchanged. At $\bar{\varepsilon}_x = 1.20\%$ the amplitudes of the end bulges have grown and some small undulations have started appearing in the central part of the test section. In the profiles of 1.30%, 1.40% and 1.55% the central undulations become more pronounced while by 1.85% they have organized themselves into a well-defined central wrinkle. We thus consider the tube to have buckled by wrinkling at a strain between 1.20% and 1.55%. In other words, the appearance and initial evolution of the central wrinkle is similar to those in the cyclic loading test in Fig. 5.5 although the onset is now bracketed between the slightly bigger axial strains of 1.20% and 1.55%. This slightly later initiation (1.09%-1.30% in cyclic loading) can probably be attributed to somewhat smaller initial imperfections in the specimen tested monotonically than those in the one tested cyclically. However, we can still claim that wrinkling initiates under approximately the same strain level irrespective of whether the tube is strained by monotonic compression or by ratcheting. This despite the fact that the axial stress in the two cases is different. In summary then, the behavior repeats the one observed for pure compression and points to the same general conclusion that plastic buckling appears to be strain rather than stress driven as first pointed out in Jiao and Kyriakides (2010).

CHAPTER 6

NUMERICAL MODELS

The problem of cyclic loading of circular tubes into the plastic rage is formulated in this chapter. The tube is modeled as an axisymmetric shell using suitably nonlinear kinematics. The elastoplastic cyclic behavior of the material is modeled using the two-surface nonlinear kinematic hardening model of Dafalis and Popov (1975, 1976) with the modifications put forward in Hassan *et al.* (1992), Hassan and Kyriakides (1994a, 1994b). The chapter also includes description of the calibration procedure required for optimal performance of this constitutive model.

6.1 AXISYMMETRIC SHELL FORMULATION

The problem of plastic buckling of long circular cylinders under axial compression was fully addressed in Bardi *et al.* (2006) using an extension of the shell formulation of Yun and Kyriakides (1990). Here we will adopt the same basic formulation, couple it to a cyclic plasticity constitutive model, and use them to analyze the buckling of cylinders under cyclic loads. Because of the challenges placed on the constitutive framework adopted, in this first attempt at the problem strictly axisymmetric buckling will be investigated as this is the dominant mode of buckling for buried offshore pipelines, which typically have D/t values less than 30. Thus we consider a thin-walled circular cylindrical shell with mid-surface radius R, wall thickness t and length $2L$ with small initial axisymmetric imperfections (see Fig. 6.1). Sanders' (1963) shell kinematics based on the assumptions of small strains and moderately small rotations are adopted, which for axisymmetric deformation reduce to

$$\varepsilon_{xx}^{o} = u_{,x} + \frac{1}{2} w_{,x}^{2}, \qquad \varepsilon_{\theta\theta}^{o} = \frac{w}{R}, \qquad \kappa_{xx} = -w_{,xx}. \tag{6.1}$$

The strains at any point on the shell are given by:

$$\varepsilon_{\alpha\beta} = (\varepsilon_{\alpha\beta}^{o} + z\kappa_{\alpha\beta})/(A_{\alpha}A_{\beta})^{1/2}, \text{ where } A_1 \cong 1, \quad A_2 \cong 1 + \frac{z}{R}. \tag{6.2}$$

For an imperfect structure with imperfection $\overline{w}(x)$ the strains become

$$\varepsilon_{\alpha\beta} = \varepsilon_{\alpha\beta}(u, w + \overline{w}) - \varepsilon_{\alpha\beta}(0, \overline{w}). \tag{6.3}$$

Equilibrium will be satisfied through the Principle of Virtual Work (*PVW*), which in the present setting can be expressed as follows:

$$2\pi R \int_{0}^{L} \left\{ N_{xx}\delta\varepsilon_{xx}^{o} + N_{\theta\theta}\delta\varepsilon_{\theta\theta}^{o} + M_{xx}\delta\kappa_{xx} \right\} \mathrm{d}x = \delta W, \tag{6.4}$$

where δW is the virtual external work and

$$\delta W = \delta W_F + 2\pi RP \int_{0}^{L} \delta w dx. \tag{6.5}$$

Here, δW_F is the virtual work of the axial force and the second term represents that of the internal pressure.

The membrane and bending moment intensities are given by

$$N_{\alpha\beta} = \int_{-t/2}^{t/2} \frac{A_1 A_2}{(A_{\alpha}A_{\beta})^{1/2}} \sigma_{\alpha\beta} \, \mathrm{d}z, \; M_{\alpha\beta} = \int_{-t/2}^{t/2} \frac{A_1 A_2}{(A_{\alpha}A_{\beta})^{1/2}} \sigma_{\alpha\beta} z \mathrm{d}z \tag{6.6}$$

(α and β not summed).

The evolution of wrinkling during cycling and the development of the anticipated localized collapse are considered by introducing the following initial imperfection to the tube

$$\overline{w} = t\left[\omega_o + \omega_1 \cos\left(\frac{\pi x}{N\lambda}\right)\right]\cos\left(\frac{\pi x}{\lambda}\right), \tag{6.7}$$

where 2λ is the wavelength of the axisymmetric buckling mode evaluated as discussed in Appendix B. The end at $x = N\lambda$ is radially free and symmetry about the specimen mid-span ($x = 0$) is assumed. Thus, the length of the domain considered is $L = N\lambda$. It is worth noting that imperfection (6.7) introduces an amplitude bias towards $x = 0$. (This is a scheme meant to represent the behavior of a long tube adopted in Bardi and Kyriakides, 2006 and found to be effective in reproducing monotonic compression experimental results.)

The problem domain is discretized by adopting the following admissible expansions for the displacements:

$$w = a_0 + \sum_{n=1}^{N_w} a_n \cos\left(\frac{n\pi x}{N\lambda}\right) \quad \text{and} \quad u = b_0 x + \sum_{n=1}^{N_u} b_n \sin\left(\frac{n\pi x}{N\lambda}\right). \tag{6.8}$$

Thus, $b_0 = \delta_x / N\lambda$ is the average axial strain and $\delta W_F = FN\lambda\delta b_0$ in (6.5) for load controlled loading and $\delta W_F = 0$ for displacement controlled loading. Substituting (6.8) into (6.4), the *PVW* becomes:

$$2\pi R \int_0^{N\lambda} \left[N_{xx}\varepsilon^o_{xx,i} + N_{\theta\theta}\varepsilon^o_{\theta\theta,i} + M_{xx}\kappa_{xx,i}\right] \mathrm{d}x\delta q_i = W_{,i}\,\delta q_i\,, i = 1,2,\ldots\ldots,N_w + N_u + 2 \tag{6.9}$$

$$(\,)_{,i} \equiv \frac{\partial(\,)}{\partial q_i} \quad \text{and} \quad \boldsymbol{q} = [a_0, a_1, \ldots, a_{N_w},\ b_0, b_1, \ldots.. b_{N_u}]^T .$$

In view of the arbitrariness of δq_i, the following algebraic equations represent equilibrium:

$$G_i(\boldsymbol{q}^* + \dot{\boldsymbol{q}}) = 2\pi R\int_0^{N\lambda} \left\{ N_{xx}\varepsilon^o_{xx,i} + N_{\theta\theta}\varepsilon^o_{\theta\theta,i} + M_{xx}\kappa_{xx,i} \right\} \mathrm{d}x - W_{,i} = 0,$$

$$i = 1,2,\ldots\ldots,N_w + N_u + 2. \tag{6.10}$$

In the incremental solution procedure followed, $\boldsymbol{q}^*$ represents the previous converged solution and $\dot{\boldsymbol{q}}$ is the increment of $\boldsymbol{q}$ required for the current solution. Similarly, $N_{\alpha\beta} = N_{\alpha\beta o} + \dot{N}_{\alpha\beta} \ldots$ etc.

The set of nonlinear equations given in (6.10) are solved by using the Newton-Raphson method, which can be written as follows:

$$G_i\Big|_{\boldsymbol{q}^{(k)}} + G_{i,j}\Big|_{\boldsymbol{q}^{(k)}} \Delta q_j^{(k)} = 0, \tag{6.11}$$

where $i, j = 1,2,\ldots\ldots,N_w + N_u + 2$. $\boldsymbol{q}$ are the displacement coefficients evaluated at the previous iteration and the converged solution at the previous load step was used as the initial guess for the current solution. The solution is updated by $\boldsymbol{q}^{(k+1)} = \boldsymbol{q}^{(k)} + \Delta\boldsymbol{q}^{(k)}$ when $\left|\Delta\boldsymbol{q}^{(k)}\right| \Big/ \left|\boldsymbol{q}^{(k)}\right| <$ tolerance (10^{-7} is adopted in this study).

The Jocabian $G_{i,j}$ in (6.11) is given as follows:

$$G_{i,j} = \int_0^{N\lambda} \left\{ N_{xx,j}\varepsilon^o_{xx,i} + N_{\theta\theta,j}\varepsilon^o_{\theta\theta,i} + M_{xx,j}\kappa_{xx,i} + N_{xx}\varepsilon^o_{xx,ij} + N_{\theta\theta}\varepsilon^o_{\theta\theta,ij} + M_{xx}\kappa_{xx,ij} \right\} 2\pi R \mathrm{d}x - W_{,ij} \tag{6.12}$$

The instantaneous constitutive equations are given by:

$$\begin{Bmatrix} \dot{N}_{xx} \\ \dot{N}_{\theta\theta} \\ \dot{M}_{xx} \\ \dot{M}_{\theta\theta} \end{Bmatrix} = \int_{-t/2}^{t/2} \begin{bmatrix} \boldsymbol{A} & z\boldsymbol{A} \\ z\boldsymbol{A} & z^2\boldsymbol{A} \end{bmatrix} \mathrm{d}z \begin{Bmatrix} \dot{\varepsilon}^{o}_{xx} \\ \dot{\varepsilon}^{o}_{\theta\theta} \\ \dot{\kappa}_{xx} \\ \dot{\kappa}_{\theta\theta} \end{Bmatrix}, \qquad (6.13)$$

where

$$\boldsymbol{A} = \begin{bmatrix} A_2/A_1 C_{11}, & C_{12} \\ C_{12}, & A_1/A_2 C_{22} \end{bmatrix}$$

and $[C_{\alpha\beta}]$ $\alpha, \beta = 1{,}2$ come from the inverse of the constitutive matrix (6.31). In the cases discussed here $N = 7$, $N_u = N_w = 11$.

Gauss's integration rule with I_x points along the axial direction and I_z points through the thickness was used in the integrations. The number of integration points was determined by a convergence study. Figure 6.2a shows the axial stress-shortening response ($\sigma_x - \delta_x/L$, where L is the axial length of the domain analyzed) for a tube with D/t of 28.01. I_x was varied from 24, 49 to 81 while I_z was kept constant ($I_z = 5$). The simulation with 24 points was slightly lower than those with 49 and 81 points, while the responses with 49 and 81 integration points were the same. Consequently, for the simulations that follow, 49 integration points in the axial direction were used. Similarly, a convergence study to evaluate the number of integration points through the thickness was performed. Cases with I_z varying from 5 to 7 and $I_x = 49$ are shown in Fig. 6.2b. The two responses are almost identical, especially the part before load maximum; so, for the simulations that follow, $I_z = 5$ was adopted.

6.2 CONSTITUTIVE MODEL

The elastoplastic cyclic behavior of SAF2507 super-duplex steel is modeled using the two-surface nonlinear kinematic hardening model of Dafalias and Popov (1975, 1976) with the modifications put forward in Hassan *et al.* (1992), Hassan and Kyriakides

(1994a, 1994b). Furthermore, this stainless steel is essentially cyclically stable and is modeled as such. The strain increments are decomposed into elastic and plastic parts as follows:

$$d\boldsymbol{\varepsilon} = d\boldsymbol{\varepsilon}^{e} + d\boldsymbol{\varepsilon}^{p}. \tag{6.14}$$

The elastic deformation is isotropic with elastic modulus E and Poisson's ratio ν, thus

$$d\boldsymbol{\varepsilon}^{e} = \frac{1}{E}[(1+\nu)d\boldsymbol{\sigma} - \nu tr(d\boldsymbol{\sigma})\boldsymbol{I}]. \tag{6.15}$$

The plastic strain increment is evaluated from the flow rule, which can be expressed as

$$d\boldsymbol{\varepsilon}^{p} = \frac{1}{H}\left(\frac{\partial f}{\partial \boldsymbol{\sigma}} \cdot d\boldsymbol{\sigma}\right)\frac{\partial f}{\partial \boldsymbol{\sigma}} \tag{6.16}$$

where H is the current plastic modulus.

In the uniaxial setting, represented in Fig. 6.3a by bcde, the plastic modulus of point d depends on the stress variables δ and δ_{in}. Both are distances measured from the *bound* XY, which is the tangent to the stress-plastic strain response at a large value of strain (point e in this case). δ is the distance of point d from the bound and δ_{in} is the distance of the last elastic state, point c, from the same line. The plastic modulus H is related to these variables as follows:

$$H(\delta, \delta_{in}) = E_{o}^{p} + h\left(\frac{\delta}{\delta_{in} - \delta}\right), \tag{6.17}$$

where E_{o}^{p} is the modulus of the bound and h will be taken as

$$h = \frac{a}{1 + b(\delta_{in}/2\sigma_{b})^{\gamma}} \tag{6.18}$$

where a, b and γ are material constants.

In the multiaxial setting the yield surface (YS) bc is represented as follows:

$$f(\boldsymbol{\sigma}-\boldsymbol{\alpha})=\left[\frac{3}{2}(\boldsymbol{s}-\boldsymbol{a})\cdot(\boldsymbol{s}-\boldsymbol{a})\right]^{1/2}=\sigma_o \tag{6.19}$$

where $\boldsymbol{\sigma}$ is the stress tensor, $\boldsymbol{\alpha}$ is the center of the yield surface in stress space and $\boldsymbol{s}$ and $\boldsymbol{a}$ are the respective deviatoric tensors. σ_o is the size of the yield surface assumed to remain constant. The yield surface is surrounded by a geometrically similar bounding surface (BS) (see Fig. 6.3b) defined by:

$$F(\bar{\boldsymbol{\sigma}}-\boldsymbol{\beta})=\left[\frac{3}{2}(\bar{\boldsymbol{s}}-\boldsymbol{b})\cdot(\bar{\boldsymbol{s}}-\boldsymbol{b})\right]^{1/2}=\sigma_b. \tag{6.20}$$

Here σ_b is the size of the BS, $\bar{\boldsymbol{\sigma}}$ is the congruent point on the BS to $\boldsymbol{\sigma}$ on the YS, $\boldsymbol{\beta}$ is the center of the BS, and $\bar{\boldsymbol{s}}$ and $\boldsymbol{b}$ are respectively their deviators. The two surfaces are geometrically similar and, as a result, points P and $\overline{\mathsf{P}}$ are congruent when they have the same normals as shown in Fig. 6.3b. Thus, the two points are related through:

$$(\bar{\boldsymbol{\sigma}}-\boldsymbol{\beta})=\frac{\sigma_b}{\sigma_o}(\boldsymbol{\sigma}-\boldsymbol{\alpha}). \tag{6.21}$$

The scalar δ is generalized as follows (see Fig. 6.3b):

$$\delta=\left[(\bar{\boldsymbol{\sigma}}-\boldsymbol{\sigma})\cdot(\bar{\boldsymbol{\sigma}}-\boldsymbol{\sigma})\right]^{1/2}. \tag{6.22}$$

The YS translates in stress space according to a chosen hardening rule that in general is defined by

$$d\boldsymbol{\alpha}=d\mu\boldsymbol{\nu},\quad \boldsymbol{\nu}\cdot\boldsymbol{\nu}=1. \tag{6.23}$$

Here $\boldsymbol{\nu}$ is the unit vector in the direction of translation and $d\mu$ is a scalar defining the amplitude of the translation.

It has been found that the kinematic hardening rule can play an important role in predicting multiaxial ratcheting (Hassan *et al.*, 1992). An important feature of the model is that the hardening rule and the calculation of plastic modulus *H* are decoupled and, as a result, the user can select the best kinematic hardening rule fitting the multiaxial ratcheting. In the present calculations the stress version of the Armstrong-Frederick hardening rule (1966) as implemented in Hassan *et al.* (1992) and Hassan and Kyriakides (1994b) is adopted so

$$\boldsymbol{\nu} = \frac{[(1-k)(\boldsymbol{\sigma}-\boldsymbol{\alpha})-k\boldsymbol{\alpha}]}{|(1-k)(\boldsymbol{\sigma}-\boldsymbol{\alpha})-k\boldsymbol{\alpha}|} \tag{6.24}$$

where k is a constant decided empirically as discussed in Section 6.3. The amount of translation $d\mu$ is chosen by satisfying the consistency condition

$$\frac{\partial f}{\partial \boldsymbol{\sigma}} \cdot d\boldsymbol{\alpha} = \frac{\partial f}{\partial \boldsymbol{\sigma}} \cdot d\boldsymbol{\sigma}. \tag{6.25}$$

The translation of the BS is coupled to that of the YS as follows:

$$d\boldsymbol{\beta} = d\boldsymbol{\alpha} - dM\boldsymbol{m}, \tag{6.26}$$

where

$$\boldsymbol{m} = \frac{(\bar{\boldsymbol{\sigma}}-\boldsymbol{\sigma})}{|\bar{\boldsymbol{\sigma}}-\boldsymbol{\sigma}|} \quad \text{and} \quad dM = \left(1-\frac{E_b^p}{H}\right)\left(\frac{d\boldsymbol{\sigma}\cdot\boldsymbol{n}}{\boldsymbol{m}\cdot\boldsymbol{n}}\right). \tag{6.27}$$

Here $\boldsymbol{n}$ is the unit normal to the YS at the current stress point (see Fig. 6.3b) and E_b^p is evaluated from

$$E_b^p = E_o^p + C_r[(\boldsymbol{b}\cdot\boldsymbol{b})^{1/2} - \boldsymbol{b}\cdot\boldsymbol{n}]. \tag{6.28}$$

This is a modification of the original model introduced by Hassan and Kyriakides (1994a, 1994b) that allows relaxation, or downward shift of the bounds. The modification was shown to be necessary in the prediction of uniaxial ratcheting. So C_r will be determined by best fitting an experiment under axial cycling loading (see parameter study of C_r shown in Fig. 7.12). When the two surfaces come into contact the BS becomes the active surface and the YS moves so as to remain tangential to it.

Finally, the tubes tested exhibited some initial plastic anisotropy (see Kyriakides *et al.*, 2005 and Bardi *et al.*, 2006). It was introduced using Hill's (1948) anisotropy, which modifies the yield function to the following:

$$f = \left[(\sigma_x - \alpha_x)^2 - (1 + \frac{1}{S_\theta^2} - \frac{1}{S_r^2})(\sigma_x - \alpha_x)(\sigma_\theta - \alpha_\theta) + \frac{1}{S_\theta^2}(\sigma_\theta - \alpha_\theta)^2 \right]^{1/2} = \sigma_o. \qquad (6.29)$$

Here $S_r = \dfrac{\sigma_{or}}{\sigma_{ox}}$, $S_\theta = \dfrac{\sigma_{o\theta}}{\sigma_{ox}}$ and $\{\sigma_{or}, \sigma_{o\theta}, \sigma_{ox}\}$ are the yield stresses in the radial, circumferential and axial directions. The parameters $\{S_r, S_\theta\}$ are determined from a special set of experiments outlined in Appendix A. The bounding surface is also modified in a similar manner becoming

$$F = \left[(\bar{\sigma}_x - \beta_x)^2 - (1 + \frac{1}{S_\theta^2} - \frac{1}{S_r^2})(\bar{\sigma}_x - \beta_x)(\bar{\sigma}_\theta - \beta_\theta) + \frac{1}{S_\theta^2}(\bar{\sigma}_\theta - \beta_\theta)^2 \right]^{1/2} = \sigma_b. \qquad (6.30)$$

The instantaneous strain increments are then given by

$$\begin{Bmatrix} d\varepsilon_x \\ d\varepsilon_\theta \end{Bmatrix} = \frac{1}{E} \begin{bmatrix} 1 + Q(2\hat{\sigma}_x - \zeta\hat{\sigma}_\theta)^2 & -\nu + Q(2\hat{\sigma}_x - \zeta\hat{\sigma}_\theta)(2\eta\hat{\sigma}_\theta - \zeta\hat{\sigma}_x) \\ -\nu + Q(2\hat{\sigma}_x - \zeta\hat{\sigma}_\theta)(2\eta\hat{\sigma}_\theta - \zeta\hat{\sigma}_x) & 1 + Q(2\eta\hat{\sigma}_\theta - \zeta\hat{\sigma}_x)^2 \end{bmatrix} \begin{Bmatrix} d\sigma_x \\ d\sigma_\theta \end{Bmatrix}$$

(6.31)

where

$$\eta = \frac{1}{S_\theta^2}, \ \zeta = \left(1 + \frac{1}{S_\theta^2} - \frac{1}{S_r^2}\right), \ Q = \frac{1}{4\sigma_o^2}\frac{E}{H}, \ \hat{\sigma}_x = \sigma_x - \alpha_x, \ \hat{\sigma}_\theta = \sigma_\theta - \alpha_\theta .$$

6.3 DETERMINATION OF MATERIAL PARAMETERS

The constitutive model parameters come from an independent uniaxial stress-strain response. The elastic modulus *E* is determined from the initial elastic loading. The modulus of the bound E_o^p, the radius of yield surface σ_o and the radius of bounding surface σ_b can be directly measured from the stress-strain curve as shown in Fig. 6.3a.

Fit parameters a, b and γ in (6.18) are determining by best fitting of nonlinear part of stress-plastic strain response shown in Fig. 6.3a. Since the monotonic (ab) and hysteresis (bcde) responses are different, we will calculate a, b and γ separately for each. We note that for monotonic loading a single parameter fit for h in (6.18) sufficed (listed under *Monot.* in Tables 6.1-6.3), whereas the more elaborate version had to be adopted for fitting the hysteresis (listed under *Cyclic* in Tables 6.1-6.3).

Values for the relaxation parameter C_r in (6.28) determined by best fitting an experiment under axial cycling loading (see Figs. 7.12 and 9.6) are listed in the same Tables.

The kinematic hardening rule has little effect on prediction of uniaxial ratcheting so in the simulations of the cyclic experiments with no pressure, the parameter k in (6.24) is assumed to be constant (0.1 in Tables 6.1 and 6.3). However, as pointed out in Hassan *et al.* (1992) and Hassan and Kyriakides (1994a), accurate prediction of biaxial ratcheting that occurs in the cyclic experiments under internal pressure requires careful calibration of this kinematic hardening rule. Consequently, a separate biaxial cyclic experiment was conducted on a tube extracted from the same mother tube as that of the test specimens in

Chapter 4. The tube was designed for material characterization, in other words it was free of wrinkles. The tube was pressurized to a hoop stress of $\sigma_\theta = 0.448\sigma_o$ and then cycled axially under load control with the cycle parameters given in Fig. 6.4a. The biaxial ratcheting that resulted is shown in Fig. 6.4b while the peak values of the induced axial (ε_{xp}) and hoop ($\varepsilon_{\theta p}$) strains are plotted vs. N in Figs. 6.5a and 6.5b respectively. Both exhibit an initial transient followed by a nearly constant rate of ratcheting. To capture the transient in ε_θ, Hassan *et al.* (1992) recommended the following form for k in the hardening rule:

$$k = k_0 + k_1 e^{-\zeta r} \text{ where } r = \int_t \frac{d}{dt}\varepsilon_e^p \, dt. \tag{6.31}$$

The constants k_0, k_1 and ζ chosen for best performance in predicting ε_θ are listed in Table 6.2, while the calculated peak strains are included in Fig. 6.5.

Different mother tubes have some differences in mechanical properties. So the constitutive model parameters used to simulate the experiments on the tubes cut from mother tube SAW6 (all experiments under pure axial cyclic loading described in Chapter 3) are listed in Table 6.1. The constitutive model parameters used to simulate the experiments using tubes cut from mother tube SAW8 (experiments under pure axial cyclic loading and internal pressure described in Chapter 4) are listed in Table 6.2. The constitutive model parameters used to simulate the experiments using tubes cut from mother tube SAW7 (experiments under pure axial cyclic loading described in Chapter 5) are listed in Table 6.3.

It’s worth pointing out that several of the cyclic fit parameters can influence the rate of ratcheting as well as the rate of growth of the wrinkles, and again these variables were selected for optimal performance of the model. The extent of the influence of the key parameters on the results will be illustrated in the parametric study in Chapter 7.

Table 6.1 Constitutive model parameters in simulations of experiments under pure axial cyclic loading (tube SAW6)

Loading	E Msi (GPa)	E_o^p ksi (GPa)	σ_o ksi (MPa)	σ_b ksi (MPa)	a Msi (GPa)	b	γ	k	C_r
Monot.	28.2 (195)	600 (4.14)	62.0 (428)	97.9 (675)	12.5 (86.2)	0	0	0.1	60
Cyclic	28.2 (195)	600 (4.14)	47.5 (328)	114 (786)	300 (2.07)	36	3	0.1	60

$$S_\theta = 1.15, \quad S_r = 0.85$$

Table 6.2 Constitutive model parameters in simulations of experiments under axial cyclic loading with internal pressure (tube SAW8)

Loading	E Msi (GPa)	E_o^p ksi (GPa)	σ_o ksi (MPa)	σ_b ksi (MPa)	a Msi (GPa)	b	γ	k_0	k_1	ζ	C_r
Monot.	28.2 (195)	200 (1.38)	59.0 (407)	105.8 (729)	10.0 (69.0)	0	0	0.04	0.11	80	60
Cyclic	28.2 (195)	200 (1.38)	45.5 (314)	111.9 (772)	130 (897)	27	3	0.04	0.11	80	60

$$S_\theta = 1.09, \quad S_r = 0.88$$

Table 6.3 Constitutive model parameters in simulations of experiments under pure axial cyclic loading described in Chapter 5 (tube SAW7)

Loading	E Msi (GPa)	E_o^p ksi (GPa)	σ_o ksi (MPa)	σ_b ksi (MPa)	a Msi (GPa)	b	γ	k	C_r
Monot.	28.2 (195)	600 (4.14)	62.0 (428)	97.9 (675)	12.5 (86.2)	0	0	0.1	40
Cyclic	28.2 (195)	600 (4.14)	47.5 (328)	108.1 (745)	300 (2069)	36	3	0.1	40

$$S_\theta = 1.15, \quad S_r = 0.85$$

CHAPTER 7

WRINKLING DUE TO AXIAL CYCLING: ANALYTICAL RESULTS

In this Chapter, the axisymmetric shell formulation and the nonlinear kinematic hardening constitutive model outlined in Chapter 6 are now used to simulate the experiments under pure axial cyclic loading presented in Chapter 3. A sensitivity study of the formulation to the imperfections and to key constitutive model parameters is then performed.

7.1 SIMULATION OF CYCLIC EXPERIMENTS

We start with a simulation of CWR6 using the geometric parameters listed in Table 3.2 and the material parameters listed in Table 6.1. The imperfections amplitudes $\{\omega_o, \omega_1\}$ in (6.7) constitute key parameters that decide the performance of the model. In this case, the values of {0.09,0.09}% were chosen for best performance regarding the prediction of the rate of ratcheting of δ_x. More on the sensitivity of the solution to these and other model parameters will follow in Section 7.2. The calculated stress-shortening response is shown in Fig. 7.1a. Following the initial preloading the model was cycled axially using the cycle variables $\{\sigma_a, \sigma_m\}$ of the experiments. A total of 183 cycles were applied. The characteristics of the calculated response are very similar to those of the corresponding experimental one in Fig. 3.4a. Figure 7.1b shows a plot of the calculated peak displacement in each cycle (δ_x^p / L) vs. N along with the corresponding experimental results. The predicted trajectory is seen to agree well with the experimental results including the initial transient, the steady-state regime and the final exponential growth. It is interesting to separate the effect of material ratcheting from the axial shortening caused by the growth of the wrinkles. So included in Fig. 7.1b with a dashed line is the axial strain (ε_{xp}) that would accumulate at a material point experiencing the same loading history (calculated by assigning zero values to the imperfection amplitudes). Interestingly, ε_{xp} follows the calculated average strain (δ_x / L) up to approximately cycle 60. Subsequently, ε_{xp} continues on a nearly linear trajectory whereas the rate of growth of δ_x / L gradually increases and becomes exponential close to $N = 150$.

Figure 7.2a shows plots of the radial displacement along the full domain of $2L = 14\lambda$ for various cycle counts ($x = 0$ represents the plane of symmetry). The amplitudes of the wrinkles are seen to grow with N with the growth of the central wrinkles being more pronounced. Indeed in cycle 183, deformation is seen to have localized around the central wrinkle. The evolution of the displacement of this wrinkle is included in Fig. 7.1b where its amplitude, $w_{\max}$, is plotted against N together with the corresponding experimental results. The predicted trajectory is seen to agree very well with the discreet values from the largest wrinkle in the experiment. Thus, even though the model was not designed to reproduce exactly the experiment—larger domain and slightly different boundary conditions--the predicted $w_{\max}$ matches very well the measurements, which confirms the veracity of the model.

The growth of the wrinkles and their localization are also illustrated in Fig. 7.2b where 3-D renderings of the configuration just before cycling commences ($\bar{\varepsilon}_{xmon}$ = 2.24%), one after cycle 150 and a third one after cycle 184 at which the net axial shortening is approximately 6.6% are shown. The place and nature of the localization are of course different from those of the experiment because of the idealized geometry, imperfection, boundary conditions and axisymmetric nature of the solution adopted. However, overall the model is seen to be able to reproduce the interaction between material ratcheting and wrinkle growth very well. It is also interesting to compare Figs. 7.2a and 7.2b with similar ones for monotonic compression shown in Figs. 7 and 8 of

Bardi *et al.*, 2006. Clearly the evolution of wrinkles in the present case is very similar to that of monotonic compression.

A second set of results from a simulation of CWR4 is shown in Fig. 7.3. In this case the critical wrinkle half-wavelength is slightly different ($\lambda = 0.281R$) but the same imperfection and constitutive model parameters are adopted (Table 6.1). Overall the simulation reproduces the experimental results shown in Fig. 3.5 very well. The calculated stress-displacement response in Fig. 7.3a tracks the experimental one very well and the rate of ratcheting of δ_x is seen in Fig. 7.3b to match the experimental rate very closely.

In view of this success the same imperfection and material parameters were used to simulate all six of the experiments in Fig. 3.6a that were pre-compressed to $\bar{\varepsilon}_{xmon} \approx 2.3\%$. The results from four of the simulations (CWR2, 4, 6 and 7) are summarized in Fig. 7.4 in the form of $\delta_x^p - N$ ratcheting plots. Despite the very different rates of ratcheting recorded in these experiments, the numerical results match the experimental ones very well from the beginning to the end. This degree of success over a broad range of stress cycle parameters validates the veracity of the model. As observed in the experimental section, these tubes had similar imperfections (see Fig. 3.6b) allowing us to run the four simulations with the same initial imperfection amplitude of $\{\omega_o, \omega_1\}$ = $\{0.09, 0.09\}\%$. As we will see below this was not possible in all cases due to differences in initial imperfections.

The same imperfection amplitudes were also used to calculate the compressive response under monotonic compression. The response is characterized by a limit load instability in the neighborhood of which deformation localizes in the fashion shown in Figs. 6 to 8 of Bardi *et al.* (2006). The limit load occurred at $\delta_x / L \equiv \bar{\varepsilon}_{Lmon}$ = 4.48%. This value compares with the five experimental values listed in Table 3.1 that have an average of 4.33%. This average and the predicted value are drawn as horizontal lines in Fig. 7.4. Clearly both fall in the parts of the $\delta_x^p - N$ ratcheting plots where the exponential growth is taking place. This confirms the experimental observation that collapse under monotonic and cyclic loads happens at very similar values of average strain if the tube imperfections are similar.

Figure 7.5 shows predictions of the ratcheting in δ_x for two additional experiments in this group: CWR3 and CWR5. Shown together with the experimental trajectories are predictions using the imperfections amplitudes found to work very well for the four experiments in Fig. 7.4, i.e., $\{\omega_o, \omega_1\}=\{0.09, 0.09\}\%$. The results for CWR5 are under-predicted and for CWR3 over-predicted (prediction drawn in dashed lines in Fig. 7.5). For a successful reproduction of the experimental rate of ratcheting the imperfection amplitudes $\{\omega_o, \omega_1\}$ for CWR5 had to be both increased to 0.34% whereas for CWR3 they had to be decreased to 0.06% (predictions drawn in solid lines in Fig. 7.5). These choices were necessary because small differences in the initial imperfections in these two tubes resulted in wrinkles of significantly different amplitudes from the other four cases after the initial pre-compression. To illustrate this point further Fig. 7.6a shows the initial wrinkle profile of CWR5 (i.e., $\bar{\varepsilon}_{xmon} = 2.2\%$, $N = 0$) together with the predicted profiles for $\{\omega_o, \omega_1\}=\{0.09, 0.09\}\%$ and $\{0.34, 0.34\}\%$. Although the axial distributions of our idealized imperfections differ from the experimental profile, the amplitude of the central wrinkles for $\{0.34, 0.34\}\%$ is very comparable to the largest wrinkle amplitude of the experiment while the amplitude of the central wrinkles in model with $\{0.09, 0.09\}\%$ is much smaller. Figure 7.6b shows similar results for CWR3. The model with $\{\omega_o, \omega_1\}= \{0.06, 0.06\}\%$ generated similar amplitude central wrinkles to the experimental ones where as for $\{0.09, 0.09\}\%$ this amplitude was somewhat over-predicted. This close relationship demonstrates that matching numerically the largest wrinkle amplitude before the onset of wrinkling provides a systematic way of selecting the model imperfection amplitudes.

The set of experiments in which the initial compressive strain $\bar{\varepsilon}_{xmon}$ was varied were also simulated with the same imperfection and constitutive model parameters. The resultant $\delta_x^p - N$ ratcheting results are compared to the experimental ones in Fig. 7.7a. Although the match between the experimental and predicted results is not perfect in all cases, the overall performance is still very good. Once again, these results indicate that the tubes tend to collapse when a critical amount of deformation or wrinkle amplitude is reached. In the results presented part of the wrinkle growth is introduced by monotonic compression. When this is relatively small then the number of cycles required to reach the critical value is larger, and when it is larger the critical deformation is reached in fewer stress cycles. Figure 7.7b shows the wrinkle profiles that develop in each of the three models using the same values of $\{\omega_o, \omega_1\}$ after initial compression. The amplitudes of the central wrinkles are very comparable to those of the corresponding experiments shown in Fig. 3.7b.

Three experiments with the same initial compressive strain $\bar{\varepsilon}_{xmon}$ and stress cycle parameters $\{\sigma_a, \sigma_m\}$ that exhibited different rates of ratcheting (see Fig. 3.8a) will be analyzed next shown in Figs. 7.8. Figure 7.8a shows the predictions using the standard values of $\{\omega_o, \omega_1\}$ together with the experimental values. The predictions are seen to differ from the measurements significantly for Exps. 9 and 11 while they are reasonable for Exp. 13. For a successful reproduction of the experimental rate of ratcheting (see Fig. 7.8b) the imperfection amplitudes $\{\omega_o, \omega_1\}$ for CWR11 had to be both increased to 0.15% whereas for CWR9 they had to be decreased to 0.05%. These values of initial imperfections were chosen by making the amplitudes of the central wrinkles—wrinkle profiles shown in Fig. 7.9–comparable to the largest wrinkle amplitude of the corresponding experiment shown in Fig. 3.8b.

7.2 SENSITIVITY OF RATCHETING ON PROBLEM PARAMETERS

The basic imperfection amplitude and the constitutive model variable C_r in (6.28) adopted in the simulations discussed in Section 7.1 (see Table 6.1) were selected for optimal performance of the model in predicting the ratcheting and onset of collapse of most of the experiments performed. Here we will illustrate the sensitivity of the results to these parameters using experiment CWR6 as the test case.

7.2.1 Imperfection Parameters

Figure 7.10a shows $\delta_x^p - N$ ratcheting results for CWR6 for various values of the main imperfection variable ω_o. Here this variable was assigned different values while all other parameters were kept at the basic case levels (see Table 6.1 and Fig. 7.1). This variable affects the rate of ratcheting during most of the loading history. Thus, as ω_o increases from 0.05% to 0.09% to 0.2% the rate of ratcheting is seen to increase with the value 0.09% producing the best agreement with the experimental results.

Figure 7.10b shows similar $\delta_x^p - N$ ratcheting results for different values of the second imperfection parameter, ω_1, with ω_o kept at the base value. This variable has relatively small effect on the rate of ratcheting during the part of the history when the wrinkle amplitude is growing at a nearly constant rate. The results clearly show however that it influences significantly the onset of localization; so as ω_1 increases the tube localizes in a fewer number of cycles. The value of 0.09% produces the best agreement with the experimental results.

Drawn in Fig. 7.10a with a dashed line are results for a tube with no imperfections (i.e., $\omega_o = \omega_1 = 0$). In this case the tube does not wrinkle or collapse and the accumulation of deformation is purely due to material ratcheting. Thus, these predictions agree with the measurements in the early party of the cycling (up to about $N = 60$) but do not capture the subsequent amplification of the rate of ratcheting that is influenced by structural effect.

In Chapter 3 it was pointed out that the machined tubular specimens used in the experiments had small thickness variations that had some influence on the ratcheting results. In the way of assessing the effect of thickness variations on the rate of ratcheting of our axisymmetric model, the following linearly varying thickness imperfection was introduced to the model:

$$t(x) = t_o[1 - \tau(1 - 2x/L)], \quad \tau = \frac{\Delta t}{t_o}, \quad 0 \le x \le L \tag{7.1}$$

where t_o is the average thickness and Δt is the amplitude of the variation. Ratcheting calculations were then performed for the loading parameters of CWR6 using three values of τ and the base case problem parameters in Table 6.1. The results are summarized in the form of $\delta_x^p - N$ ratcheting plots in Fig. 7.11. Although the thickness variations in the test specimens were not axisymmetric, their amplitudes were typically of the order of 1% of the mean thickness. The results show that for axisymmetric variations of this amplitude this type of imperfection affects mainly the onset of collapse. At much larger amplitudes (e.g., 2.5%) the rate of ratcheting in the steady state part of the simulation is also affected somewhat. For the present set of simulations the values of $\tau = 0$ was found to produce the best predictions. This proved to be different for the predictions of the pressurized results discussed in Chapter 8.

7.2.2 Constitutive Model Parameters

Next we consider two parameters of the constitutive model, C_r and σ_b, that influence material ratcheting and localization of wrinkles. As pointed out in Hassan *et al.*

(1992), if the bound is held the rate of ratcheting progressively decays and eventually ratcheting stops (deceleration illustrated in Fig. 7.12 for $C_r = 0$). One way of correcting this performance of the model is to allow the bound to shift downwards, or relax. This is achieved by the introduction of the second term in Eq. (6.28) with C_r (*relaxation coefficient*) governing the rate of relaxation (see Hassan and Kyriakides, 1994a, 1994b for details). The results in Fig. 7.12 demonstrate that as C_r increases the rate of ratcheting increases. The value of 60 was found to best reproduce the rate of ratcheting in this material.

The size of the bounding surface, σ_b, is another variable that affects the rate of ratcheting. Reducing σ_b decreases the plastic modulus during a stress cycle, increases the final plastic strain, which in turn results in an increase in the rate of ratcheting. The effect of this parameter on the rate of ratcheting is illustrated in Fig. 7.13 where $\delta_x^p - N$ ratcheting plots for three values of σ_b are compared to the experimental results of CWR6 with all other parameters kept at their base case values. The optimum value adopted in the simulations was σ_b = 114 ksi (786 MPa).

7.2.3 Effect of Anisotropy

The anisotropy of the tubes introduced by the manufacturing process affects the mechanical behavior of the tubes including their ratcheting strains. The anisotropy parameters $\{S_\theta, S_r\}$ = {1.15,0.85} in (6.29) and (6.30) were determined in separate experiments as discussed in Appendix A. Figure 7.14 shows the ratcheting responses for CWR6 using these values as well results with no anisotropy ($\{S_\theta, S_r\}$ = {0,0}). At the beginning of the $\delta_x^p - N$ trajectories the two results are similar but at higher values of N cycles, the isotropic results continue on a nearly linear trajectory whereas the anisotropic case gradually increases and becomes exponential when approaching collapse. This illustrates that, as was the case for monotonic compression (Kyriakides *et al.*, 2005; Bardi *et al.,* 2006), initial anisotropy plays a decisive role in the prediction of wrinkling and the onset of collapse and, consequently, it must be properly characterized and included in the model.

CHAPTER 8

WRINKLING DUE TO AXIAL CYCLING AND INTERNAL PRESSURE: ANALYTICAL RESULTS

In this Chapter, the axisymmetric shell formulation and the nonlinear kinematic hardening constitutive model outlined in Chapter 6 are used to simulate the experiments involving axial cyclic loading under constant internal pressure presented in Chapter 4.

8.1 SIMULATION OF A REPRESENTATIVE EXPERIMENT

It is once more instructive to start with the simulation of a representative experiment. In this regard we choose Exp. CWR34 using the geometric and loading parameters listed in Table 4.1. The material parameters of the corresponding tube (SAW8) are listed in Table 6.2. The critical wrinkle half wavelength was evaluated as outlined in Appendix B to be $\lambda = 0.537R$. The axisymmetric imperfection amplitudes $\{\omega_o, \omega_1\}$ were chosen again for best performance in the prediction of the rate of ratcheting of δ_x, which in this case were found to be $\{0.13, 0.13\}\%$. A thickness imperfection of $\tau = 2.0\%$ (see (7.1)) was also introduced.

The calculated axial stress-shortening response is shown in Fig. 8.1a. Following the initial preloading ($\bar{\varepsilon}_{xmon}$= 2.04%) the model was cycled axially using the cycle variables $\{\sigma_a, \sigma_m\}$ of the experiment. A total of 278 cycles were applied. The characteristics of the calculated response are very similar to those of the corresponding experimental one in Fig. 4.3a. Figure 8.1b shows a plot of the calculated peak displacement in each cycle (δ_x^p / L) vs. N along with the corresponding experimental results. The predicted trajectory is seen to agree well with the experimental results including the initial transient, the steady-state regime and the final exponential growth. It is interesting to separate the effect of material ratcheting from the axial shortening caused by the growth of the wrinkles. So included in Fig. 8.1b with a dashed line is the axial strain (ε_x^p) that would accumulate at a material point experiencing the same biaxial loading history (calculated by assigning zero values to the imperfection amplitudes). Interestingly, ε_x^p follows the calculated average strain (δ_x / L) very well up to approximately cycle 150. Subsequently, ε_x^p continues on a nearly linear trajectory whereas the rate of growth of δ_x / L gradually increases and becomes exponential close to $N = 270$.

Figure 8.2a shows axial profiles of the radial displacement, w, at various cycle counts ($x = 0$ represents the plane of symmetry). The first profile (N = 0) represents the small axisymmetric wrinkles formed during the initial monotonic compression. As the cycling progresses the amplitude of the winkles grows and simultaneously the circumference of the tube expands. After about 210 cycles the amplitude of the central wrinkle is seen to accelerate as deformation localizes here. The evolution of the displacement of this wrinkle is included in Fig. 8.1b where its amplitude, $w_{\max}$, is plotted against N together with the corresponding experimental results. The predicted trajectory is seen to agree very well with the discreet values from the largest wrinkle in the experiment.

The wrinkles and their localization are also illustrated in Fig. 8.3 where 3-D renderings of the configuration just before cycling commences ($\bar{\varepsilon}_{xmon}$ = 2.04%), one after cycle 210 and a third one after cycle 286, at a net axial shortening of approximately 4.3%, are shown. The place and nature of the localization are of course different from those of the experiment because of the idealized geometry, imperfections, and boundary conditions adopted. However, overall the model is seen to be able to reproduce the interaction between material ratcheting and wrinkle growth very well.

The predicted ratcheting in the hoop strain is compared to measured values in Fig. 8.2b. Because of the growing wrinkles the evolution of the hoop strain differs at different points along the length of the tube. In the experiment this strain was measured at the two locations marked as SG1 and SG2 in Fig. 4.4a. Since the domain of the model does not match that of the tube tested, we select to report the strains at two points that approximate the experimental ones (SG1 and SG2 in Fig. 8.2a). The calculated strains at SG1 agree very well with the measured values. At SG2 the predictions initially also agree with the measurements but differ after cycle 200 because in the model this point was affected by the localization of the central wrinkle. Included in Fig. 8.2b is the hoop strain that would accumulate for a material point experiencing the same biaxial loading history (dashed line). The results can be seen to agree very well with those calculated for SG1 indicating that this point represents the mean value along the length of the model. We point out that this degree of agreement is only possible because of the calibration of the hardening rule outlined in the Section 6.3.

Finally, Fig. 8.4a shows a plot of the calculated hoop strain at SG1 ($\varepsilon_{\theta 1}$) vs. the net shortening δ_x^p / L which illustrates the nature of the biaxial ratcheting that takes place. The results compare very favorably with the corresponding experimental plot in Fig. 4.5. Included in Fig. 8.4b is the corresponding biaxial ratcheting trajectory experienced by a material point that undergoes the same cyclic history. The two plots agree well up to the point when the wrinkle amplitude starts to accelerate causing an exponential grown in δ_x^p / L.

As was the case for axial cycling without pressure in Chapter 7, the results and particularly the rate of axial ratcheting and the number of cycles at collapse are influenced by the choice of initial imperfection introduced in the model. Although each of the three imperfection variables plays a somewhat different role (see Figs. 7.10 and

7.11), here we have chosen to keep $\tau = 2.0\%$ and assign the same values to ω_o and ω_1. Figure 8.5 shows how the value of these imperfection amplitudes affects the calculated axial ratcheting response ($\delta_x^p / L - N$). Although initially the rate of ratcheting follows the measurements for all cases, larger amplitude causes collapse to occur earlier and smaller later. Interestingly, the value chosen for the final simulation is one for which the amplitude of the largest wrinkle after the initial monotonic compression is close to the amplitude of the largest wrinkle at the same point in the experiment (compare value for $N = 0$ in Fig. 8.2a and in Fig. 4.4a). Thus this became a guideline for choosing $\{\omega_o, \omega_1\}$ for the rest of the simulations.

8.2 SUMMARY OF RESULTS OF SIMULATIONS OF OTHER EXPERIMENTS

The same constitutive model parameters and for most cases the same imperfection amplitudes have been used to simulate all of the rest of the experiments shown in Chapter 4. The results will be presented below in summary form.

Calculations were first performed for the four cases tested at the same $\bar{\varepsilon}_{xmon}$ and σ_a but pressurized to different levels. Predicted δ_x^p / L-N ratcheting results are compared to the experimental ones in Fig. 8.6 with which they are seen to agree very well. The average strain levels at which collapse becomes imminent are also in good agreement with the monotonic compression values ($\bar{\varepsilon}_{Lmon}$). This level of agreement however was only possible by selecting the initial imperfection amplitudes a bit smaller for CWR44 and larger for CWR42 than the values chosen for most of the rest of the experiments ($\{\omega_o, \omega_1\}$ given in Fig. 8.6). These choices were necessary because small differences between the initial imperfections in these four tubes resulted in wrinkles of significantly different amplitudes after the initial pre-compression as evidenced by the wrinkle profiles shown in Fig. 4.8b. To illustrate this point further Fig. 8.7a shows the wrinkle profiles that develop in each of the four models using the chosen values of $\{\omega_o, \omega_1\}$ after the initial compression of 2.5% at the appropriate pressure level. Although the axial distributions of our idealized imperfections differ from those in Fig. 4.8b, the amplitudes of the central wrinkles in Fig. 8.7a are very comparable to the largest wrinkle amplitude of the corresponding experiment. This close relationship demonstrates that matching numerically the largest wrinkle amplitude before the onset of wrinkling provides a systematic way of selecting the model imperfection amplitudes.

For the three pressurized cases in this set of experiments we also present a comparison between the measured and calculated values of ε_θ vs. N in Fig. 8.7b. The calculated values correspond to the points SG1 and SG2 marked with solid bullets in the corresponding wrinkle profile in Fig. 8.7b. These locations were again chosen to approximately match the locations of the physical strain gages marked in the same manner on the experimental wrinkle profiles in Fig. 4.8b. All calculated trajectories are seen to agree well with the corresponding experimental ones. This degree of agreement was also dependent on making the correct choice of $\{\omega_o, \omega_1\}$.

Thus Fig. 8.8a shows comparisons of predicted δ_x^p / L-N ratcheting plots from the three experiments tested at the same pressure $(0.59 P_o)$, pre-compressed to $\bar{\varepsilon}_{xmon} \approx 2.0\%$ but cycled at different σ_a (i.e., CWR32-34). The numerical results match the experimental ones very well in the early stages of ratcheting and quite well in the regions of exponential growth of δ_x^p that precipitates collapse. The ratcheting in the hoop strain was also predicted well for all three cases shown in Fig. 8.8b. This degree of success is possible because the imperfections of these three specimens resulted in very similar wrinkles in the test section following the initial compression of 2.0% (see Fig. 4.11b).

Figure 8.9 shows comparisons of predicted δ_x^p / L-N ratcheting plots from the three experiments tested at the same pressure $(0.49 P_o)$, pre-compressed to $\bar{\varepsilon}_{xmon} \approx 2.0\%$

but cycled at different σ_a (i.e., CWR24, 25, 31). The numerical results match the experimental ones very well in the early stages of ratcheting and the regions of exponential growth of δ_x^p that precipitates collapse. This level of agreement however was only possible by selecting the initial imperfection amplitudes different from most of the rest of the experiments ($\{\omega_o,\omega_1\}$ given in Fig. 8.9). These choices were made so that the largest wrinkle amplitude before the onset of wrinkling in simulations could match numerically the corresponding experimental results (compare Fig. 8.10b and Fig. 4.13b). The ratcheting in the hoop strain was also predicted very well for all three cases shown in Fig. 8.10a.

Figure 8.11 compares measured and calculated δ_x^p / L-N ratcheting plots from two cases tested at the same pressure ($0.59P_o$) and with the same stress amplitude (σ_a= 68 ksi—469 MPa) but were pre-compressed to different average strain levels (i.e., CWR34 and 39). Once again δ_x^p / L was predicted very well for both cases and so was that of $\varepsilon_{\theta p}$ shown in Fig. 8.12a. Figure 8.12b plotted the simulated profiles following the initial monotonic compressions of 2.0% for CWR34 and 2.5% for CWR 39. The largest wrinkle amplitudes of the two profiles compare well with the corresponding experimental ones shown in Fig. 4.15b.

Figure 8.13 compares measured and calculated δ_x^p / L-N ratcheting plots from two cases tested at the same pressure ($0.22P_o$) and with the same stress amplitude (σ_a= 56 ksi—386 MPa) but were pre-compressed to different average strain levels (i.e., for CWR35 $\bar{\varepsilon}_{xmon}$ = 2.0% and for 40 $\bar{\varepsilon}_{xmon}$ = 2.5%). δ_x^p / L is again predicted very well for both cases and so is that of $\varepsilon_{\theta p}$ shown in Fig. 8.14a. Figure 8.14b shows the simulated profiles following the initial monotonic compressions of 2.0% for CWR35 and 2.5% for CWR 40. The largest wrinkle amplitudes of both profiles matched well with the corresponding experimental results shown in Fig. 4.17b.

CHAPTER 9

ANALYTICAL RESULTS FROM TUBES THAT WERE CYCLED BEFORE WRINKLING

In Chapter 5 we described experiments in which the initial compression was terminated well before the onset of wrinkling. It was shown that compressive strain accumulated by ratcheting tends to initiate wrinkling at the same approximate strain as that of monotonic compression. These experiments are simulated in this Chapter using the axisymmetric shell formulation and the nonlinear kinematic hardening constitutive model outlined in Chapter 6.

9.1 SIMULATIONS OF BUCKLING EXPERIMENTS UNDER PURE AXIAL CYCLING

Again, we start with the simulation of a representative experiment and in this case Exp. CWR19 is chosen using the geometric parameters listed in Table 5.1 and the material parameters of the corresponding tube (SAW7) listed in Table 6.3. The critical wrinkle half wavelength was evaluated as outlined in Appendix B to be $\lambda = 0.300R$. As in the case of buckling under monotonic axial compression the model requires seeding with an initial geometric imperfection. In this case $\{\omega_o, \omega_1\} = \{0.02, 0.02\}\%$ was chosen which is significantly smaller than the values used for the pre-wrinkled tube simulations (see sensitivity of the solution to $\{\omega_o, \omega_1\}$ later in this Section).

The calculation is similar to those discussed earlier in Chapter 7. The resultant stress-shortening response is shown in Fig. 9.1. Following the initial pre-compression of 0.99%, the model was cycled axially using the cycle variables $\{\sigma_{a1}, \sigma_{m1}\}$ of the experiments (Table 5.1). A total of 410 cycles were applied during which the tube ratcheted to $\delta_x^p / L = 0.0235$. The characteristics of the calculated response are very similar to those of the corresponding experimental one in Fig. 5.1a. Figure 9.2 shows plots of the calculated peak axial displacement (δ_x^p / L) and the maximum radial displacement in each cycle ($w_{\max}(0)/R$) vs. N along with the corresponding experimental results. Both sets of predictions are seen to be in very good agreement with the measurements. Both replicate the initial transient that lasts about 100 cycles and then settle into a nearly constant rate of growth maintaining approximately a ratio of 0.5 expected from incompressibility. Clearly, the main contributor here is material ratcheting, however simultaneously the wrinkle amplitude grows gradually.

Figure 9.3 shows a set of deformed generators at different average strains and N during the loading history. After 10 cycles, when the average strain is 1.02%, the wrinkles are barely discernible. By cycle 67 and an average strain of about 1.5% they have grown slightly and become more pronounced by cycle 170 when $\bar{\varepsilon}_x$ = 1.89%. Thus, by the end of this phase of loading history at N = 410 and $\bar{\varepsilon}_x$ = 2.35%, the wrinkles are fully developed very much as was the case in the experiment.

As in the experiment, the $w_{\max} - N$ plot in Fig. 9.2 does not show any sudden change in its rate of growth, making it difficult to pinpoint any strong tendency of the wrinkled solution becoming dominant (remember that for monotonic loading the bifurcation is nearly tangential to the trivial solution). Included in the figure with a dashed line is the critical bifurcation strain calculated for this tube assuming the loading was monotonic (this is also marked with an arrow (←) in Fig. 9.3). Clearly, this strain level is in reasonable agreement with the neighborhood in which the wrinkles start to become discernible in Fig. 9.3.

The same constitutive model parameters were used to simulate the second phase of the experiment with the higher mean stress (σ_{m2} = 33.94 ksi—234 MPa). A total of 200 additional cycles were applied and the results are included in Figs. 9.1-9.3. The structure ratchets at a higher rate, and this is reflected in the stress-displacement response in Fig. 9.1 and in the $\delta_x^p / L - N$ and $w_{\max} - N$ plots in Fig. 9.2. All sets of predictions are seen to follow the experimental results quite closely. At the same time, the wrinkles are also growing at a faster rate. The wrinkle amplitude starts to grow faster around cycle 530 and during the last 25 cycles grows in a nearly exponential manner. The simulation was terminated after cycle 610 when the tube showed signs of eminent collapse. The average strain level at which similar tubes developed a limit load instability under monotonic loading ($\bar{\varepsilon}_{Lmon}$) is seen once more to coincide with the strain level at which the rate of ratcheting experiences exponential growth.

In summary then, the model with the set of parameters chosen is seen to reproduce with accuracy all aspects of this very nonlinear structural behavior including the onset of buckling and localization instabilities. The other two cyclic experiments were also simulated using the same imperfection and constitutive model parameters (specimen geometric and loading cycle variables given in Table 5.1). The results are similar to those of Exp. CWR19 and thus only the ratcheting predictions are shown in Fig. 9.4 along with the corresponding experimental results. The model is seen to replicate the ratcheting rate of δ_x in the first phase of these experiments very well. In the second phase the ratcheting rate is reproduced very well for CWR15 and somewhat less well for CWR18. In both cases the final exponentially growing part of the record occurs at the same approximate level as in the experiments and the corresponding level at which the tube develops a limit load under uniaxial compression.

The imperfection amplitudes and the constitutive model parameters adopted in the model for the conduct of the simulations above can influence the predictions. Section 7.2 presented a detailed study of the effect of these parameters from which some general guidelines for the values that result in optimal performance of the model in predicting the observed behavior were established. These guidelines formed also the basis for the present calculations but some modifications had to be introduced to reflect the new cyclic loading conditions. Thus for example, for the pre-wrinkled tubes cycled in Chapter 7 the imperfection amplitudes were $\{\omega_o, \omega_1\} =$ {0.09, 0.09}%. Here the cycling was commenced well before any wrinkles developed. Consequently the two amplitudes had to be reduced to {0.02, 0.02}% in order for the rate of ratcheting to be reproduced correctly. Figure 9.5 shows how these imperfection parameters affect the rate of growth of δ_x^p as a function of *N* for four values of imperfection amplitudes, (0, 0.02, 0.05, 0.09)%. In the absence of an imperfection ($\omega_o = \omega_1 = 0$) the tube does not wrinkle and the recorded shortening is strictly due to the ratcheting of the material strain that is governed by the constitutive model parameters. Despite this, during the first phase of the experiment ($N \leq 410$) the predictions remain very close to the measurements supporting the relatively slow growth of the wrinkle amplitude reported in the experiment. During the second phase of the test, wrinkle growth becomes more dominant and the predictions are seen to under-predict the measurements. By contrast, when the imperfection amplitudes are assigned the value of 0.09%, the ratcheting rate of δ_x is over-predicted somewhat for $200 < N \leq 410$ and significantly subsequently. For imperfection amplitudes of 0.05% the predictions are closer to the measurements but remain higher. The best predictions were yielded by $\omega_o = \omega_1 = 0.02\%$ which was adopted in the simulations presented in the previous section.

Figure 9.6 shows the effect of the relaxation coefficient C_r of the constitutive model (see (6.28)) on the predicted results for CWR19. Hassan *et al.* (1992) pointed out that if the bound is kept fixed the rate of ratcheting becomes progressively slower and can eventually lead to shakedown. This trend is illustrated in Fig. 9.6 for $C_r = 0$. The second term in (6.28) allows the bound to shift downwards, or relax (Hassan and Kyriakides, 1994a, 1994b). The results in the figure demonstrate that as C_r increases the rate of ratcheting increases. The value of 40 was found to best reproduce the rate of ratcheting for the tube geometry and material used in the present set of experiments.

9.2 SIMULATION OF BUCKLING DUE TO AXIAL CYCLING UNDER INTERNAL PRESSURE

We now conduct a similar simulation but for a case where the onset of wrinkling due to axial strain ratcheting is examined in the presence of internal pressure. Experiment 47 was first pressurized to $0.59P_o$, then pre-compressed to a strain of 0.92% and subsequently cycled axially with the cycle parameters given in Table 5.1 (material parameters listed in Table 6.2). Results from the numerical simulation are shown in Figs. 9.7-9.9. It is important to note that pre-straining of 0.92% does not cause wrinkling at this pressure level. Small initial geometric imperfections of the same amplitude as the unpressurized cases were again introduced to the model (i.e., $\{\omega_o, \omega_1\} = \{0.02, 0.02\}\%$).

Figure 9.7 shows the calculated axial stress-shortening response, which is seen to follow the corresponding experimental results in Fig. 5.4a quite faithfully. The axial ratcheting is better quantified in the $\delta_x^p / L - N$ results plotted in Fig. 9.8 along with the experimental counterpart. Axial ratcheting follows the experimental trend very well indeed. Figure 9.9 shows a set of deformed generators at different levels of average axial strain developed after N cycles. The deformation of the generators illustrates the evolution of wrinkling in the test section. Following compression to a strain of 0.98%, the generator appears essentially free of wrinkles. After 40 cycles, when the average strain is 1.19%, the wrinkles are barely discernible. By cycle 70 and an average strain of 1.30% they have grown slightly and become more pronounced by cycle 195 when $\bar{\varepsilon}_x$ = 1.54%. Subsequently the wrinkles grow so that by the end of the first phase of the loading history at N = 310 and $\bar{\varepsilon}_x$ = 1.66%, the wrinkles are fully developed very much as was the case in the experiment. The wrinkles grow further in the second phase of the loading history.

As in the experiment, the $w_{\max} - N$ plot in Fig. 9.8 does not show any sudden change in its rate of growth, making it difficult to pinpoint any strong tendency of the wrinkled solution becoming dominant (remember that for monotonic loading the bifurcation is tangential to the trivial solution).

The critical bifurcation buckling strain predicted for this case, marked on the monotonic response in Fig. 9.7 with "↓", is $\varepsilon_C = 1.42\%$. This value is also marked on the $\bar{\varepsilon}_x$ axis in Fig. 9.9 with "←". What can be concluded is that this strain level is in reasonable agreement with the neighborhood in which the wrinkles start to become discernible. This happens despite the fact that the maximum stress level of the cycles is lower than the critical stress under monotonic loading while the modulus is much higher. Thus, the analysis concurs with the experimental observation (Section 5.2) that the onset of plastic wrinkling is strain rather than stress driven.

CHAPTER 10

CONSTRAINED PIPELINE STARTUP-SHUTDOWN CYCLING

In Chapter 1, a possible scenario that can lead to shell-type buckling of trenched pipelines from the shutdown and startup cycles was discussed. In subsequent Chapters a modeling framework was developed and shown to reproduce the interaction of ratcheting and wrinkling. The model is now used to numerically simulate the actual startup/shutdown cycling of axially constrained pipelines in order to examine the effect they have on the possible limit states of axial collapse and burst.

10.1 SIMULATION OF PIPES UNDER THERMAL-PRESSURE CYCLIC LOADING

Startup of a pipeline results in flow of hot hydrocarbons at an elevated pressure. This situation is modeled as a long pipe that is stress free but fully axially constrained. The pipe is pressurized to the chosen level with the temperature staying constant resulting in increase of hoop stress as shown in Fig. 10 .1a (①-②, see also Klever *et al.*, 1994). (Note, small compressive/tensile strains left for the installation are neglected.) In the present case this results in a hoop stress of $\sigma_\theta = 0.7\sigma_o$. Simultaneously, because of the axial constraint the pipe develops some axial tension that can be seen in Fig. 10.1b. As flow of hot hydrocarbons commences, the temperature increases by ΔT taking us to ③ (here $\Delta T =$ 300°C) and placing the pipe into axial compression as shown in Fig. 10.1b (the thermal coefficient of expansion $\alpha = 13.5 \times 10^{-6}$/°C). Shutdown in case of cleaning and evacuation/inspection, the flow is stopped, the pressure is released (④), and the temperature returns back to that of the seafloor taking us back to ①. When the line is restarted it is assumed to trace the same path and so does the next shutdown. Indeed, we assume that all such cycles follow the path shown in Fig. 10.1a.

The pipe considered in this example has a D/t = 28.4 and the same material properties as those of the tubes used in this study. The model is the same as that in Chapter 8 with imperfection amplitudes of $\{\omega_o, \omega_1\} = \{0.13, 0.13\}\%$. We also adopt the constitutive model as calibrated (i.e., any effects on mechanical properties caused by the change in temperature are neglected). The effect of temperature is included by subtracting $\alpha \Delta T \mathbf{I}$ from the strain increments in Eq. (6.14). For full axial constraint $d\varepsilon_x$ is set to zero and ΔT is prescribed incrementally.

Figures 10.1 and 10.2 show detailed results from the first 200 cycles. The resultant nearly parallelogram shaped $\sigma_x - \sigma_\theta$ loops are seen in Fig. 10.1b to drift to the right as N increases, which can be viewed as a form of cyclic relaxation (see Fig. 4 in Hassan and Kyriakides, 1994a). The induced hoop stress-strain response (at $x = 0$) is shown in Fig. 10.2a where the hoop strain is clearly seen to be ratcheting. Figure 10.2b in turn shows the evolution of the axial stress with the cycled ΔT. In concert with the results in Fig. 10.1b the axial stress loop tends to shift towards somewhat higher values as the cycling progresses.

The effect on the structural integrity of the pipe is shown in Figs. 10.3. In view of the loading imposed the average axial strain does not change however the wrinkle amplitude does increase with N and this is shown in Fig. 10.3a where Δw from 1000 cycles is plotted vs. N (Δw is the difference between the maximum and minimum radial displacements of the most deformed wrinkle). For this ΔT the wrinkle amplitude grows slightly during the first 100 cycles but subsequently, the axial stress cycle stabilizes and the wrinkling stops growing, which can be viewed as a form of shakedown. This stabilization is confirmed in Fig. 10.1b, which includes the $\sigma_x - \sigma_\theta$ loop for the 1000th cycle. It is seen to be essentially coincident with the corresponding loop from the 200th cycle. However, as can be seen in Fig. 10.3b the average hoop strain, $\bar{\varepsilon}_\theta$, continues to grow with N; it starts at a value of 0.843% and grows to 1.90% after 1000 cycles ($\bar{\varepsilon}_\theta$ averaged over the tube length). Nevertheless this growth is very modest and should pose no danger to the integrity of the structure provided this number of cycles in not exceeded.

Similar calculations were performed for $\Delta T =$ 400ºC and 500ºC at the same pressure level. The results are included in summary form in Figs. 10.3. The wrinkle amplitude Δw is seen in Fig. 10.3a to grow more significantly with N at the higher values of ΔT. However, after 1000 cycles Δw remains very small indicating that collapse is not of concern even at these high cycle counts. The rate of growth of $\bar{\varepsilon}_\theta$, included in Fig. 10.3b, also increases with ΔT. The values remain modest after 200 cycles for all temperatures considered but grow significantly after 1000 cycles especially for $\Delta T =$ 500ºC. Such values should be of special concern in the case of seam-welded pipes and at points of stress concentrations like flanges. However, $\Delta T =$ 500ºC is not often encountered in practice and 1000 cycles is excessive for most pipelines designed for a lifespan of 20 years.

The effect of the pipe D/t was examined in a set of similar cyclic calculations for $P = 0.7 P_o$ and $\Delta T =$ 300ºC for pipes of lower D/t values of 24 and 20. Ratcheting results for D/t values of 28.4, 24 and 20 are compared in Fig. 10.4. Figure 10.4a shows that decreasing the D/t reduces the level of the $\Delta w - N$ trajectory, reducing even further the possibility of collapse in a reasonable number of cycles. By contrast, the $\bar{\varepsilon}_\theta - N$ results are seen in Fig. 10.4b to be unaffected by D/t.

In summary, for the pipe geometries and material properties considered the main effect of the $P - \Delta T$ cycling is a relatively slow growth of the hoop strain. For a reasonable number of cycles this ratcheting is relatively benign. Axial wrinkling grows so slowly that its effect can be neglected at least in the main part of the pipeline that is free of stress concentrations.

10.2 SIMULATION OF PIPES UNDER AXIAL STRAIN-PRESSURE CYCLIC LOADING

In the preceding section the pipe was axially constrained and the axial cycling was induced by changing its temperature. For completeness we also consider the related situation where the axial cycling is performed mechanically like it was done in the experiments performed for this study. Thus, the rectangular $\sigma_\theta - \Delta T$ loading path of Fig. 10.1a is now replaced by the $\sigma_\theta - \Delta\varepsilon_x$ path shown in Fig. 10.5a. The cycle starts at point ① where the pipe has a small tensile axial strain of 0.05%. The pressure is then increased inducing $\sigma_\theta = 0.7\sigma_o$ (②) while the axial strain is kept constant (at 0.05%). Because of the axial constraint the pipe develops some axial tension that can be seen in Fig. 10.5b. The pressure is fixed and a compressive axial strain of $\Delta\varepsilon_x$ = -2% is applied. At point ③ in Fig. 10.5a the pressure is gradually reduced to zero (④). The cycle is completed by removing the axial strain returning back to ①. All following cycles trace the same path.

Figures 10.5-10.7 show the stresses and strains induced by 50 cycles. The resultant $\sigma_x - \sigma_\theta$ loops are seen in Fig. 10.5b to shrink somewhat. Figure 10.6a shows and the hoop stress-strain response (at x = 0); clearly here the hoop strain is ratcheting reaching a maximum value of 7.07% after 50 cycles. Figure 10.6b in turn shows the evolution of the axial stress with the cycled $\Delta\varepsilon_x$.

Figure 10.7 shows axial profiles of the radial displacement, w, at various cycle counts ($x = 0$ represents the plane of symmetry). The profile for N = 0 represents the small axisymmetric wrinkles formed during the initial pressurization and the compression induced at point ③ during the first cycle. As the cycling progresses the amplitude of the winkles grows and simultaneously the circumference of the tube expands. In contrast to the profiles shown in Fig. 8.2a for axial cyclic loading with constant internal pressure the localization of wrinkles is modest as the amplitudes of the wrinkles are increasing nearly uniformly. However, the rate of growth of the amplitude is rather large as is the growth of the average hoop strain. Thus, at this stage such a pipeline would be in danger of either collapse or burst.

Similar calculations were performed for different values of $\Delta\varepsilon_x$ at the same pressure level. The results are included in summary form in Figs. 10.8. The wrinkle amplitude Δw is seen in Fig. 10.8a to grow more significantly with *N* at the higher values of $\Delta\varepsilon_x$ whereas for $\Delta\varepsilon_x \leq 1.5\%$, Δw remains very small indicating that collapse is not of concern even after 200 cycles. So, we can conclude that the threshold value of $\Delta\varepsilon_x$ for no danger of collapse for tubes with $D/t = 28.4$ and pressure level $P = 0.7P_o$ is about 1.5%.

The rate of growth of $\bar{\varepsilon}_\theta$, included in Fig. 10.8b, also increases with $\Delta\varepsilon_x$. The values are very high for all $\Delta\varepsilon_x$ considered. Such levels of accumulated hoop strain should be of concern for seam-welded pipe and at girth welds.

CHAPTER 11

SUMMARY AND CONCLUSIONS

The ratcheting, buckling and wrinkling of circular tubes under stress-controlled axial cycling and axial cycling under constant internal pressure was investigated through a combination of experiments and analyses. This chapter summarizes the procedures used, the major finds and the conclusions drawn in each of the components of the study.

11.1 EXPERIMENTS ON PRE-WRINKLED TUBES

Experiments were conducted for both loadings using super duplex stainless steel tubes with D/t of about 28.5. Ten experiments were first performed under pure axial cycling in which specially designed tubular specimens were first compressed to strain levels high enough for mild wrinkles to form; they were then cycled axially under stress control about a compressive mean stress. In a solid, this type of cycling results in the progressive accumulation of compressive strain (material ratcheting). In the present setting, material ratcheting was accompanied by progressive growth of the amplitude of the preexisting wrinkles. The initial wrinkles first grew uniformly with the number of cycles at a nearly constant rate. This, coupled with the material ratcheting, caused the tube to shorten at a nearly linear rate with the number of cycles applied. When the wrinkles reached a critical amplitude their rate of growth accelerated while simultaneously deformation started to localize, usually at one site. The growth of localization accelerated, with each cycle becoming exponential and resulting in localized collapse of the tube. The shortening-N trajectories exhibit an initial transient, an extended linear regime and a fast growing one that terminates in collapse. The two mechanisms behind this behavior are material ratcheting and structural degradation in the form of wrinkle growth. The two mechanisms cooperate, with the wrinkle growth being the one responsible for collapse.

Thirteen experiments were then performed in which the tubes were axially cycled under constant internal pressure. Here, tubes were first pressurized to a chosen level and compressed sufficiently for small amplitude wrinkles to appear on the surface of the tubes; the specimens were then cycled axially in stress control about a compressive mean stress. The cycling results again in accumulation of axial compressive strain and growth of the wrinkles but is also accompanied by gradual expansion of the diameter of the tube. Both the hoop strain and the wrinkle amplitude initially grow nearly linearly with N. But again beyond a certain amplitude the wrinkle growth accelerates, localizes usually at one site and leads to collapse. In all experiments conducted the tubes collapsed due to wrinkle localization. In other words, for the problem parameters considered the other possible limit state of burst due to excessive wall thinning induced by hoop strain growth did not materialize as the hoop strain accumulated stayed at relatively small levels.

The following observations can be made from the experiments:

(a) Collapse under cyclic loading was found to occur when the average strain in the tube reached a level that corresponds to the average strain at the load maximum under monotonic loading. This was the case for both loadings considered. This provides a practical way of estimating the life expectancy of a wrinkled tube that is experiencing cyclic loading.

(b) The number of cycles to collapse is governed by the level of the initial pre-strain, and by the mean stress and amplitude of the load cycles and also by the internal pressure applied.

(c) As is the case for monotonic loading, initial geometric imperfections can reduce the average strain at failure and the corresponding number of cycles.

(d) In the experiments with internal pressure, the hoop strain accumulated during the cycling remained at relatively low levels.

11.2 EXPERIMENTS ON TUBES WITHOUT PRE-WRINKLING

Separate experiments were performed in order to investigate whether material strain ratcheting can initiate wrinkling. Tubes of the same geometry ($D/t \approx$ 28.7) and material were cycled in a similar manner but the cycling was commenced at smaller compressive strain levels well before the appearance of wrinkles. During the cycling the surface of the tube was periodically scanned with a very sensitive laser displacement transducer for signs of non-trivial deformation. It was found that initially the tube shortened uniformly due to pure material ratcheting. At some stage small amplitude non-uniformities started appearing on the surface of the tube, which gradually organized themselves into axisymmetric wrinkles. The wavelengths of such wrinkles were approximately the same as those of wrinkles formed under monotonic compression. Even more importantly, the strain levels at which they appeared coincided with the critical wrinkling strain levels measured under monotonic loading. This happened despite the fact that the maximum compressive stress of the cycles was smaller than the bifurcation stress under pure compression. In other words, the onset of wrinkling appears to be strain rather than stress driven, a result that is contrary to the hitherto general understanding that plastic bifurcation buckling is stress-driven.

11.3 ANALYSIS ON PRE-WRINKLED TUBES

The two sets of pre-wrinkled tube experiments were simulated numerically using nonlinear axisymmetric shell kinematics coupled with the two-surface plasticity model of Dafalias and Popov (1975, 1976) along with modifications of this model recommended for ratcheting applications by Hassan *et al.* (1992) and Hassan and Kyriakides (1992, 1994a, 1994b). The shell domain analyzed was assigned small initial axisymmetric imperfections with a small bias in order to facilitate localization. The amplitudes of these imperfections were chosen for optimal performance of the model in predicting the rate of ratcheting and the onset of localization. The plasticity model was calibrated to measured stress-strain data of SAF2507 super duplex stainless steel. A sensitivity study of the formulation to the imperfections and to key constitutive model parameters was also performed.

The numerical model was found to reproduce the material ratcheting, the evolution of wrinkles and their eventual localization very well over the whole range of problem parameters tested. Furthermore, it confirmed that collapse under cyclic loadings materializes when the wrinkles reach a critical level, and that the average strain at collapse corresponds to that at the onset of collapse under monotonic loading.

Like most buckling problems, the present problems exhibit sensitivity to initial geometric and other imperfections. The initial imperfections were difficult to characterized. Instead, their effect was quantified by measuring the amplitude of the induced wrinkles following the initial preloading. The measured amplitude was used as the basis for selecting the amplitude assigned to the axisymmetric imperfections introduced to the models.

11.4 ANALYSIS ON TUBES WITHOUT PRE-WRINKLING

The structural and material models were also used to simulate the tubes that were not pre-wrinkled under pure axial cycling and combination of axial cycling and constant internal pressure. In this case, the shell domain analyzed was assigned significantly smaller initial axisymmetric imperfections than the values used for the pre-wrinkled tube simulations. The numerical model reproduced with accuracy the initial pure material ratcheting. The imperfection amplitude initially grew insignificantly but much faster when the induced strain reached the level at which the tube bifurcates into the wrinkling mode under pure compression confirming the experimental observations. Once formed, the wrinkle amplitude grew with cycling and eventually lead to localization and collapse. It was again confirmed that collapse under cyclic loadings materializes when the wrinkles reach a critical level, and that the average strain at collapse corresponds to that at the onset of collapse under monotonic loading.

11.5 SIMULATION OF STARTUP-SHUTDOWN CYCLES OF AXIAL CONSTRAINED PIPELINE

After proving its veracity, the numerical model developed was used to simulate thermomechanical cycling of axially restrained pipelines due to periodic start-up and shutdown. The cycles considered involve pressurization, followed by heating, depressurization and cool down. This cyclic loading causes ratcheting of the hoop strain and gradual growth of wrinkles. Sample results presented show that for realistic pressure and temperature levels the pipes considered are not in danger of either bursting or of developing localized collapse provided the number of cycles applied is kept below a few hundred.

Table 3.1 Specimen parameters and critical variables measured in monotonic axial buckling experiments

CWR No.	Tube No.	D in (mm)	t in (mm)	$\frac{D}{t}$	$t_{\min} - t_{\max}$ in (mm)	Ξ_o (%)	σ_C ksi (MPa)	ε_C %	λ / R	σ_L ksi (MPa)	$\bar{\varepsilon}_{Lmon}$ %
10	SAW6	2.2532 (57.23)	0.0788 (2.00)	28.57	0.0782-0.0796 (1.99-2.02)	1.78	102.5† (707)	1.48†	0.289†	111.20 (767)	4.13
12	SAW6	2.2516 (57.20)	0.0778 (1.98)	28.94	0.0772-0.0788 (1.96-2.00)	2.05	103.8† (716)	1.46†	0.287†	114.26 (788)	4.39
14	SAW6	2.2542 (57.26)	0.0794 (2.02)	28.39	0.079-0.0798 (2.01-2.03)	1.00	103.6† (715)	1.50†	0.290†	111.28 (767)	4.25
20	SAW7	2.2536 (57.24)	0.0785 (2.00)	28.71	0.0778-0.0794 (1.98-2.02)	2.03	101.5-103.8 (700-716)	1.15-1.45	0.240-0.260	116.8 (806)	4.50
21	SAW7	2.2531 (57.23)	0.0785 (2.00)	28.70	0.0778-0.0788 (1.98-2.01)	1.27	101.1-104.5 (697-721)	1.15-1.60	0.264-0.326	0.264-0.326	4.42

† Bifurcation Analysis, $L = 3$ in (76.2 mm)

Table 3.2 Geometric and material parameters of wrinkling under cyclic loading experiments

CWR No.†	D in (mm)	t in (mm)	$\frac{D}{t}$	$t_{\max}$ - $t_{\min}$ in (mm)	Ξ_o (%)	σ_{xmon} ksi(MPa)	$\bar{\varepsilon}_{xmon}$ (%)	σ_m ksi (MPa)	σ_a ksi (MPa)	N_C	$\bar{\varepsilon}_f$ (%)	$\frac{\lambda}{R}$††
2	2.2510 (57.18)	0.0784 (1.99)	28.71	0.0794/0.0773 (2.02/1.96)	2.67	105.98 (730.9)	2.43	43.38 (299.9)	62.60 (431.7)	480	4.79	0.281
3	2.2525 (57.21)	0.0788 (2.00)	28.59	0.0794/0.0783 (2.02/1.99)	1.40	108.40 (747.6)	2.29	44.25 (305.2)	64.15 (442.4)	403	4.61	0.282
4	2.2482 (57.10)	0.0761 (1.93)	29.54	0.0770/0.0752 (1.96/1.91)	2.36	107.21 (739.4)	2.18	36.88 (254.3)	70.33 (485.0)	340	4.76	0.281
5	2.2504 (57.16)	0.0773 (1.96)	29.11	0.0786/0.0760 (2.00/1.93)	3.42	106.41 (733.9)	2.30	30.57 (210.8)	75.84 (523.0)	58	4.52	0.279
6	2.2569 (57.33)	0.0805 (2.04)	28.01	0.0813/0.0798 (2.06/2.03)	1.86	108.53 (748.5)	2.24	37.71 (260.1)	70.82 (488.4)	182	4.45	0.287
7	2.2468 (57.07)	0.0754 (1.92)	29.79	0.0759/0.0745 (1.93/1.89)	1.86	109.69 (756.5)	2.34	37.71 (260.1)	71.98 (496.4)	111	4.29	0.277
8	2.2496 (57.14)	0.0768 (1.95)	29.29	0.0779/0.0758 (1.98/1.93)	2.73	110.13 (759.5)	3.00	39.80 (274.5)	70.33 (485.0)	130	4.97	0.279
9	2.2513 (57.18)	0.0778 (1.98)	28.94	0.0785/0.0773 (1.99/1.96)	1.54	107.07 (738.4)	2.61	36.74 (253.4)	70.33 (485.0)	271	5.64	0.281
11	2.2508 (57.17)	0.077 (1.95)	29.23	0.0779/0.0761 (1.98/1.93)	2.34	108.31 (747.0)	2.65	37.98 (261.9)	70.33 (485.0)	83	4.56	0.279
13	2.2529 (57.22)	0.0784 (1.99)	28.74	0.0791/0.0775 (2.00/1.97)	2.04	109.63 (756.1)	2.60	39.30 (271.0)	70.33 (485.0)	235	5.09	0.281

† Tube No.: SAW6. †† Calculated values

Table 4.1 Geometric and loading parameters of axial cyclic loading under internal pressure experiments (Tube No. SAW8)

CWR No.	D in (mm)	t in (mm)	$\frac{D}{t}$	$t_{\max}$ - $t_{\min}$ in (mm)	Ξ_o (%)	$\frac{P}{P_o}$	σ_{xmon} ksi(MPa)	$\bar{\varepsilon}_{xmon}$ (%)	σ_m ksi (MPa)	σ_a ksi (MPa)	N_C	$\bar{\varepsilon}_f$ (%)	$\frac{\lambda}{R}$
44	2.2560 (57.31)	0.0805 (2.04)	28.02	0.0809/0.0802 (2.05/2.03)	0.43	0	106.9 (737)	2.50	50.9 (351)	56.0 (386)	1441	5.42	0.303
35	2.2528 (57.22)	0.079 (2.01)	28.52	0.0796/0.0784 (2.02/1.99)	0.76	0.222	103.4 (713)	2.00	47.4 (327)	56.0 (386)	296	3.55	0.421
36	2.2526 (57.22)	0.079 (1.98)	28.51	0.0795/0.0787 (2.02/2.00)	0.50	0.222	102.7 (708)	2.01	42.7 (294)	60.0 (414)	430	4.04	0.430
40	2.2488 (57.12)	0.0767 (1.95)	29.32	0.0774/0.0761 (1.97/1.93)	0.85	0.229	103.4 (713)	2.51	47.4 (327)	56.0 (386)	152	3.85	0.427
24†	2.2539 (57.25)	0.0788 (2.00)	28.60	0.0792/0.0783 (2.01/1.99)	0.57	0.490	94.2 (650)	2.01	38.2 (264)	56.0 (386)	144	3.21	0.487
25†	2.2537 (57.24)	0.0787 (2.00)	28.64	0.0792/0.0784 (2.01/1.99)	0.51	0.490	94.4 (651)	2.01	36.4 (251)	58.0 (400)	97	3.08	0.500
31†	2.2504 (57.16)	0.078 (1.98)	28.85	0.0782/0.0777 (1.99/1.97)	0.32	0.490	95.5 (659)	2.00	41.5 (287)	54.0 (372)	212	3.64	0.489
41	2.2552 (57.28)	0.0798 (2.03)	28.26	0.0806/0.079 (2.05/2.00)	1.00	0.490	97.1 (670)	2.51	41.1 (287)	56.0 (386)	78	3.52	0.489
32	2.2526 (57.22)	0.0789 (2.00)	28.55	0.0794/0.0783 (2.02/1.99)	0.70	0.594	87.5 (603)	2.01	27.5 (189)	60.0 (414)	413	3.80	0.532
33	2.2522 (57.21)	0.0787 (2.00)	28.62	0.0794/0.0782 (2.02/1.99)	0.76	0.595	86.4 (596)	2.02	22.4 (155)	64.0 (441)	348	3.72	0.543
34	2.2536 (57.24)	0.0794 (2.02)	28.38	0.0801/0.0785 (2.03/1.99)	1.01	0.590	86.8 (599)	2.04	18.8 (130)	68.0 (469)	284	3.65	0.548
39	2.2519 (57.20)	0.0782 (1.99)	28.80	0.0788/0.0774 (2.00/1.97)	0.90	0.599	87.1 (601)	2.51	19.1 (132)	68.0 (469)	147	3.96	0.566
42	2.2530 (57.23)	0.0785 (1.99)	28.70	0.0792/0.0775 (2.01/1.97)	1.08	0.597	88.0 (607)	2.50	32.0 (221)	56.0 (386)	38	3.23	0.520

† Tube No.: SAW7

Table 4.3 Geometric and critical stress and deformation parameters for monotonic compression under internal pressure cases

CWR No.	Tube No.	D in (mm)	t in (mm)	$\frac{D}{t}$	$\frac{P}{P_o}$	σ_C† ksi(MPa)	ε_C† (%)	ω_o (%)	ω_1 (%)	σ_L ksi (MPa)	$\bar{\varepsilon}_{Lmon}$ (%)
45	SAW8	2.2538 (57.25)	0.079 (2.01)	28.53	0.593	82.0 (565)	1.49	-	-	90.2 (621)	3.44
30	SAW7	2.2517 (57.19)	0.0779 (1.98)	28.90	0.495	89.6 (618)	1.46	-	-	98.4 (678)	3.17
Anal.	SAW8	2.2536 (57.24)	0.0794 (2.02)	28.38	0.222	99.1 (683)	1.47	0.13	0.13	111.0 (765)	3.84
Anal.	SAW8	2.2536 (57.19)	0.0794 (2.02)	28.38	0	103.0 (710)	1.45	0.04	0.04	121.4 (837)	4.92

† Bifurcation Analysis

Table 5.1 Geometric and material parameters of wrinkling under axially cyclic loading experiments

CWR No.	D in (mm)	t in (mm)	$\frac{D}{t}$	σ_{xmon} ksi(MPa)	$\bar{\varepsilon}_{xmon}$ (%)	σ_{m1} ksi(MPa)	σ_{a1} ksi(MPa)	N_1	$\bar{\varepsilon}_{x1}$ (%)	ε_C (%)	σ_{m2} ksi(MPa)	σ_{a2} ksi(MPa)	N_2	$\bar{\varepsilon}_f$ (%)	$\frac{\lambda}{R}$
15	2.2520 (57.21)	0.0781 (1.98)	28.83	98.3 (679)	0.80	24.3 (168)	74.0 (511)	410	1.90	1.30-1.45	31.9 (222)	74.0 (511)	609	4.93	0.255-0.372
18	2.2532 (57.24)	0.0788 (2.00)	28.60	98.2 (678)	0.92	24.2 (167)	74.0 (511)	490	2.14	1.28-1.55	31.9 (222)	74.0 (511)	632	4.62	0.325-0.373
19	2.2524 (57.22)	0.0782 (1.98)	28.80	100.2 (691)	0.99	26.2 (180)	74.0 (511)	410	2.29	1.30-1.60	33.9 (237)	74.0 (511)	607	5.23	0.262-0.368
47†	2.2547 (57.27)	0.0796 (2.02)	28.33	77.8 (537)	0.92	21.8 (151)	56.0 (386)	310	1.71	1.09-1.30	28.6 (198)	56.0 (386)	30	5.37	0.551-0.643

† With the internal pressure $P = 0.59P_o$

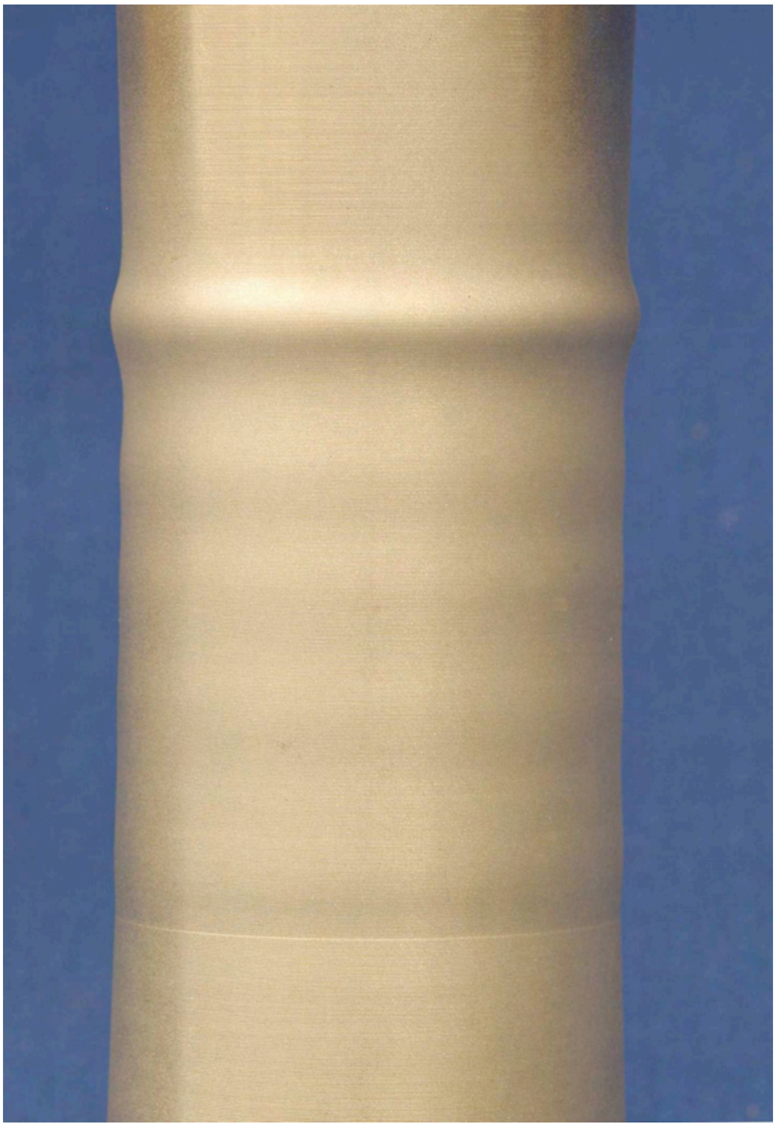

Fig. 1.1 Photograph of a stainless steel tube after axial cyclic loading showing axisymmetric wrinkles (from Jiao and Kyriakides, 2009).

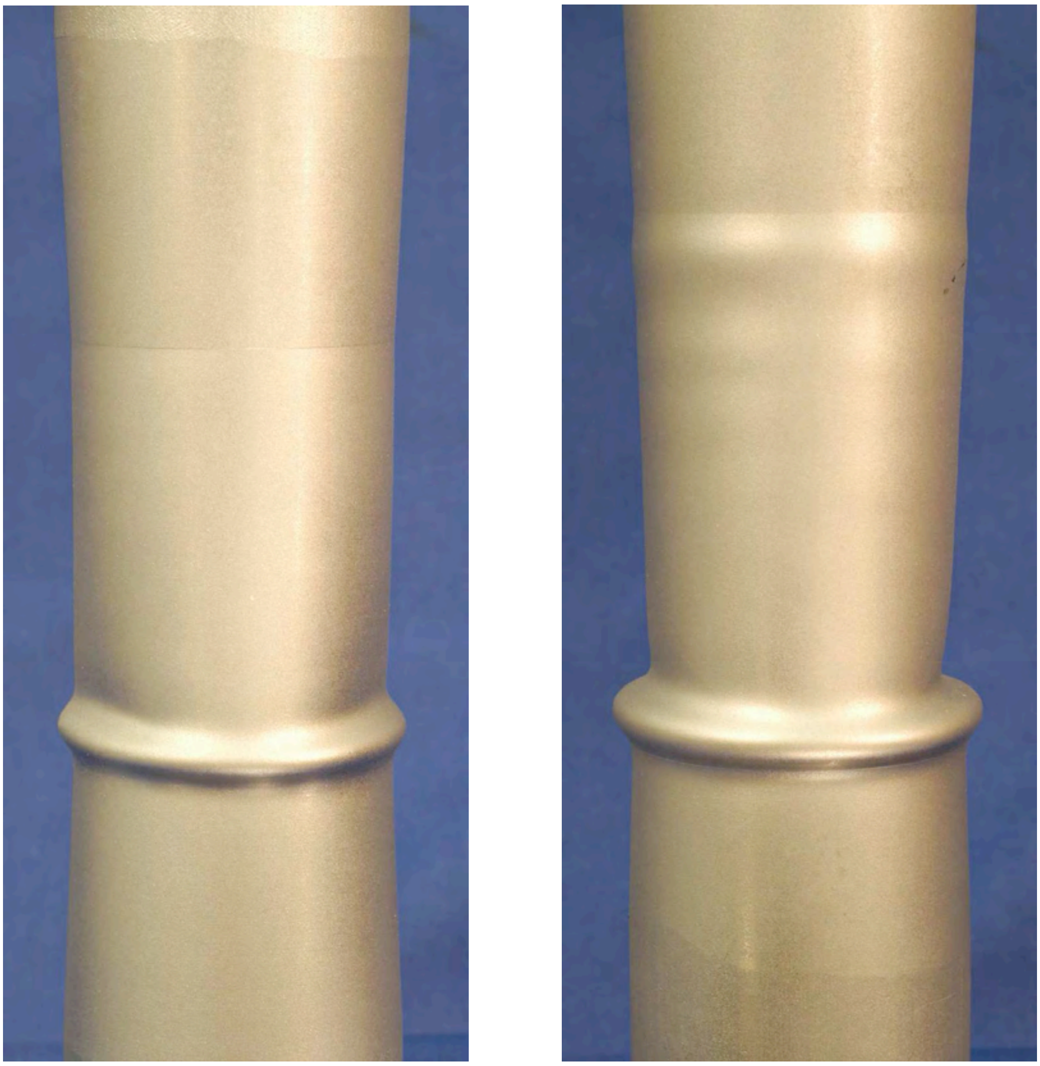

(a) Mode 2 (b) Mode 3

Fig. 1.2 Localized non-axisymmetric wrinkles in stainless steel tubes (from Bardi and Kyriakides, 2006).

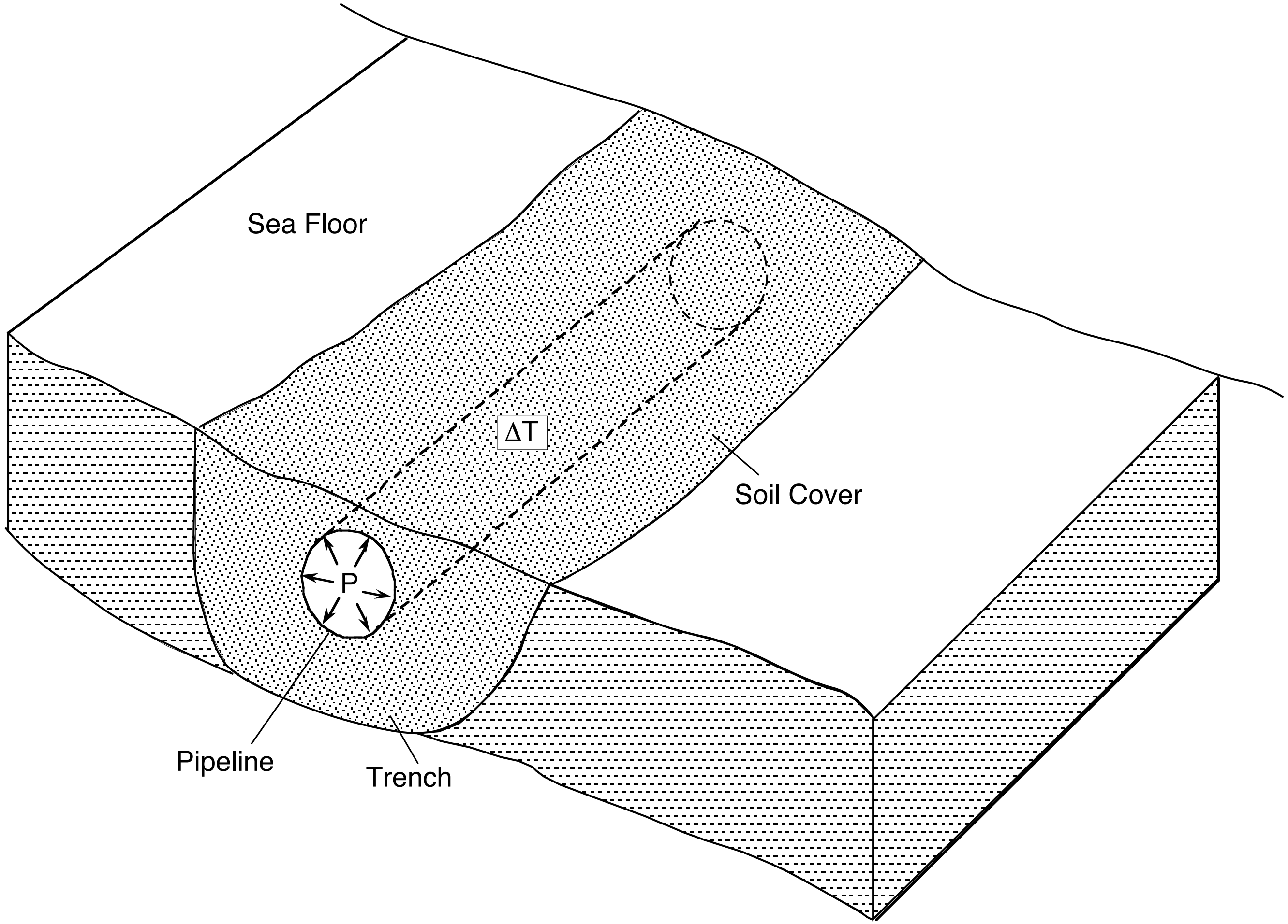

Fig. 1.3 Offshore pipeline under axial compression due to the passage of hot hydrocarbons.

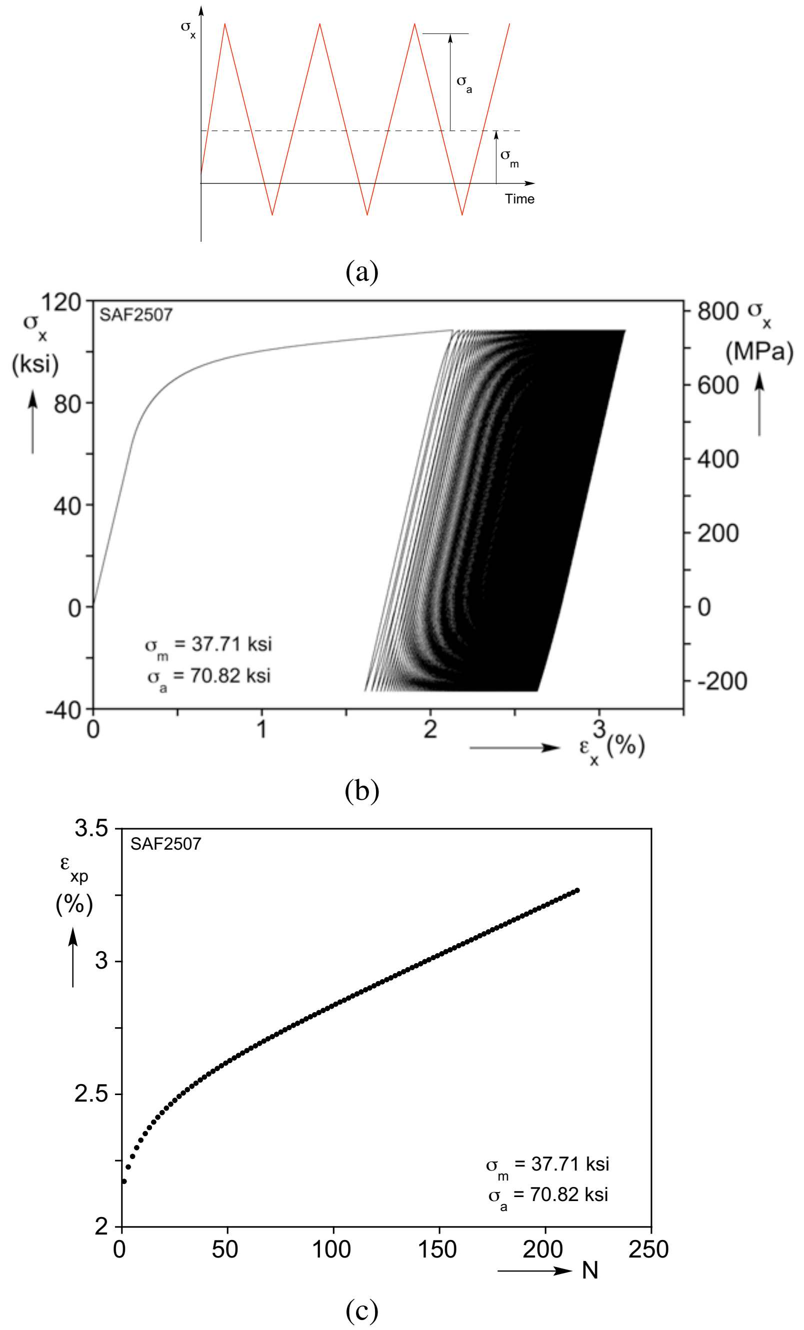

Fig. 1.4 Uniaxial ratcheting results of SAF2507: (a) saw-tooth axial stress function (b) axial stress-strain response (c) peak axial strain vs. *N*.

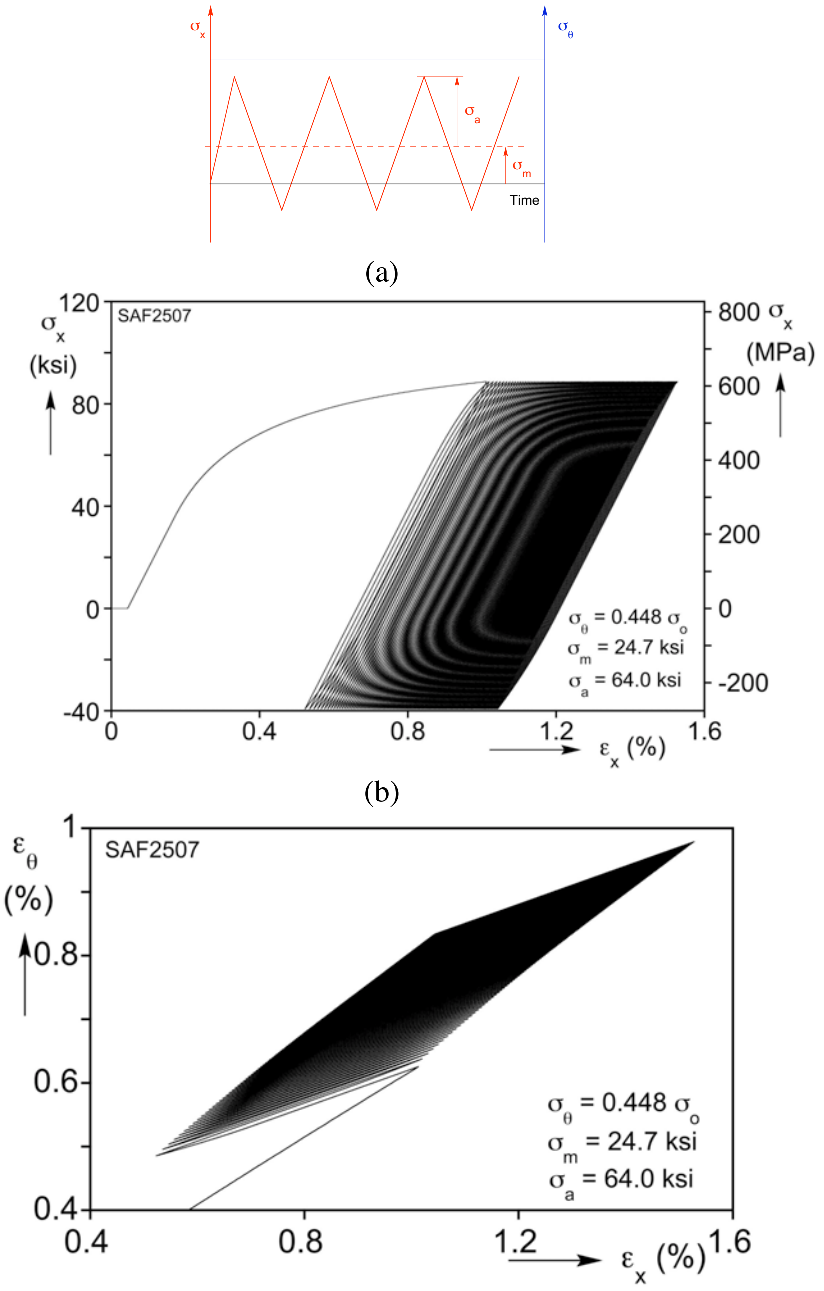

(a)

(b)

(c)

Fig. 1.5 Biaxial ratcheting results of SAF2507: (a) saw-tooth axial stress function and constant hoop stress (b) axial stress-strain response and (b) axial-circumferential strain response.

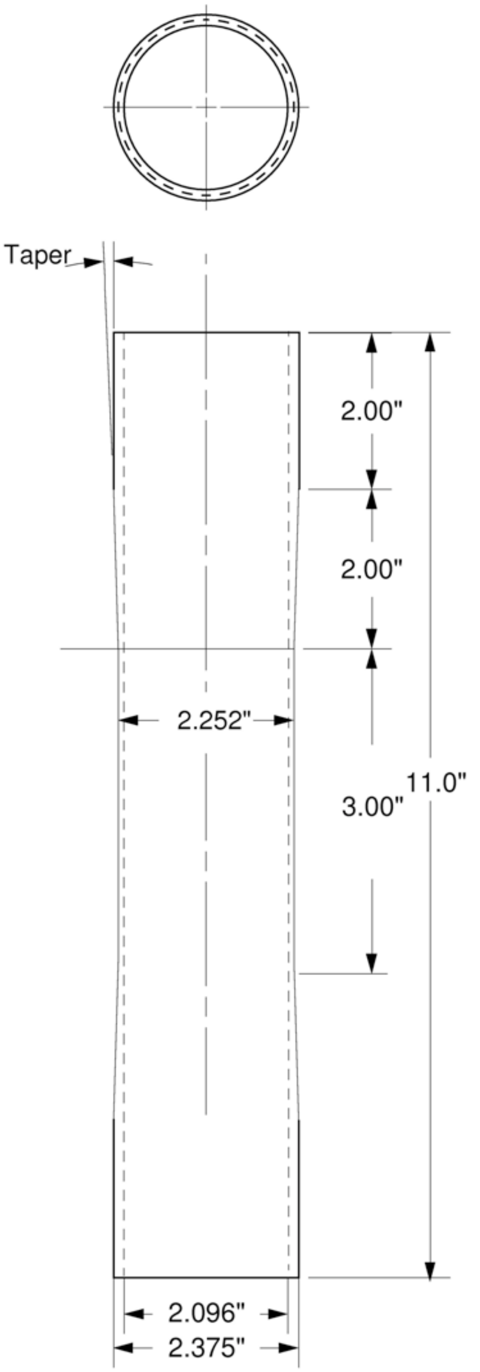

Fig. 2.1 Test specimen geometry for axial cyclic loading.

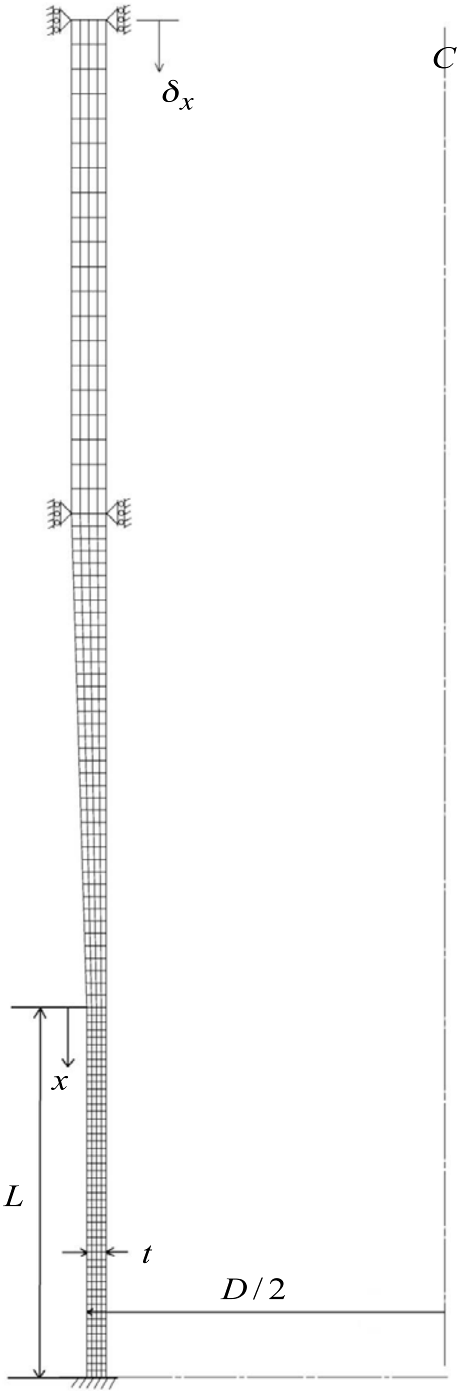

Fig. 2.2 Mesh and boundary conditions in the finite element model.

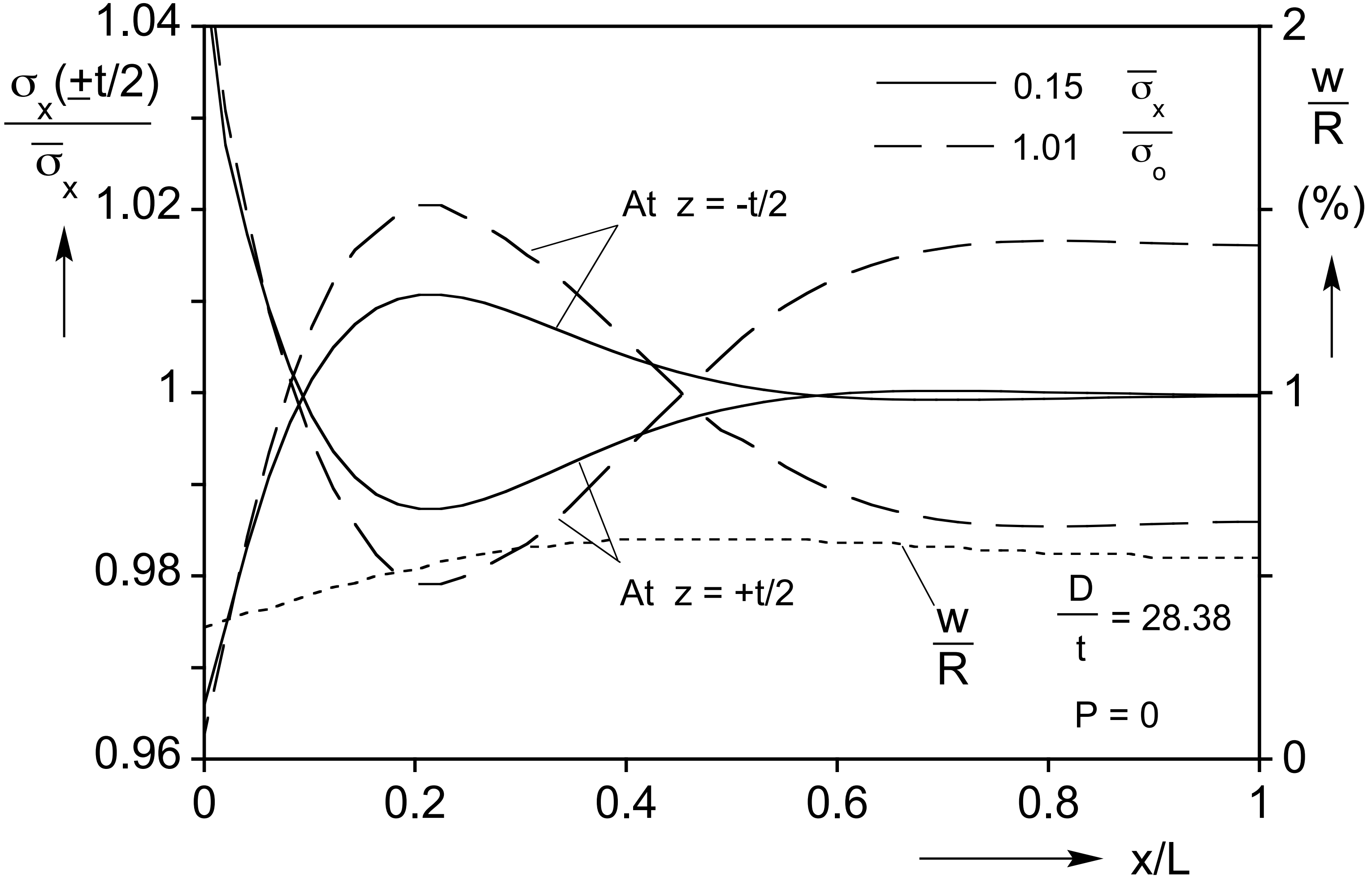

Fig. 2.3 Calculated stress and displacement profile in the test section at two stress levels.

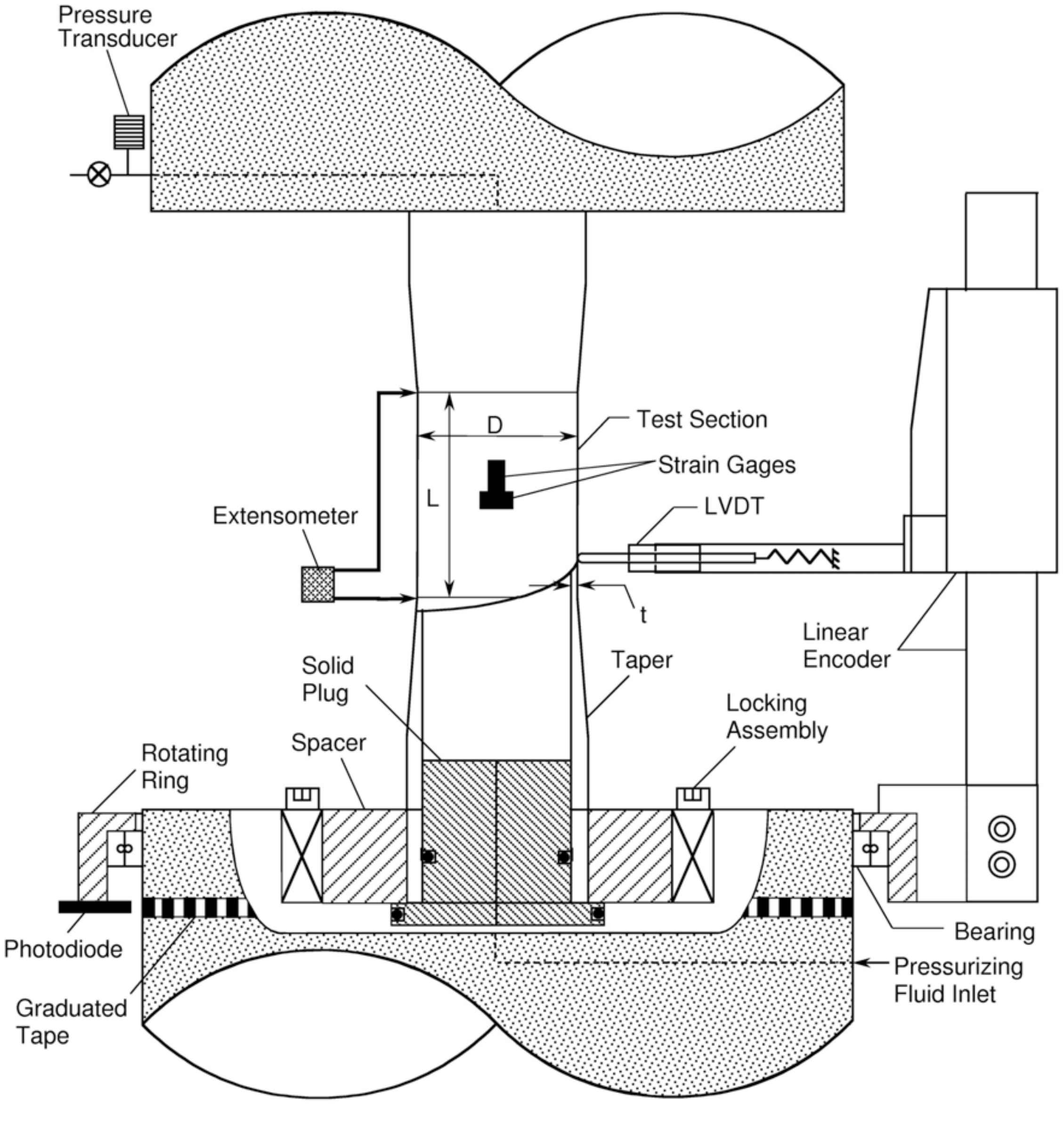

Fig. 2.4 Scaled schematic of experimental setup for axial cyclic loading experiments.

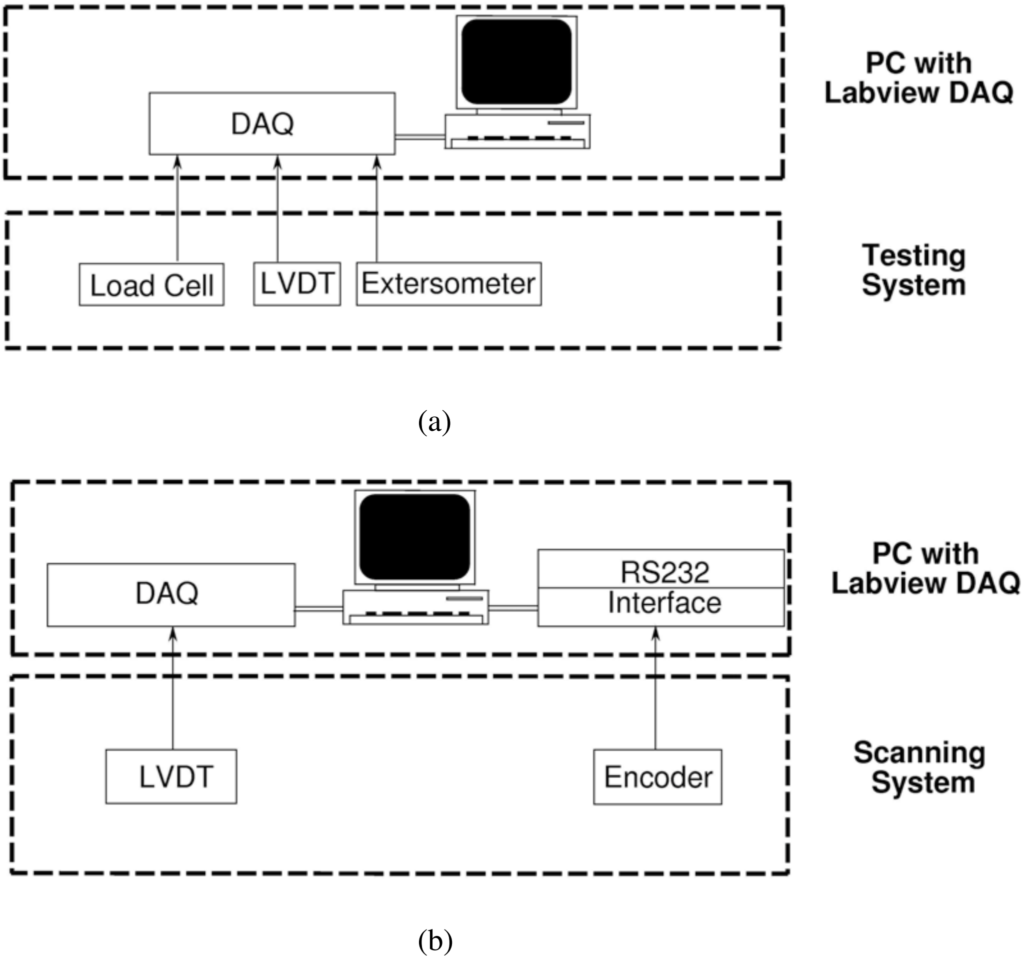

Fig. 2.5 Flowchart of two data acquisition systems used in the axial cyclic loading experiments.

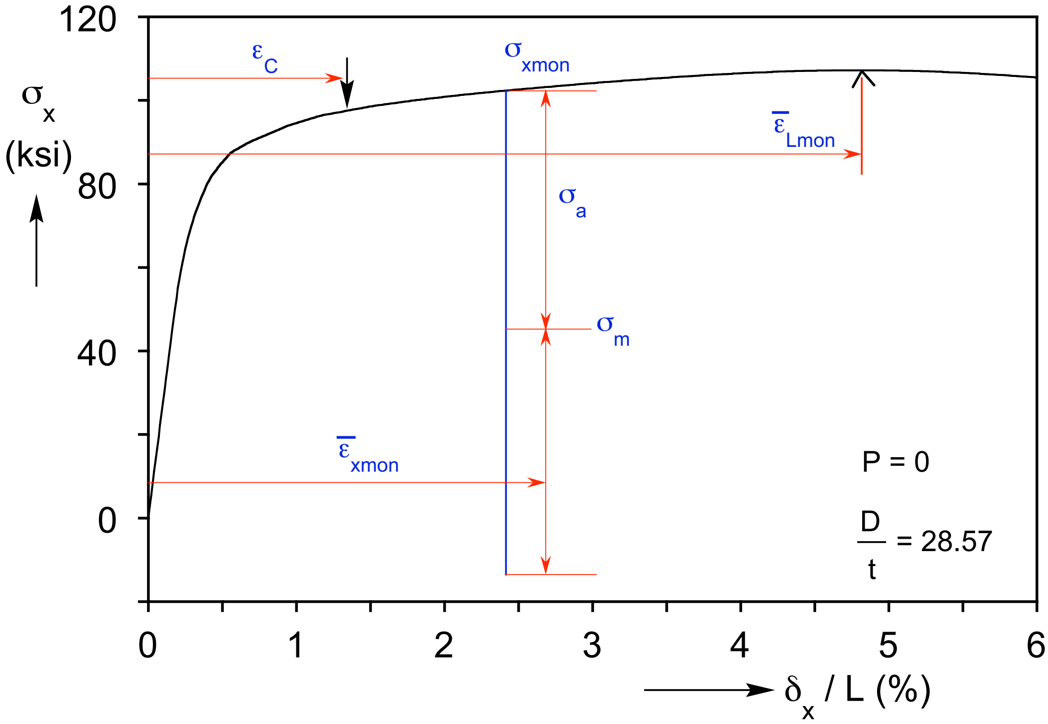

(a)

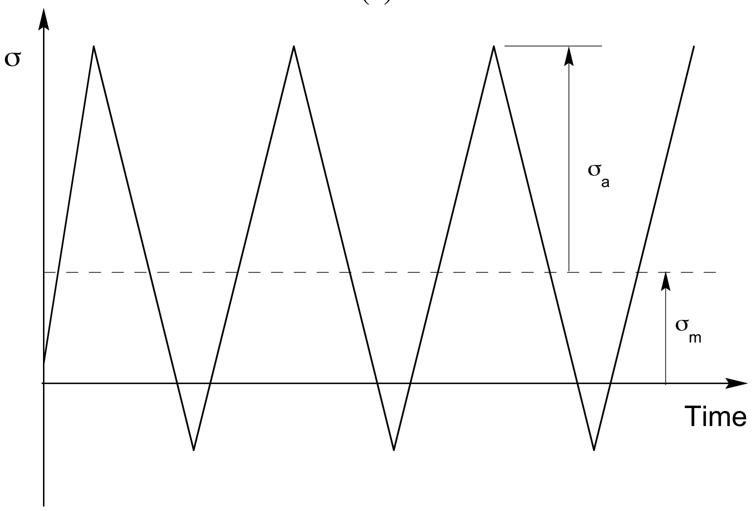

(b)

Fig. 2.6 (a) Monotonic compression stress-shortening response showing the initial pre-staining to $\varepsilon_C < \bar{\varepsilon}_{xmon} < \bar{\varepsilon}_{Lmon}$ and the stress parameters $\{\sigma_m, \sigma_a\}$ of the cycles that follow. (b) Cyclic stress history applied in the experiments.

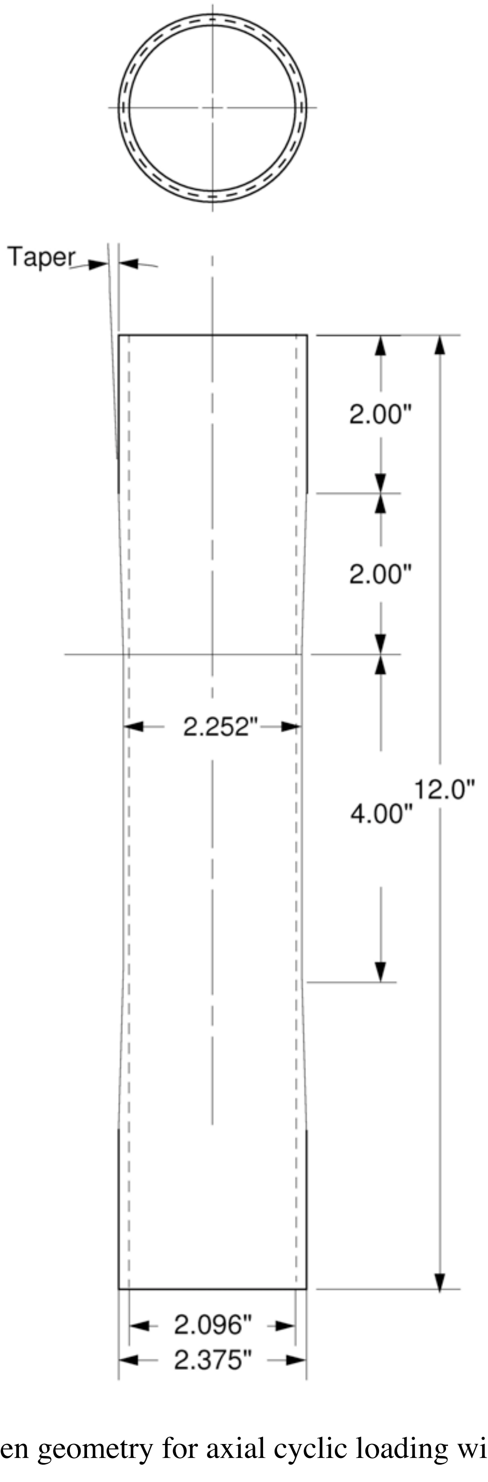

Fig. 2.7 Test specimen geometry for axial cyclic loading with internal pressure.

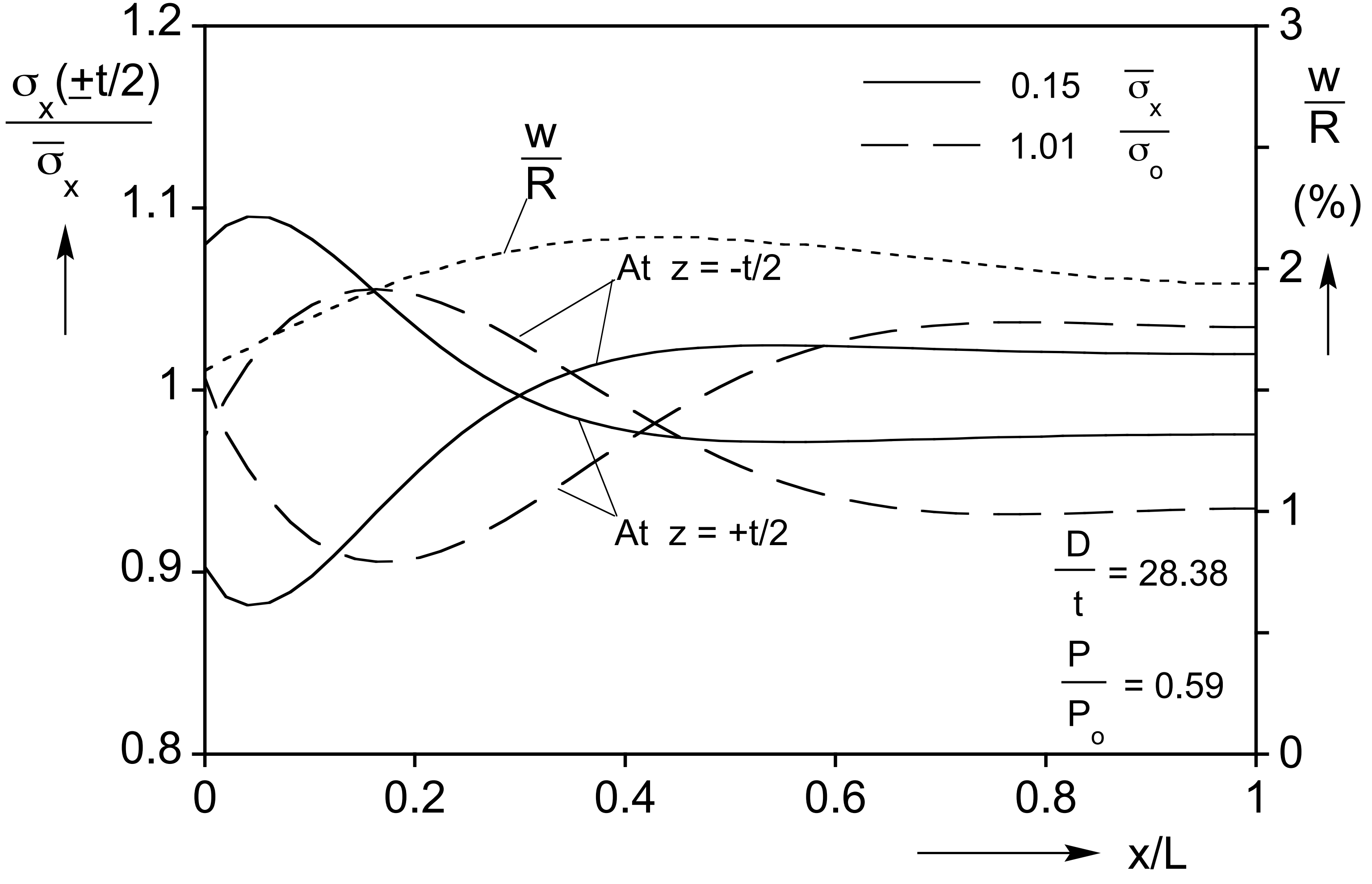

Fig. 2.8 Calculated stress and displacement profile in the test section at two stress levels.

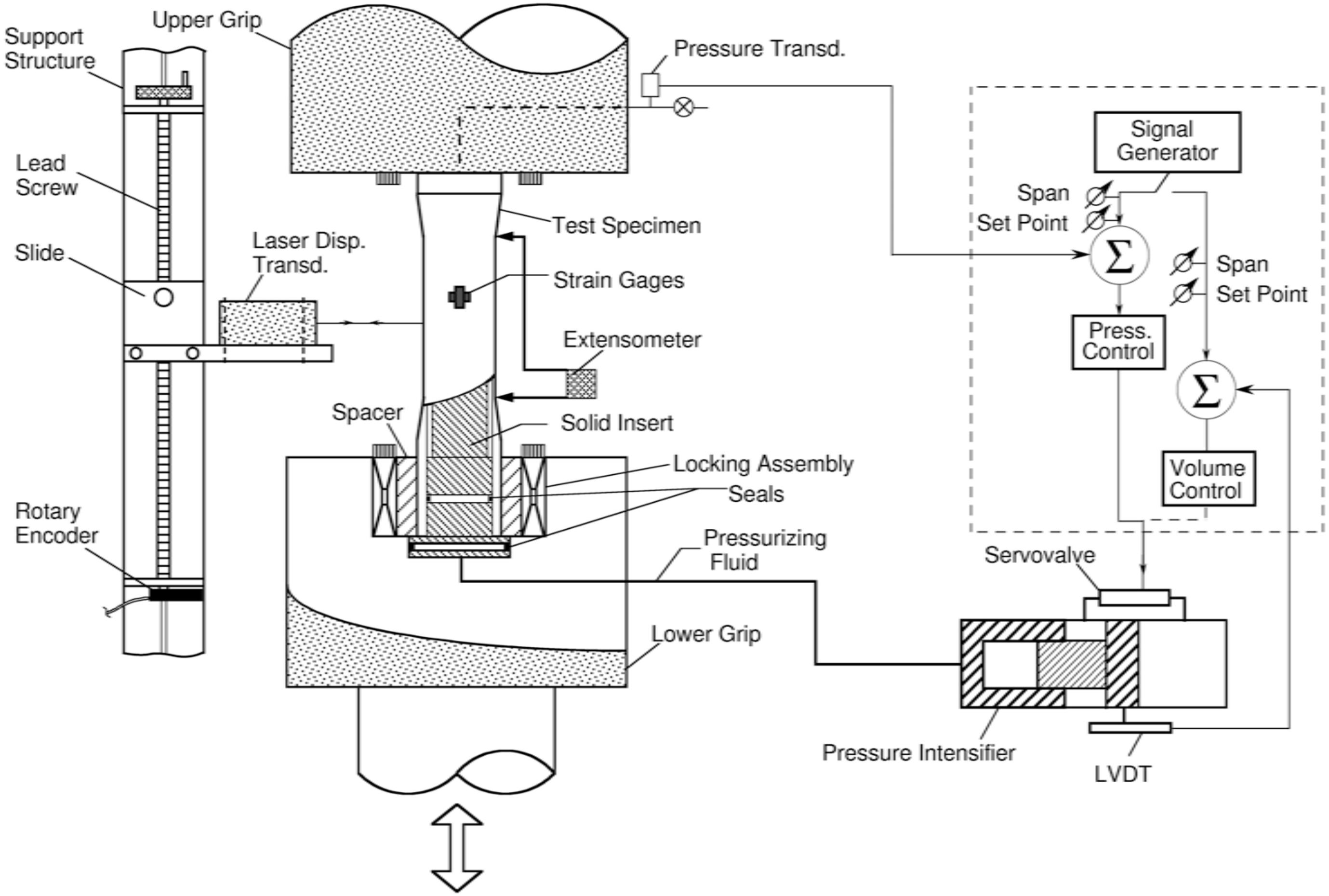

Fig. 2.9 Scaled schematic of experimental setup for experiments under axial cyclic loading and internal pressure.

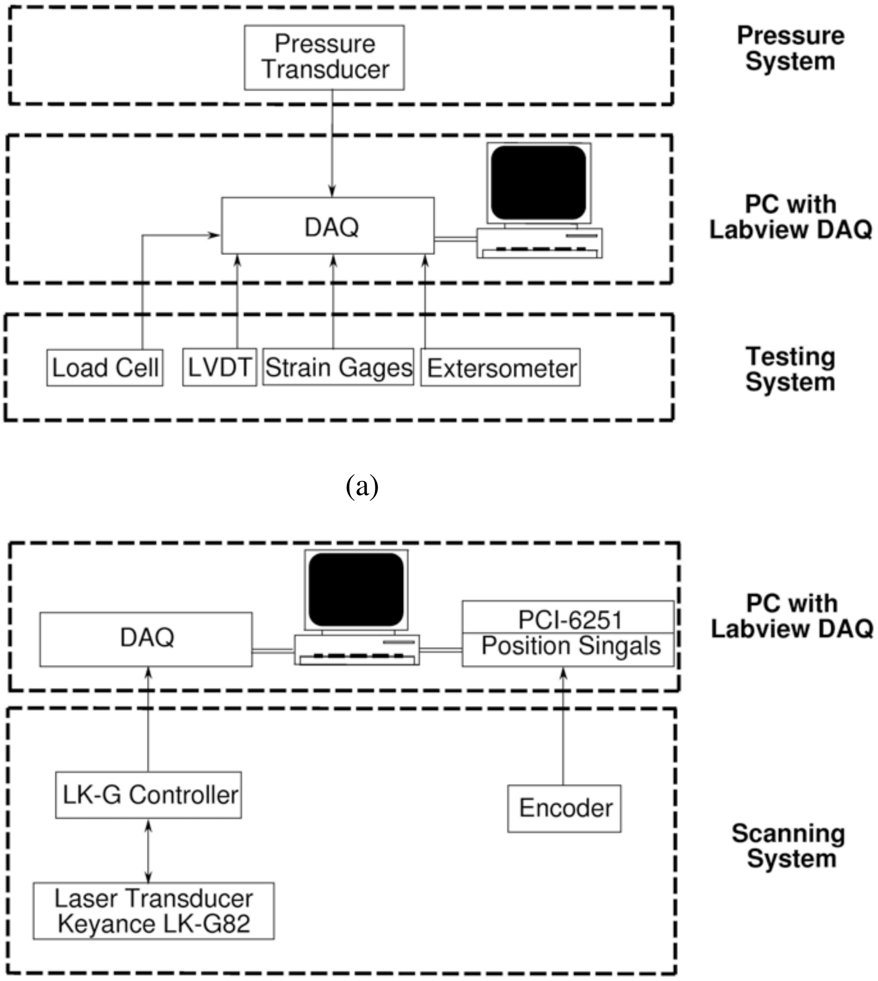

(a)

(b)

Fig. 2.10 Flowchart of two data acquisition systems used in the experiments under axial cyclic loading and internal pressure.

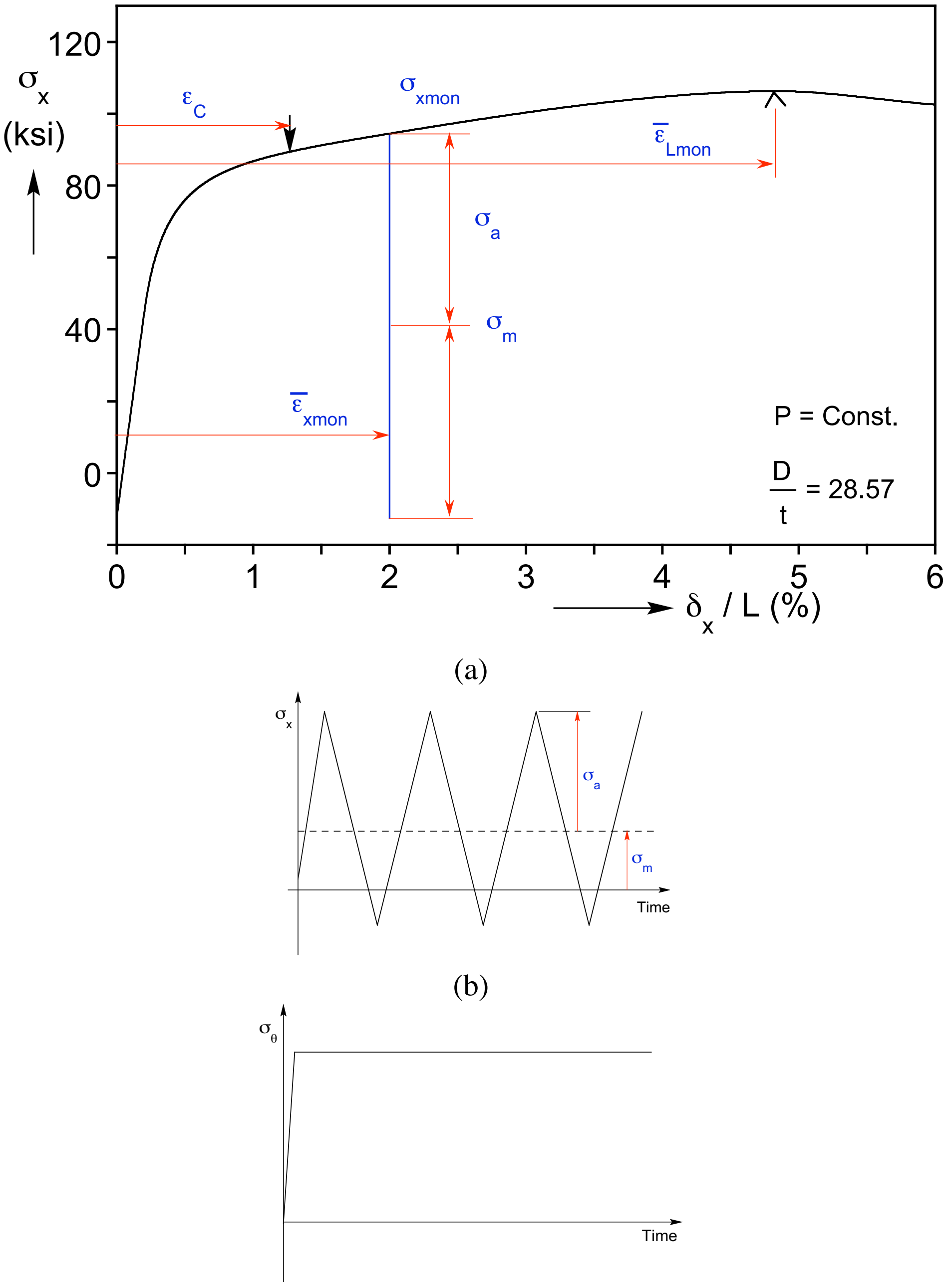

(a)

(b)

(c)

Fig. 2.11 (a) Monotonic compression stress-shortening response under constant internal pressure showing the initial pre-staining to $\varepsilon_C < \bar{\varepsilon}_{xmon} < \bar{\varepsilon}_{Lmon}$ and the stress parameters $\{\sigma_m, \sigma_a\}$ of the cycles that follow. (b) Cyclic axial stress history and (c) constant hoop stress applied in the experiments.

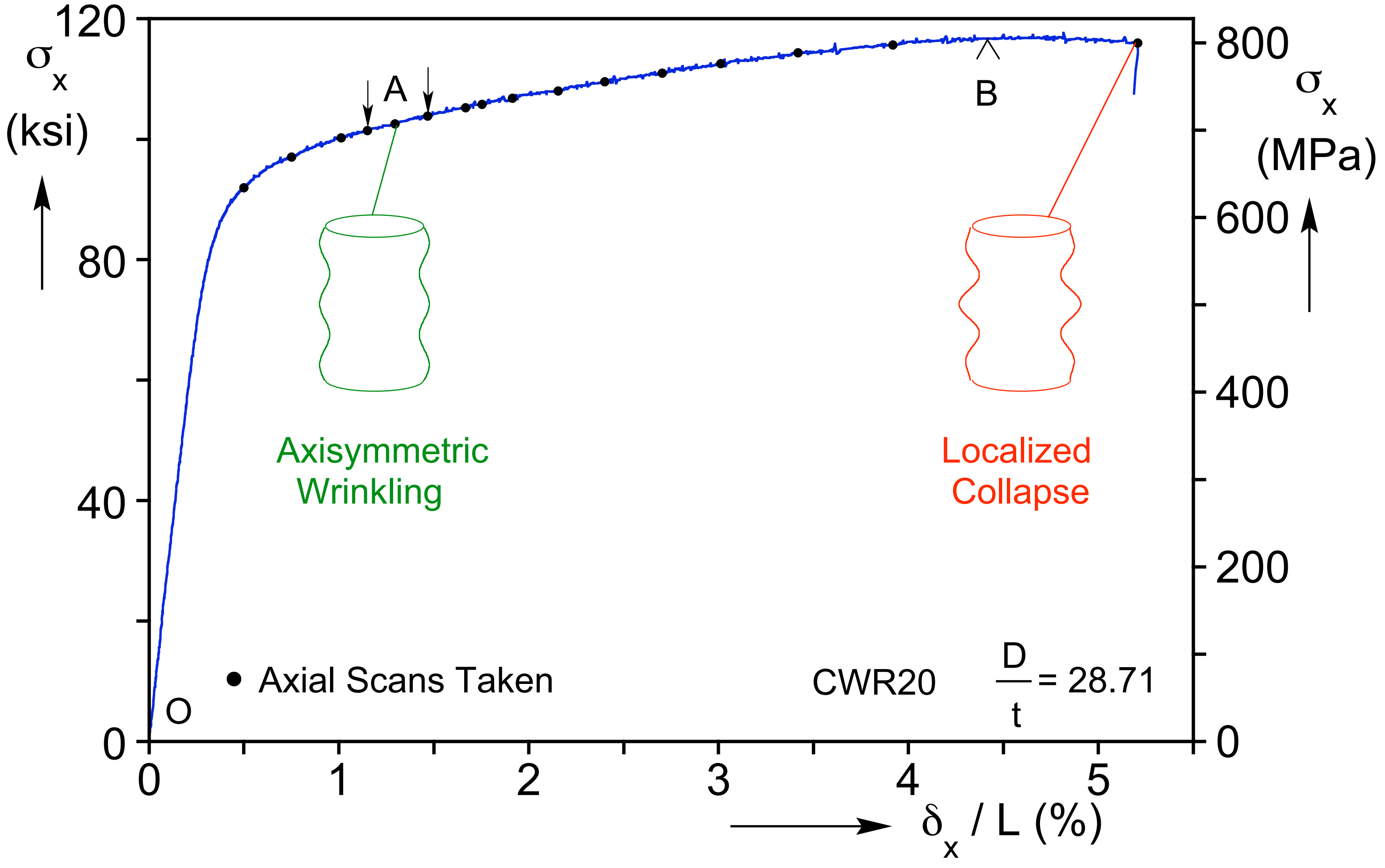

Fig. 3.1 Monotonic compressive response of tube CWR20.

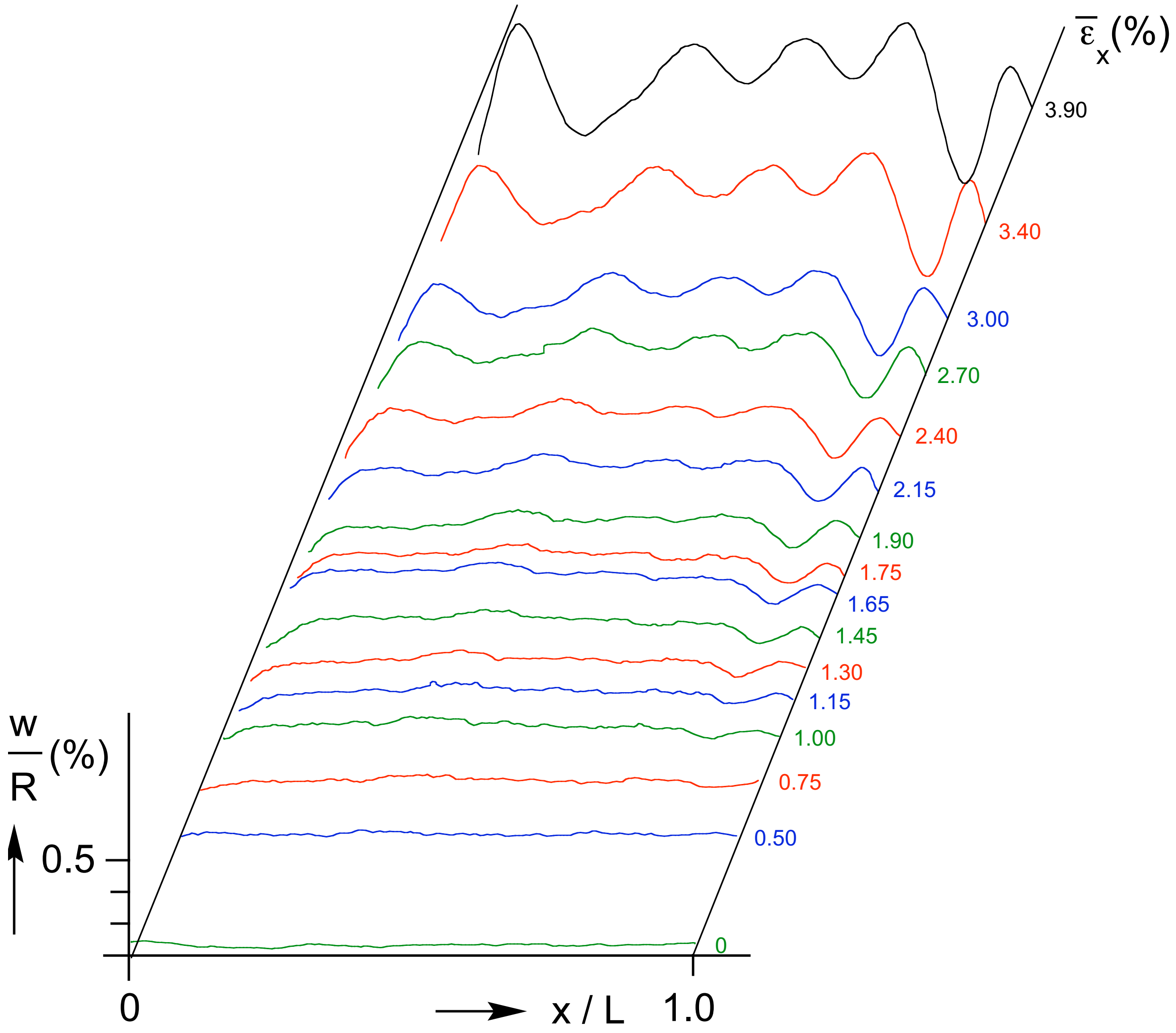

Fig. 3.2a Radial displacement axial profiles at different average strain levels during the monotonic compression test in Fig. 3.1 that show the evolution of the wrinkles.

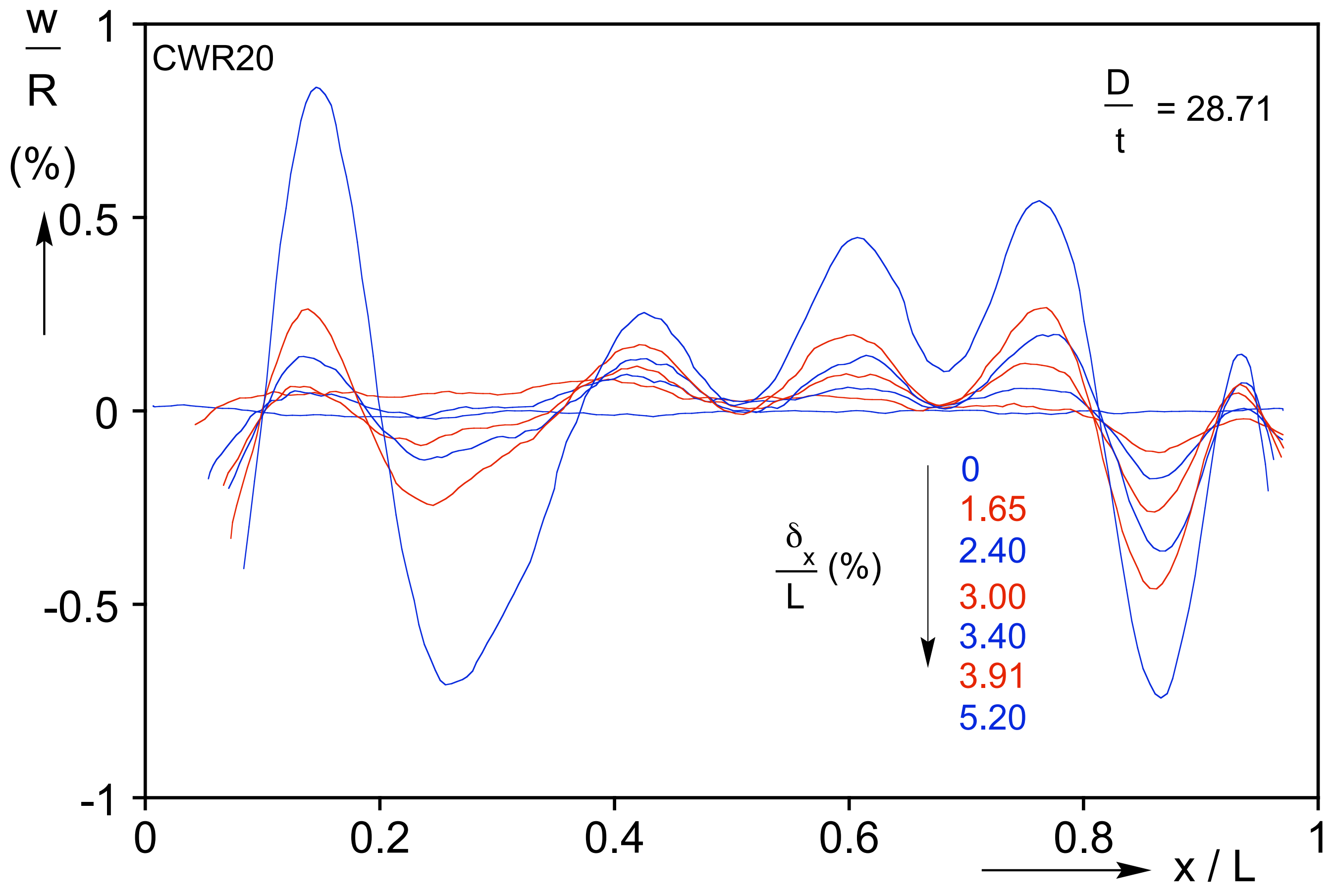

Fig. 3.2b Axial scans showing the evolution of wrinkles and their localization at higher strain levels.

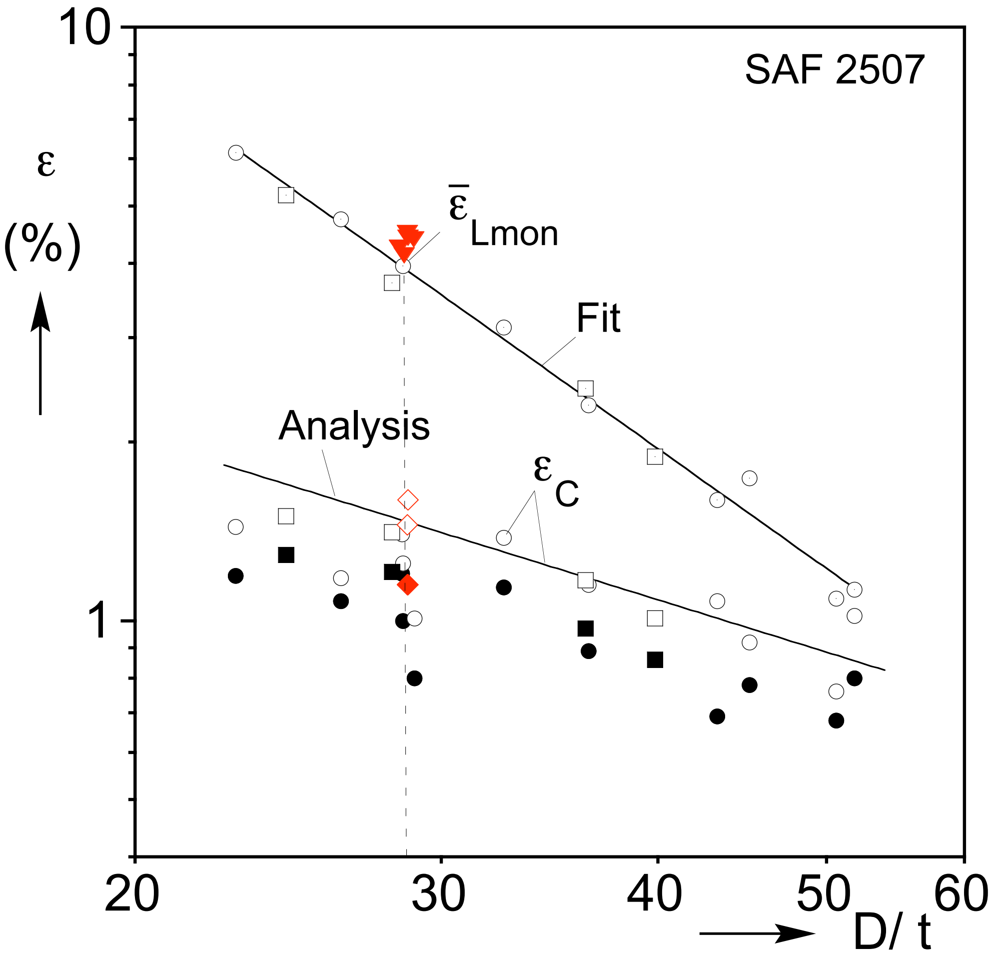

Fig. 3.3 Critical wrinkling strains (ε_C) and limit strains ($\bar{\varepsilon}_{Lmon}$) vs. D/t from fifteen experiments of Bardi and Kyriakides (2006) and from present study for $D/t \cong 28.5$.

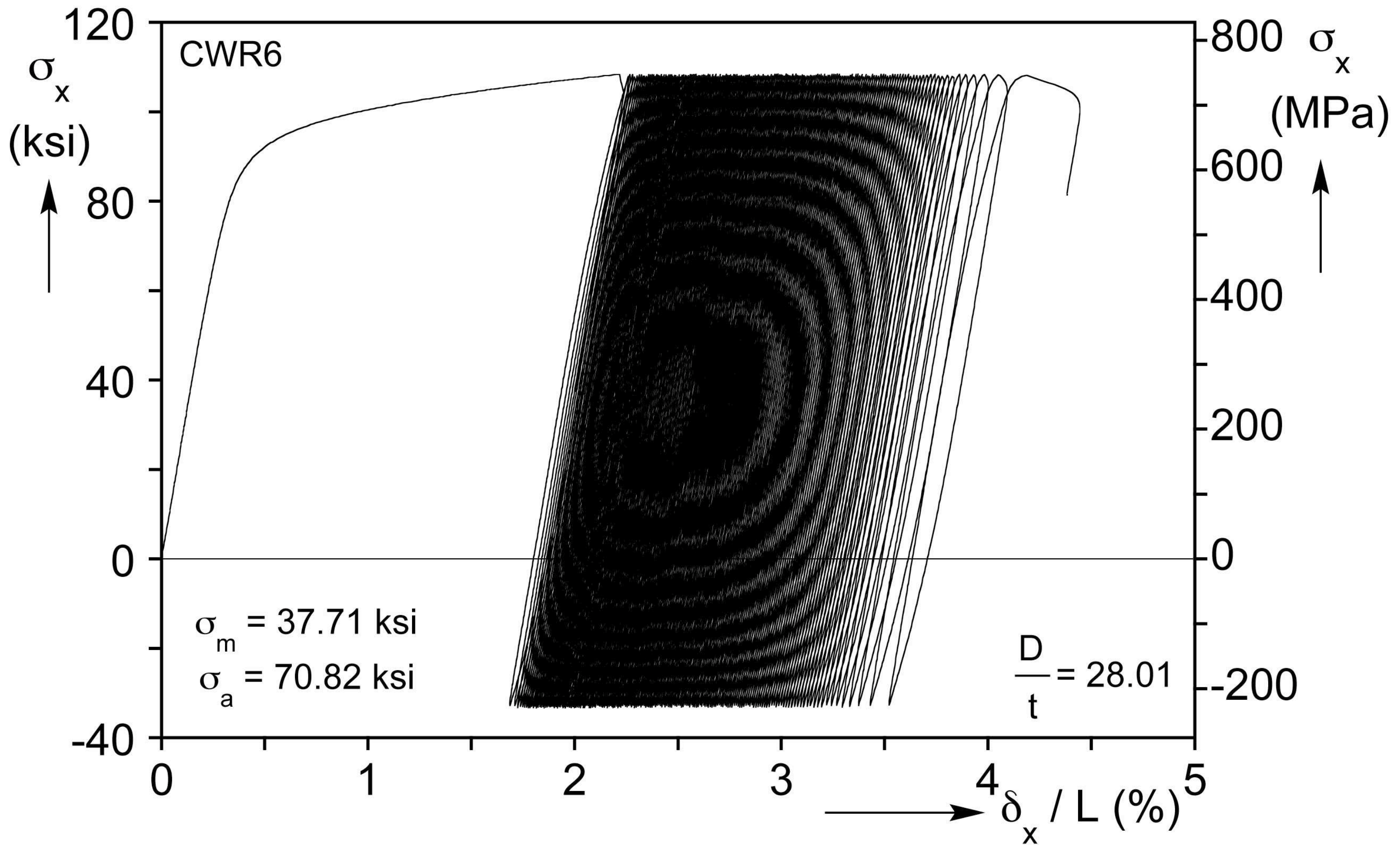

Fig. 3.4 Results from cyclic loading experiment CWR6. (a) Axial stress-shortening response,

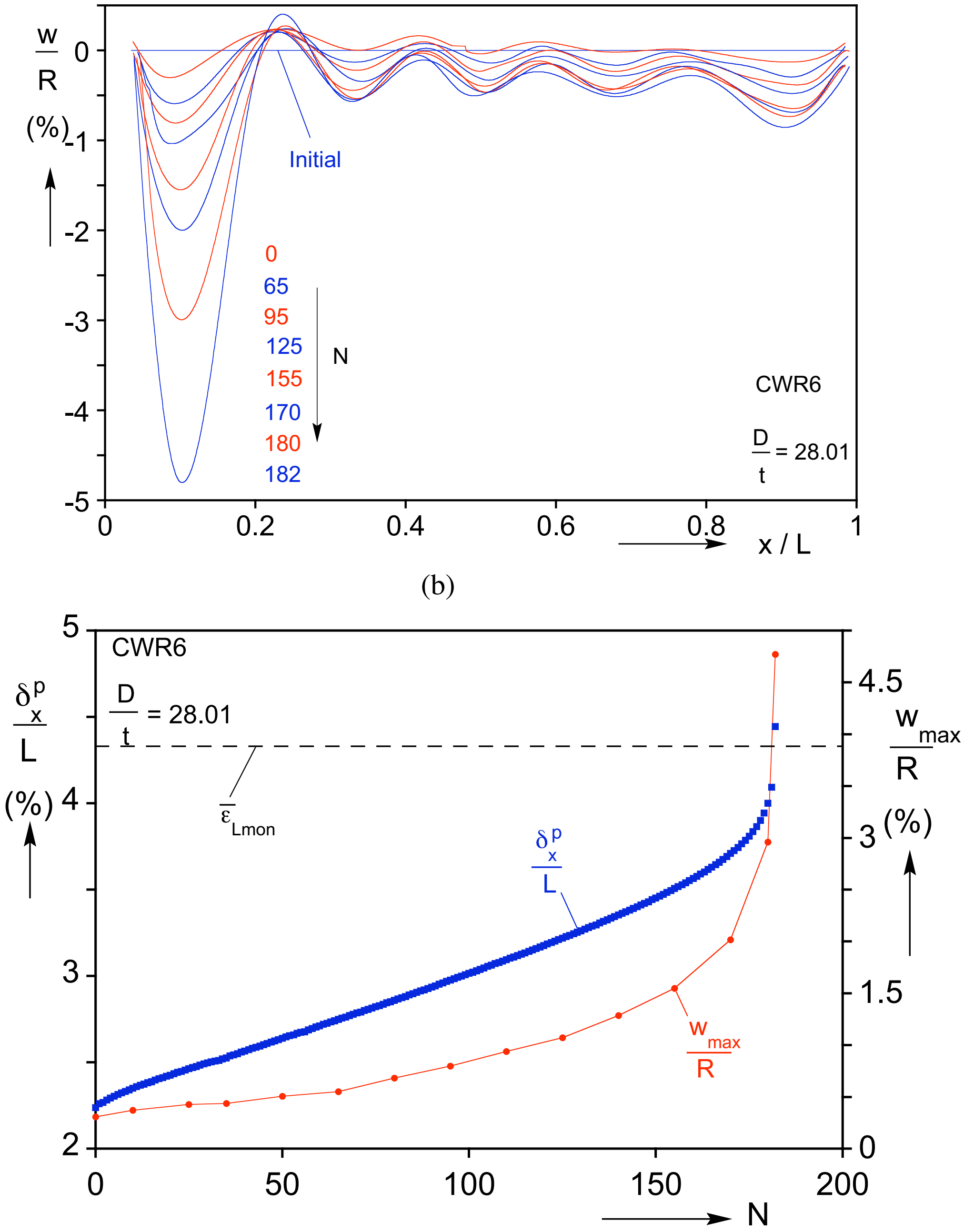

Fig. 3.4 (b) Axial scans showing evolution of wrinkles during the cycling. (c) Peak axial cycle displacement vs. *N* and corresponding maximum radial displacement in wrinkles.

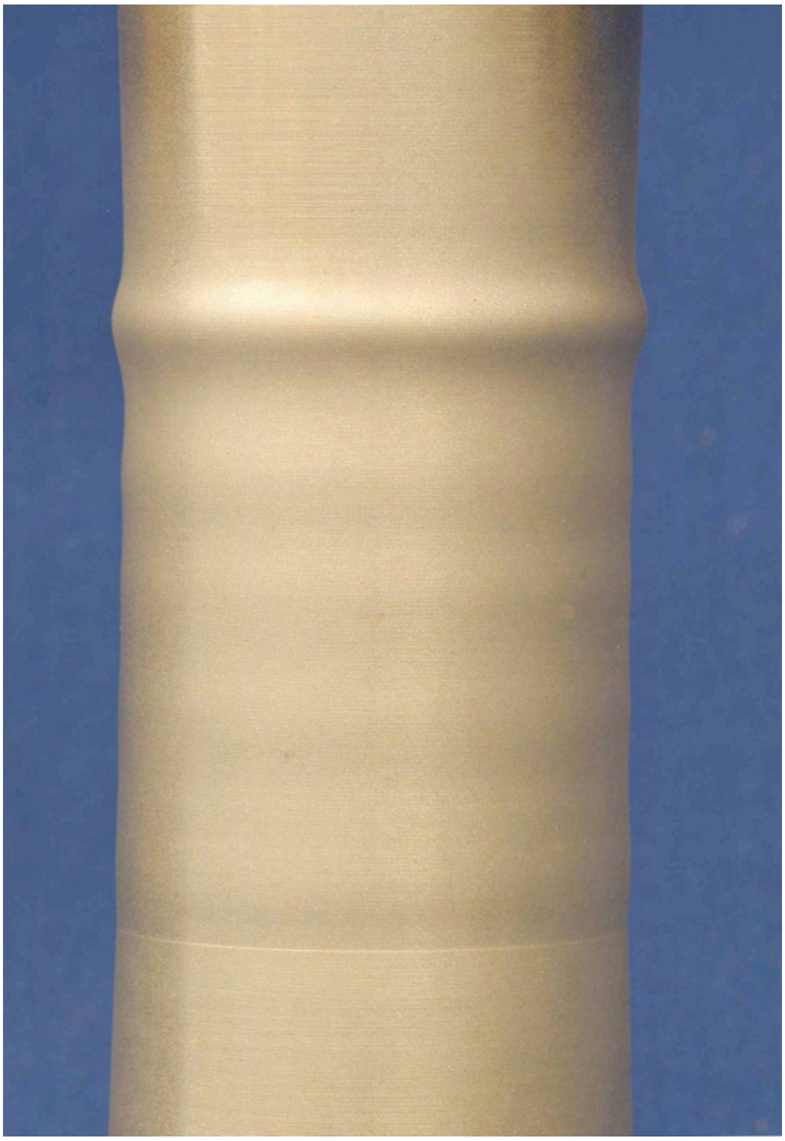

Fig. 3.4 (d) Photograph of specimen CWR6 at the end of cycling showing wrinkles and localization at one end.

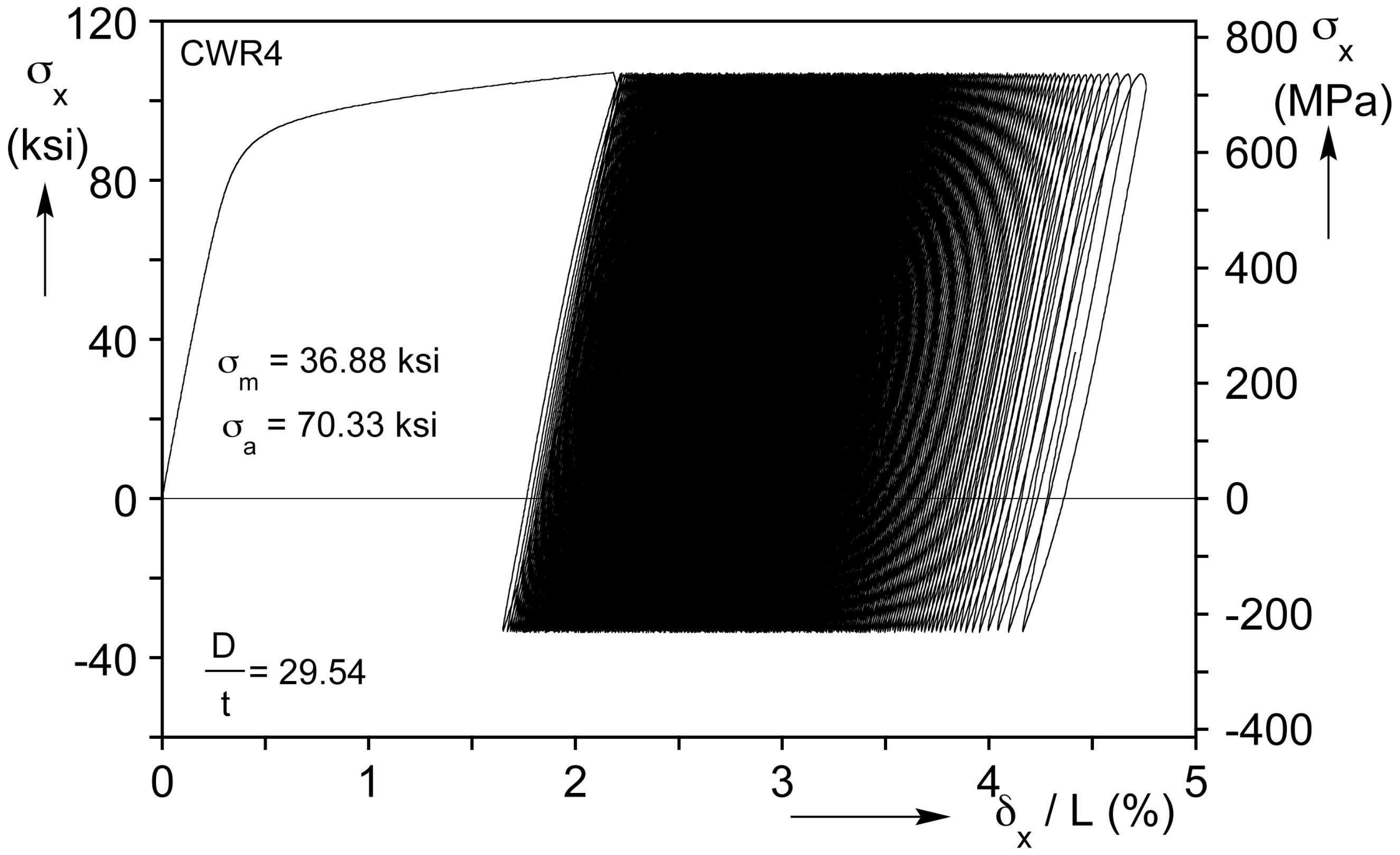

Fig. 3.5 Results from cyclic loading experiment CWR4. (a) Axial stress-shortening response.

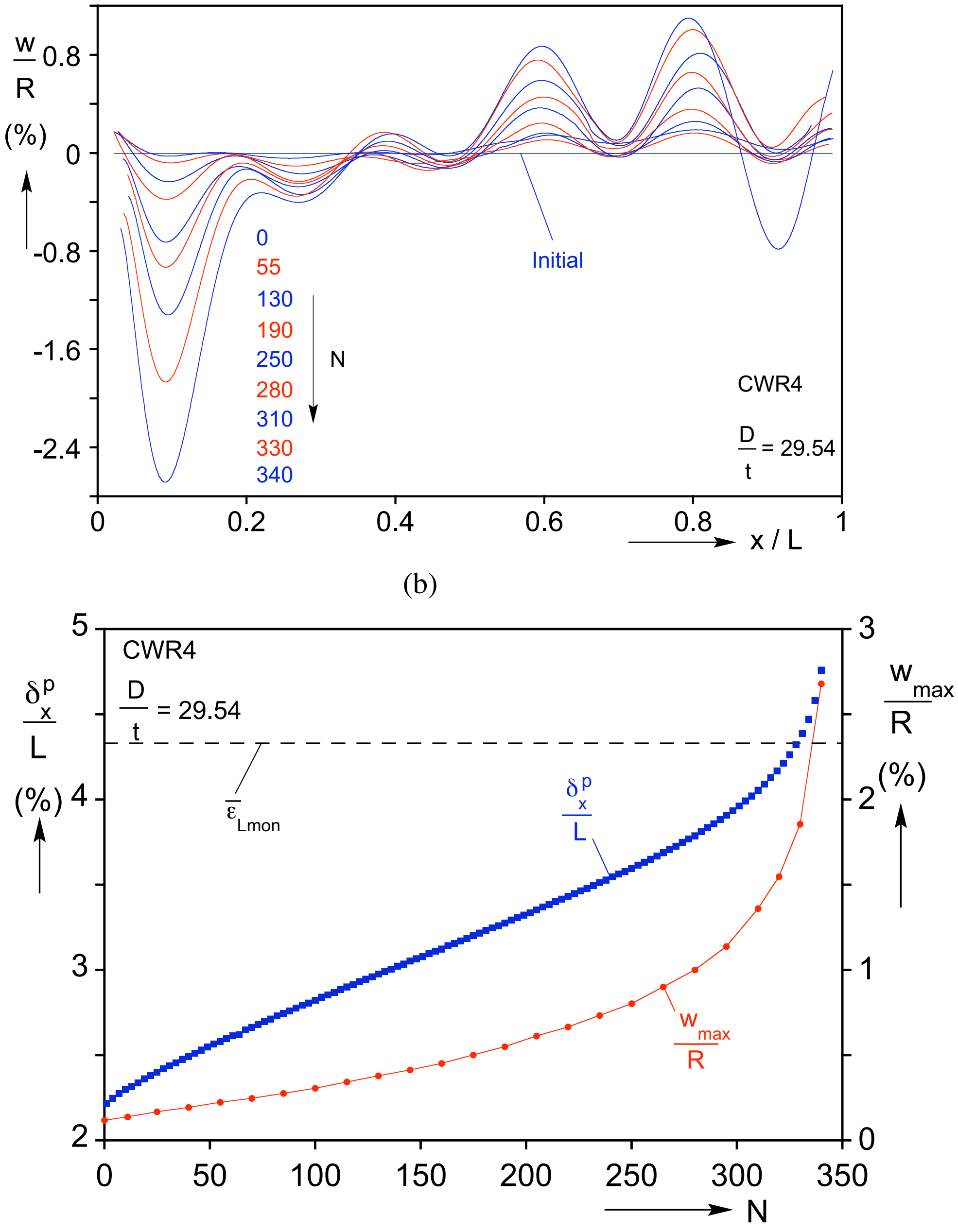

(b)

(c)

Fig. 3.5 (b) Axial scans showing evolution of wrinkles during the cycling. (c) Peak axial displacement in cycles vs. *N* and corresponding maximum radial displacement in wrinkles.

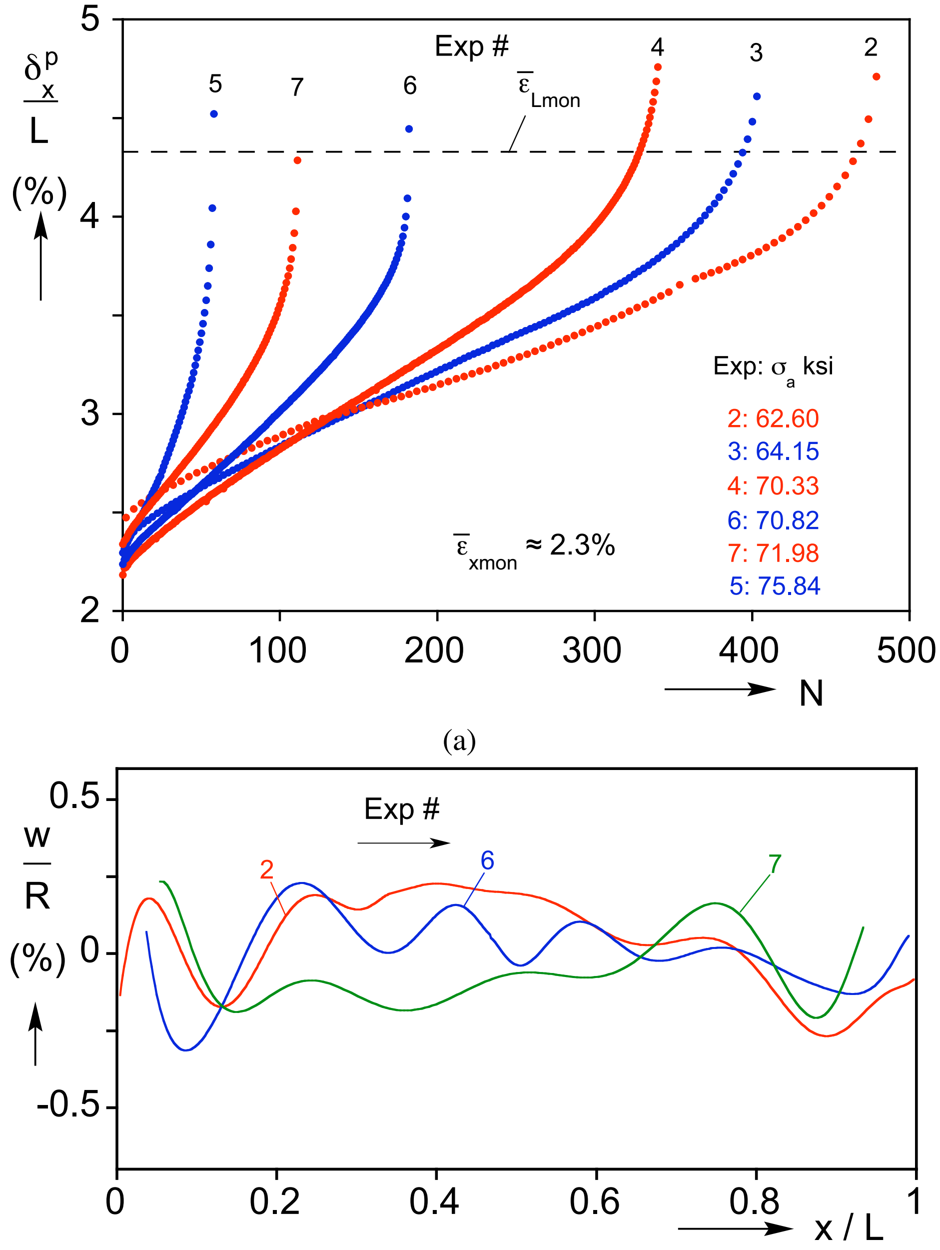

(a)

(b)

Fig. 3.6 (a) Peak displacement per cycle vs. *N* from six experiments with approximately the same initial pre-straining. (b) Axial scans of CWR2, CWR6 and CWR7 specimens showing wrinkles with approximately the same amplitude.

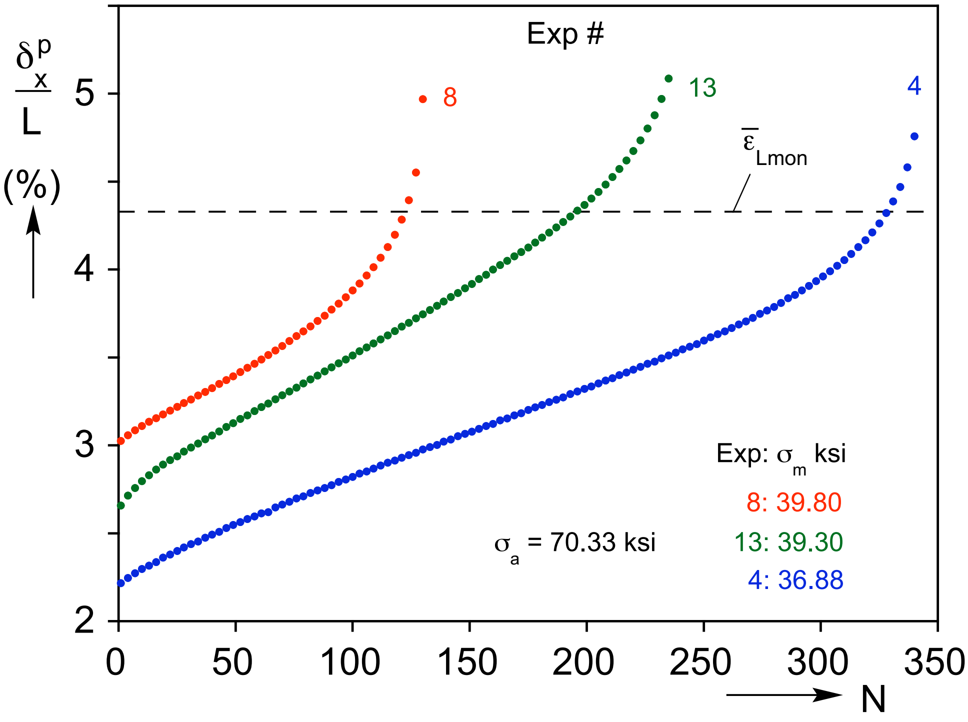

(a)

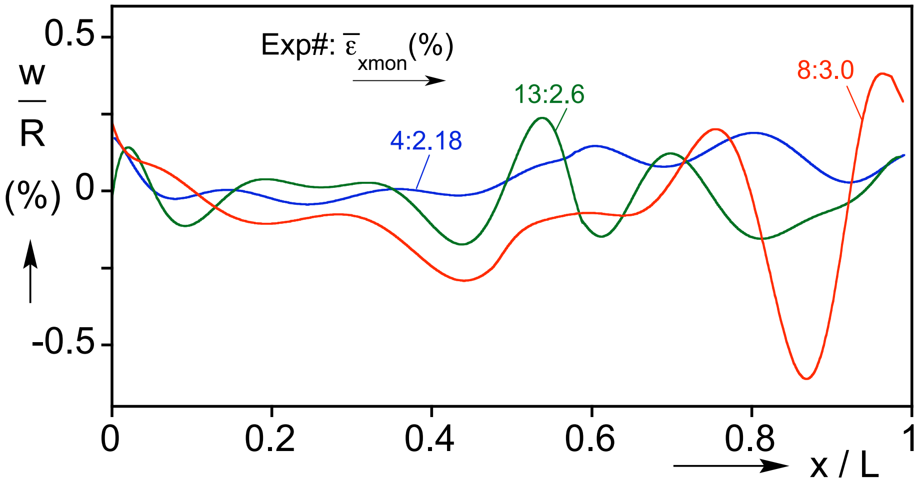

(b)

Fig. 3.7 (a) Peak displacement per cycle vs. *N* from three experiments with different initial pres-straining and the same stress cycle amplitude. (b) Axial scans of the three specimens showing wrinkles with different amplitude.

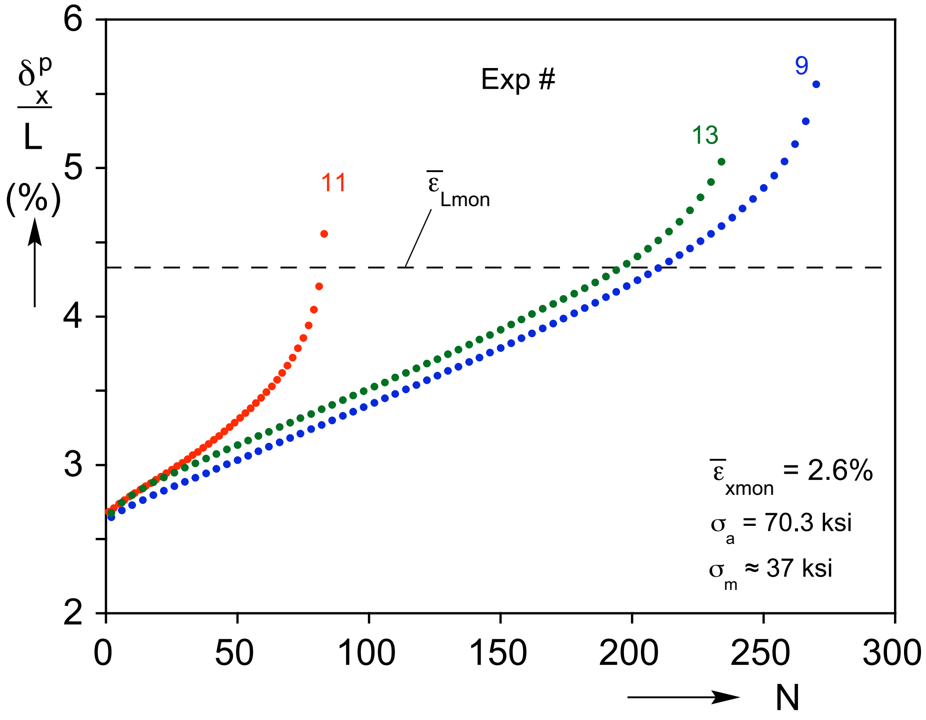

(a)

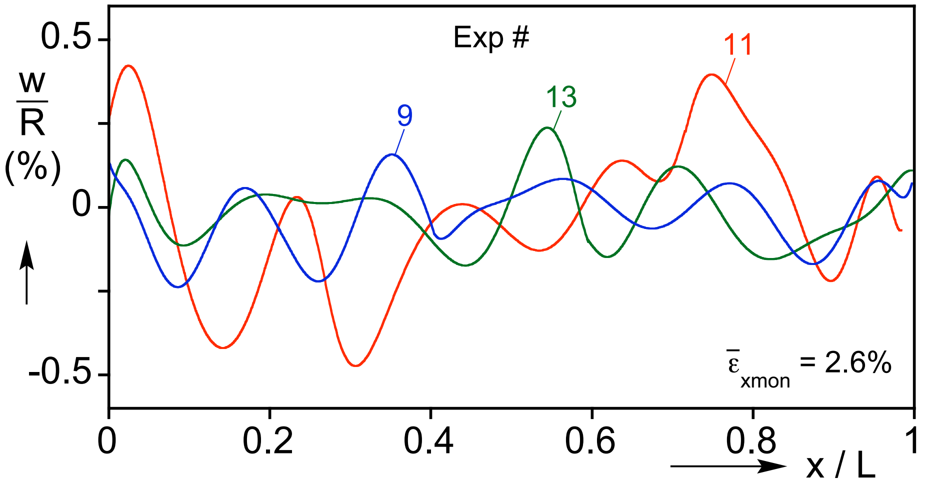

(b)

Fig. 3.8 (a) Peak displacement per cycle vs. *N* from three experiments with the same initial pre-straining and cycle parameters. (b) Differences in the amplitude of the wrinkles that develop during the initial pre-straining causing difference in the rate of ratcheting and in the average strain at collapse.

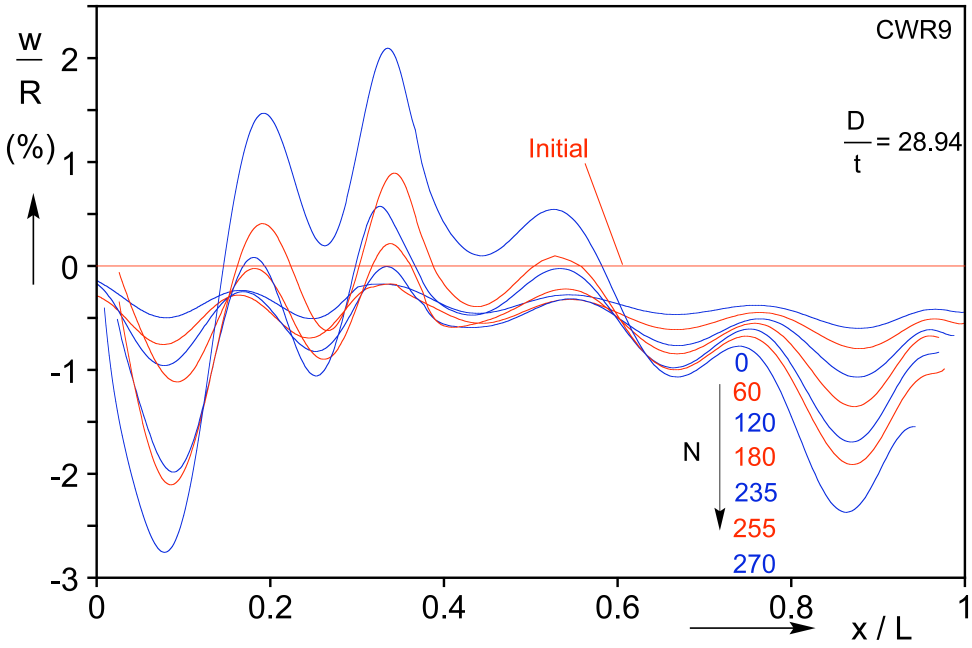

(a)

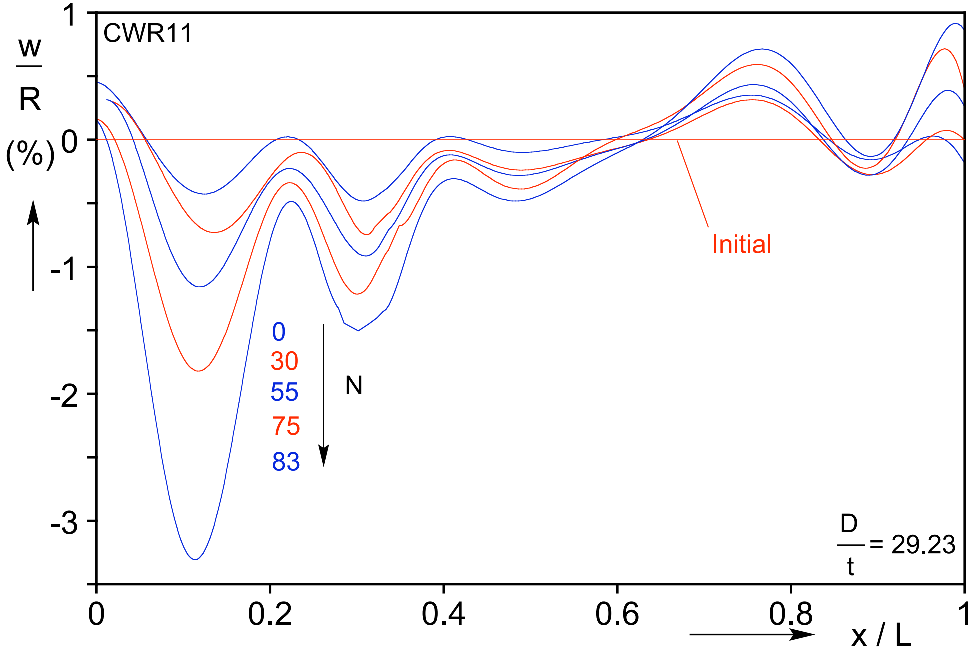

(b)

Fig. 3.9 Axial scans showing evolution of wrinkles during the cycling for (a) CWR9 and (b) CWR11.

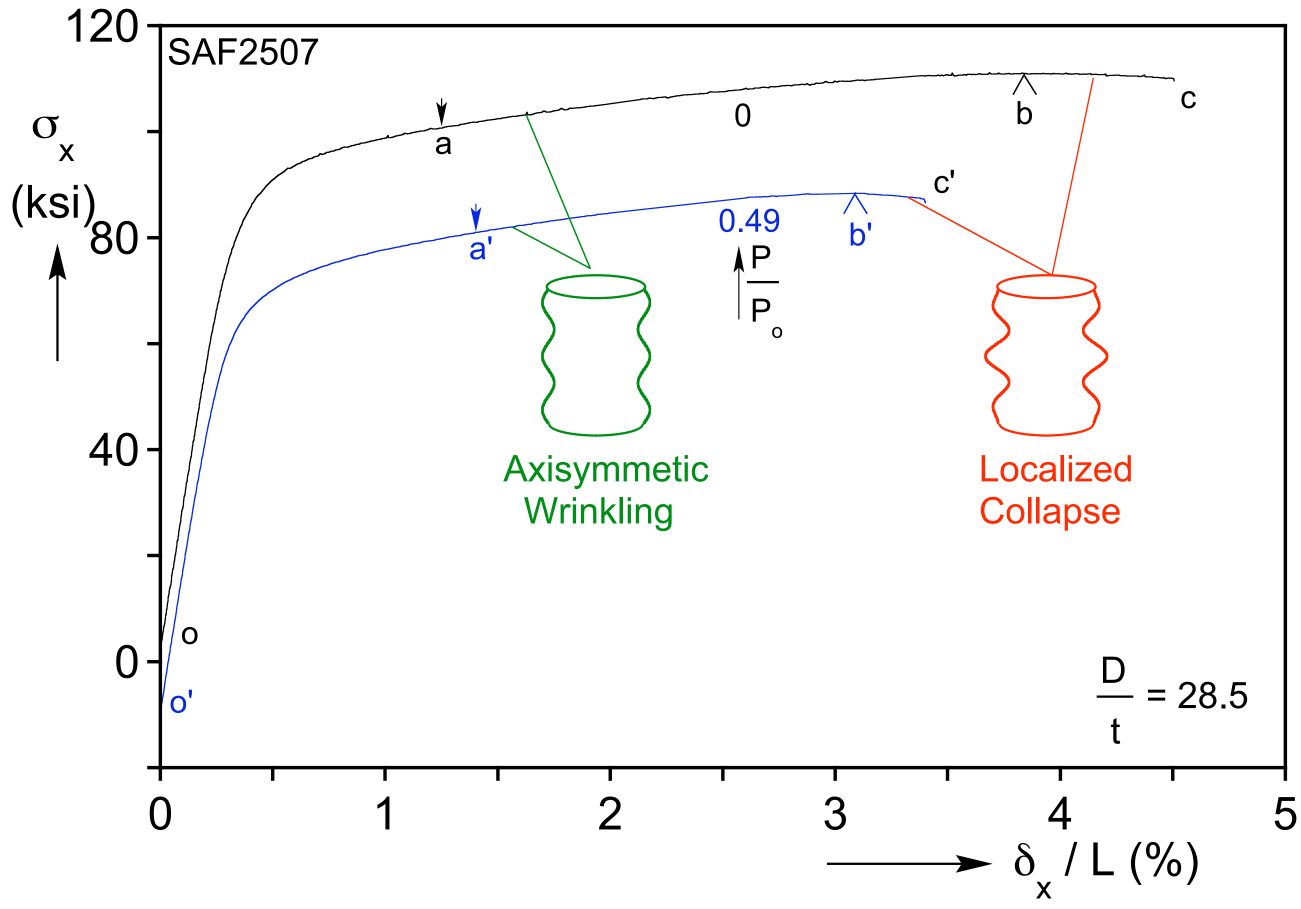

Fig. 4.1 Typical stress-shortening responses of inelastic circular tubes from a pure compression test and a compression test under internal pressure. Shown are the onsets of wrinkling (a and a’) followed by axisymmetric collapse (b and b’) and localization (bc and b’c’).

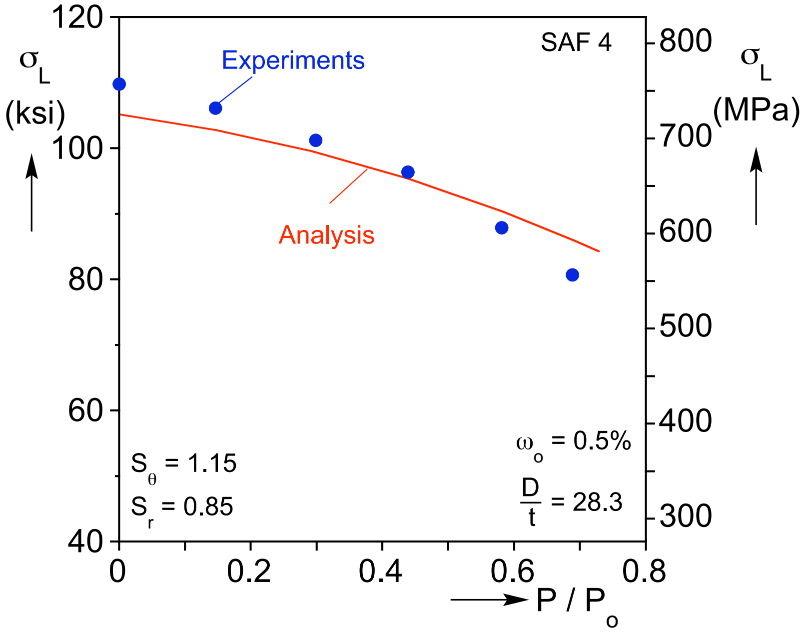

(a)

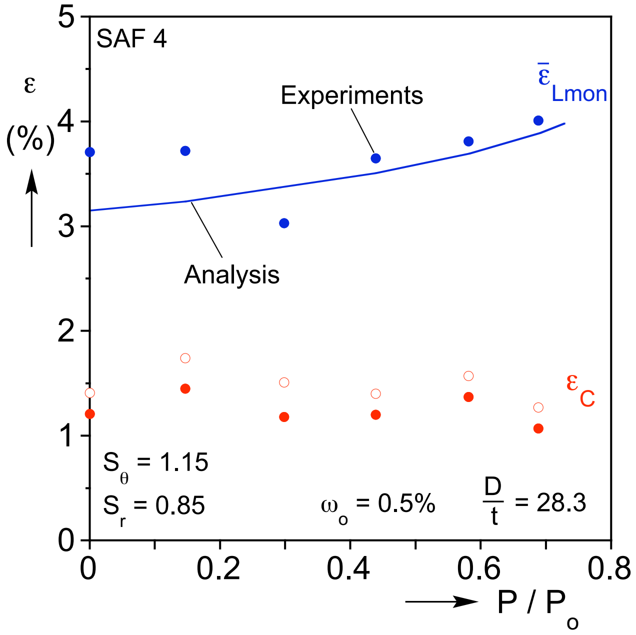

(b)

Fig. 4.2 Limit stress (a) and critical strains (b) as a function of internal pressure for D/t = 28.3. Experiments and predictions from Paquette and Kyriakides (2006).

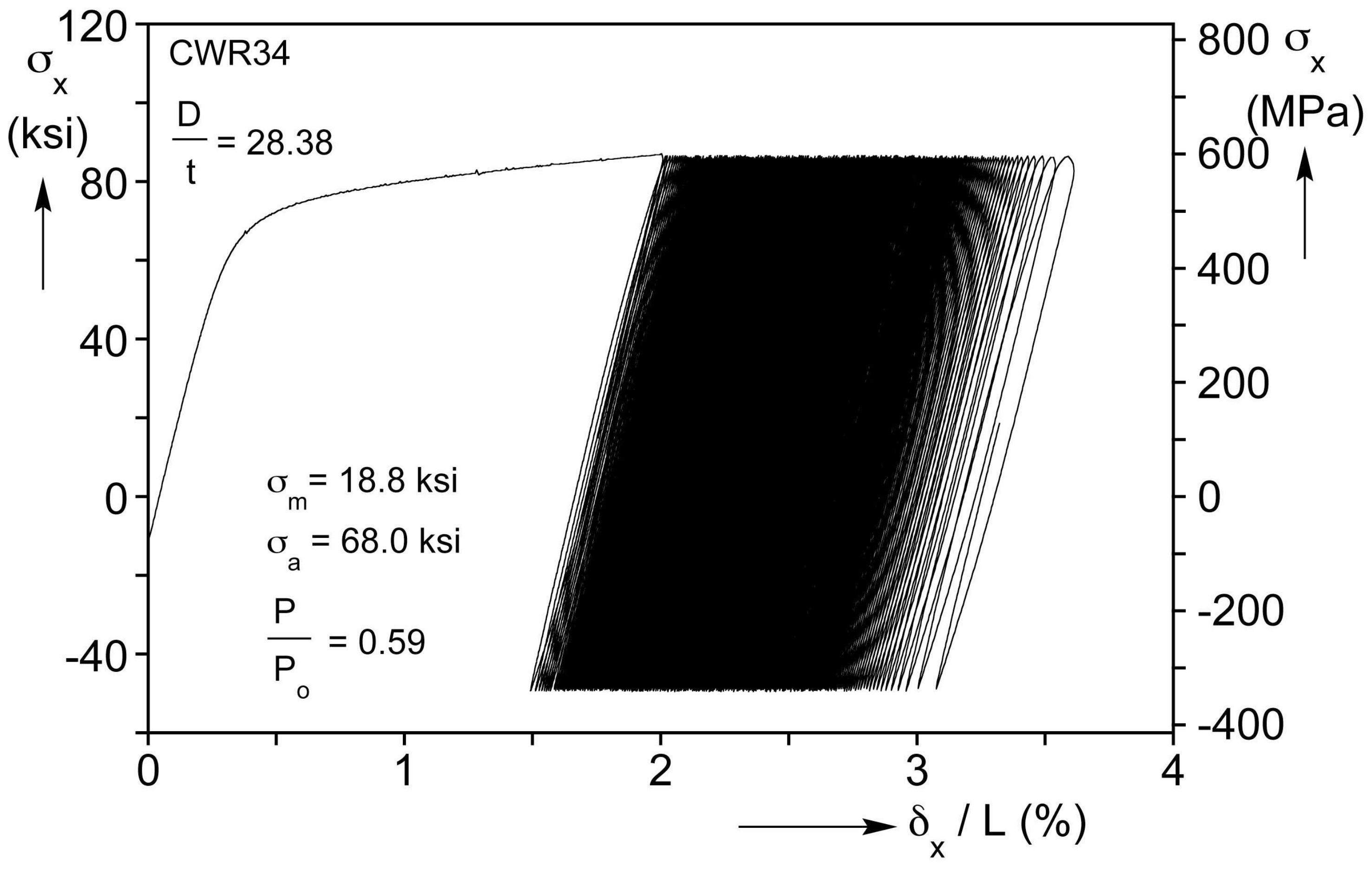

Fig. 4.3a Axial stress-shortening response from cyclic loading experiment CWR34.

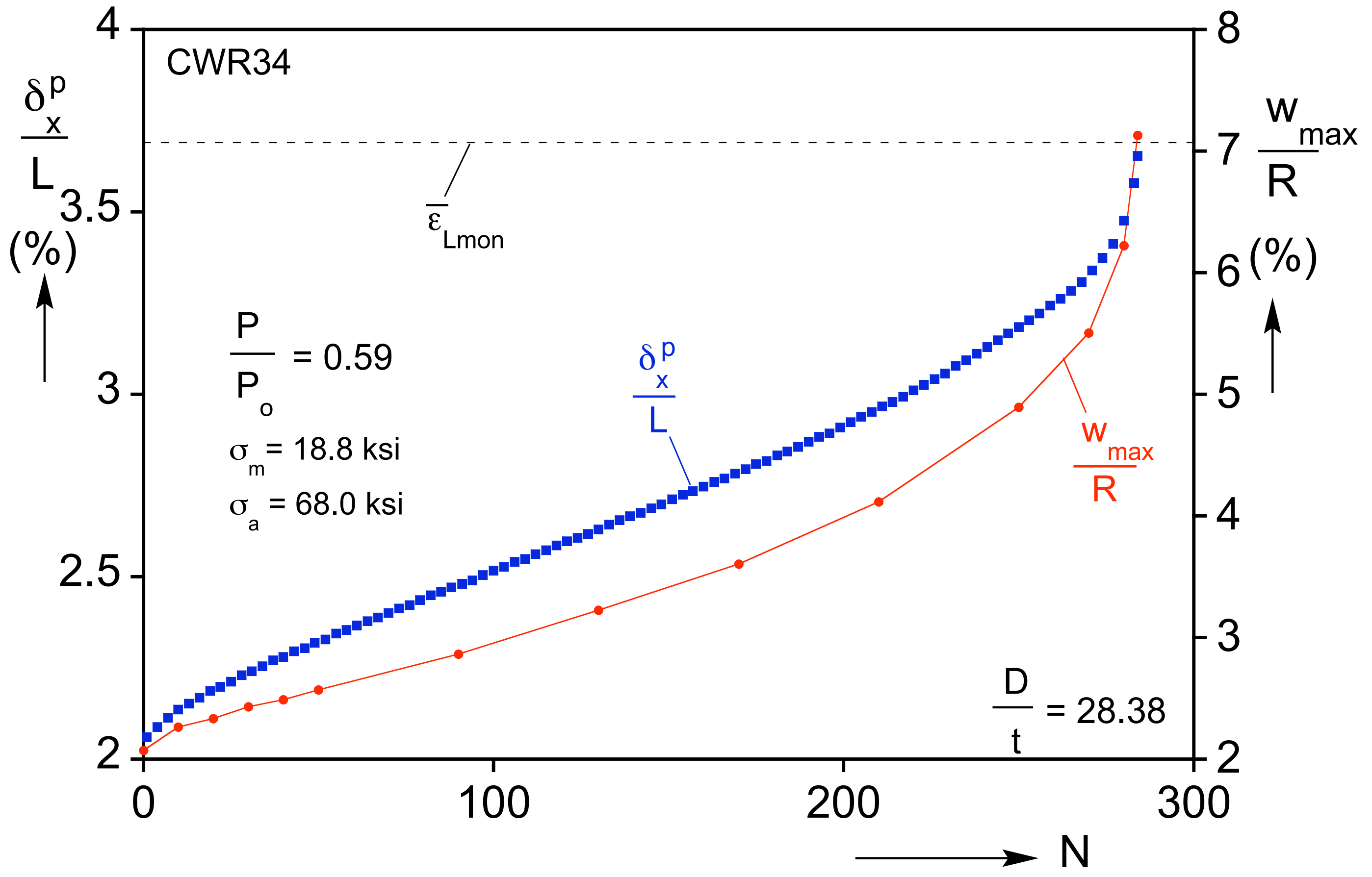

Fig. 4.3b Peak axial displacement and corresponding maximum wrinkle normal displacement vs. *N*.

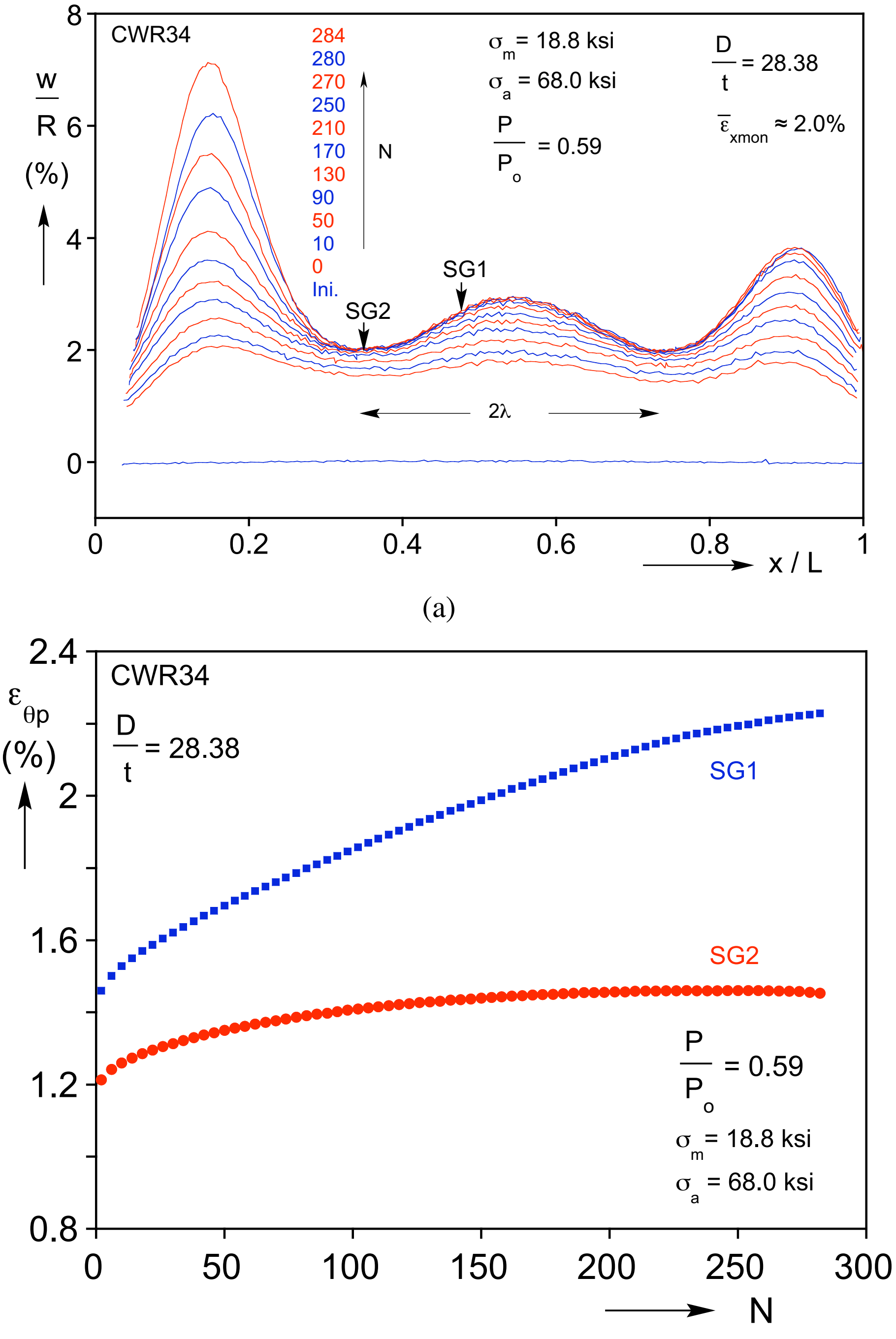

(a)

(b)

Fig. 4.4 (a) Axial scans showing evolution of wrinkles during the cycling. (b) Peak circumferential strains at two locations in the test section vs. *N*.

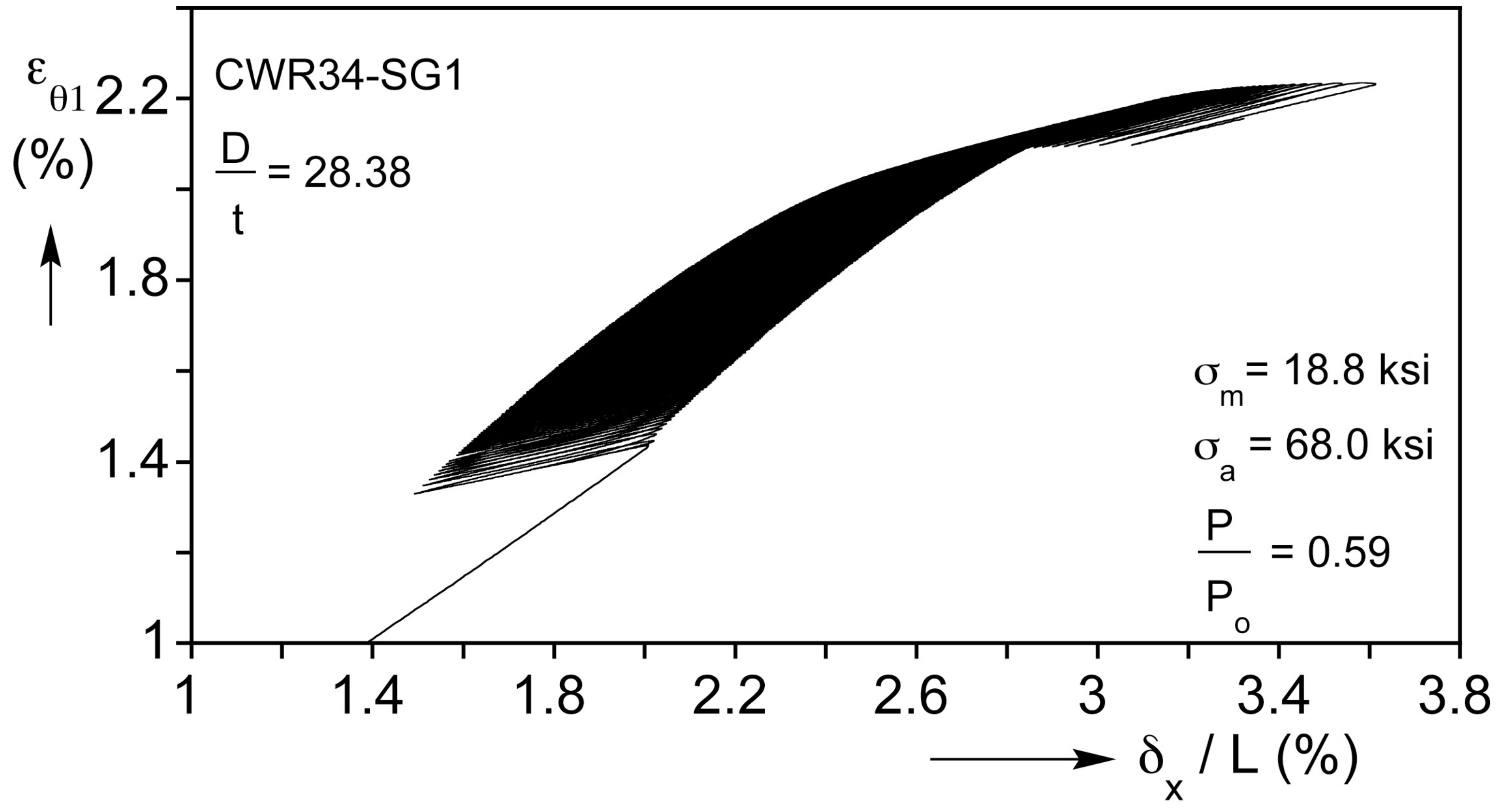

Fig. 4.5 Axial-circumferential strain response from experiment CWR34 that illustrates the biaxial ratcheting that takes place.

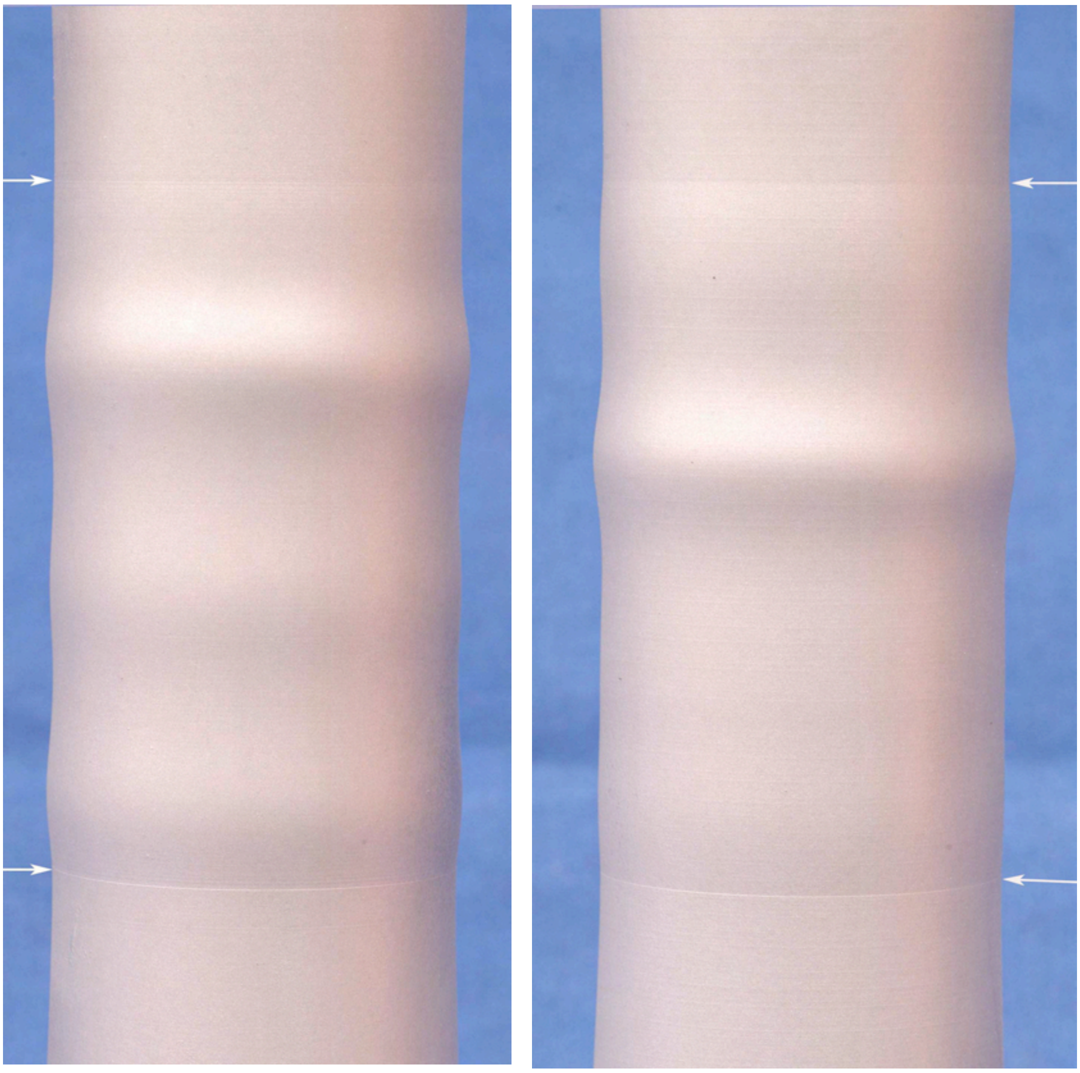

(a) CWR39

(b) CWR42

Fig. 4.6 Photographs of specimens CWR39 and CWR42 at the end of cycling showing wrinkles and their localization. Arrows indicate edges of test sections.

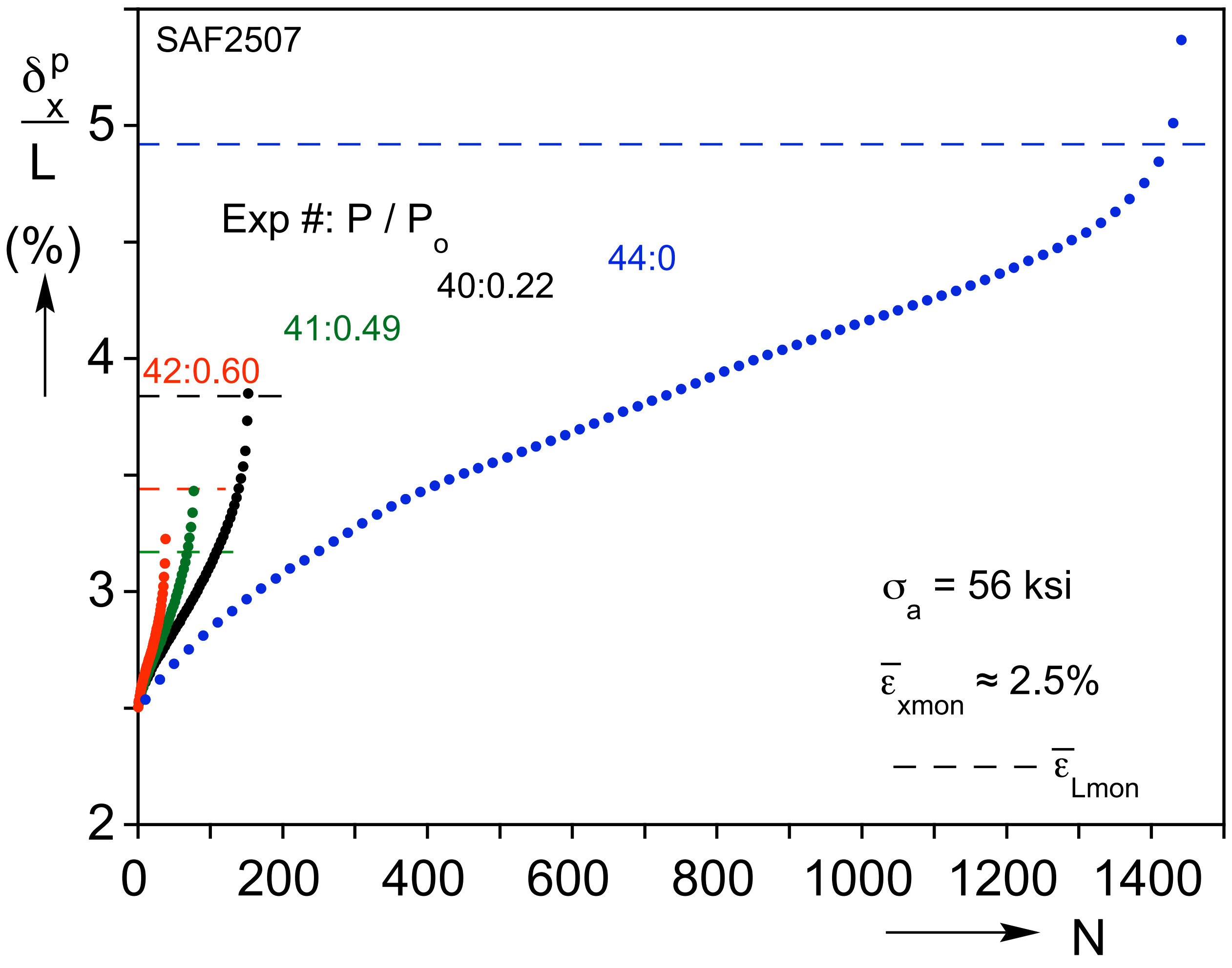

Fig. 4.7 Peak axial displacement vs. *N* from four tubes tested with the same pre-strain and cycle stress amplitude but different internal pressure.

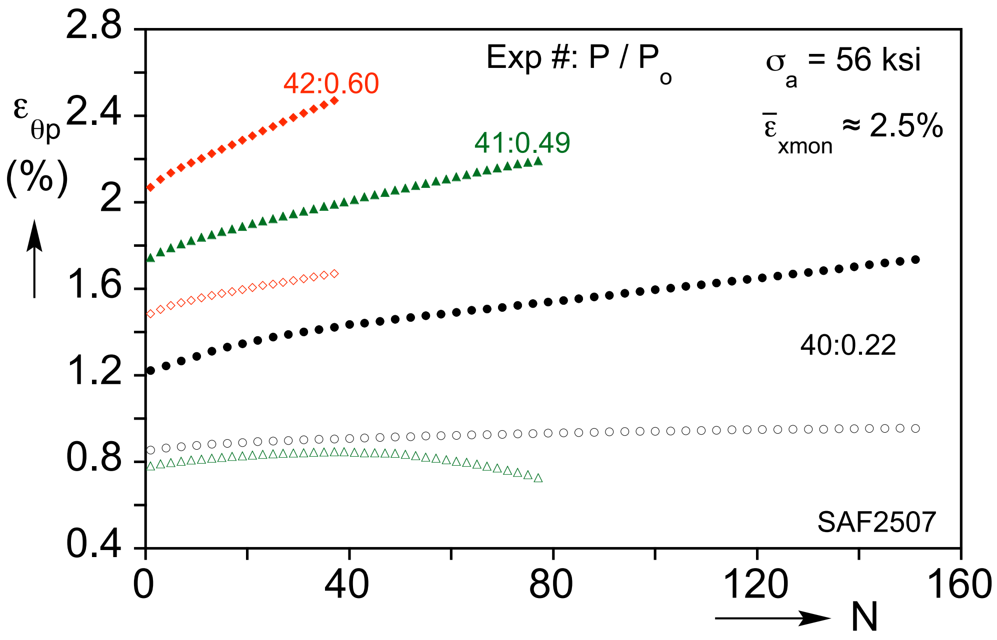

(a)

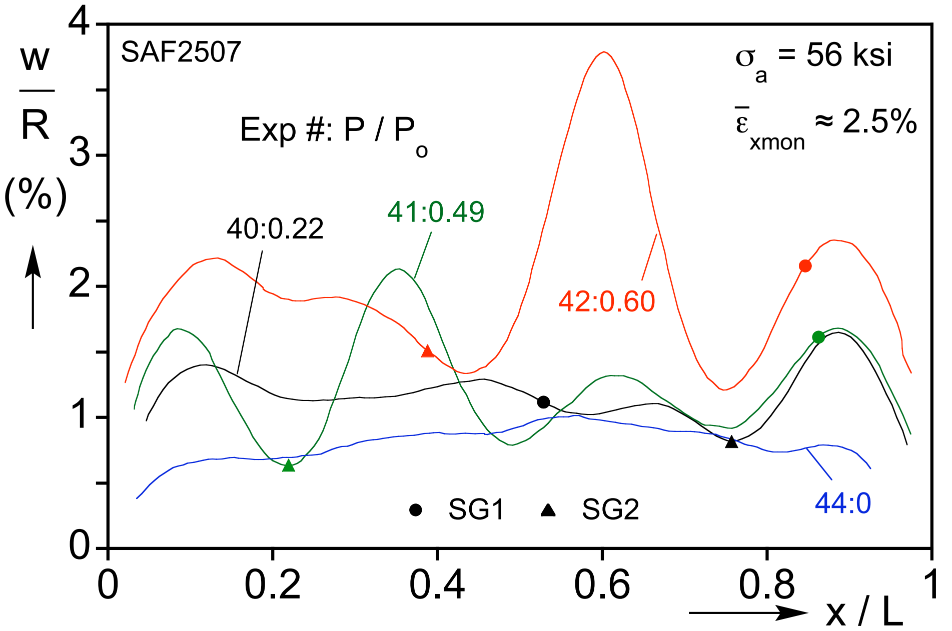

(b)

Fig. 4.8 (a) Peak circumferential strain vs. *N* from the three pressurized tubes in Fig. 4.7. (b) Wrinkle profiles following the pre-straining corresponding to four tubes in Fig. 4.7.

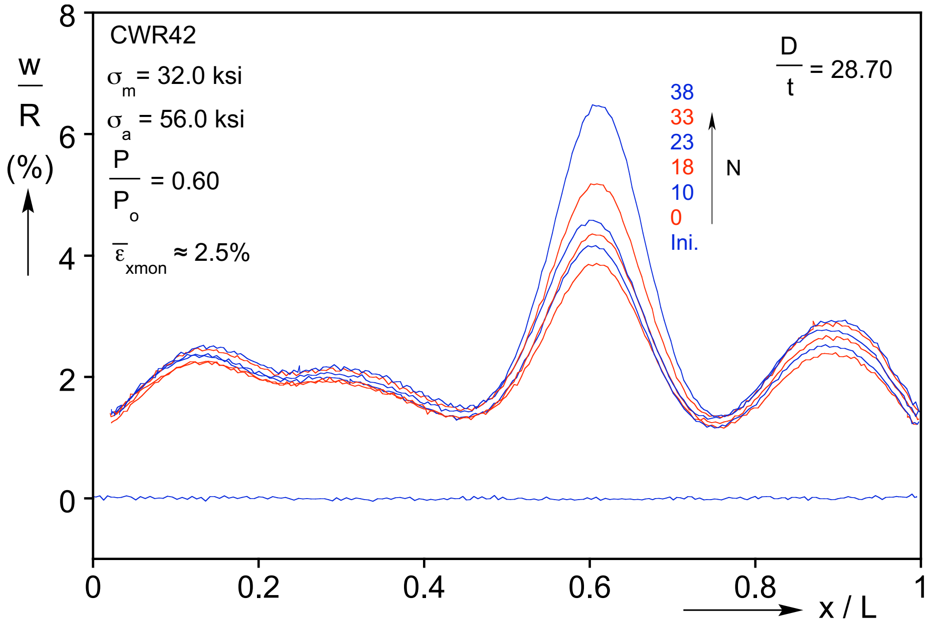

(a)

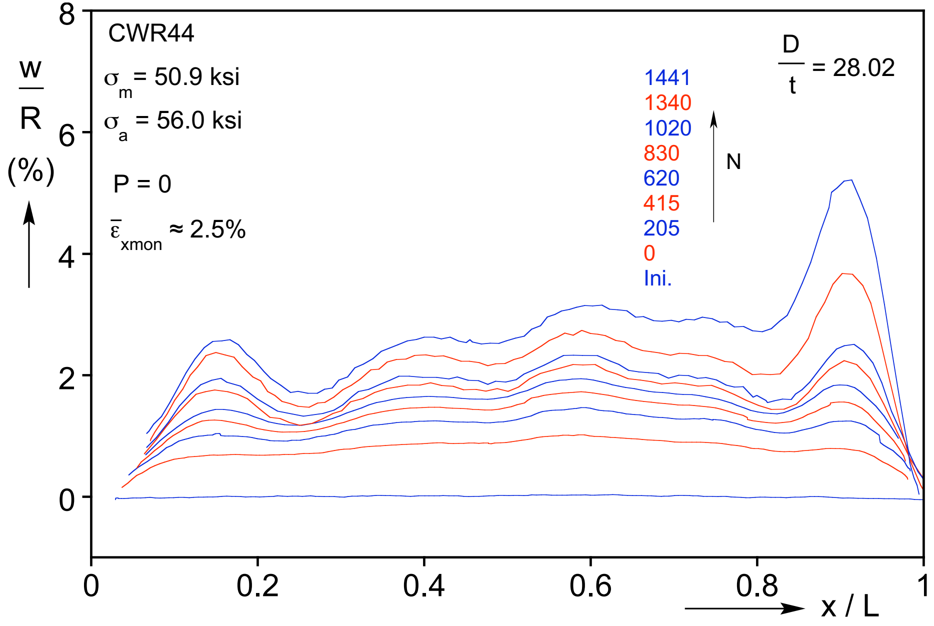

(b)

Fig. 4.9 Axial scans showing evolution of wrinkles during the cycling for (a) CWR42 and (b) CWR44.

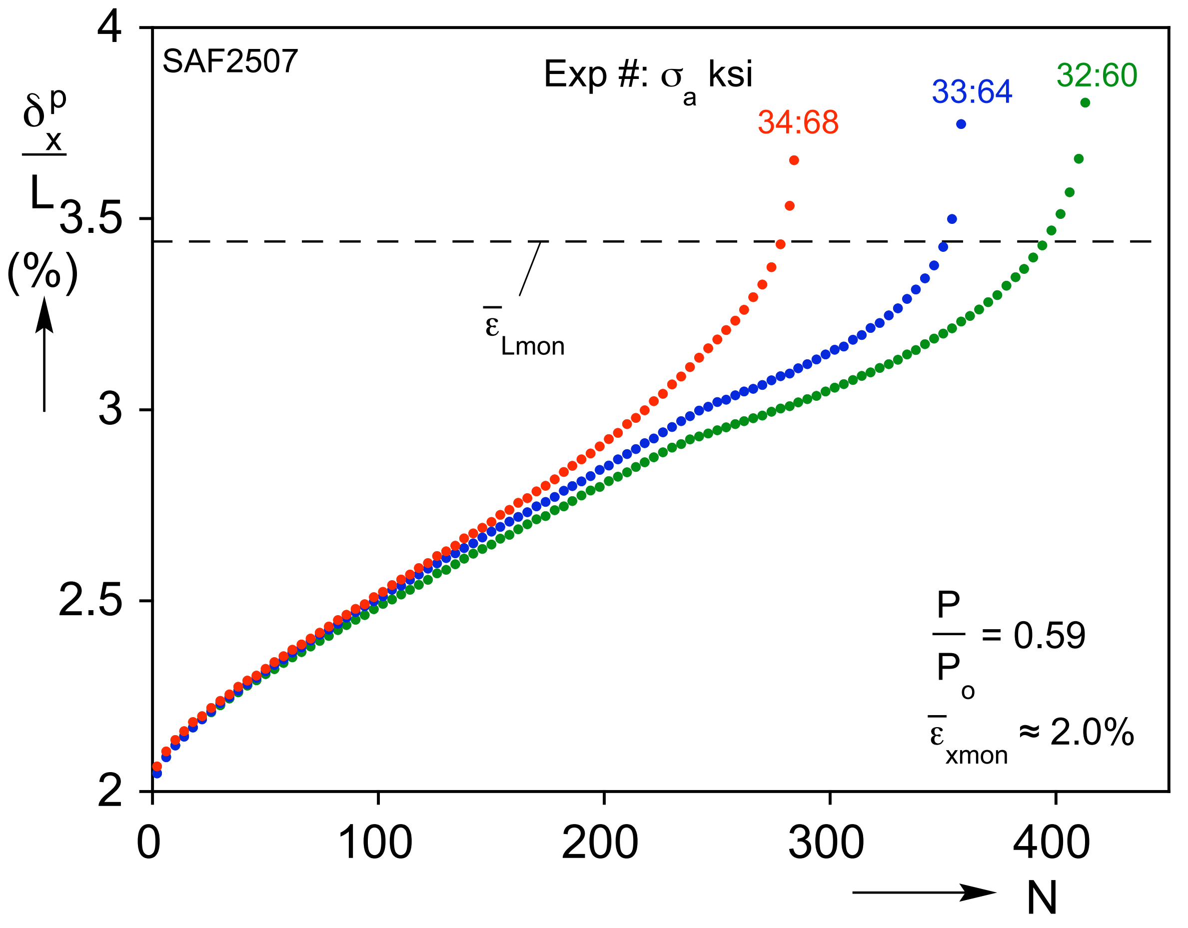

Fig. 4.10 Peak axial displacement vs. *N* from three tubes tested with the same pre-strain and internal pressure but different axial cycle amplitudes.

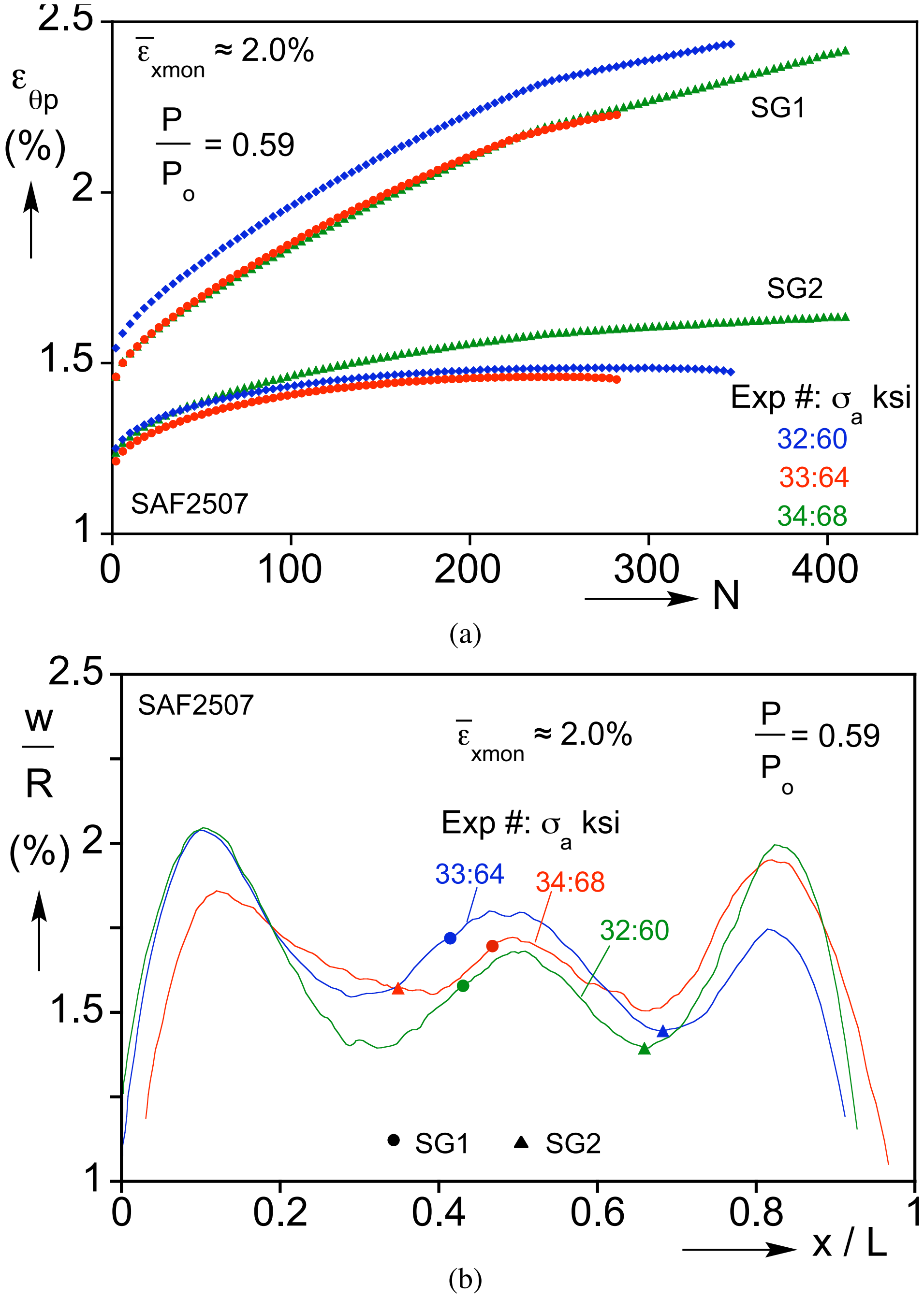

Fig. 4.11 (a) Peak circumferential strain vs. *N* and (b) wrinkle profiles following the pre-straining corresponding to three tubes in Fig. 4.10.

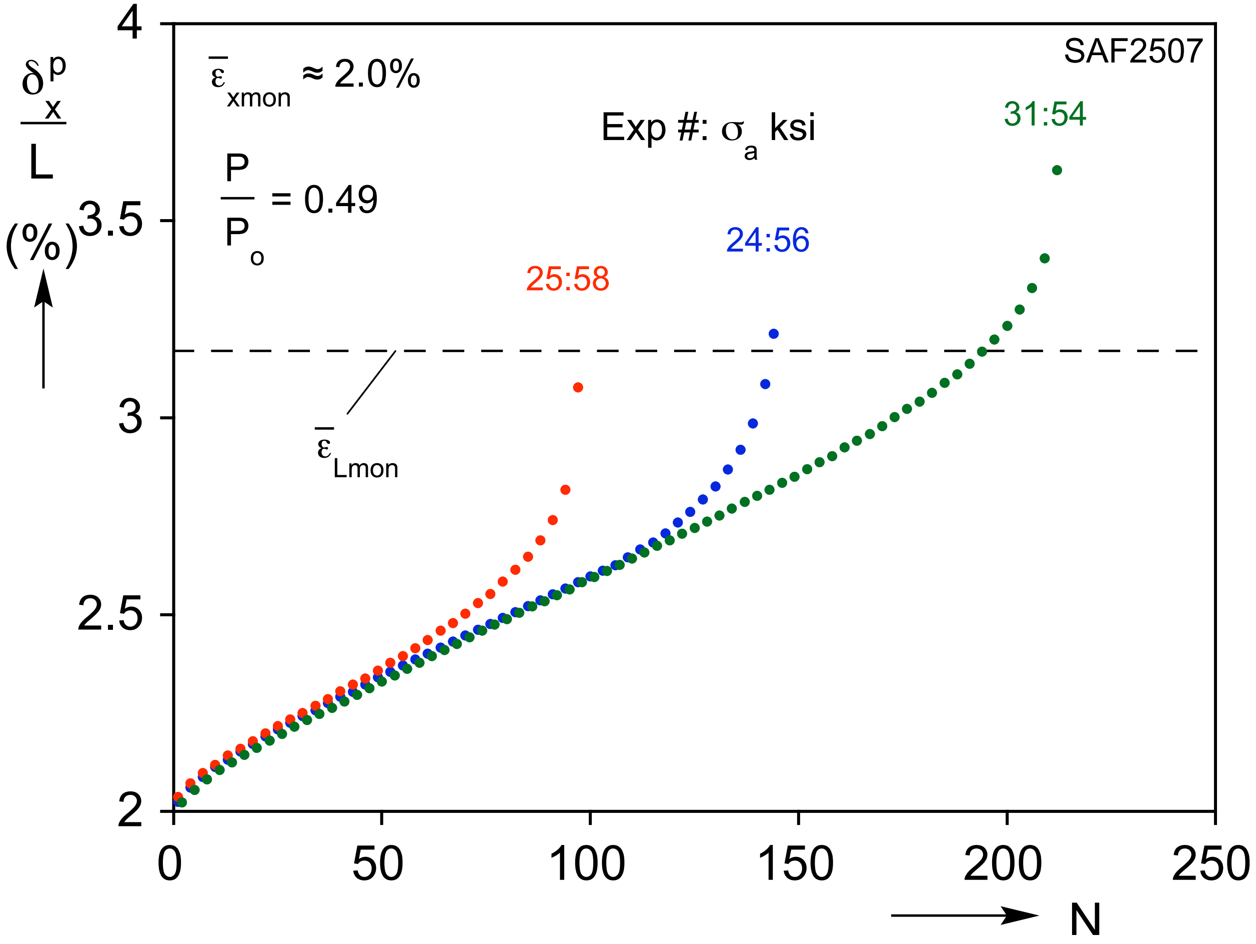

Fig. 4.12 Peak axial displacement per vs. *N* from three tubes tested with the same pre-strain and internal pressure but different axial cycle amplitudes.

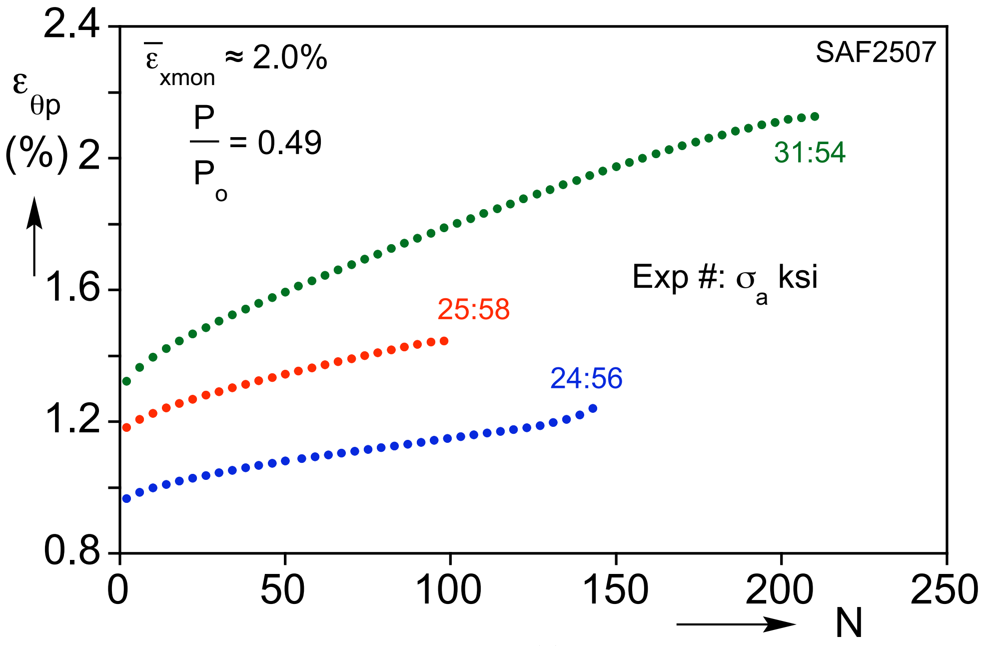

(a)

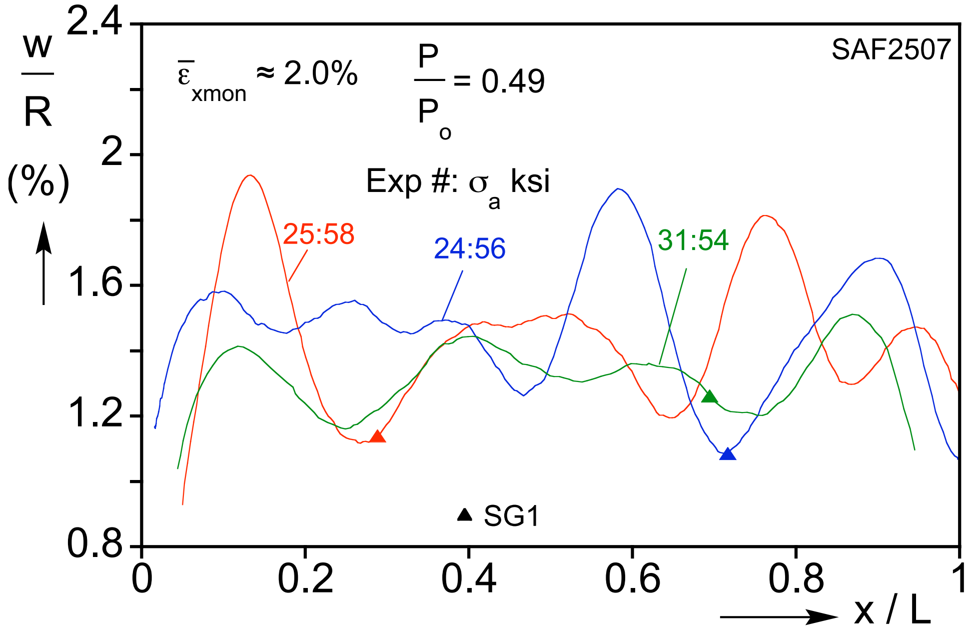

(b)

Fig. 4.13 (a) Peak circumferential strain vs. *N* and (b) wrinkle profiles following the pre-straining corresponding to three tubes in Fig. 4.12.

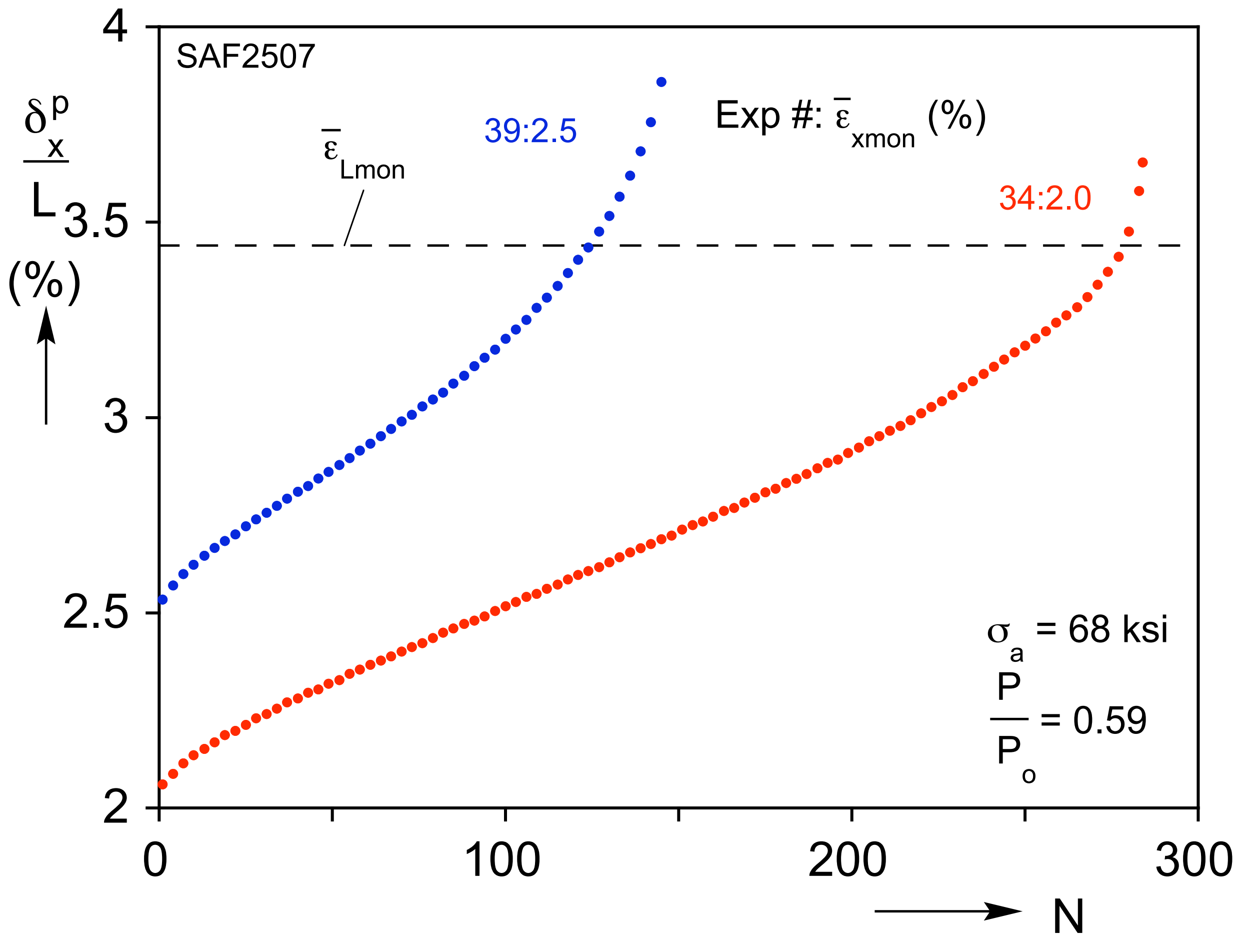

Fig. 4.14 Peak axial displacement per vs. *N* from two tubes tested with the same internal pressure ($0.59P_o$) and axial cycle amplitude but different pre-strains.

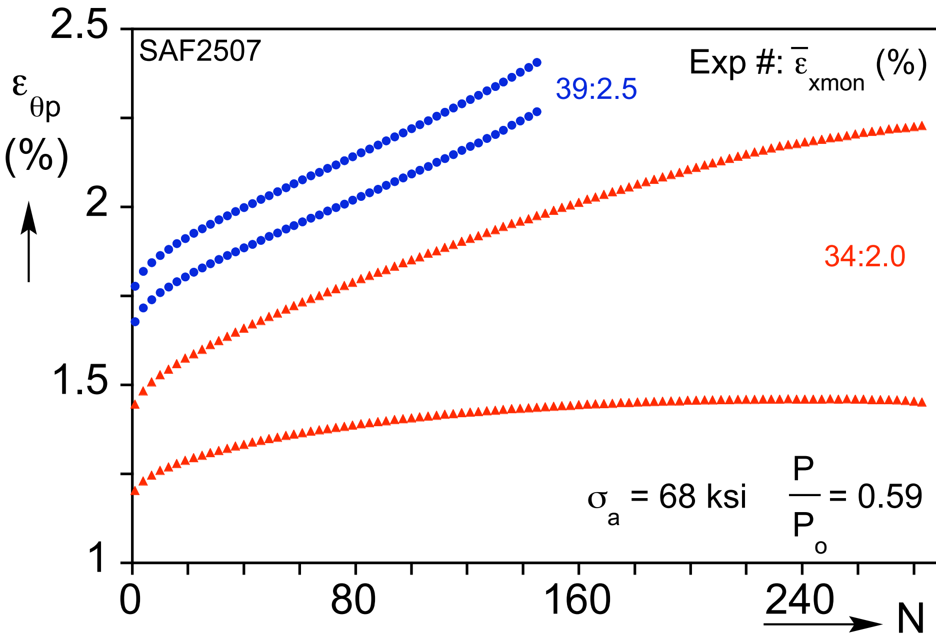

(a)

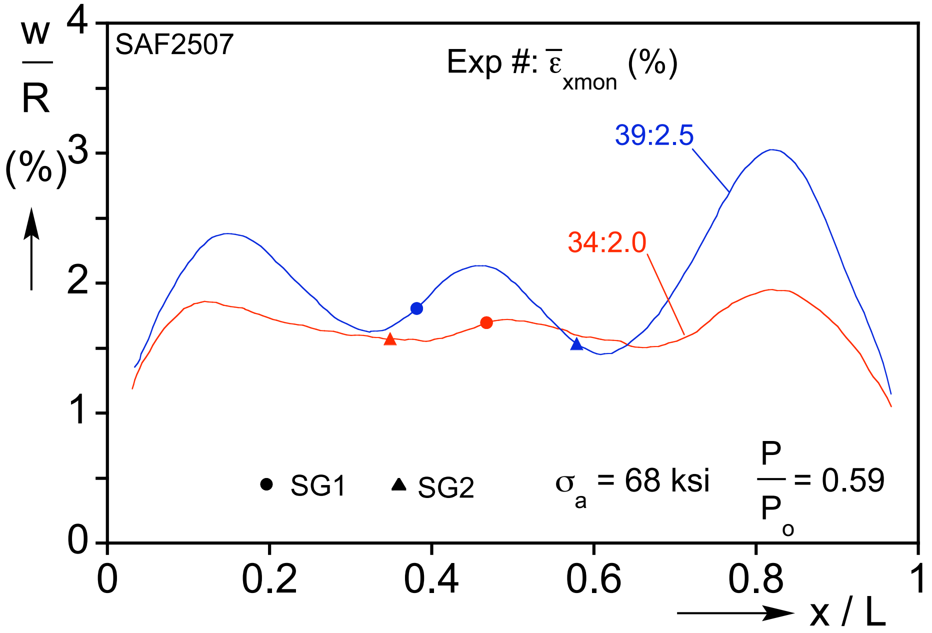

(b)

Fig. 4.15 (a) Peak circumferential strain vs. *N* and (b) wrinkle profiles following the pre-straining corresponding to two tubes in Fig. 4.14; note the difference in the wrinkle amplitudes resulting from the different level of pre-straining.

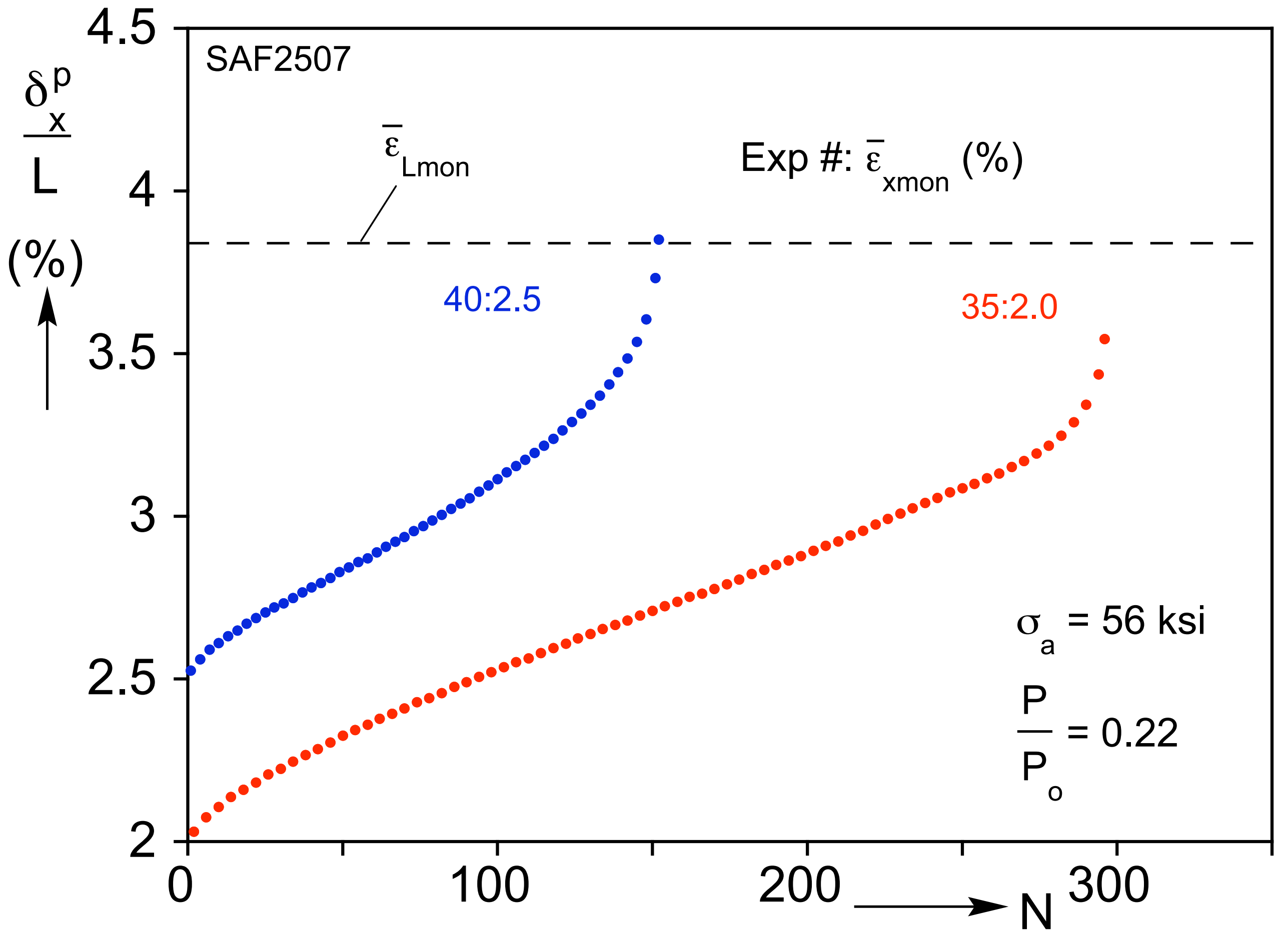

Fig. 4.16 Peak axial displacement per vs. *N* from two tubes tested with the same internal pressure ($0.22P_o$) and axial cycle amplitude but different pre-strains.

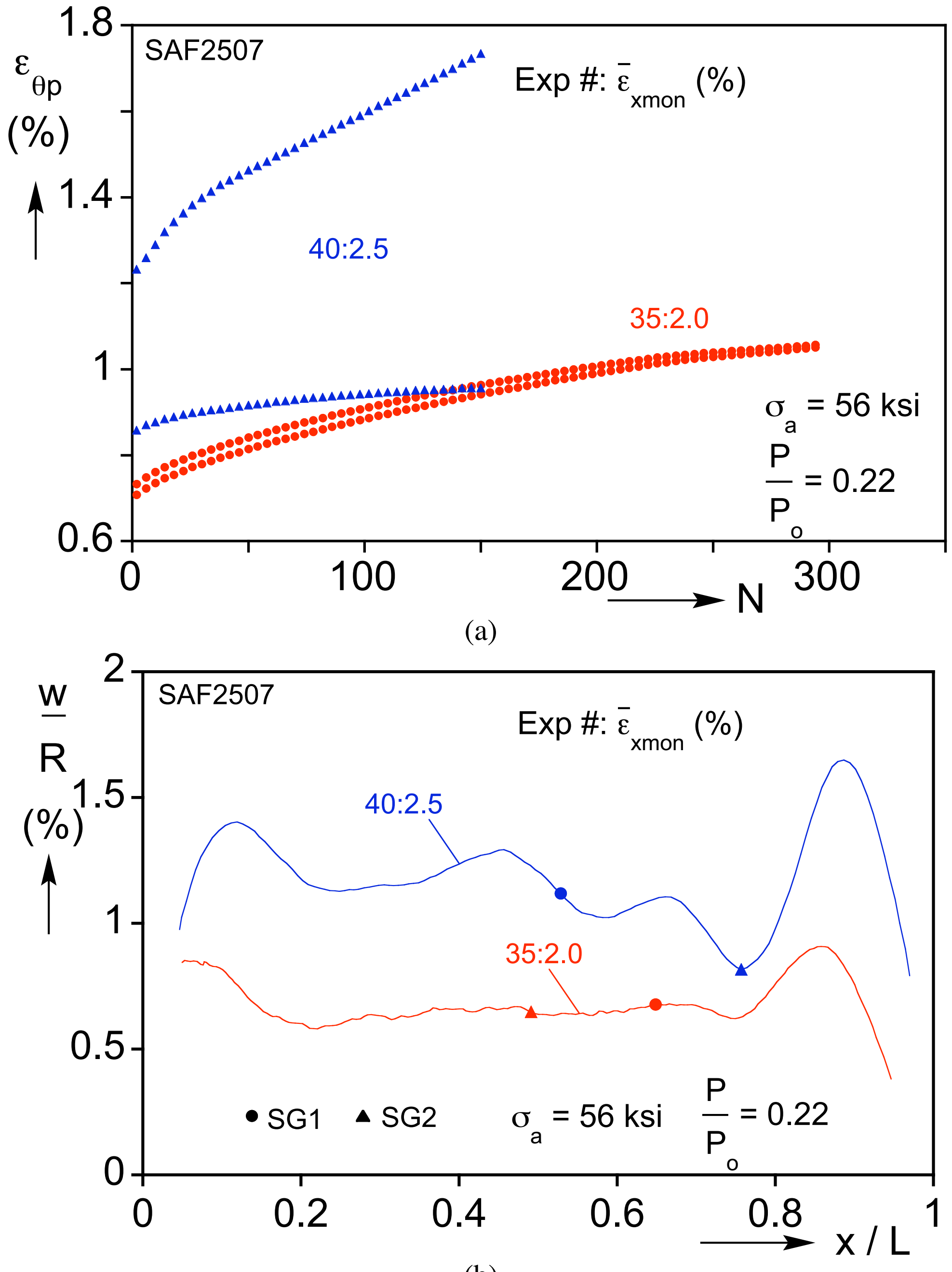

(a)

(b)

Fig. 4.17 (a) Peak circumferential strain vs. *N* and (b) wrinkle profiles following the pre-straining corresponding to two tubes in Fig. 4.16; note the difference in the wrinkle amplitudes resulting from the different pre-straining and the shorter wavelength compared to Fig. 4.15 due to the lower pressure.

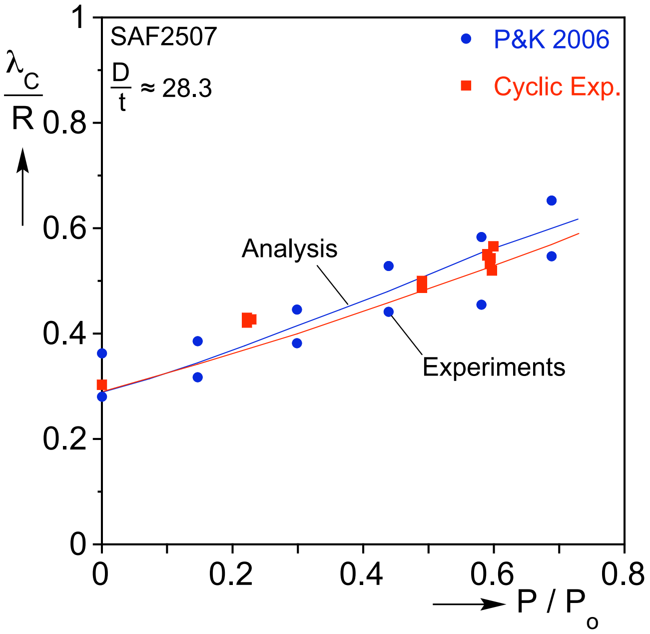

(a)

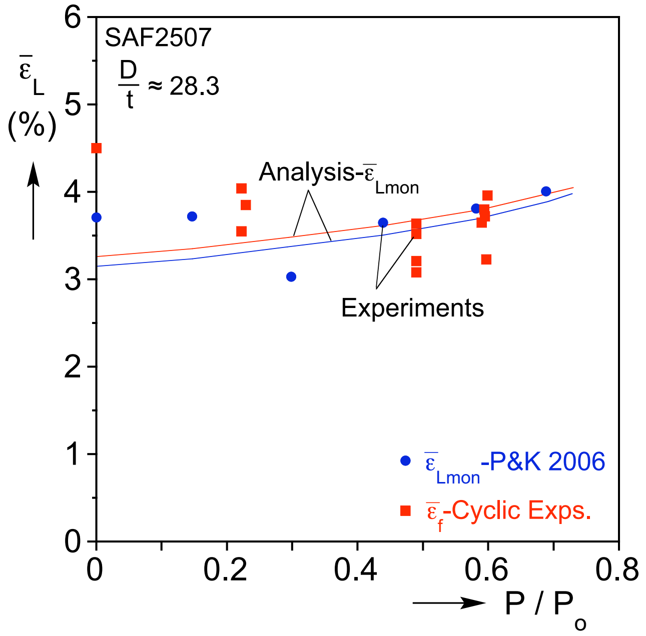

(b)

Fig. 4.18 (a) Wrinkle wavelength vs. pressure and (b) limit and collapse strains vs. pressure. Included are results from monotonic experiments of Paquette and Kyriakides (2006) and cyclic experiments from present study.

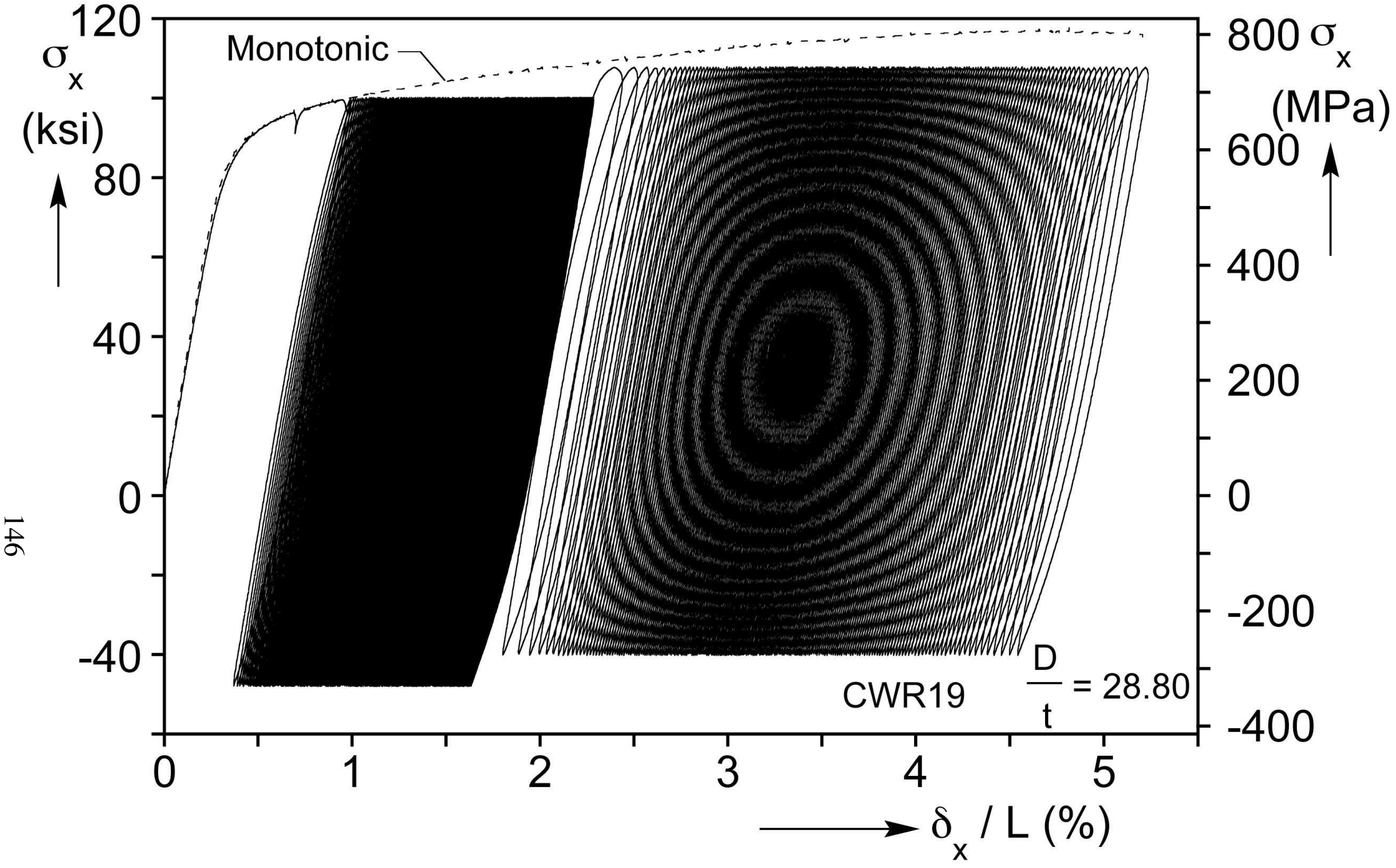

Fig. 5.1a Axial stress-shortening response from a cyclic loading experiment that was not pre-wrinkled.

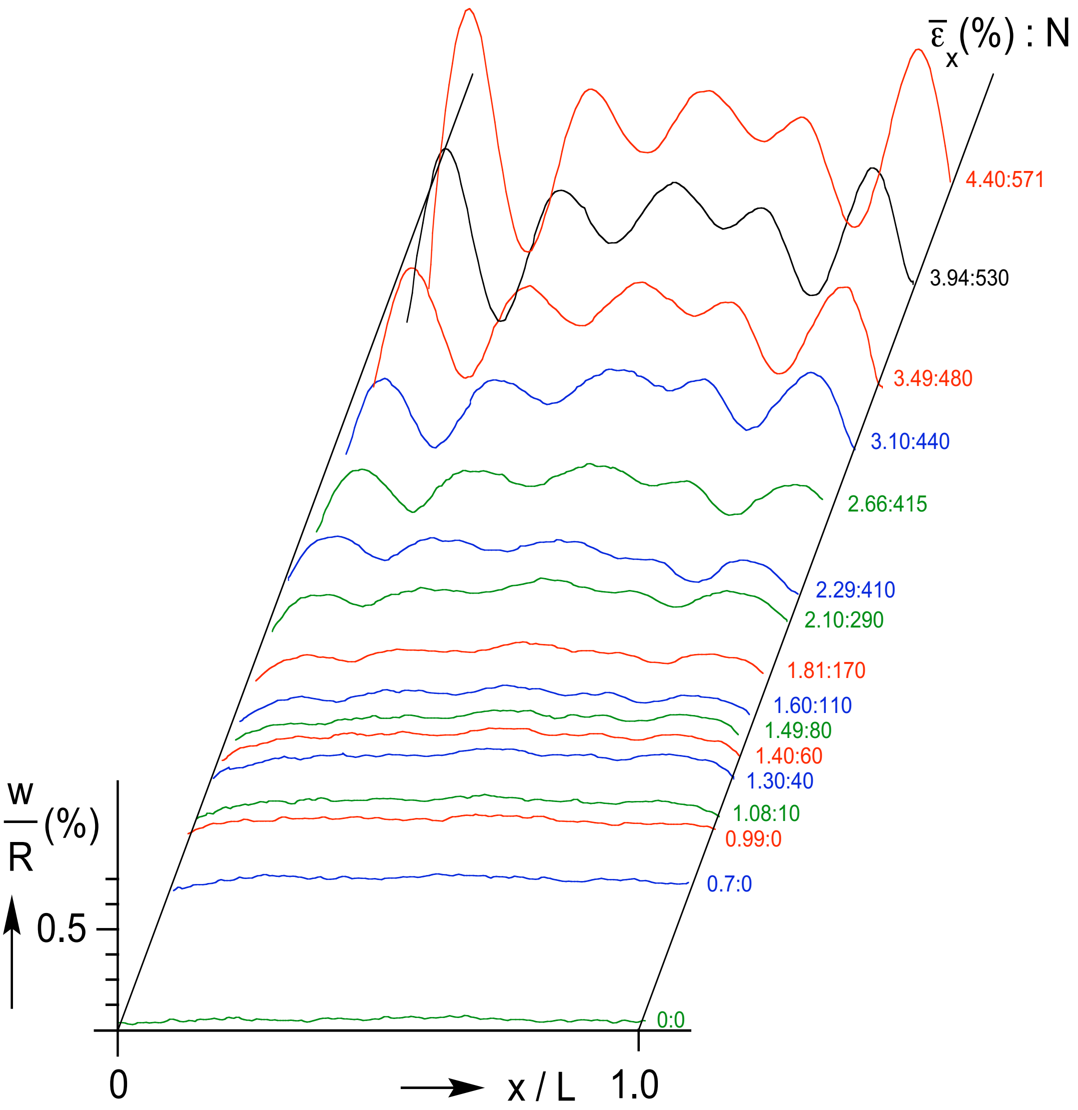

Fig. 5.1b Radial displacement axial profiles after different number of cycles showing the growth and localization of wrinkles for CWR19.

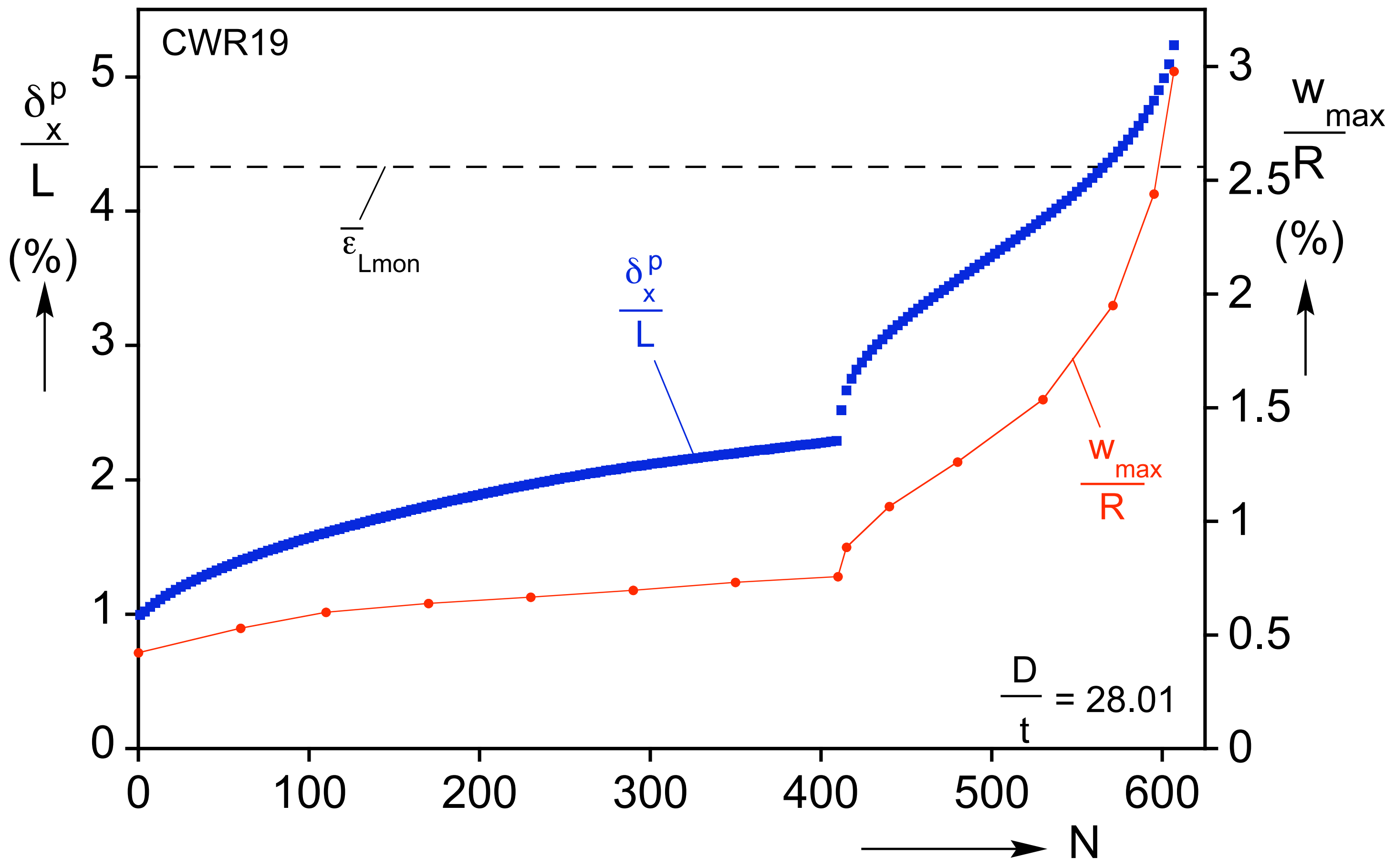

Fig. 5.1c Peak axial displacement per cycle vs. *N* and corresponding maximum radial displacement in wrinkles of CWR19.

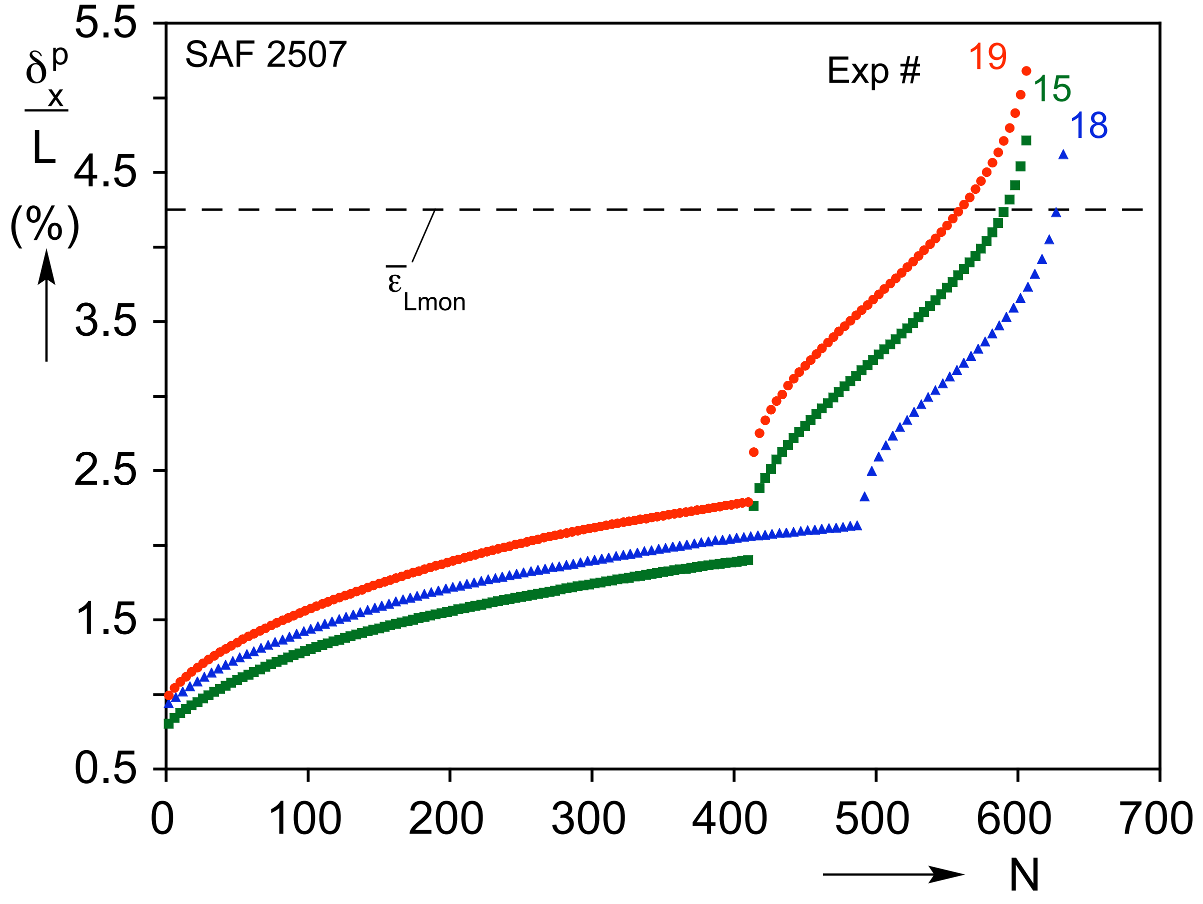

Fig. 5.2 Peak displacement per cycle vs. *N* from three experiments that were not pre-wrinkled. Experiments had slightly different initial pre-straining.

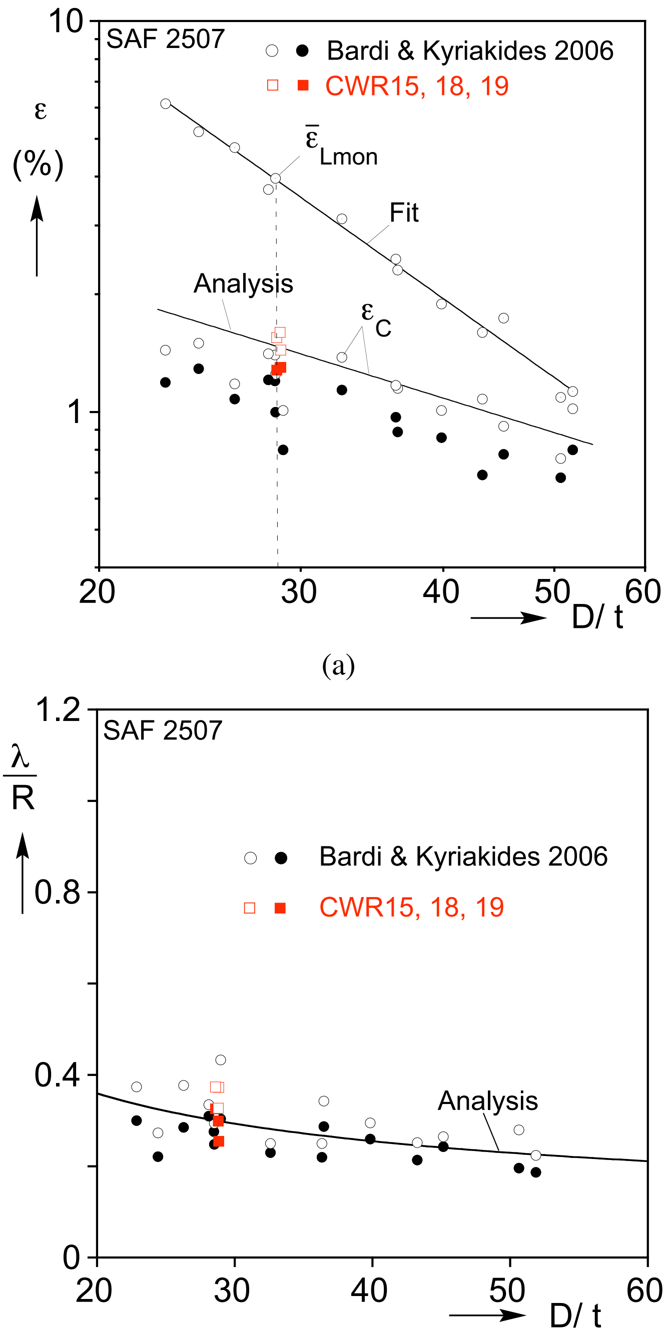

(a)

(b)

Fig. 5.3 (a) Critical wrinkling strain vs. D/t and (b) wrinkle wavelength vs. D/t. Included are results from monotonic compression experiments of Bardi and Kyriakides (2006) and cyclic experiments from present study with $D/t \cong 28.5$.

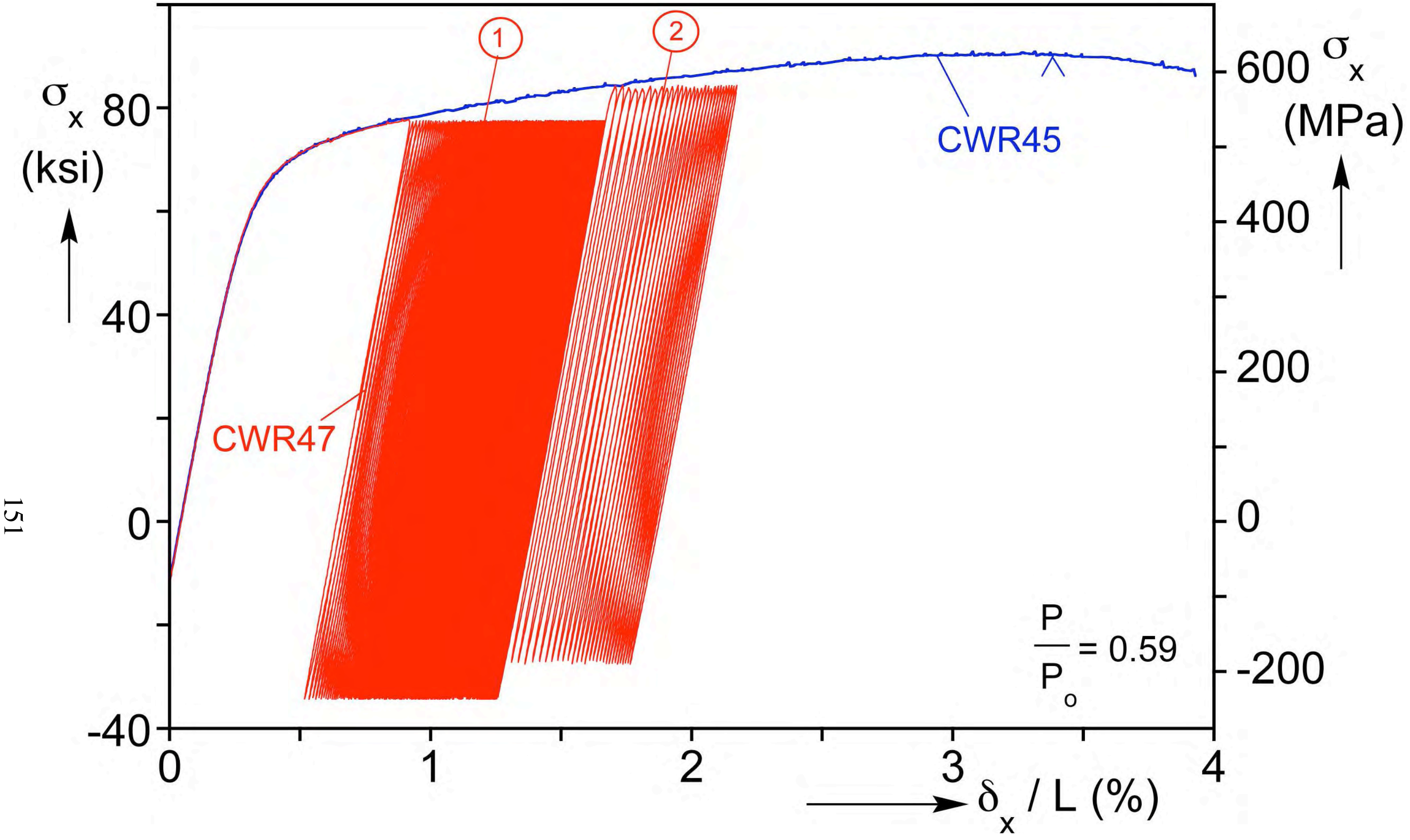

Fig. 5.4a Axial stress-shortening response from monotonic compression test CWR45 and cyclic loading test CWR47 that was not pre-wrinkled tested at the same internal pressure.

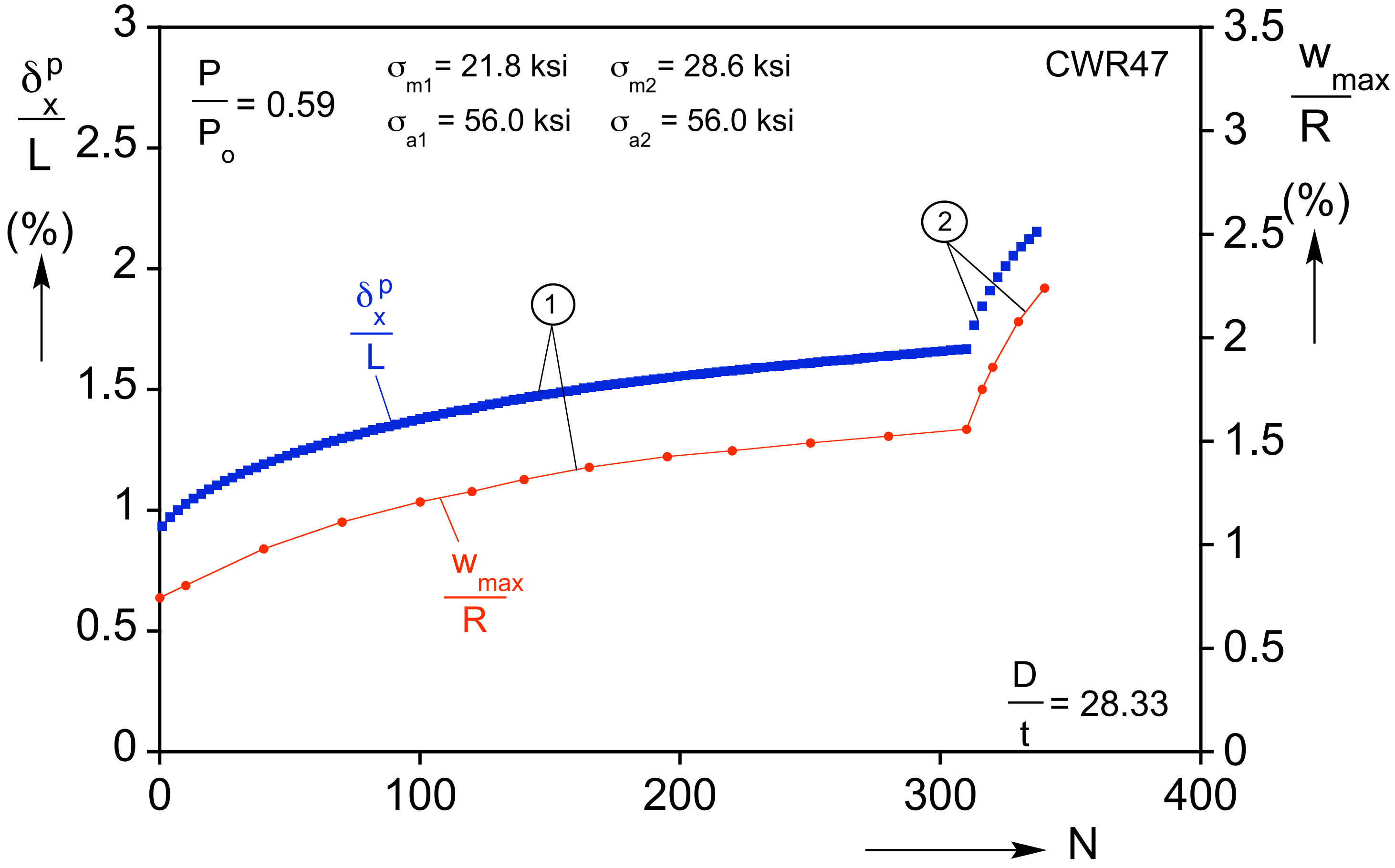

Fig. 5.4b Peak axial displacement and corresponding maximum wrinkle normal displacement vs. *N*.

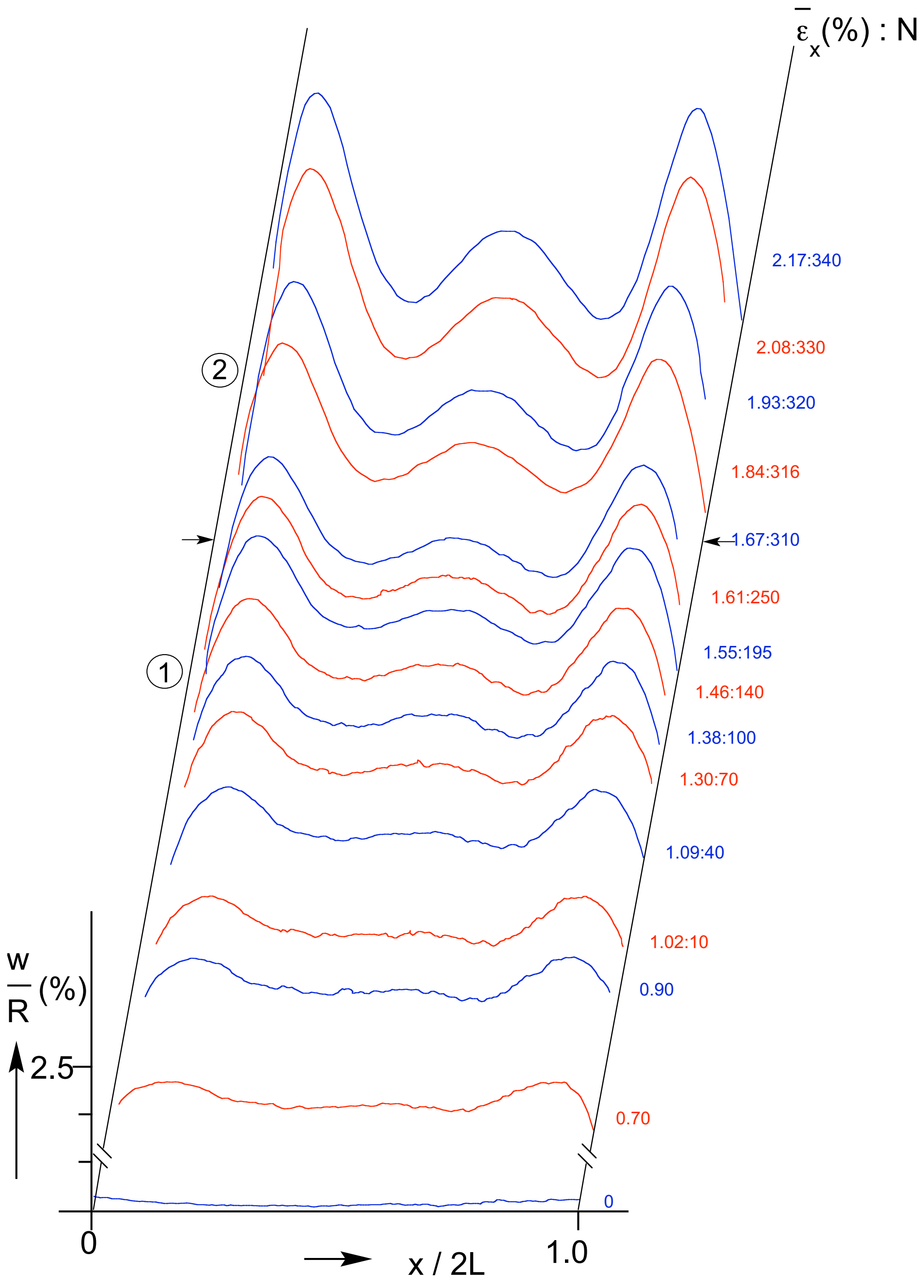

Fig. 5.5 Axial profiles of normal tube displacement after different number of cycles showing the growth and localization of wrinkles for CWR47.

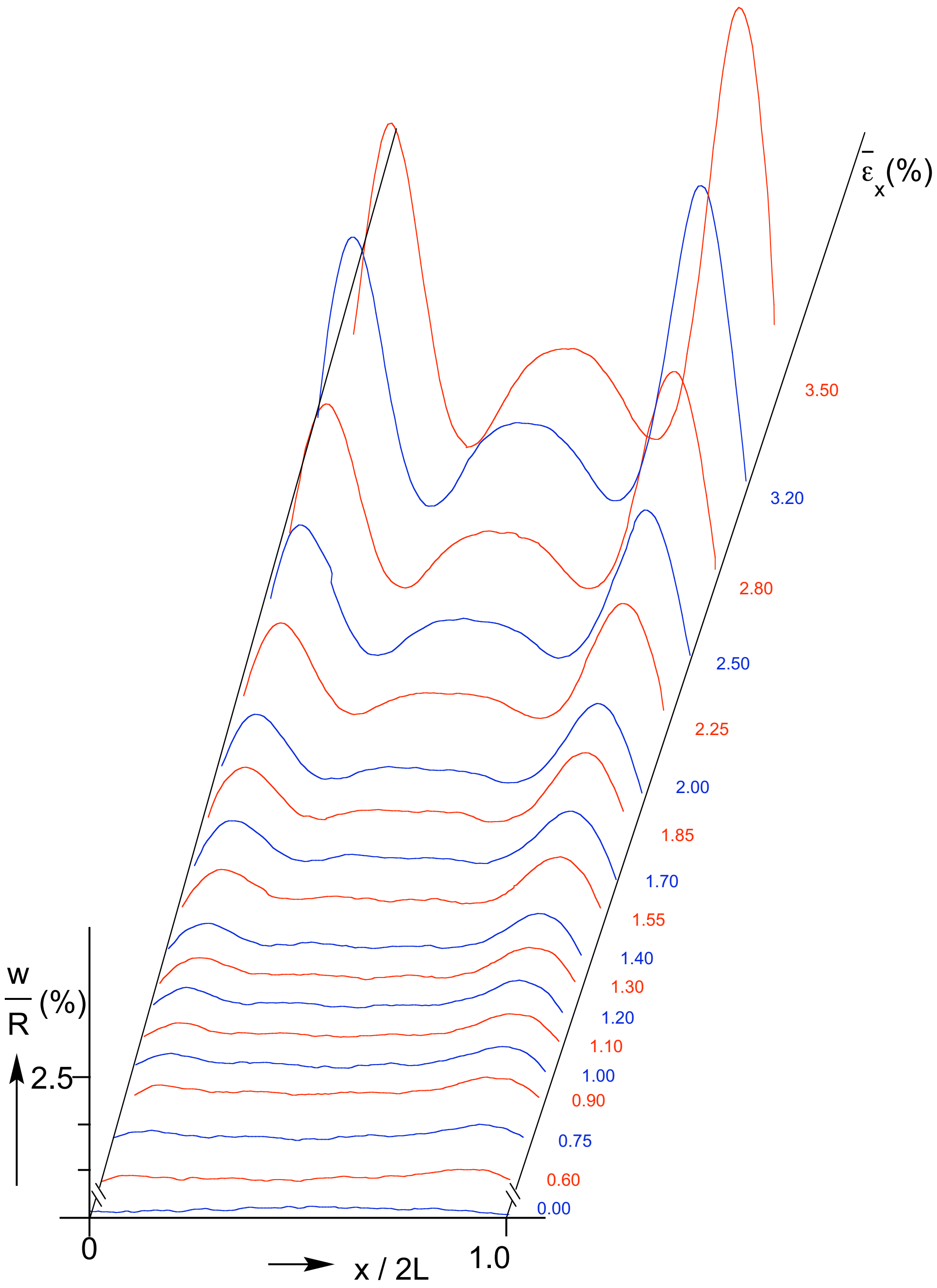

Fig. 5.6 Axial profiles of normal tube displacement recorded at different average strain levels during monotonic compression of CWR45 that show the evolution of the wrinkles.

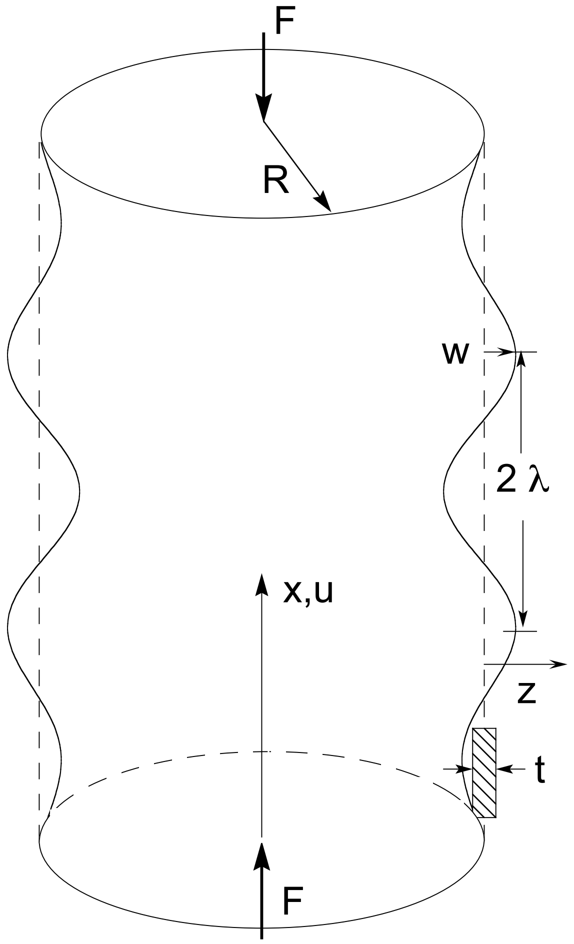

Fig. 6.1 Axisymmetric buckling of a cylindrical shell under axial compression.

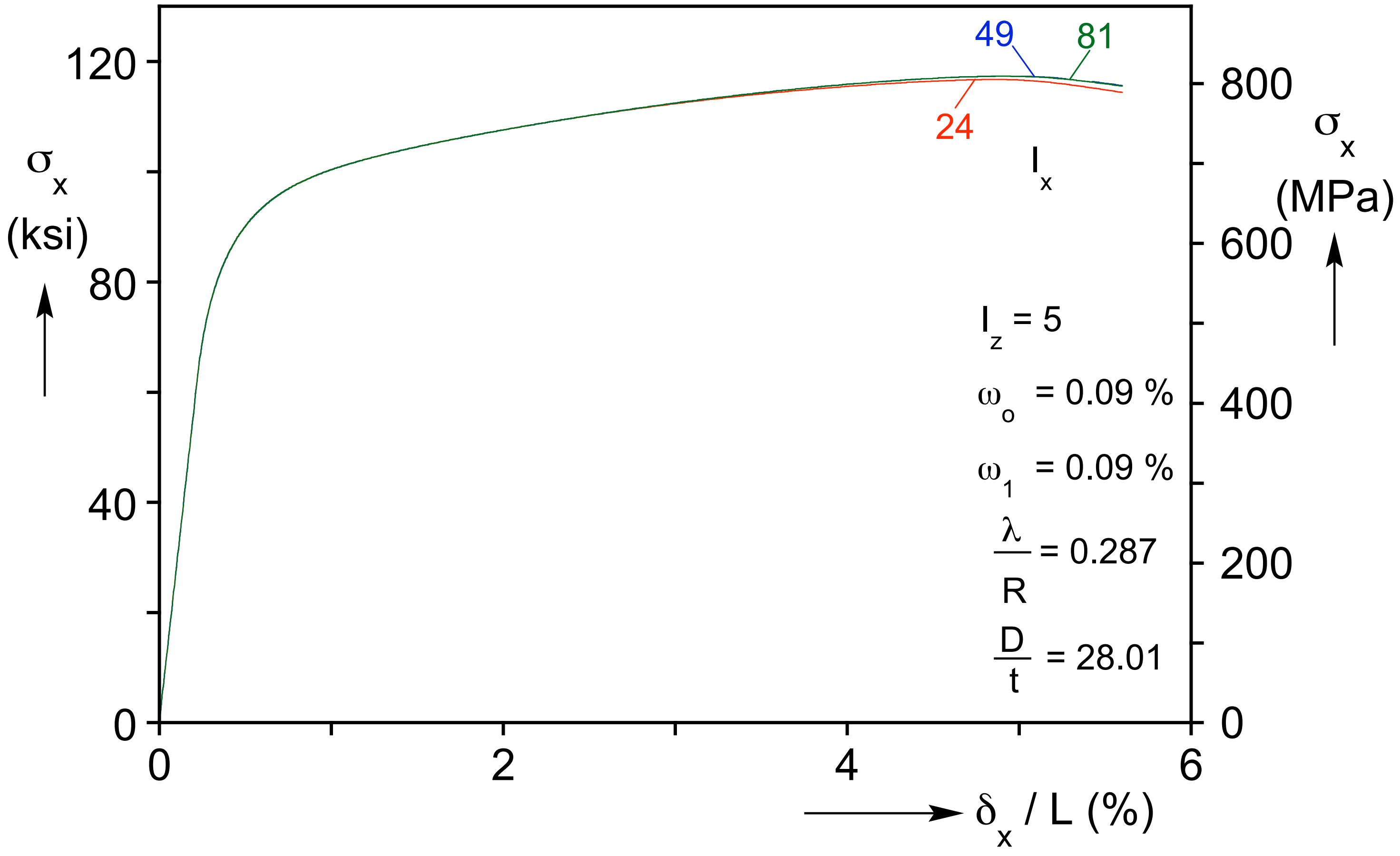

Fig. 6.2a Convergence study regarding the number of Gauss integration points in the axial direction.

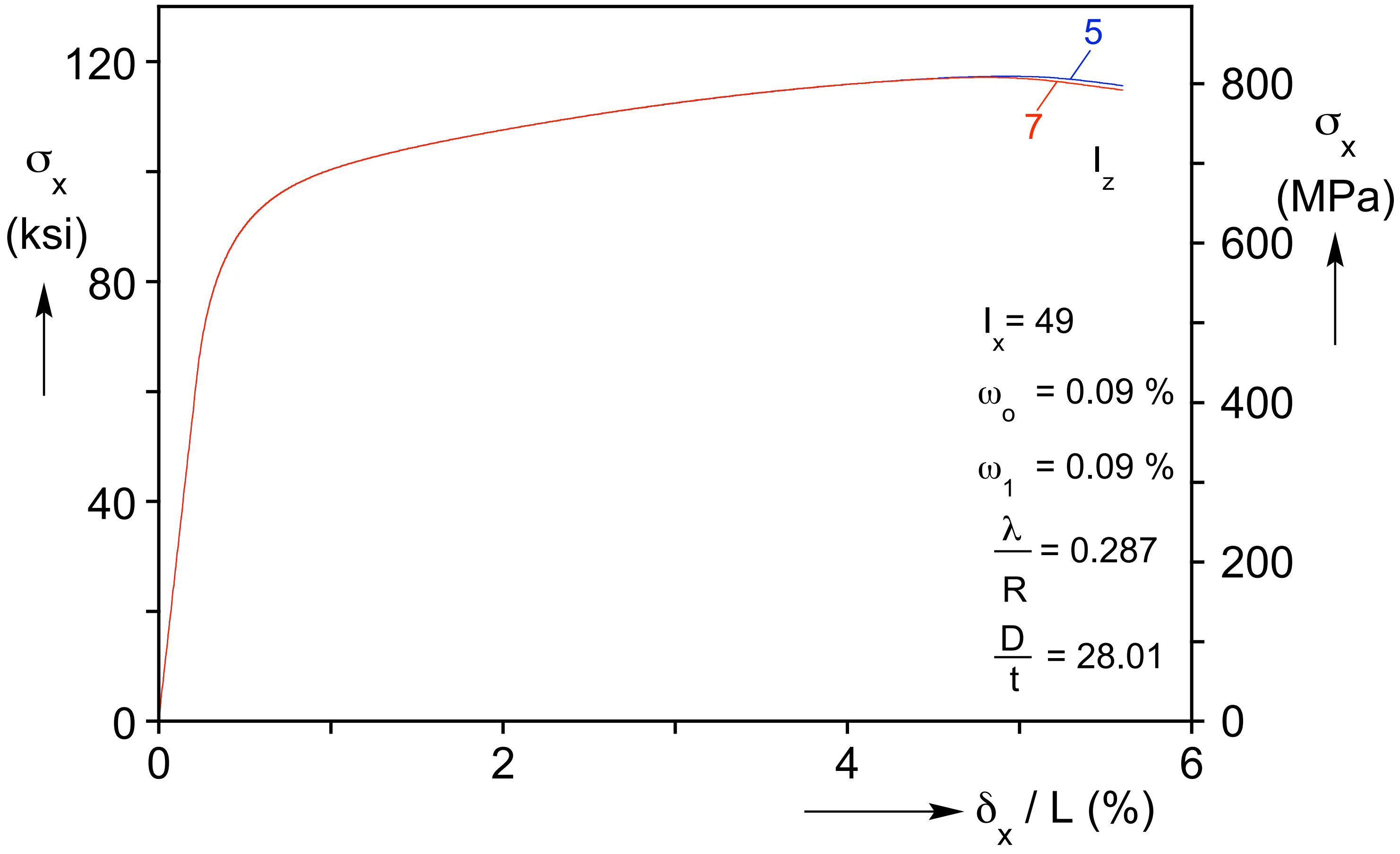

Fig. 6.2b Convergence study regarding the number of Gauss integration points in the thickness.

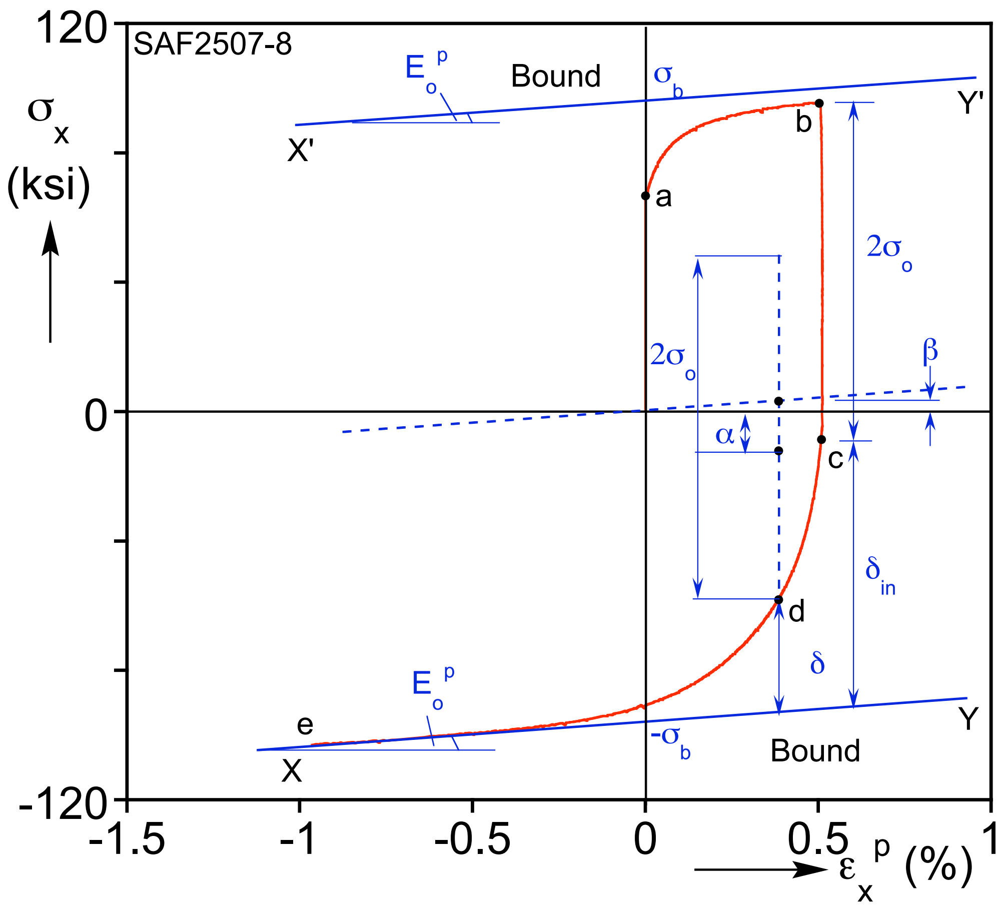

Fig. 6.3a Uniaxial stress-strain parameters for the Dafalias-Popov model.

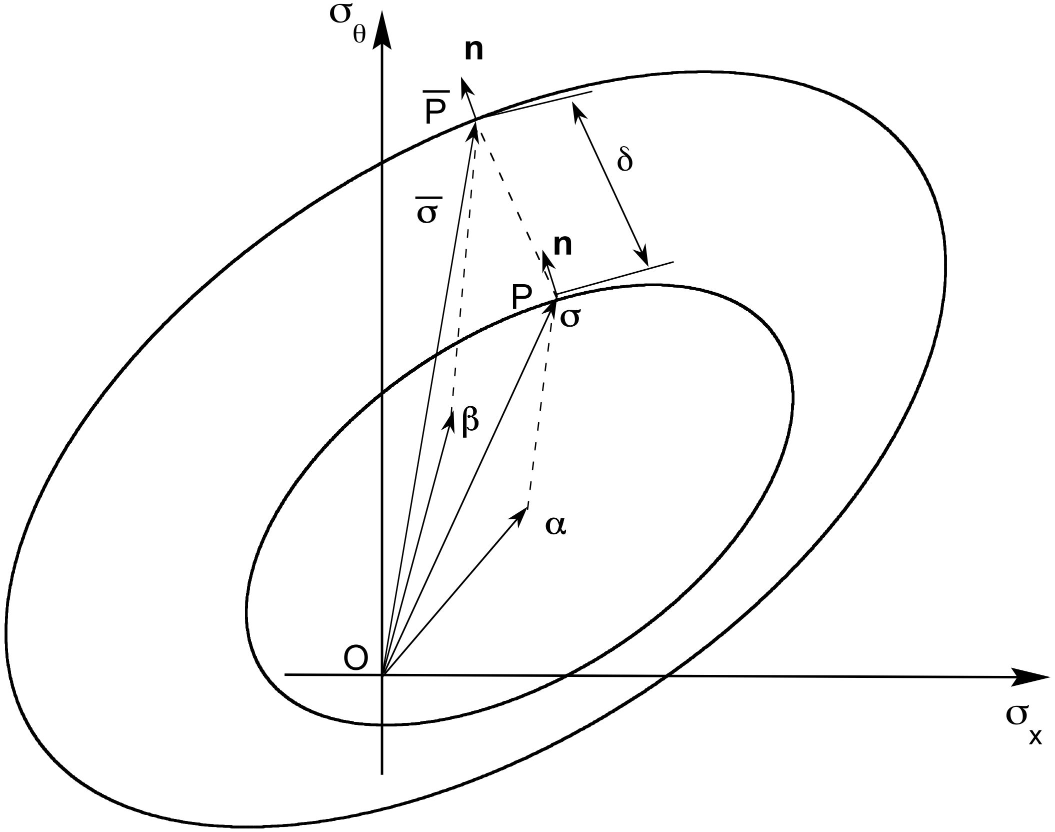

Fig. 6.3b Yield and bounding surfaces and associated variables of the Dafalias-Popov model.

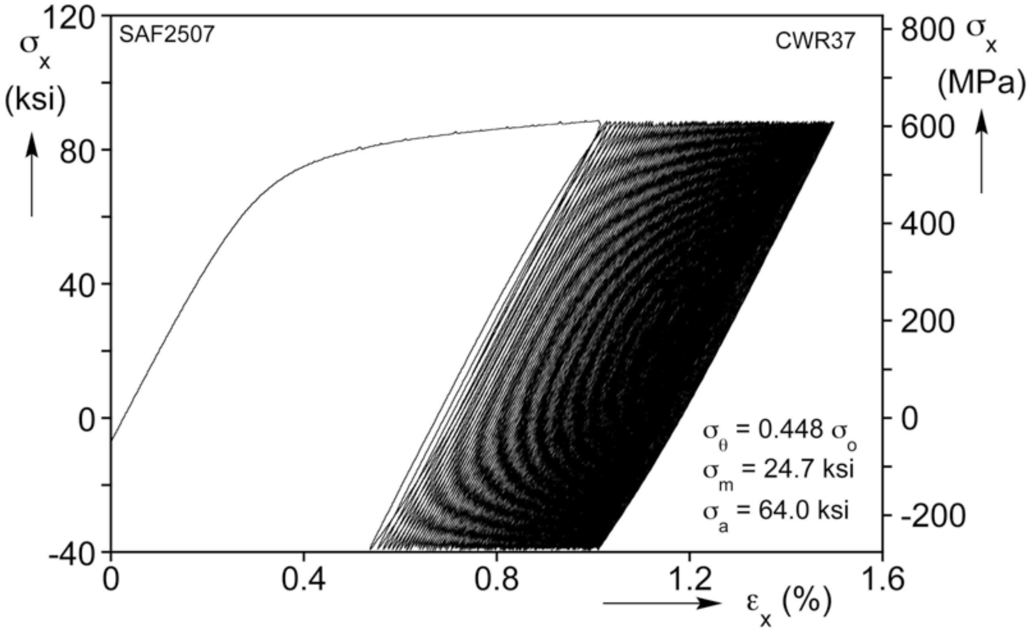

(a)

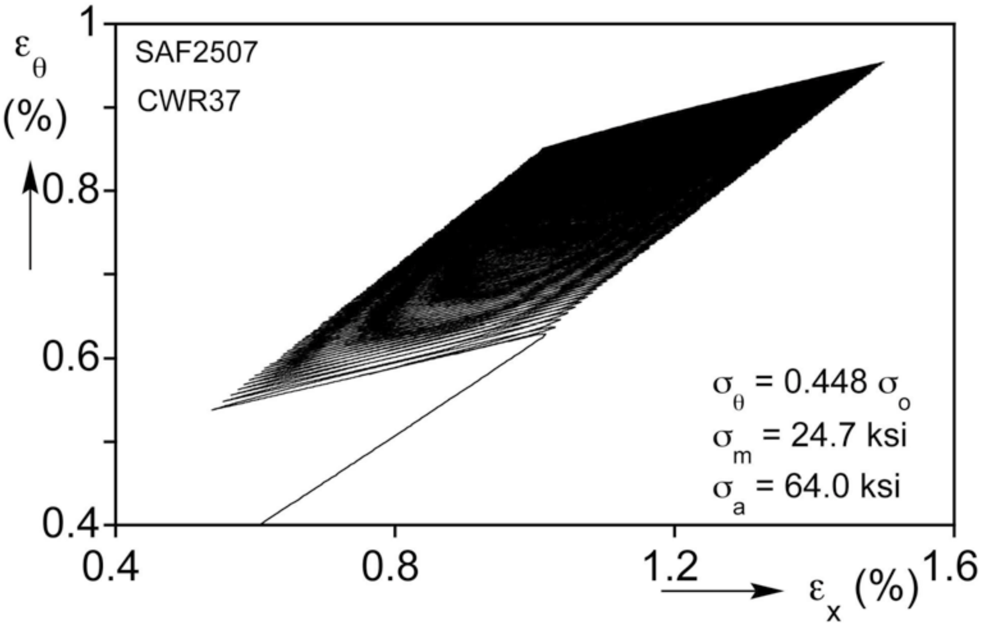

(b)

Fig. 6.4 Results from a biaxial ratcheting material test: (a) axial stress-strain response and (b) axial-circumferential strain response.

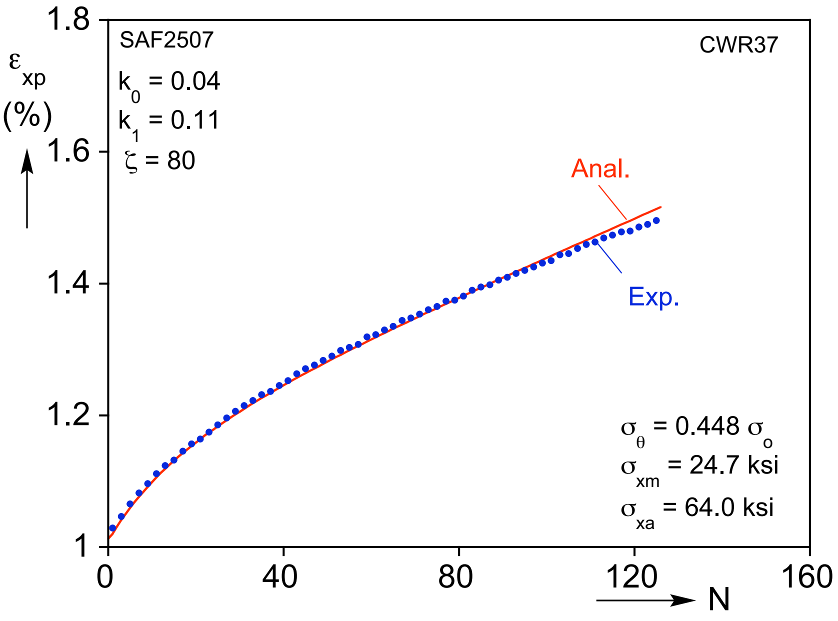

(a)

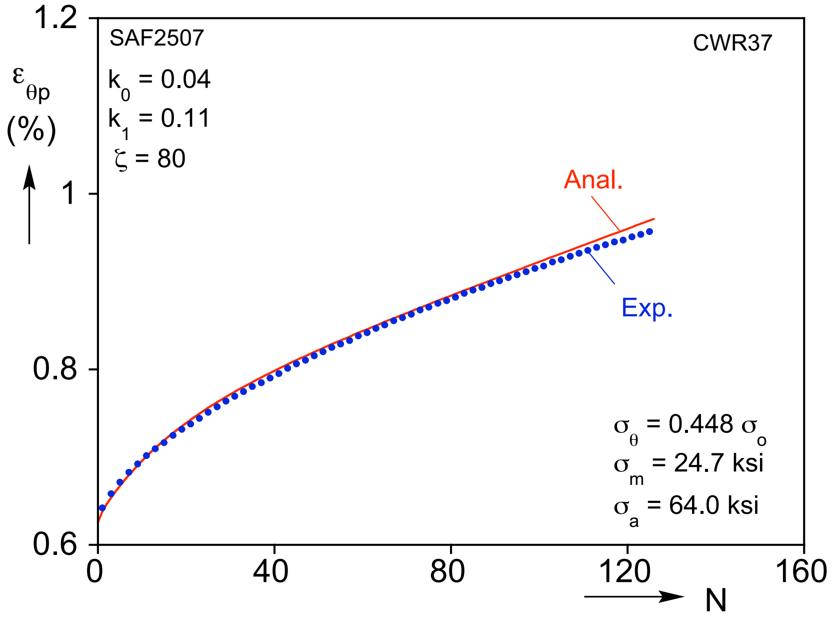

(b)

Fig. 6.5 (a) Comparison of measured and calculated peak axial strain vs. *N* and (b) peak circumferential strain vs. *N* responses.

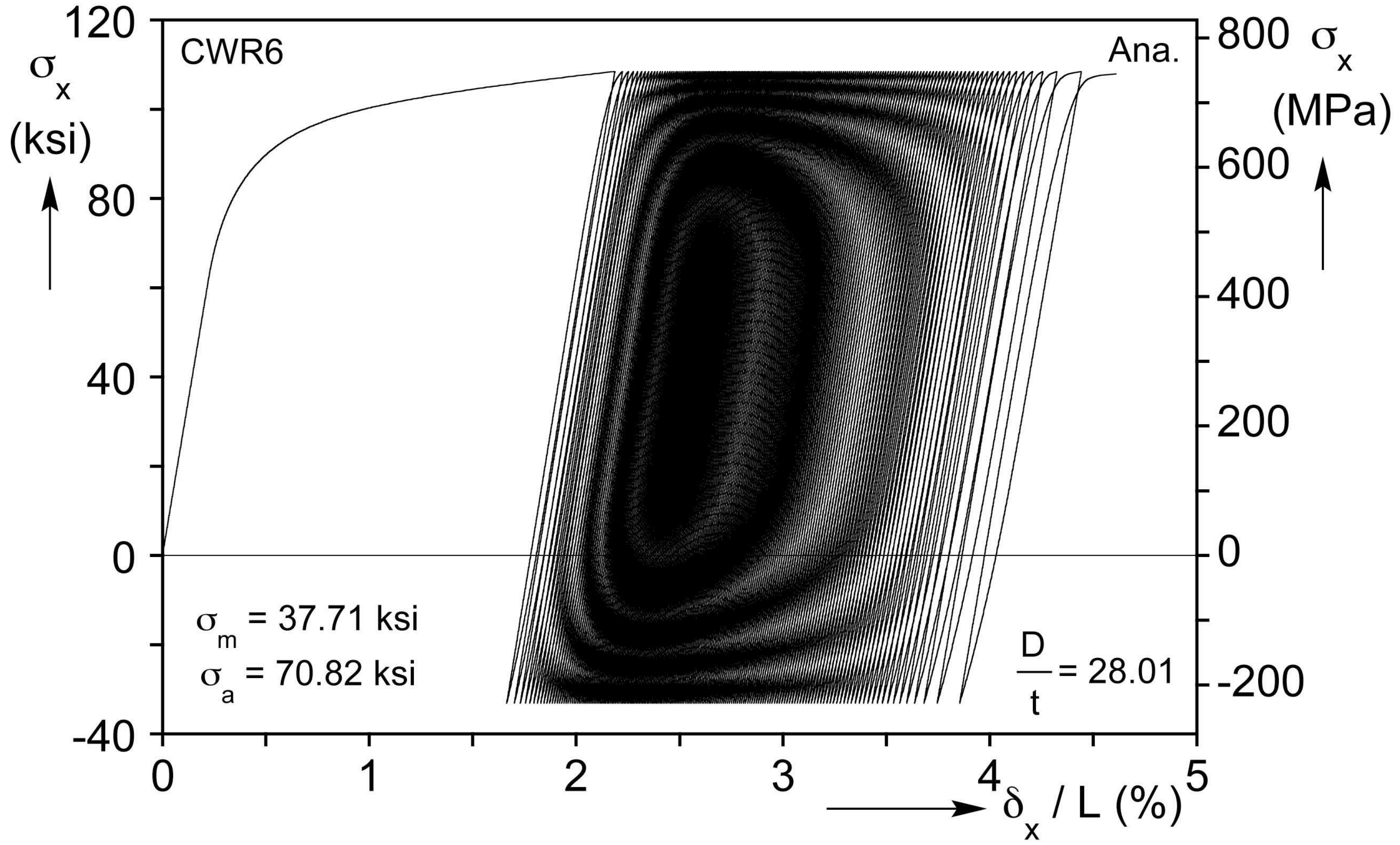

Fig. 7.1a Calculated axial stress-shortening response for CWR6.

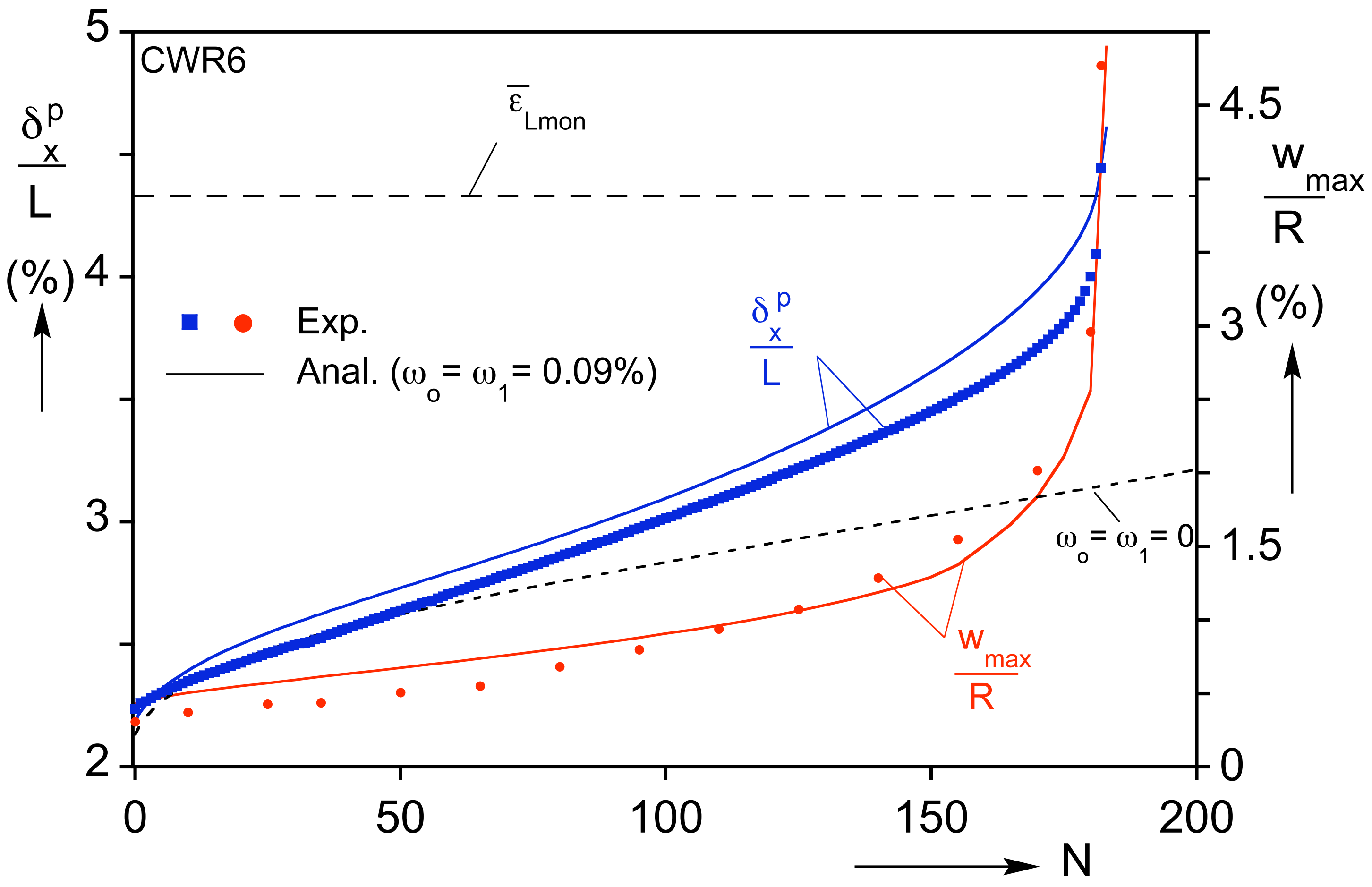

Fig. 7.1b Comparison of measured and calculated peak axial displacement vs. *N* and maximum radial displacement in wrinkles.

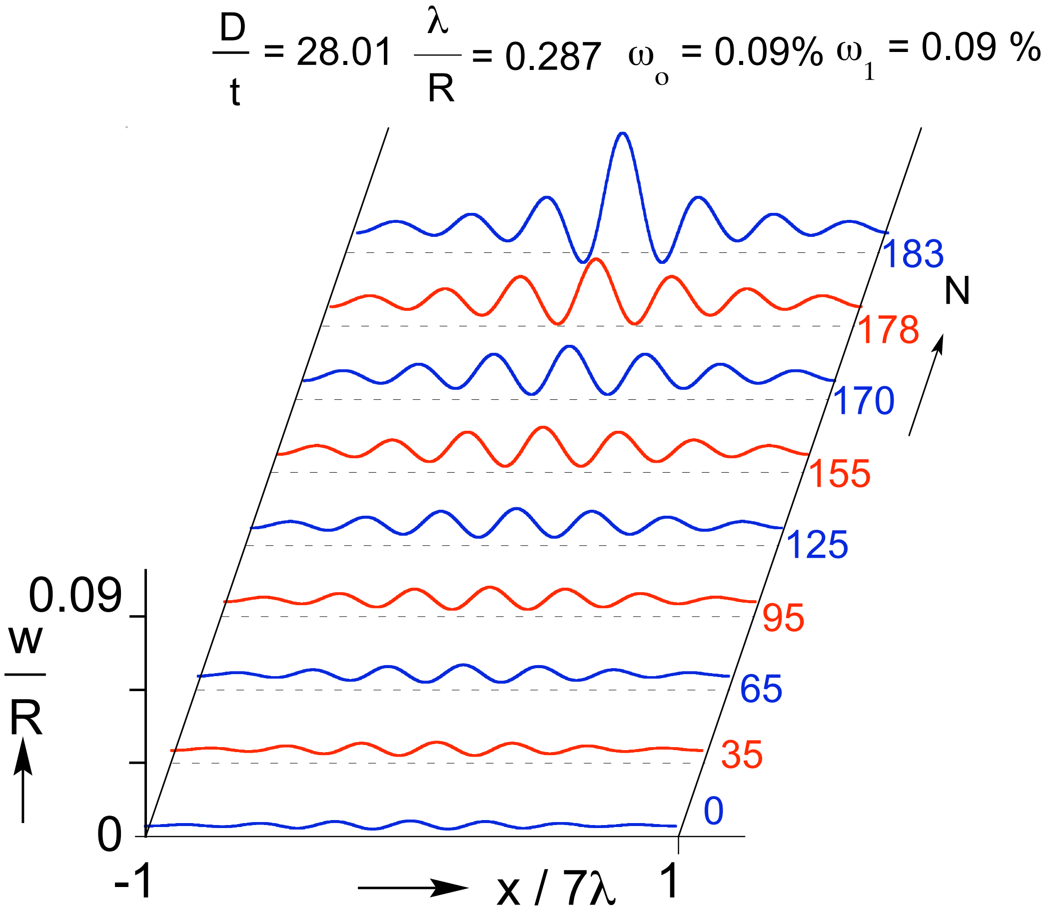

Fig. 7.2a Calculated radial displacement axial profiles after different number of cycles showing the growth and localization of wrinkles for CWR6.

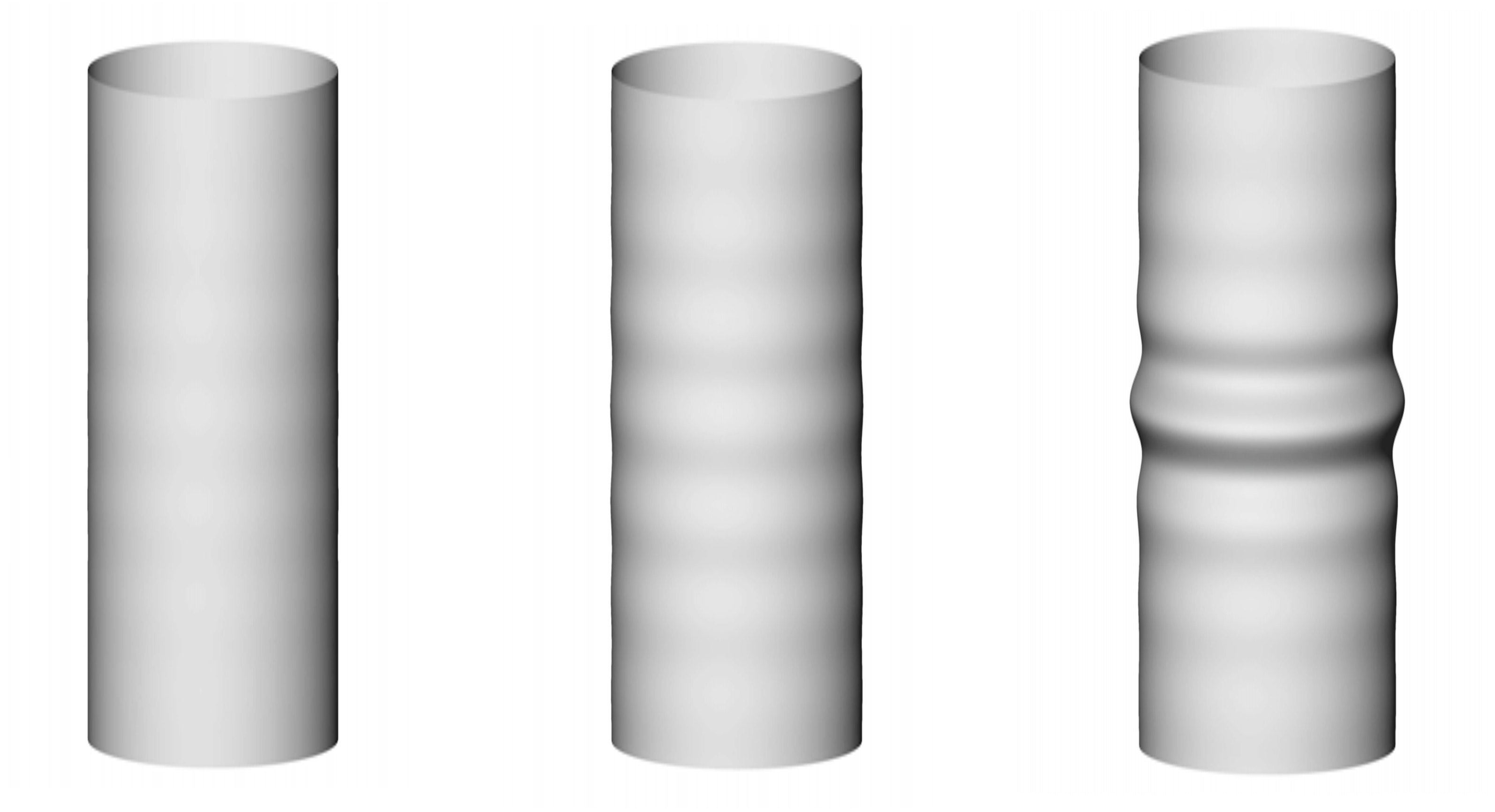

$N = 0$ $N = 150$ $N = 184$

Fig. 7.2b Tube deformed configurations at the onset of cycling, after 150 and 184 cycles.

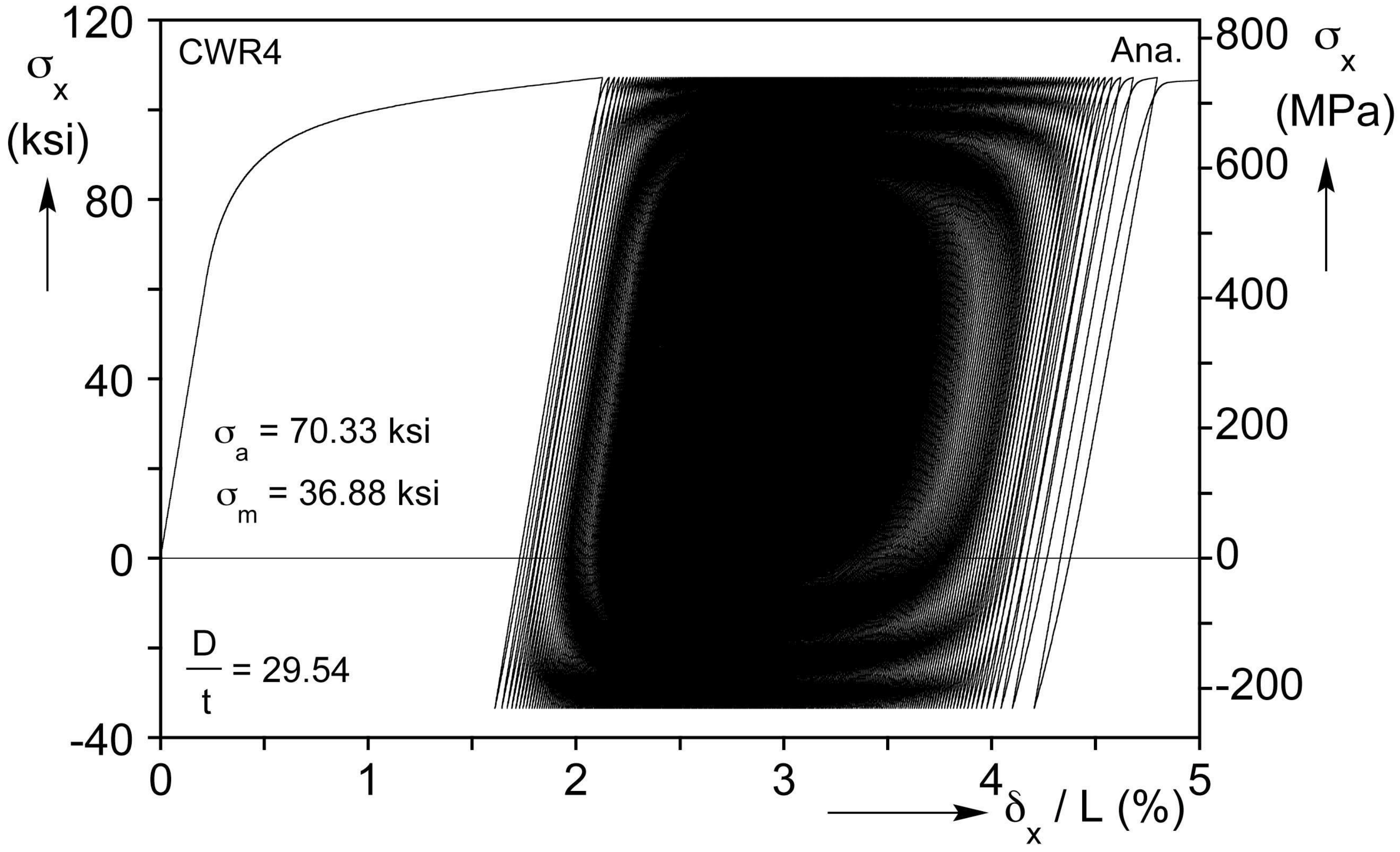

Fig. 7.3a Calculated axial stress-shortening response for CWR4.

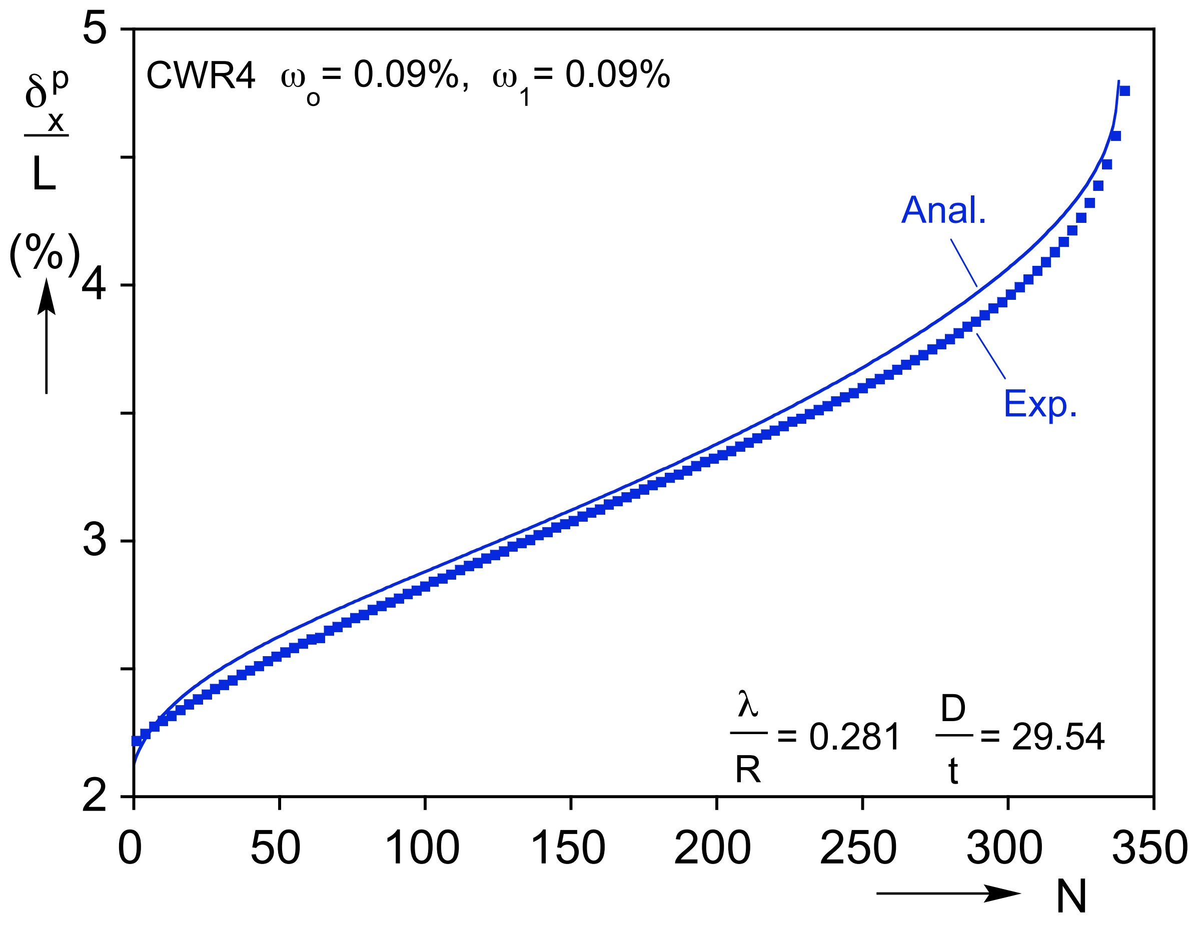

Fig. 7.3b Comparison of measured and calculated peak axial displacement vs. *N*.

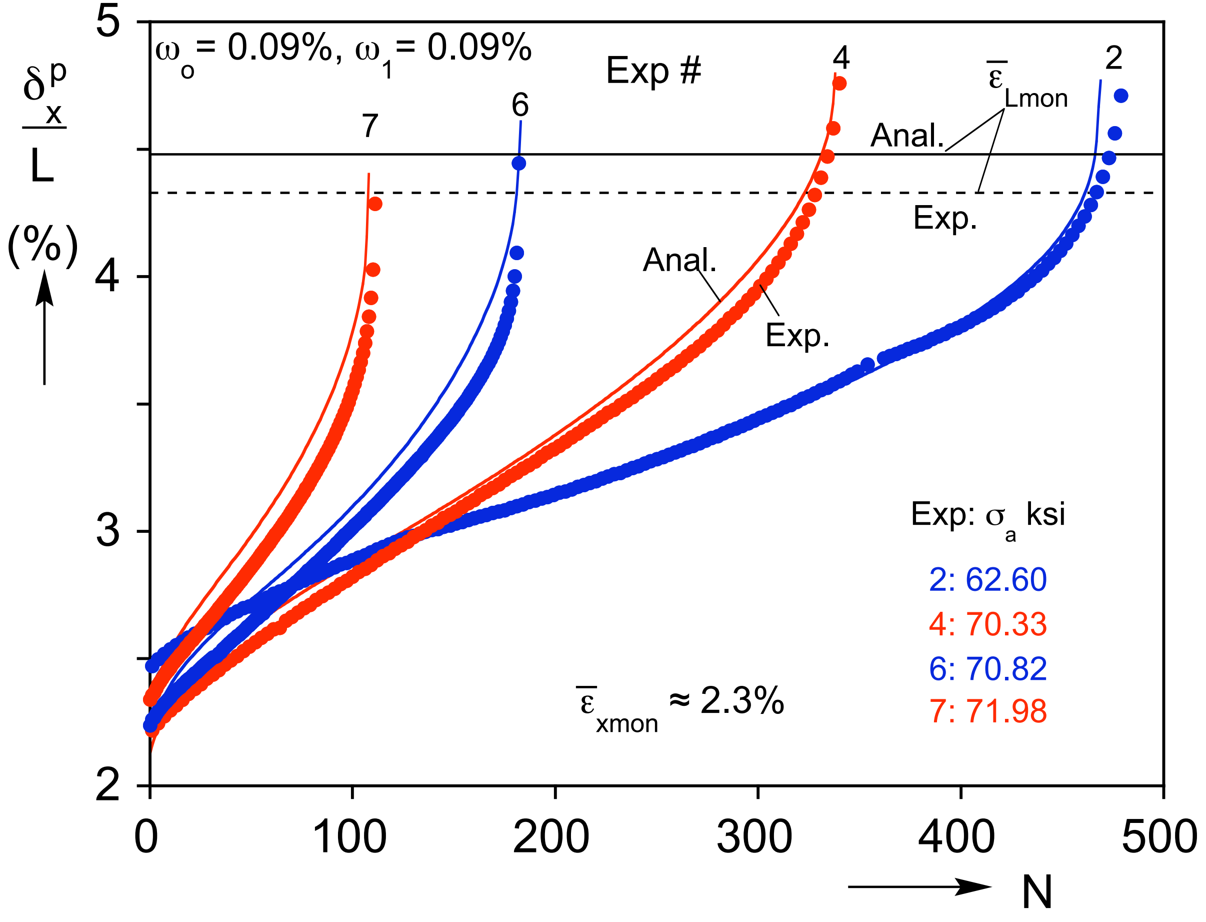

Fig. 7.4 Comparison of measured and calculated peak displacements vs. *N* from four experiments with approximately the same initial pre-straining.

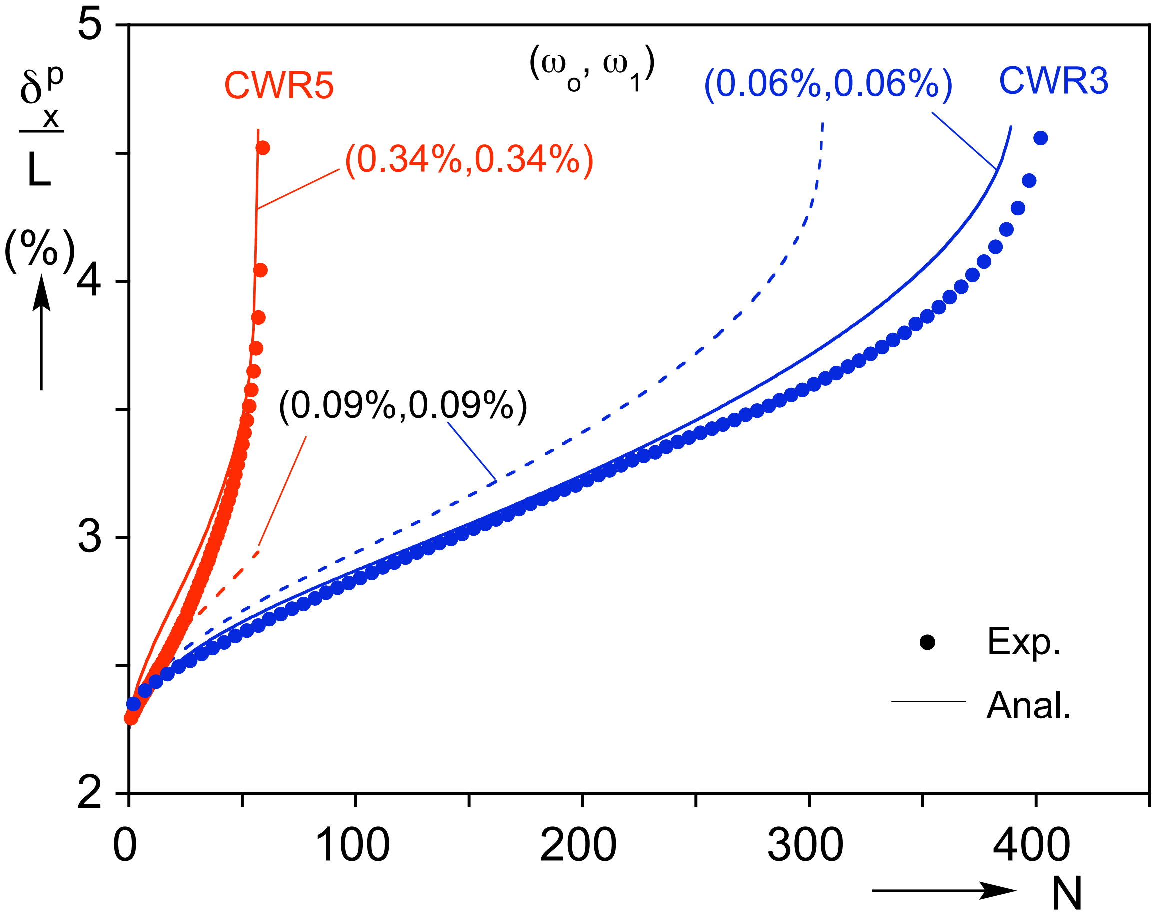

Fig. 7.5 Comparison of measured and calculated peak displacement vs. N from two experiments with approximately the same initial pres-straining. The imperfection parameters used in the simulations were different from those used in Fig. 7.4.

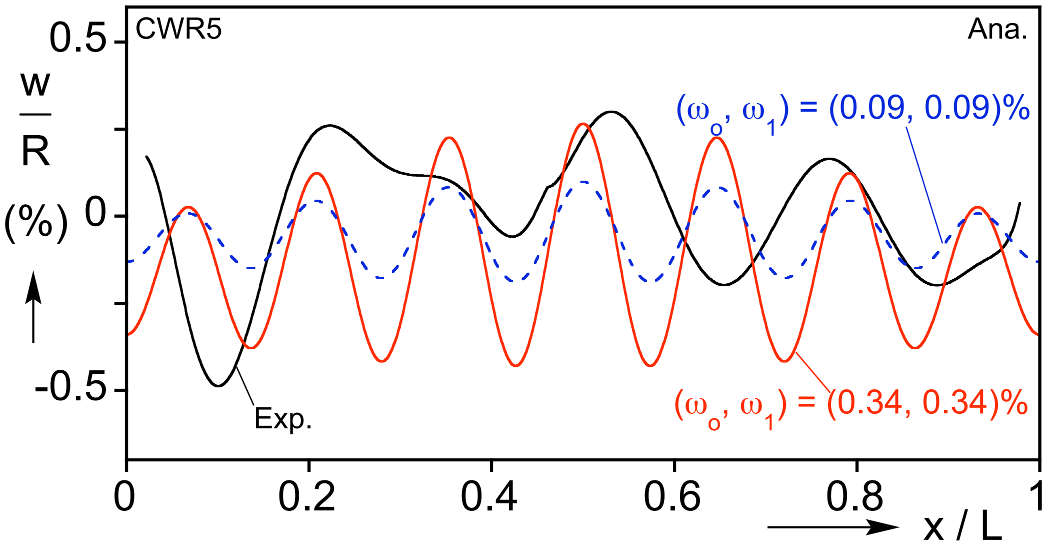

(a)

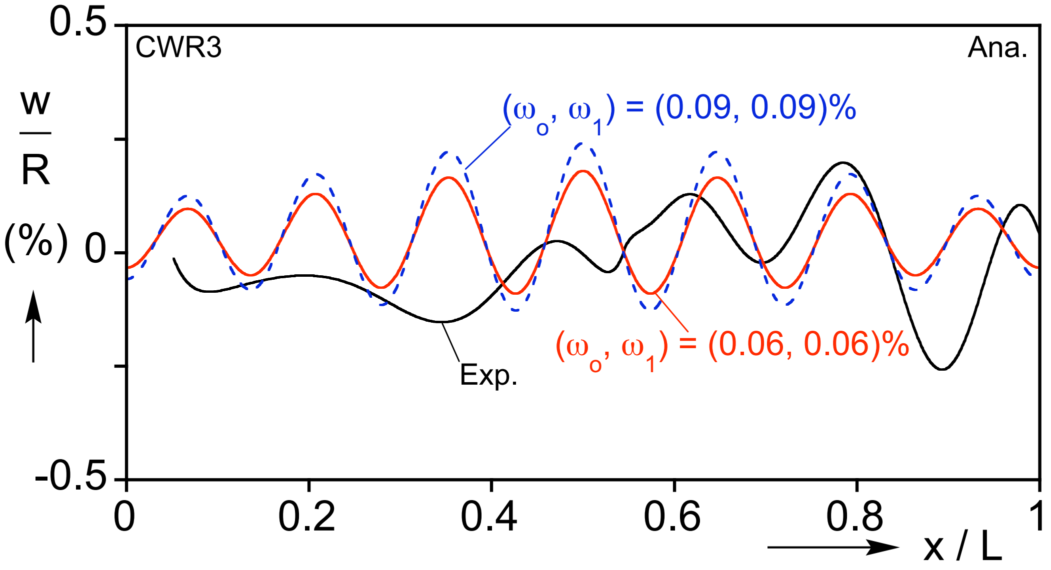

(b)

Fig. 7.6 Comparison of measured and calculated wrinkle profiles at the end of the monotonic loading with different initial imperfections for (a) CWR5 and (b) CWR3.

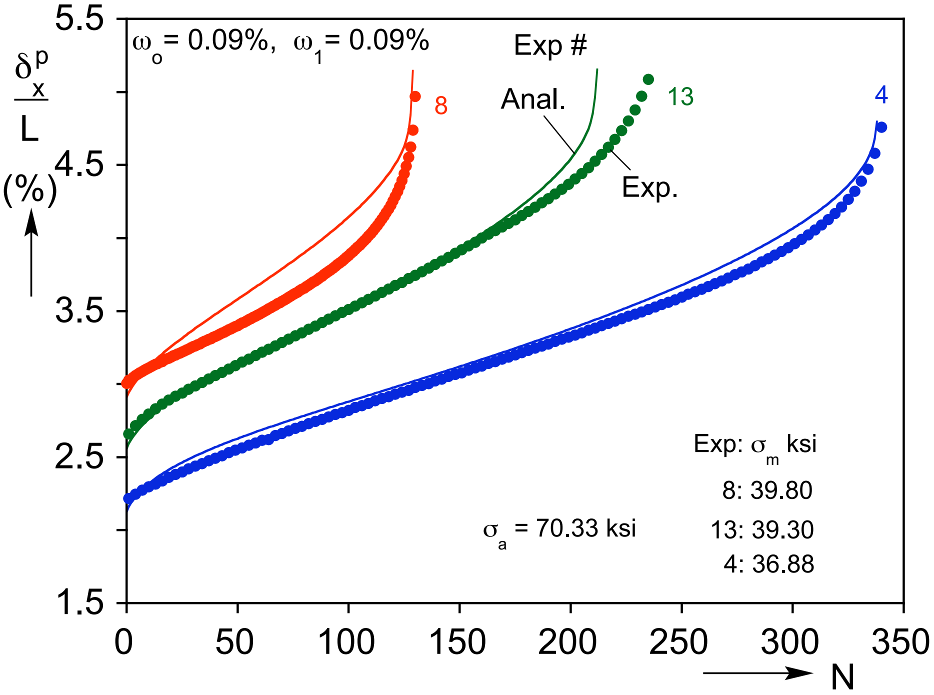

(a)

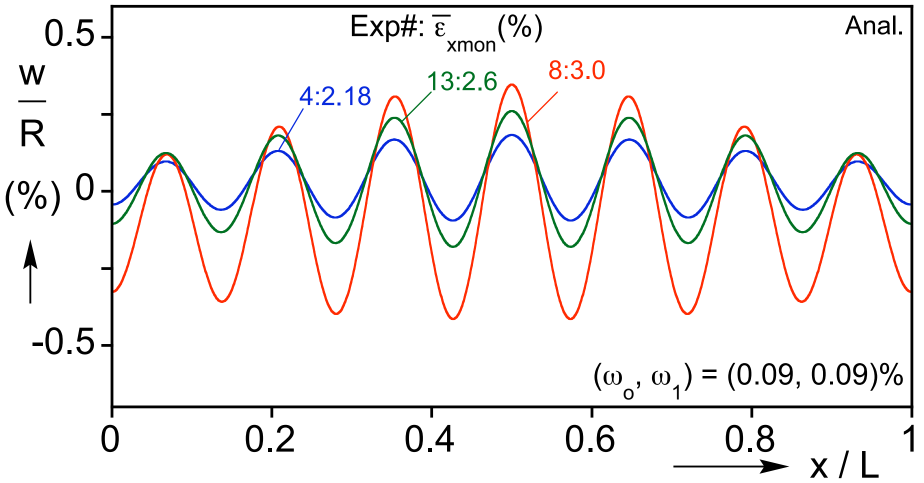

(b)

Fig. 7.7 (a) Comparison of measured and calculated peak displacement vs. *N* from three experiments with different initial pres-straining and the same stress cycle amplitude. (b) Calculated wrinkles at the end of the monotonic loading showing the effects of pre-straining.

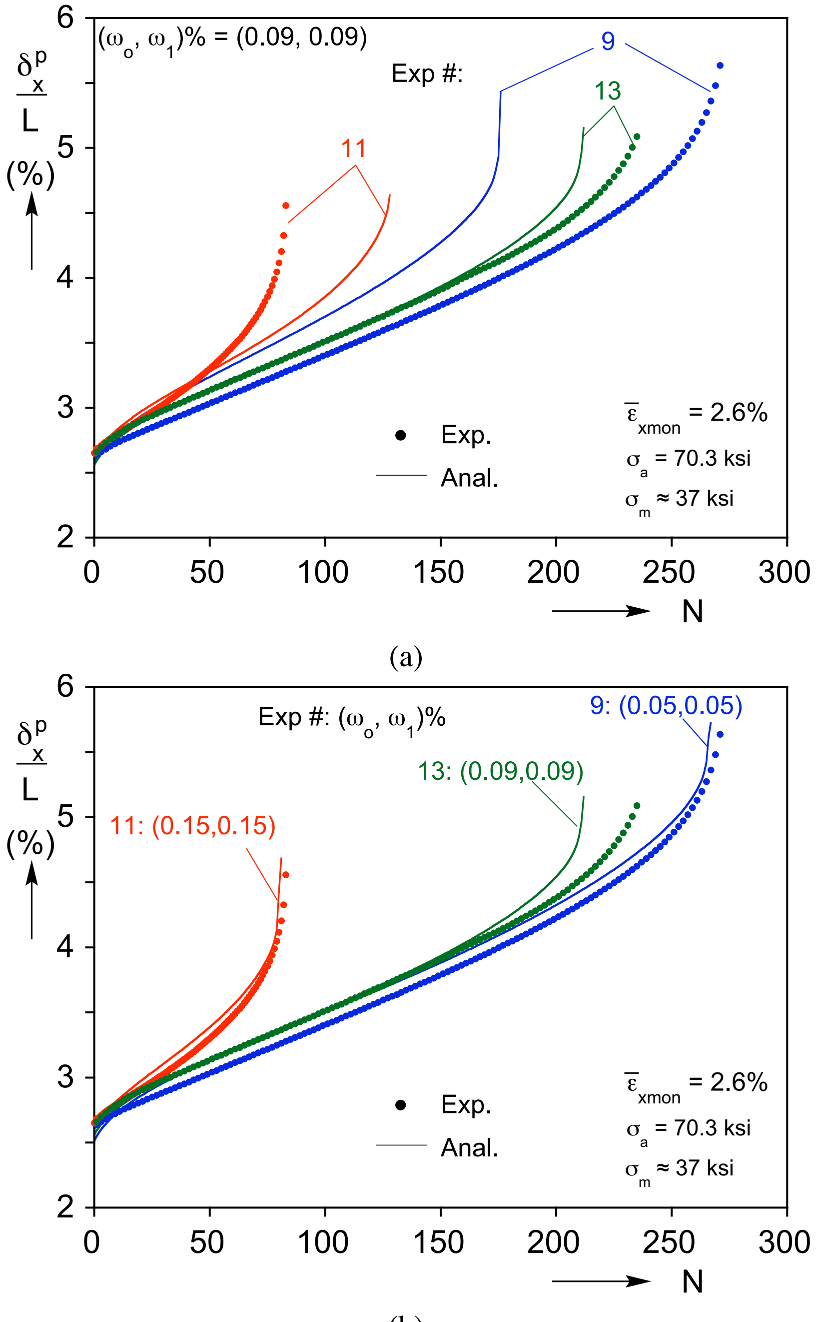

Fig. 7.8 Comparison of measured and calculated peak displacement vs. *N* from three experiments with the same initial pre-straining and stress cycle parameters. (a) Predictions for the basic imperfection amplitude and (b) predictions for customized imperfection amplitudes.

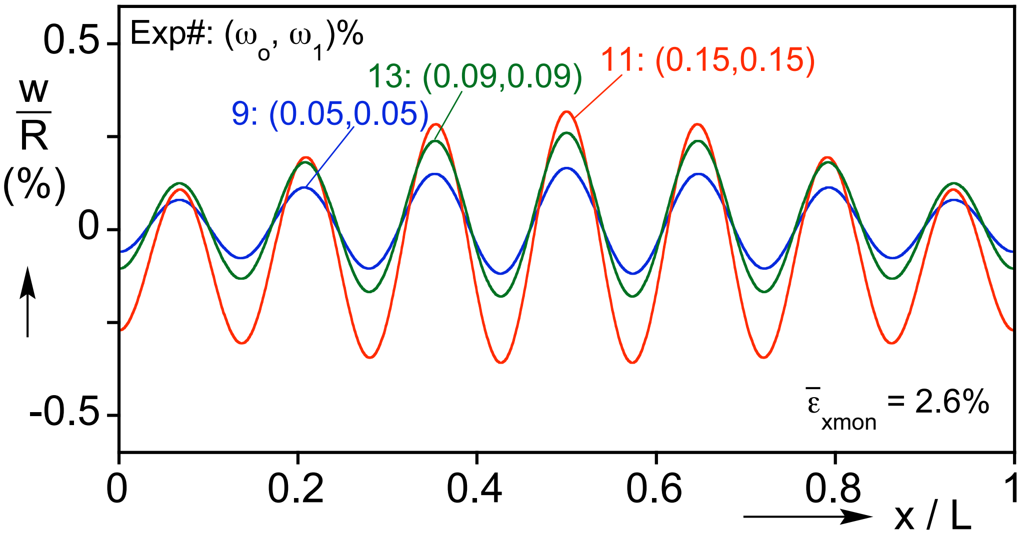

Fig. 7.9 Calculated wrinkles at the end of the monotonic loading showing the effects of initial imperfections. The maximum wrinkle amplitudes are comparable to the experimental results in Fig. 3.8b.

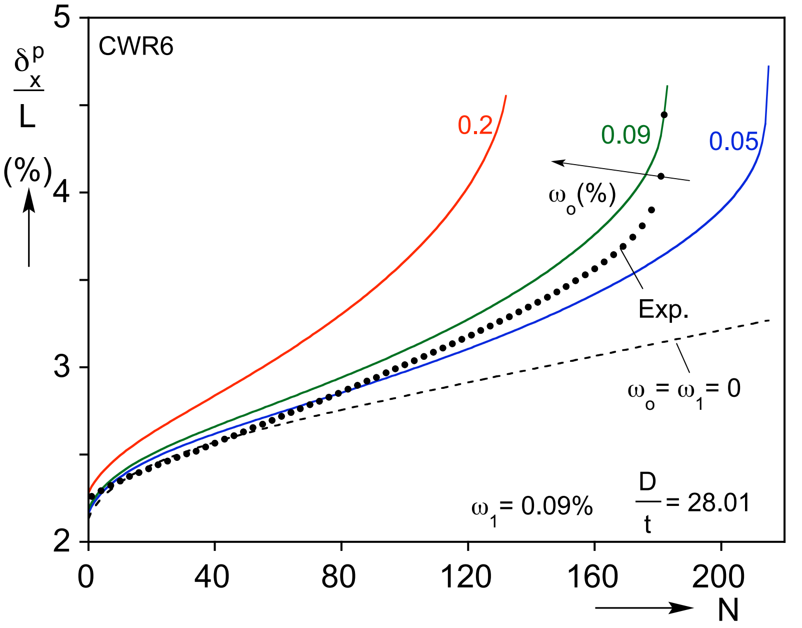

(a)

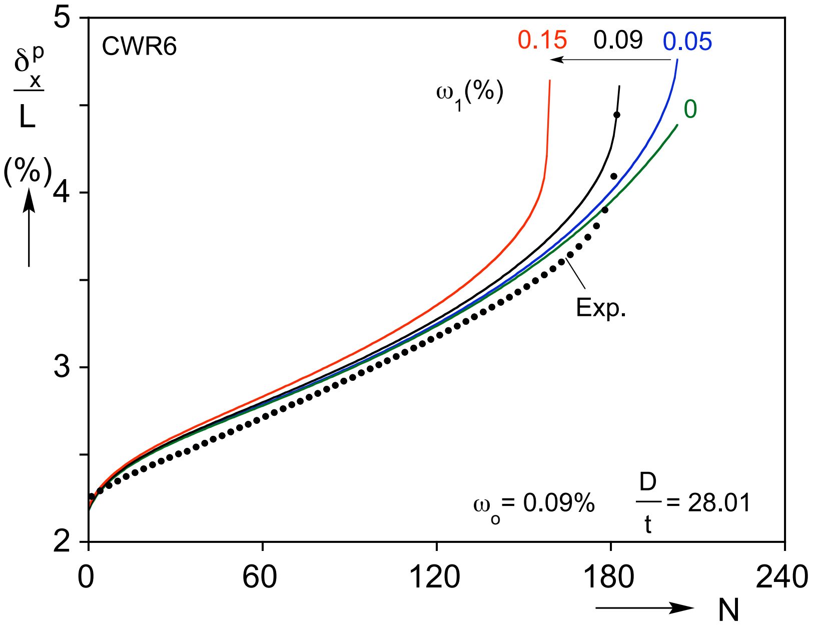

(b)

Fig. 7.10 Effect of imperfection parameters on calculated $\delta_x^p - N$ ratcheting response. (a) Variation of ω_o and (b) variation of ω_1.

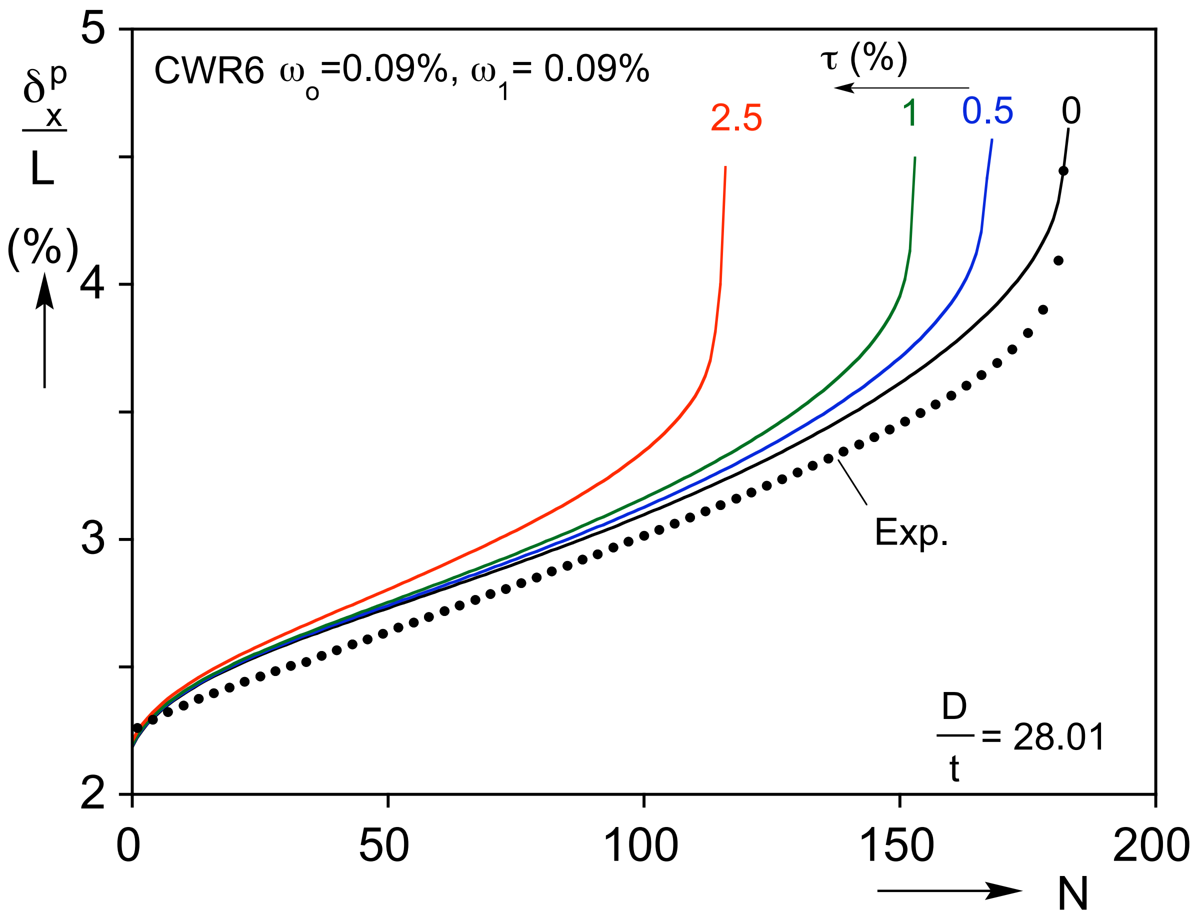

Fig. 7.11 Effect of thickness variation along the tube length on calculated $\delta_x^p - N$ ratcheting response.

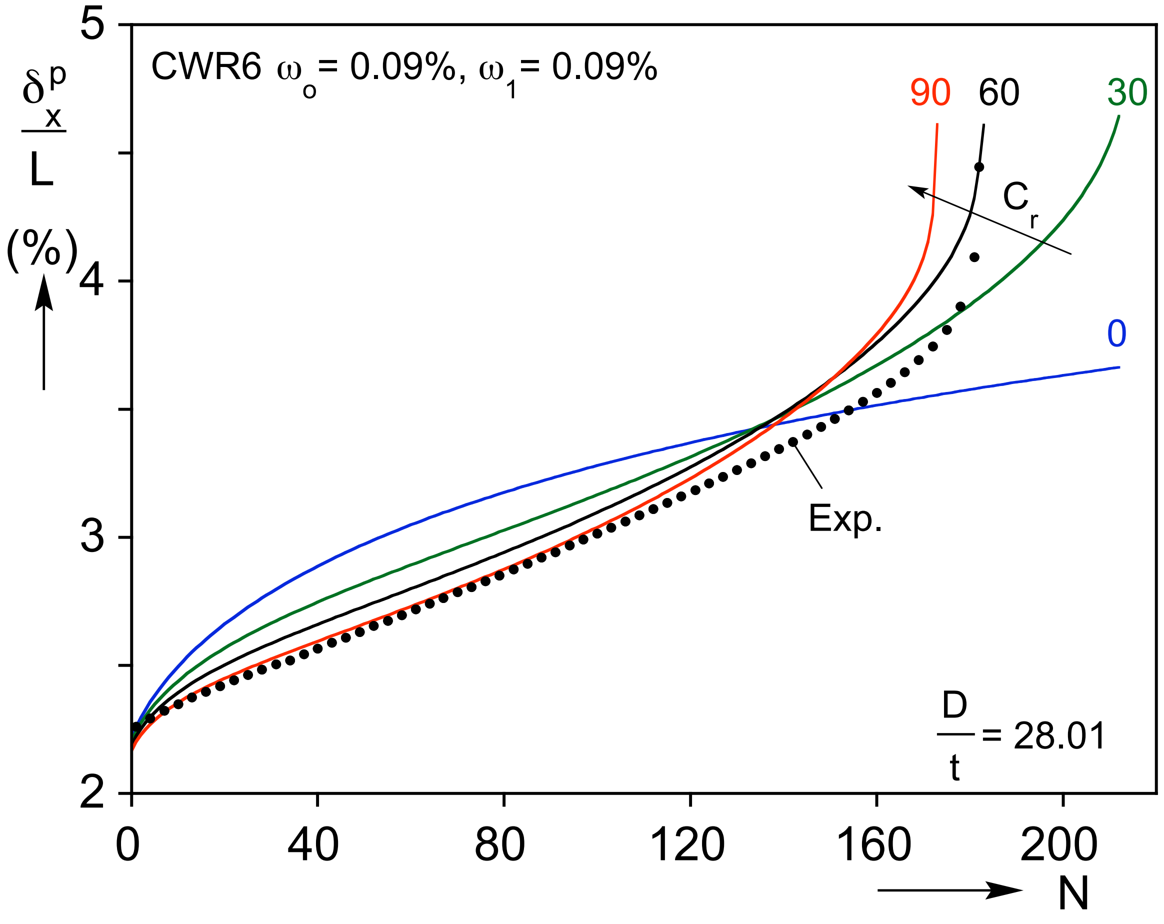

Fig. 7.12 Effect of relaxation coefficient C_r on calculated $\delta_x^p - N$ ratcheting response.

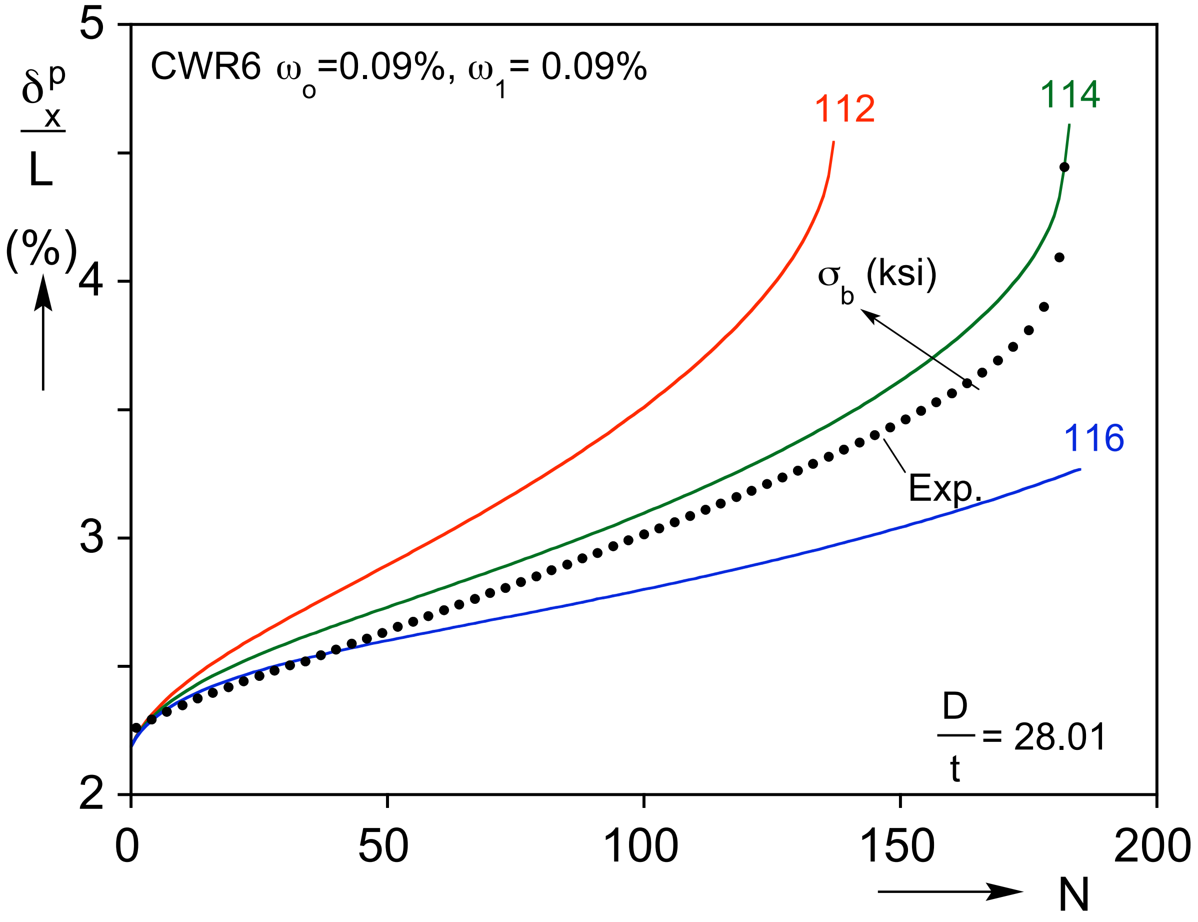

Fig. 7.13 Effect of bounding surface size σ_b on calculated $\delta_x^p - N$ ratcheting response.

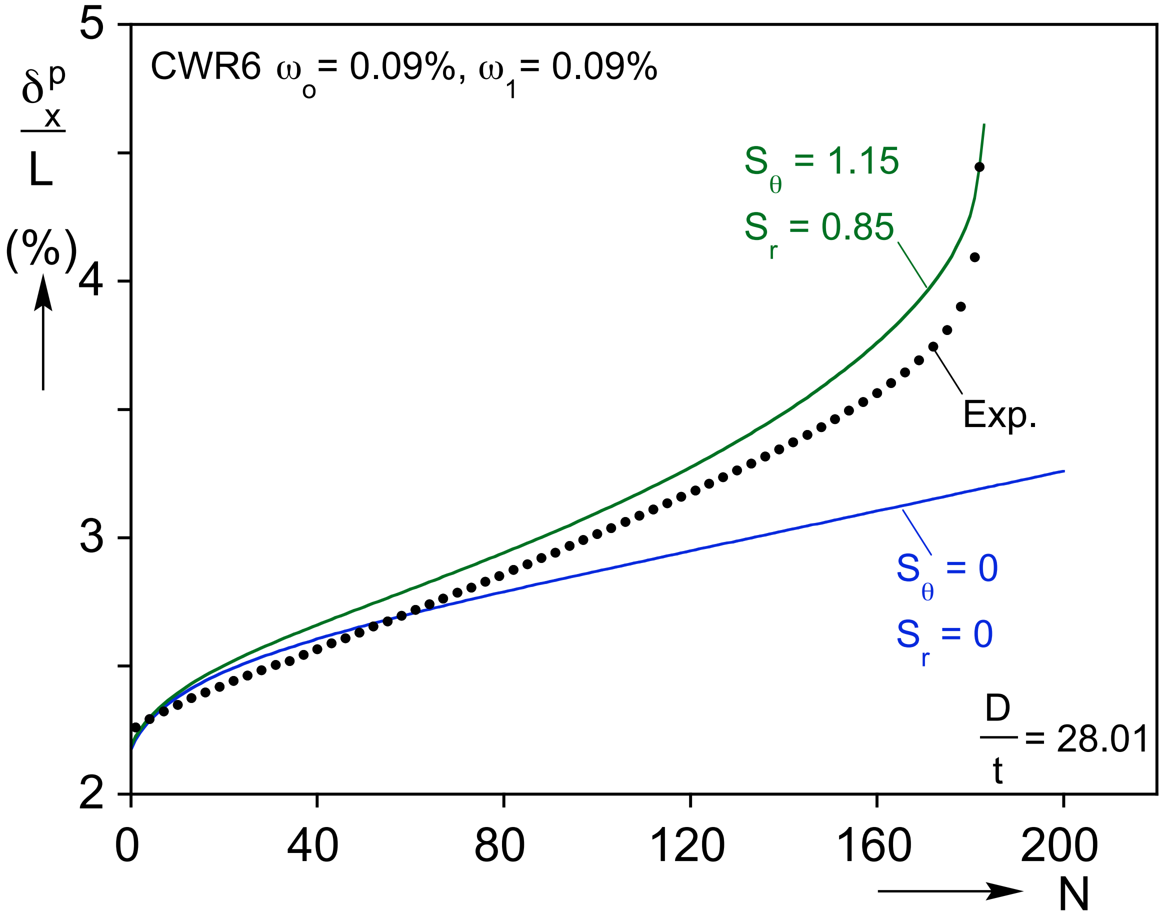

Fig. 7.14 Effect of anisotropy on calculated $\delta_x^p - N$ ratcheting response.

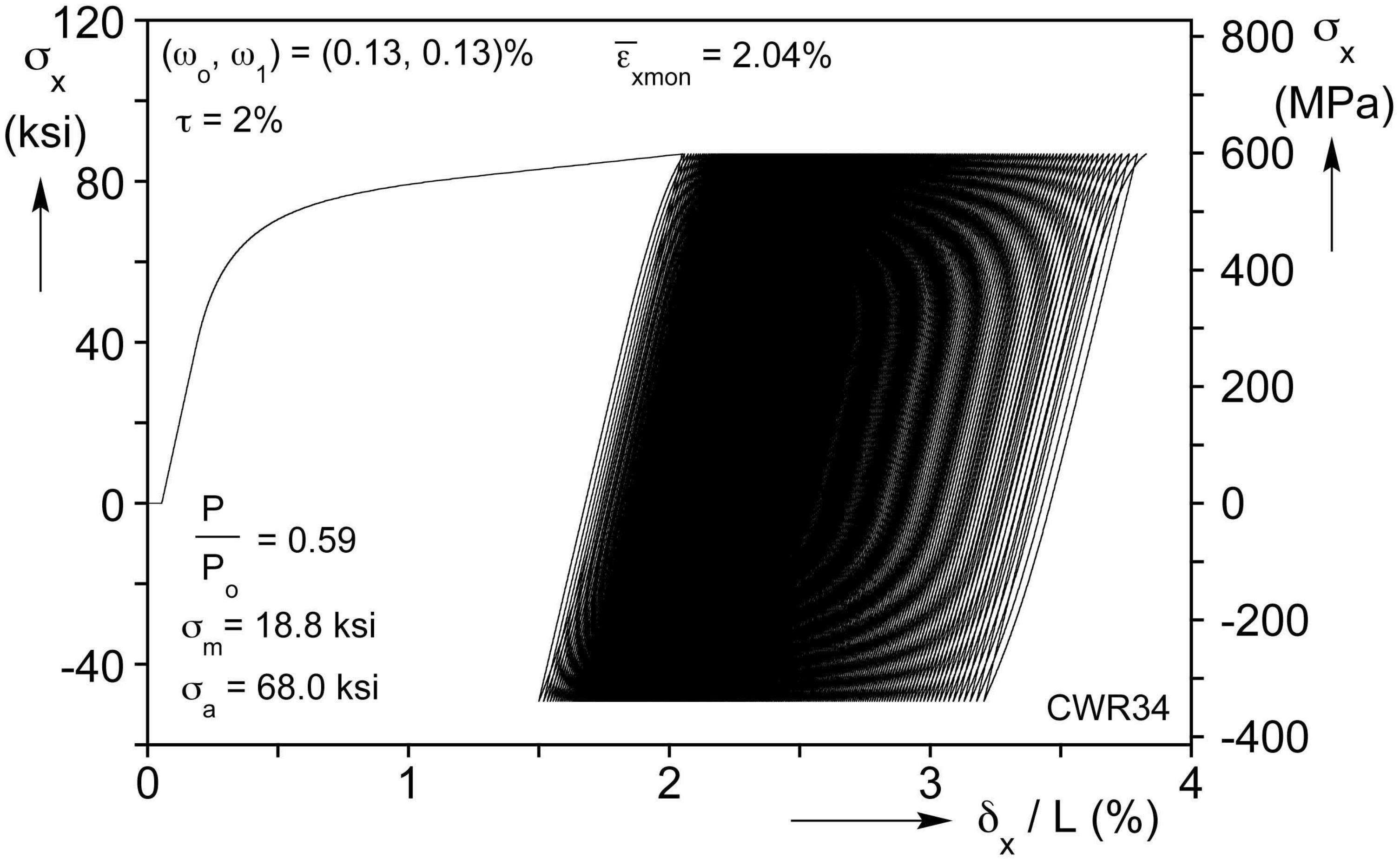

Fig. 8.1a Calculated axial stress-shortening response for CWR34.

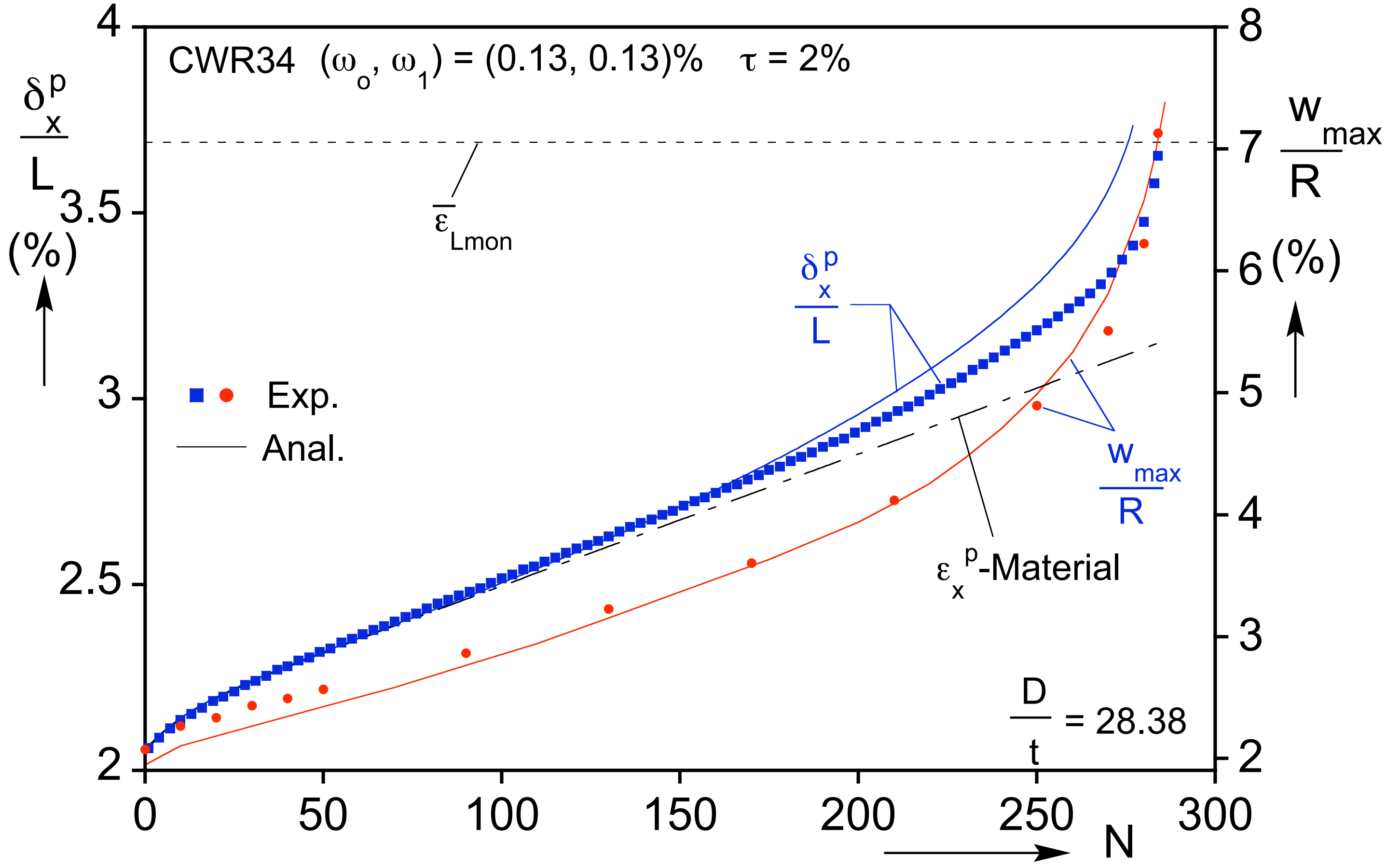

Fig. 8.1b Comparison of measured and calculated peak axial displacement and maximum radial displacement vs. *N* for CWR34.

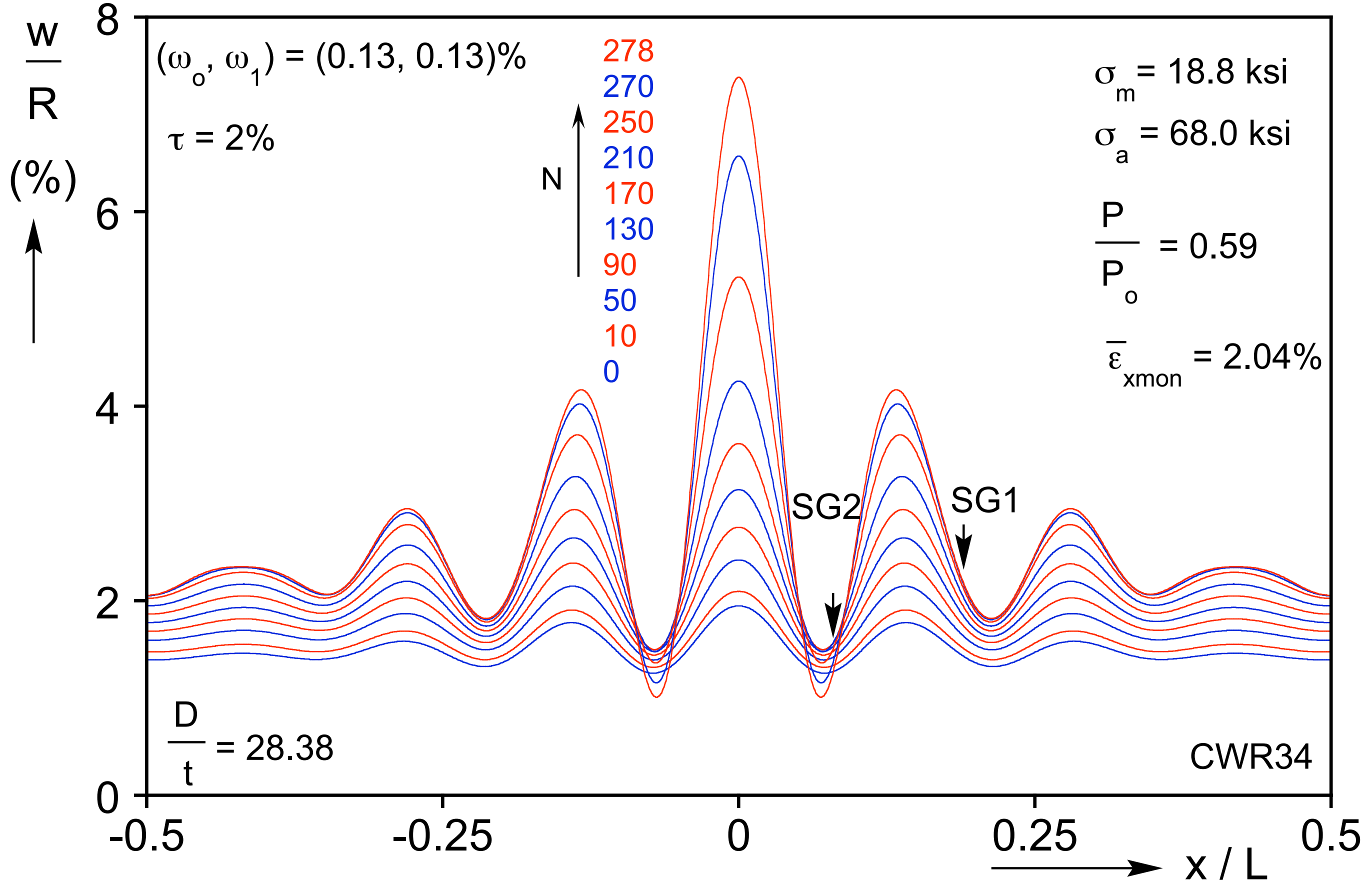

Fig. 8.2a Calculated radial displacement axial profiles after different number of cycles showing the growth and localization of wrinkles for CWR34.

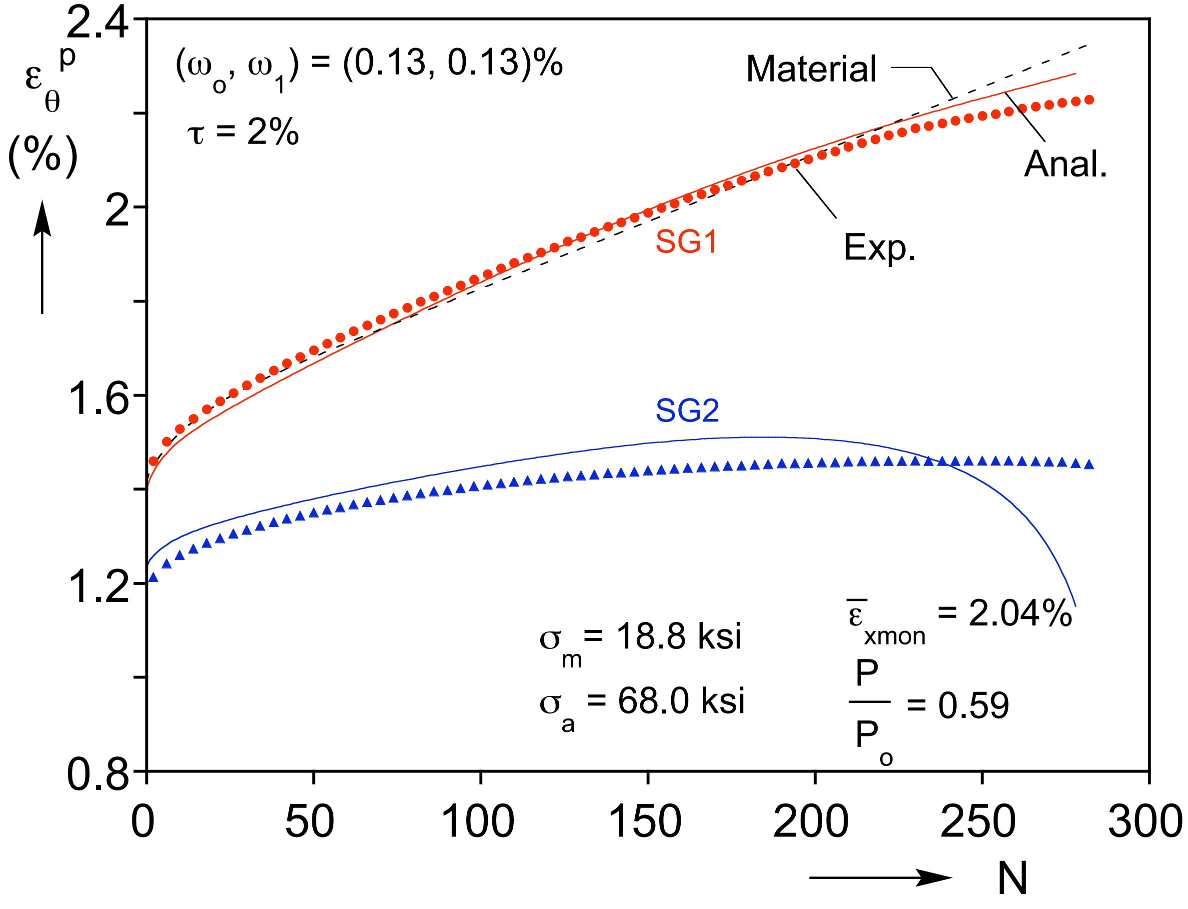

Fig. 8.2b Comparison of measured and calculated peak circumferential strains at two locations on the test section vs. *N* for CWR34.

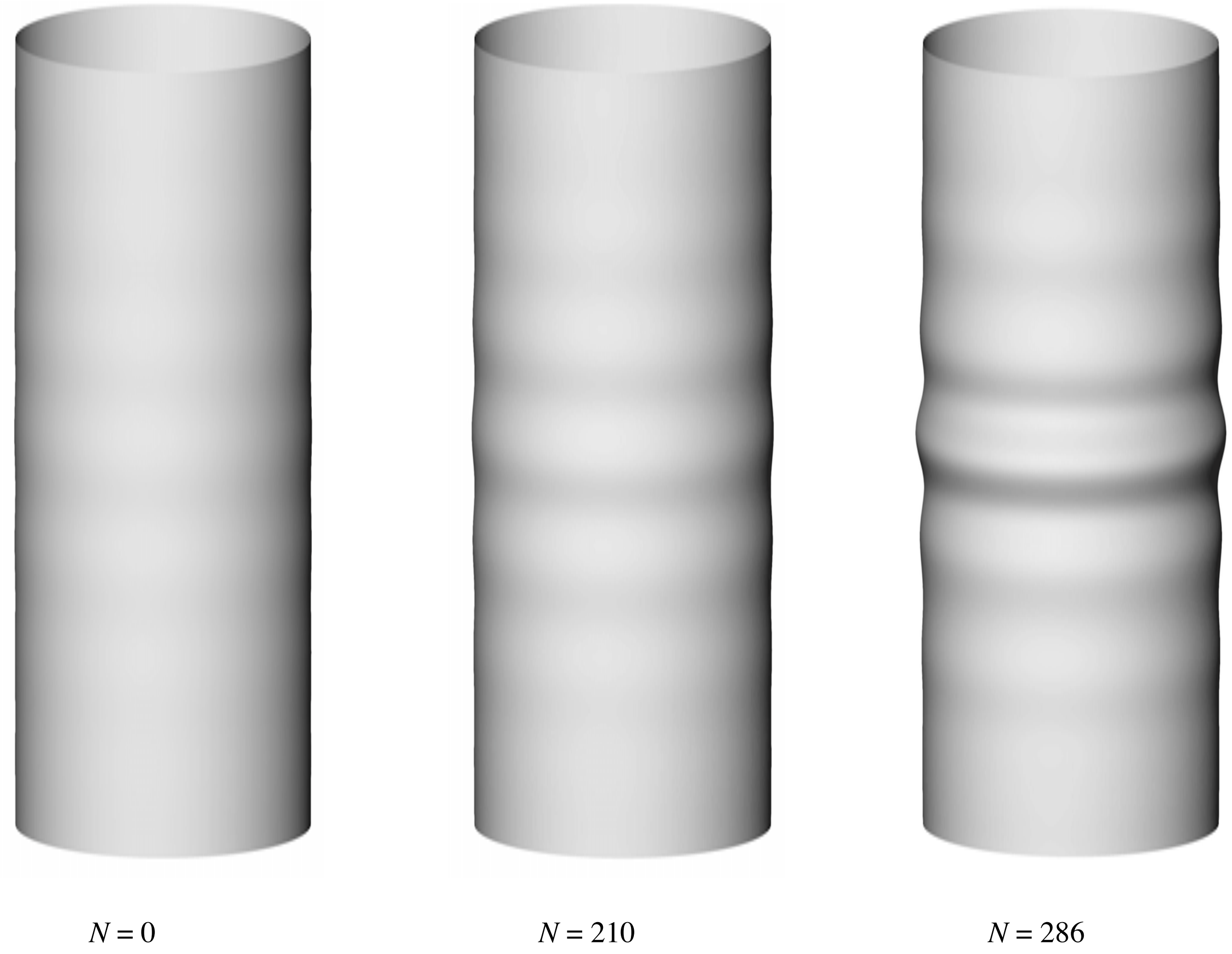

Fig. 8.3 Tube deformed configurations at the onset of cycling, after 210 and 286 cycles.

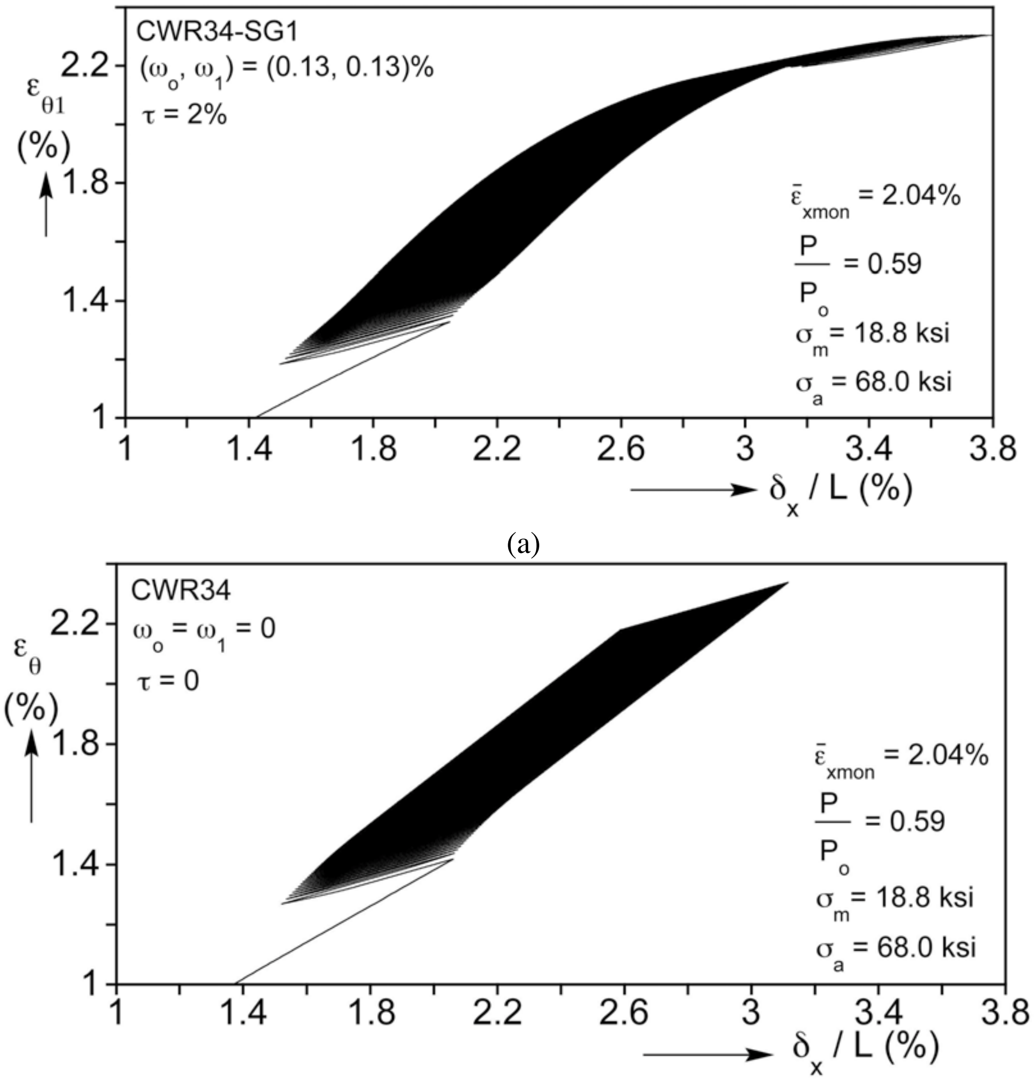

(a)

(b)

Fig. 8.4 (a) Calculated axial-circumferential strain response for CWR34 and (b) corresponding material response for the same cyclic loading history.

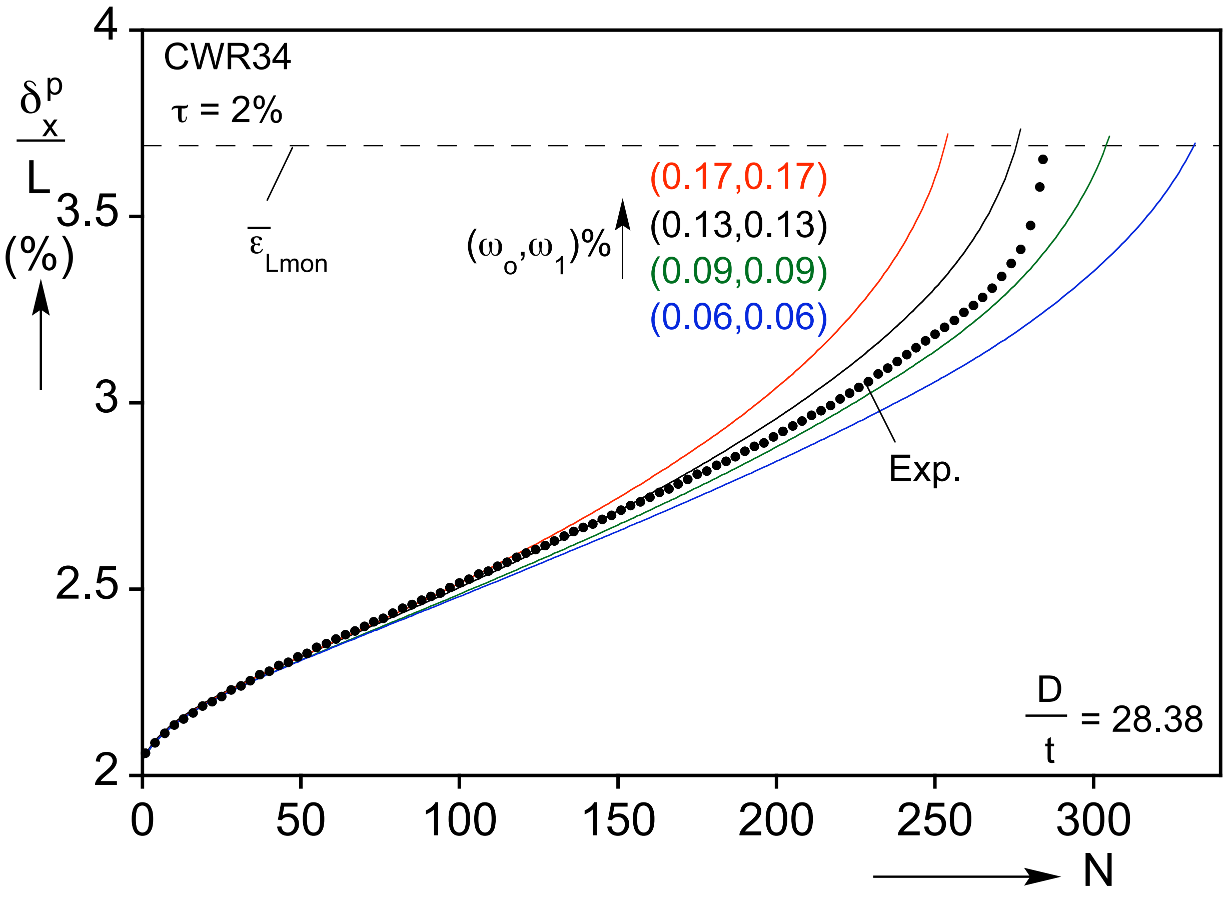

Fig. 8.5 Effect of imperfection amplitudes on calculated $\delta_x^p / L - N$ ratcheting plot for CWR34.

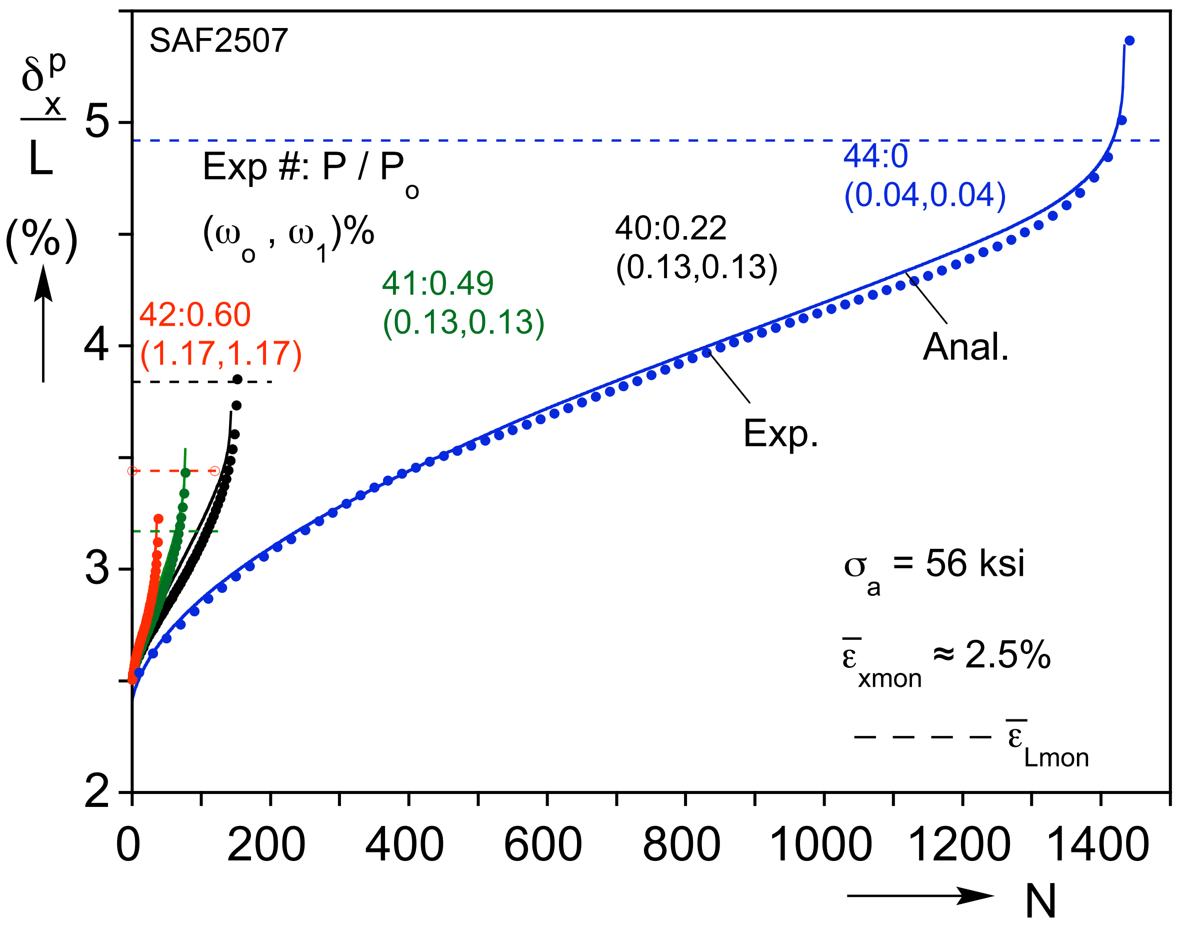

Fig. 8.6 Comparison of measured and calculated $\delta_x^p / L - N$ responses for four experiments cycled under different pressure levels but with the same initial pre-strain and stress cycle amplitude.

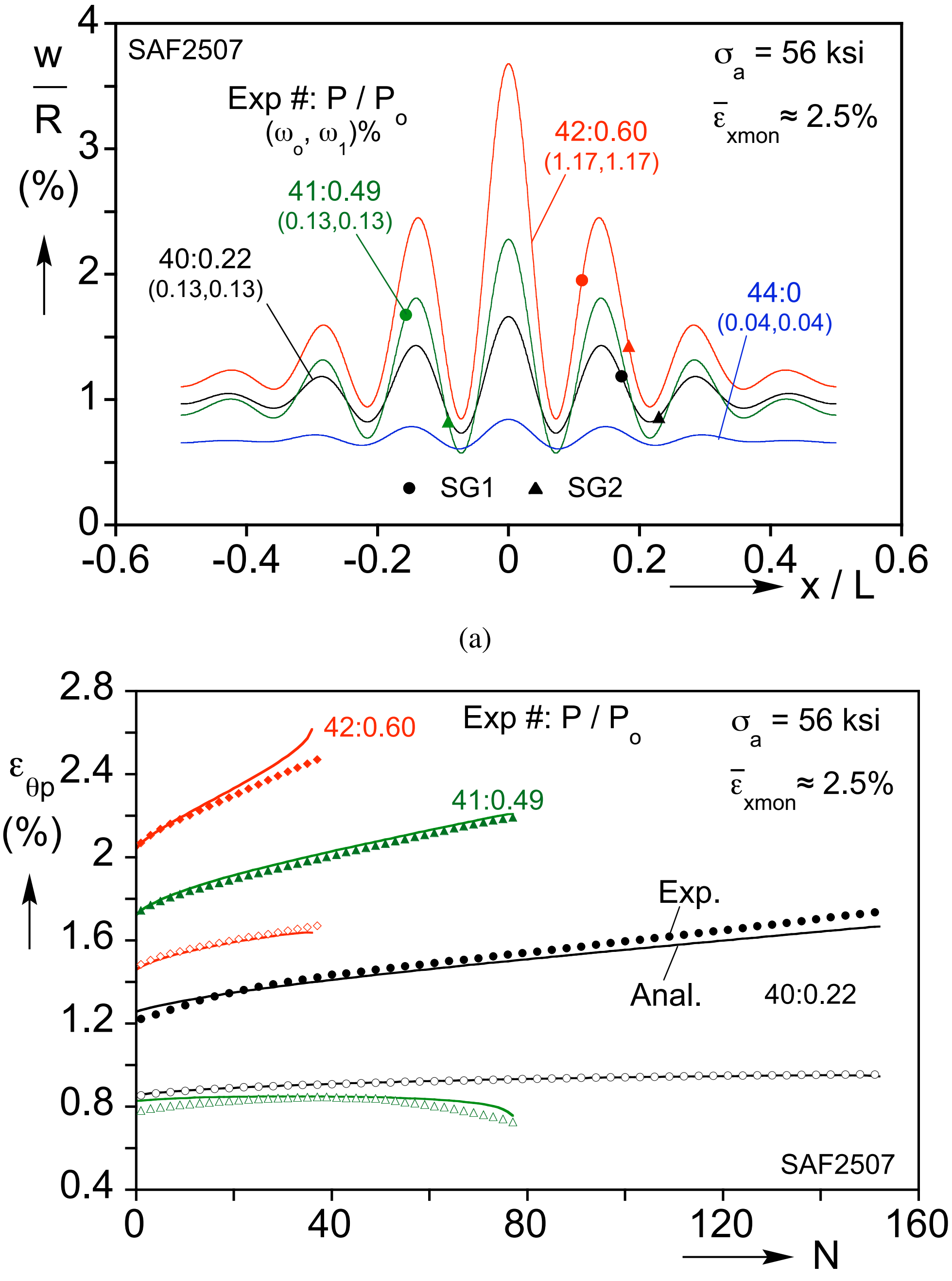

(a)

(b)

Fig. 8.7 (a) Calculated wrinkle profiles developed following the initial pre-straining (b) comparison of measured and calculated peak $\varepsilon_{\theta p} - N$ responses for the three pressurized experiments in Fig. 8.6.

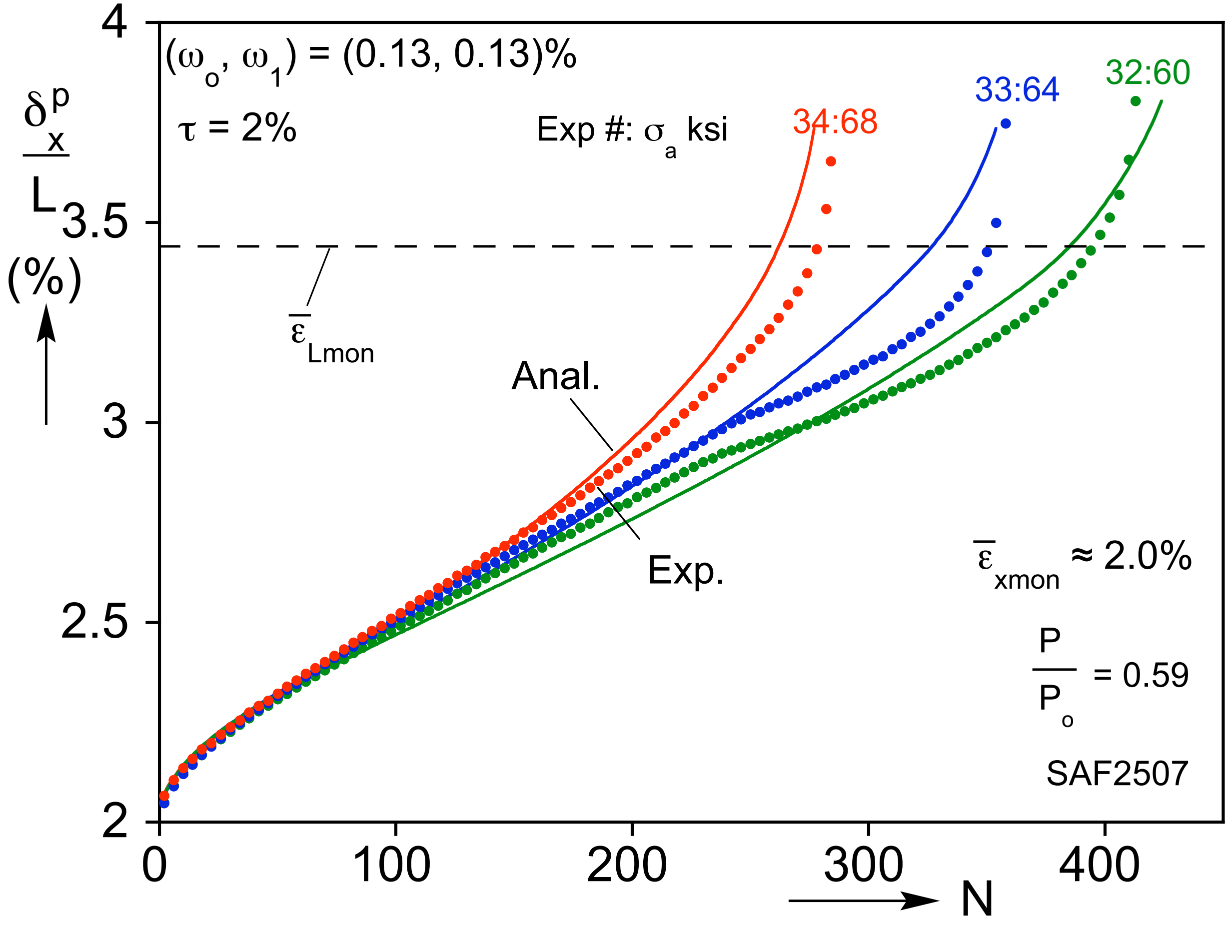

Fig. 8.8a Comparison of measured and calculated $\delta_x^p / L - N$ responses for three tubes tested with the same pre-strain and internal pressure but different axial cycle amplitudes.

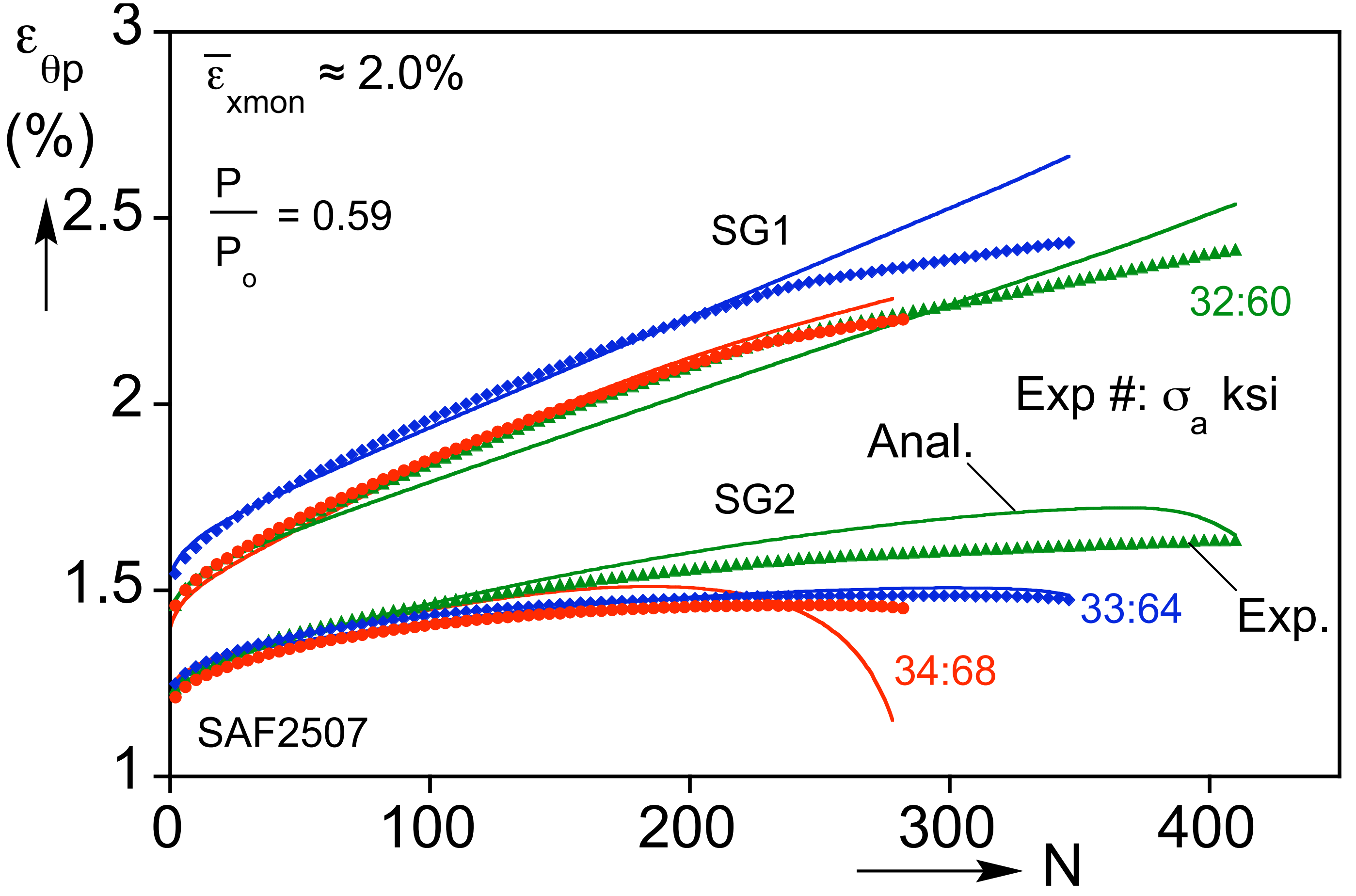

Fig. 8.8b Comparison of measured and calculated peak circumferential strain vs. *N* for three tubes shown in Fig. 8.8a.

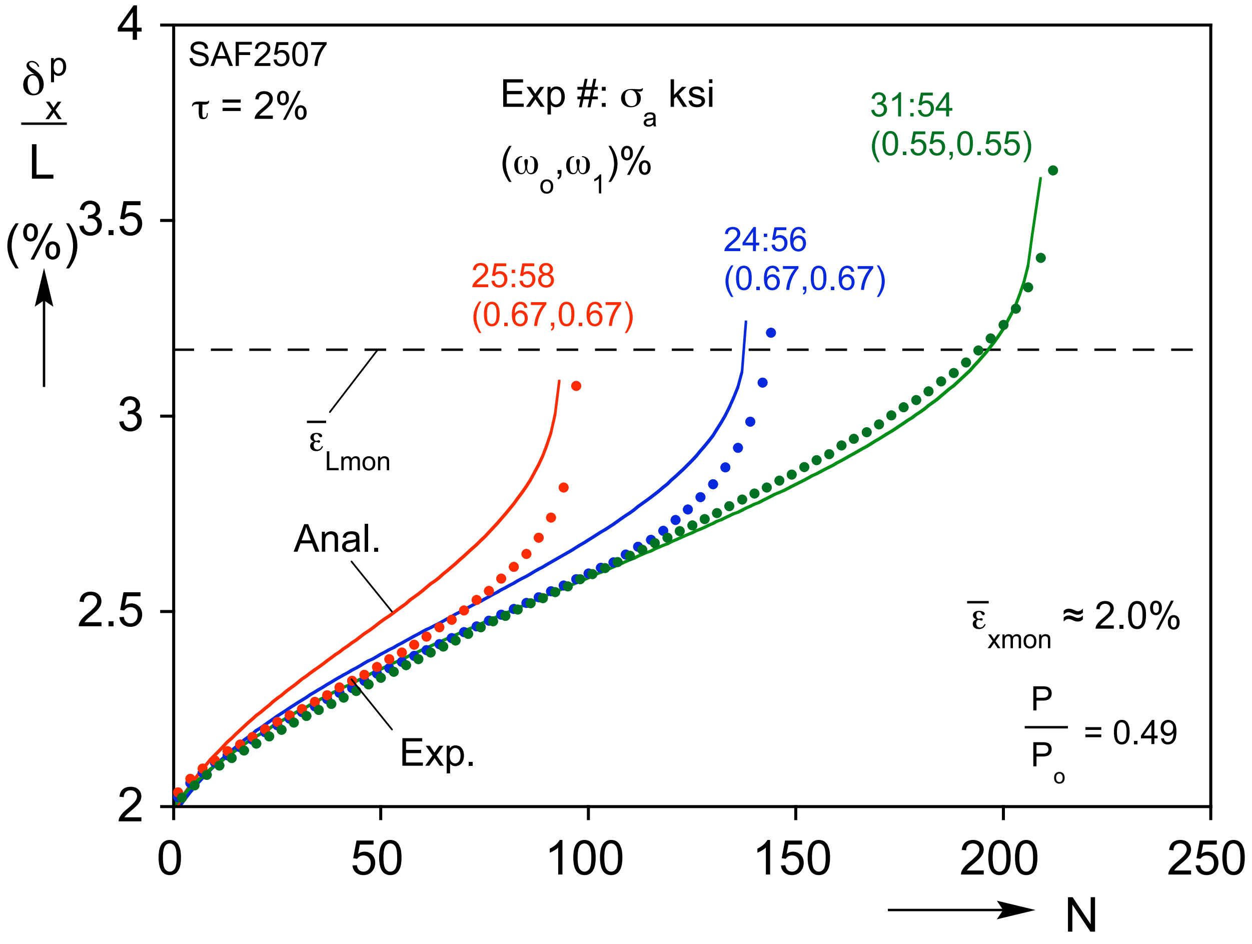

Fig. 8.9 Comparison of measured and calculated $\delta_x^p/L-N$ responses for three tubes tested with the same pre-strain and internal pressure but different axial cycle amplitudes.

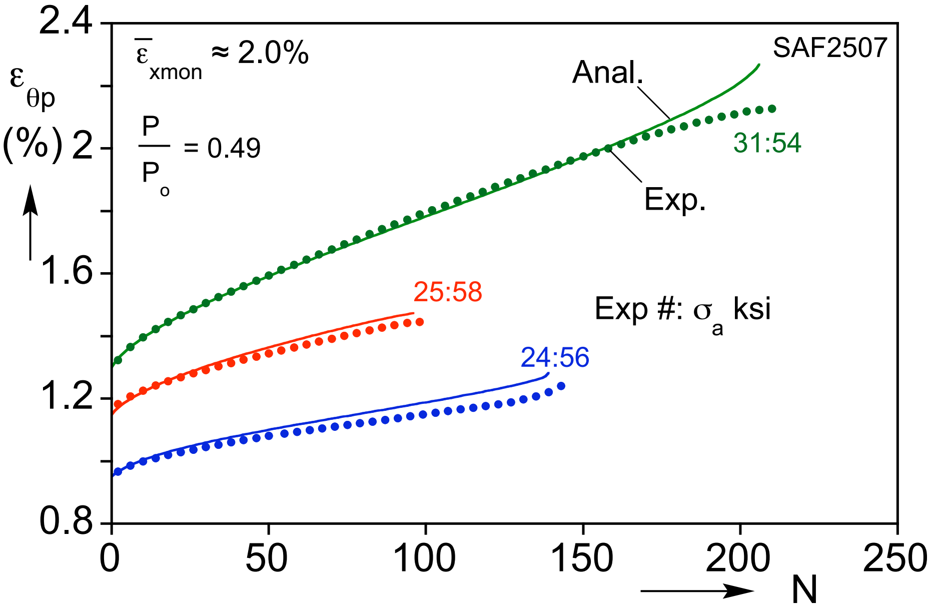

(a)

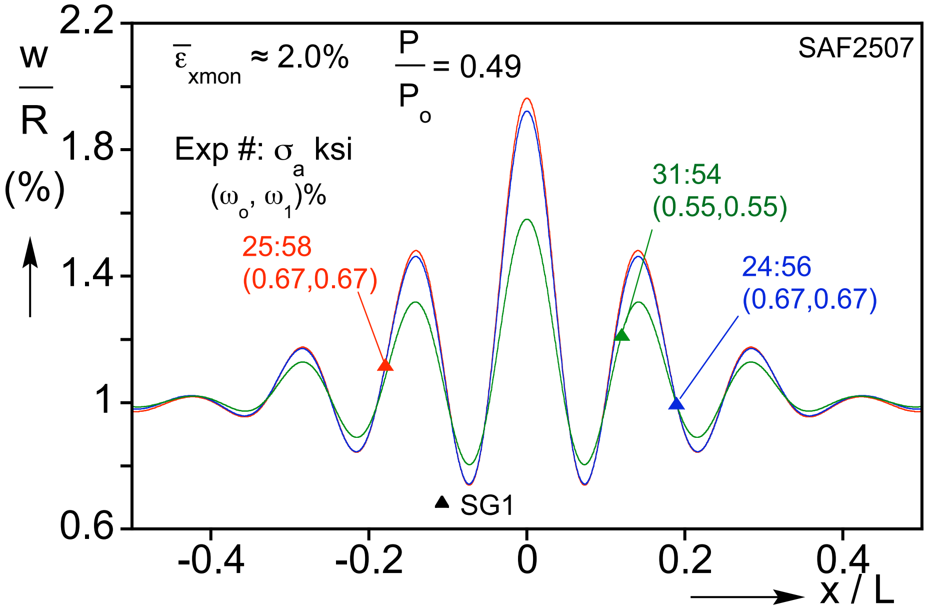

(b)

Fig. 8.10 (a) Comparison of measured and calculated peak circumferential strain vs. *N* and (b) calculated wrinkle profiles following the pre-straining corresponding to three tubes in Fig. 8.9.

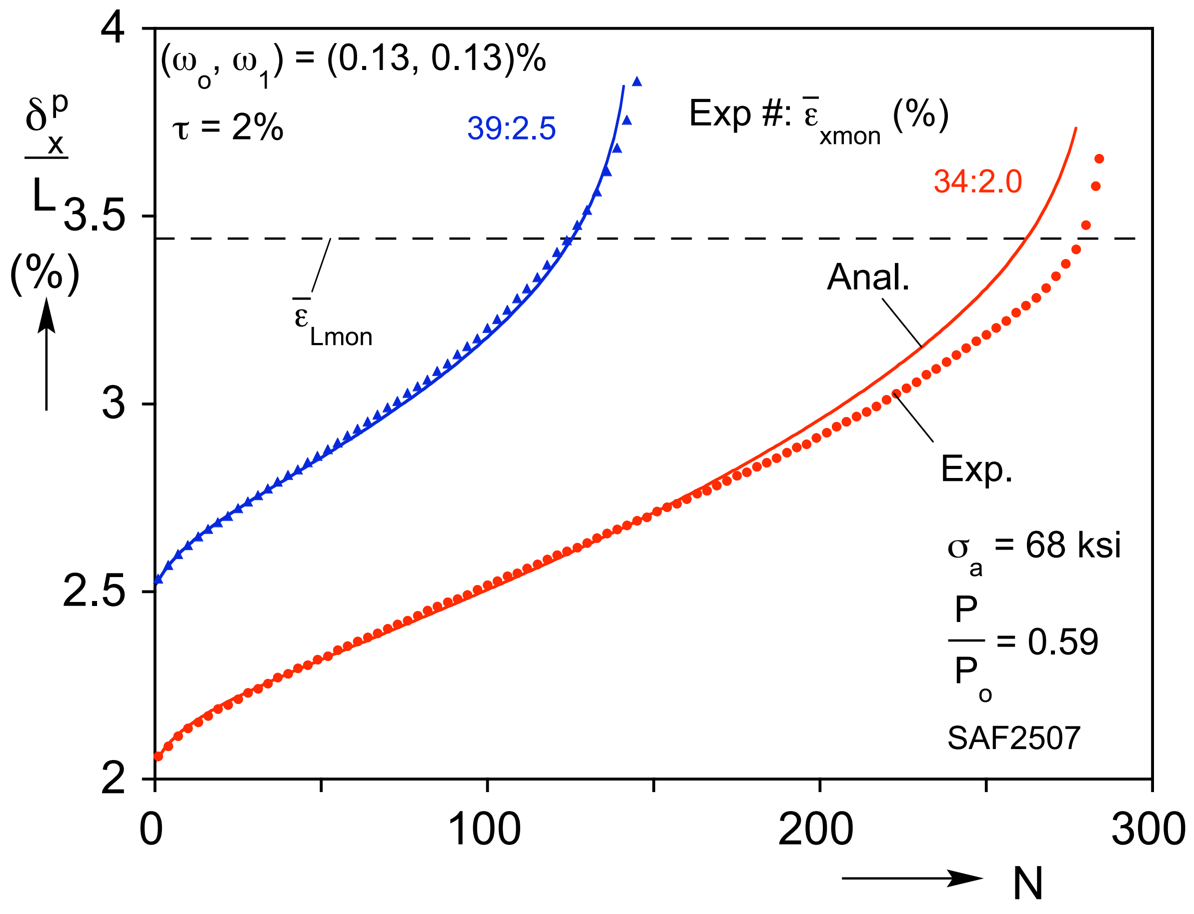

Fig. 8.11 Comparison of measured and calculated $\delta_x^p / L - N$ responses for two tubes tested with the same internal pressure and axial cycle amplitude but different pre-strains.

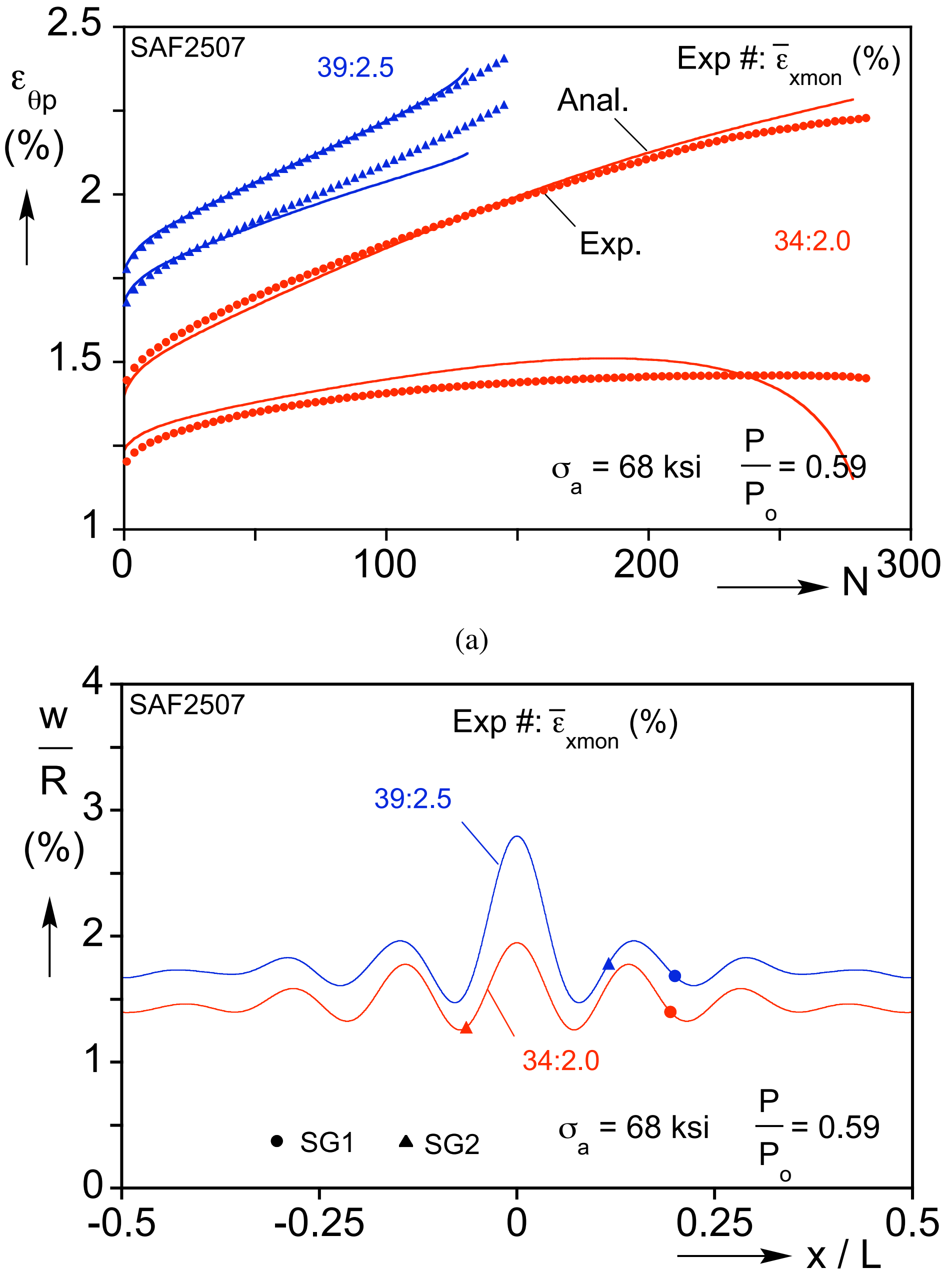

(a)

(b)

Fig. 8.12 (a) Comparison of measured and calculated peak circumferential strain vs. *N* and (b) calculated wrinkle profiles following the pre-straining corresponding to three tubes in Fig. 8.11.

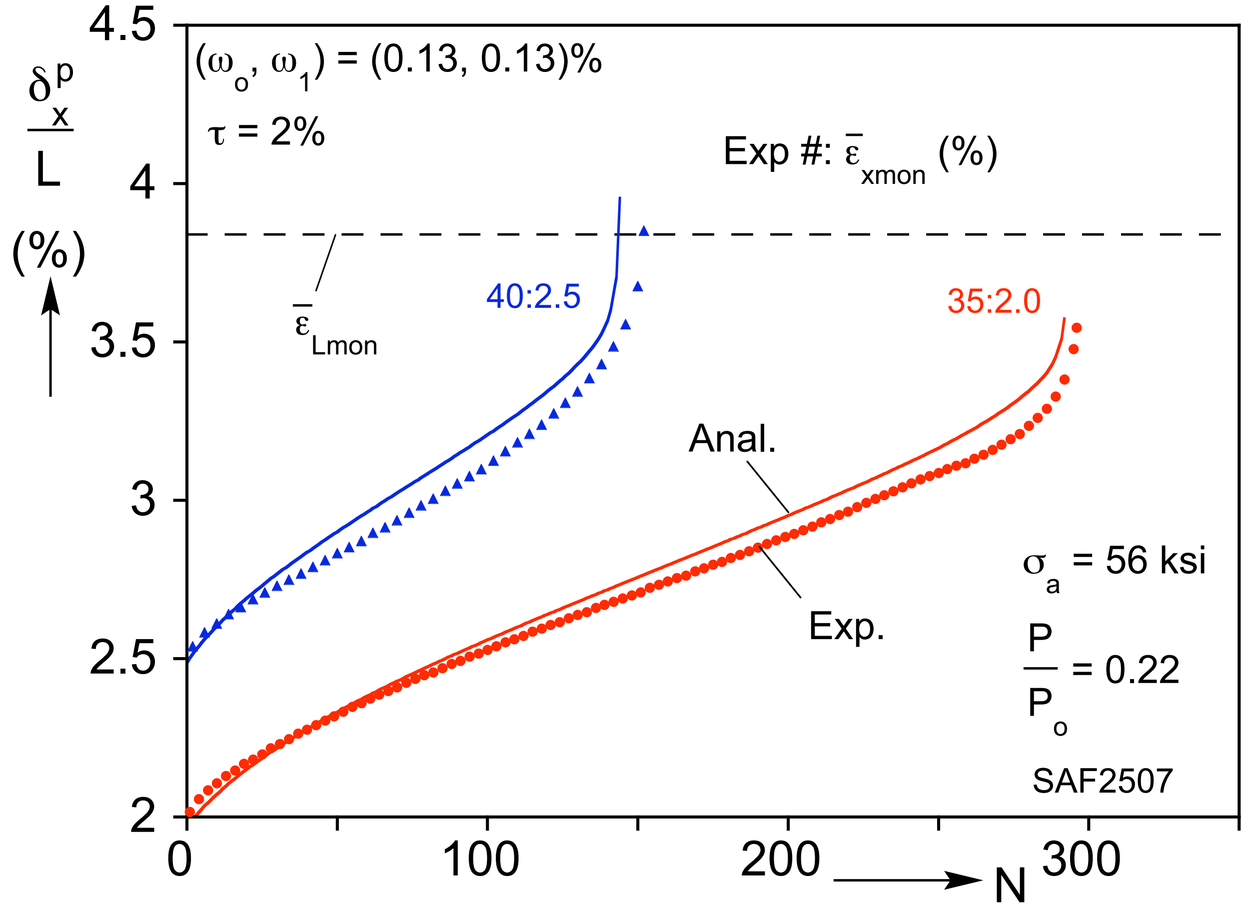

Fig. 8.13 Comparison of measured and calculated $\delta_x^p / L - N$ responses for two tubes tested with the same internal pressure and axial cycle amplitude but different pre-strains.

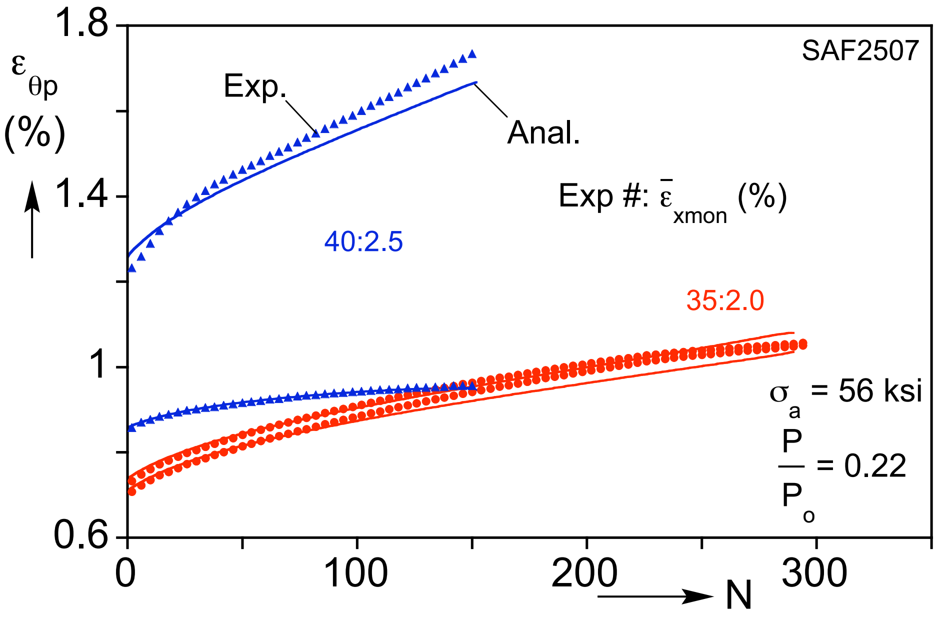

(a)

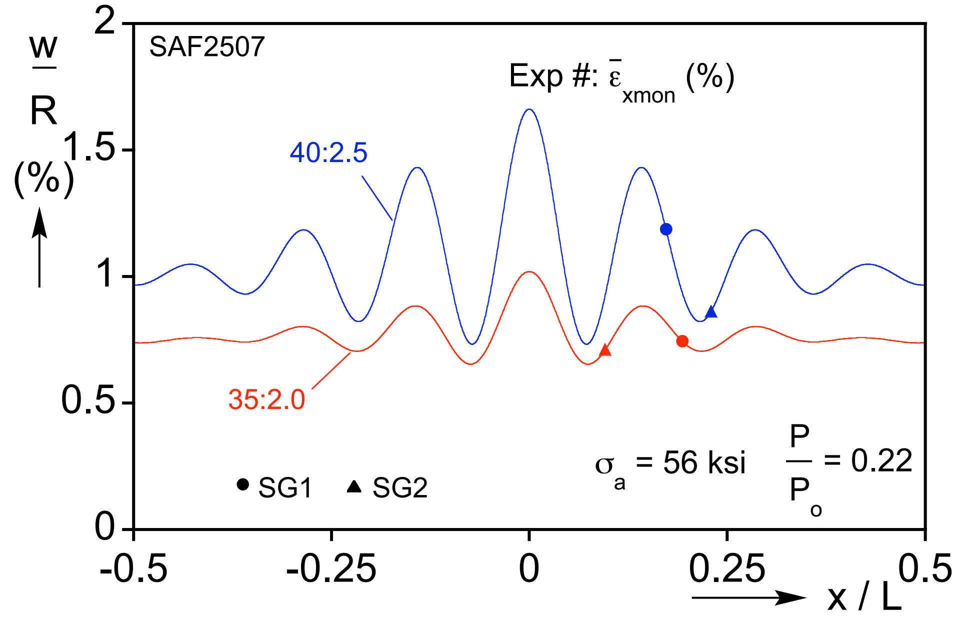

(b)

Fig. 8.14 (a) Comparison of measured and calculated peak circumferential strain vs. *N* and (b) calculated wrinkle profiles following the pre-straining corresponding to three tubes in Fig. 8.13.

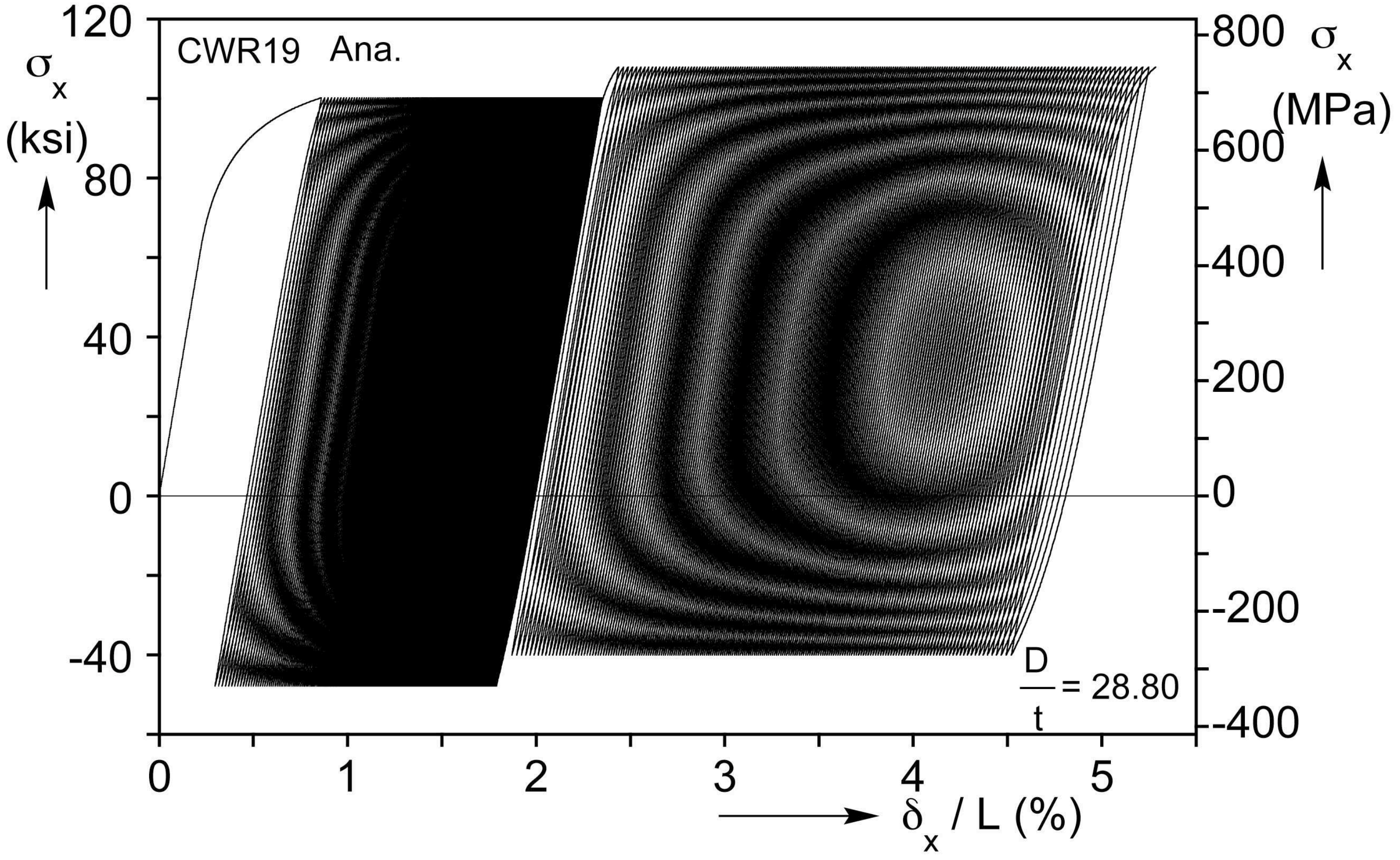

Fig. 9.1 Calculated axial stress-shortening response for CWR19 that was not pre-wrinkled.

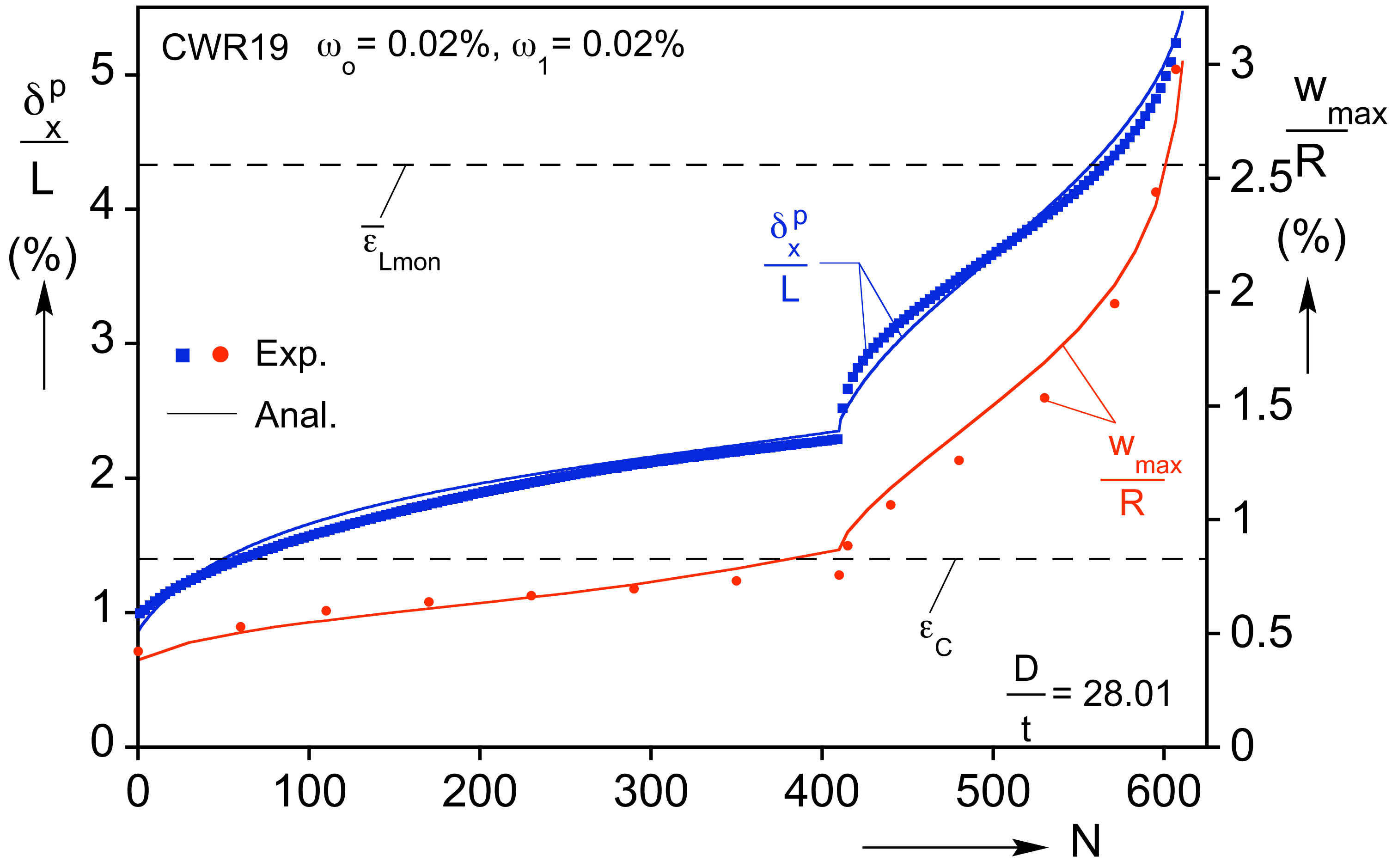

Fig. 9.2 Comparison of measured and calculated peak axial displacement and maximum radial displacement vs. *N*.

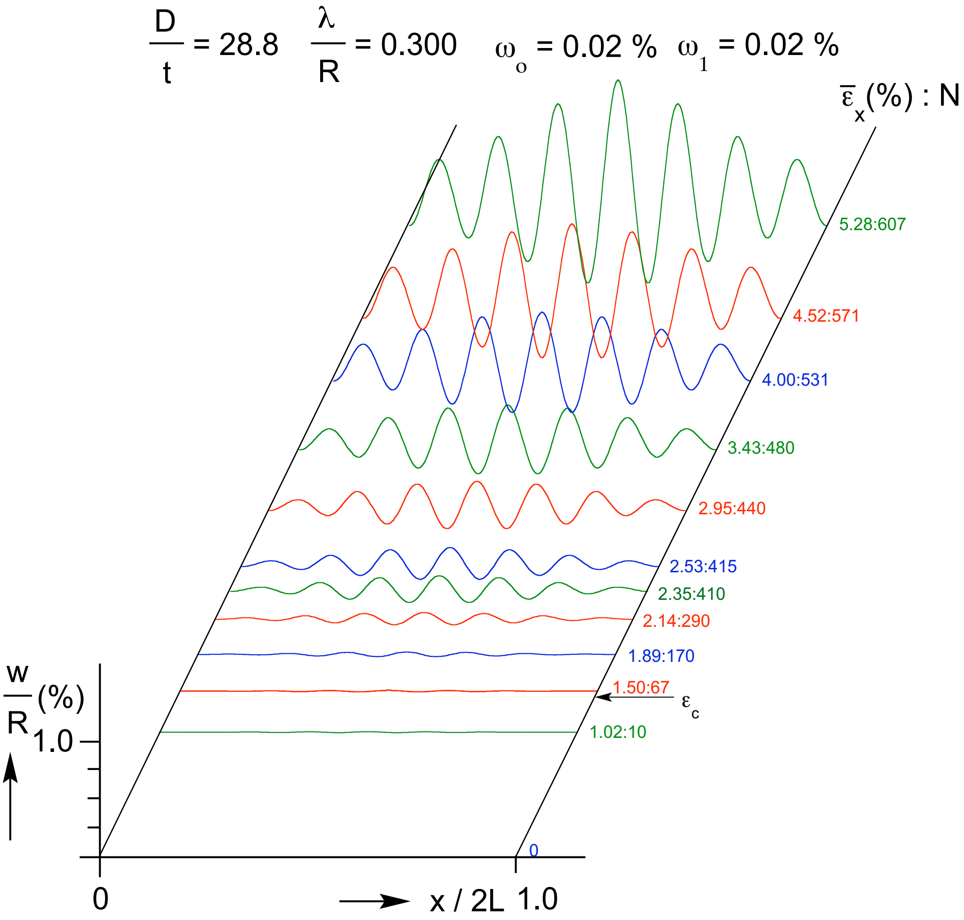

Fig. 9.3 Calculated radial displacement axial profiles after different number of cycles showing the growth and localization of wrinkles for CWR19.

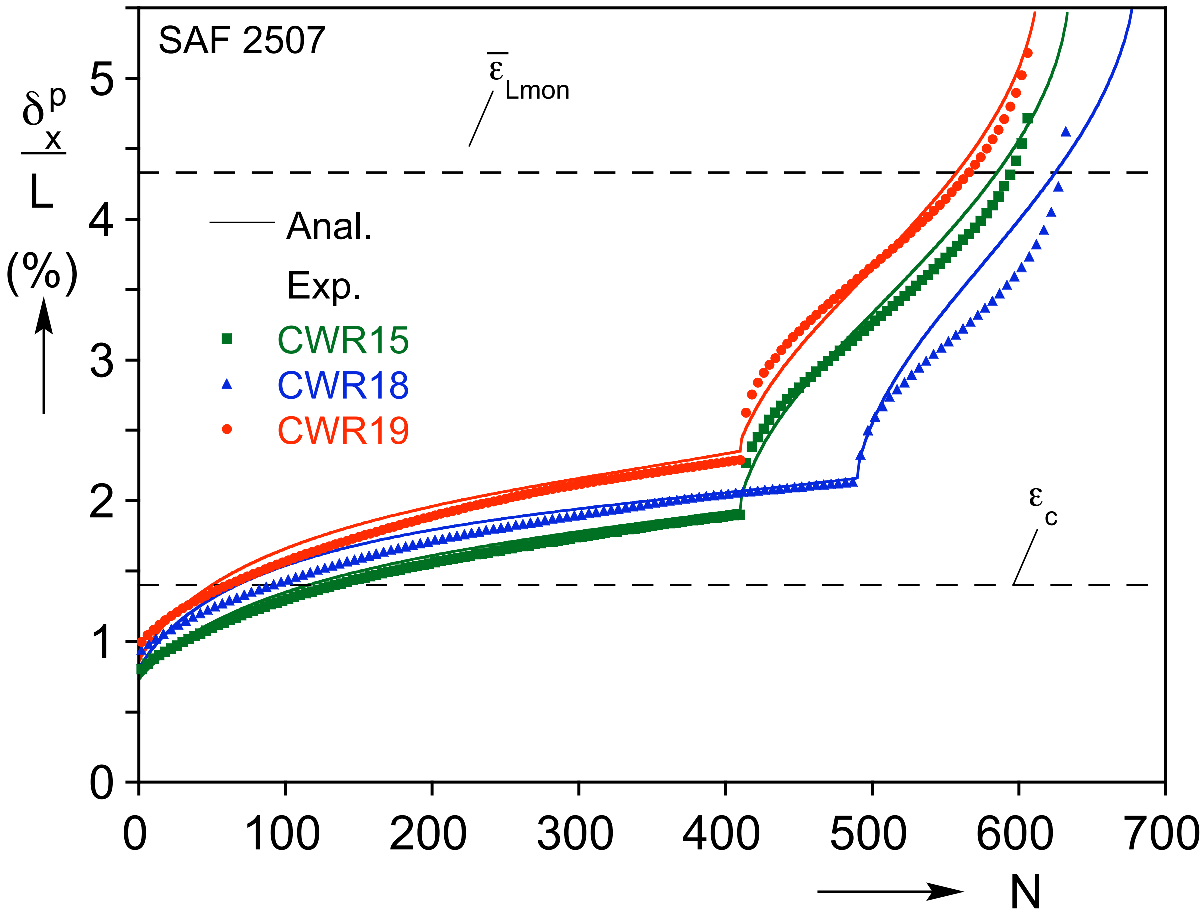

Fig. 9.4 Comparison of measured and calculated peak displacements per cycle vs. *N* from three experiments with slightly different initial pre-straining.

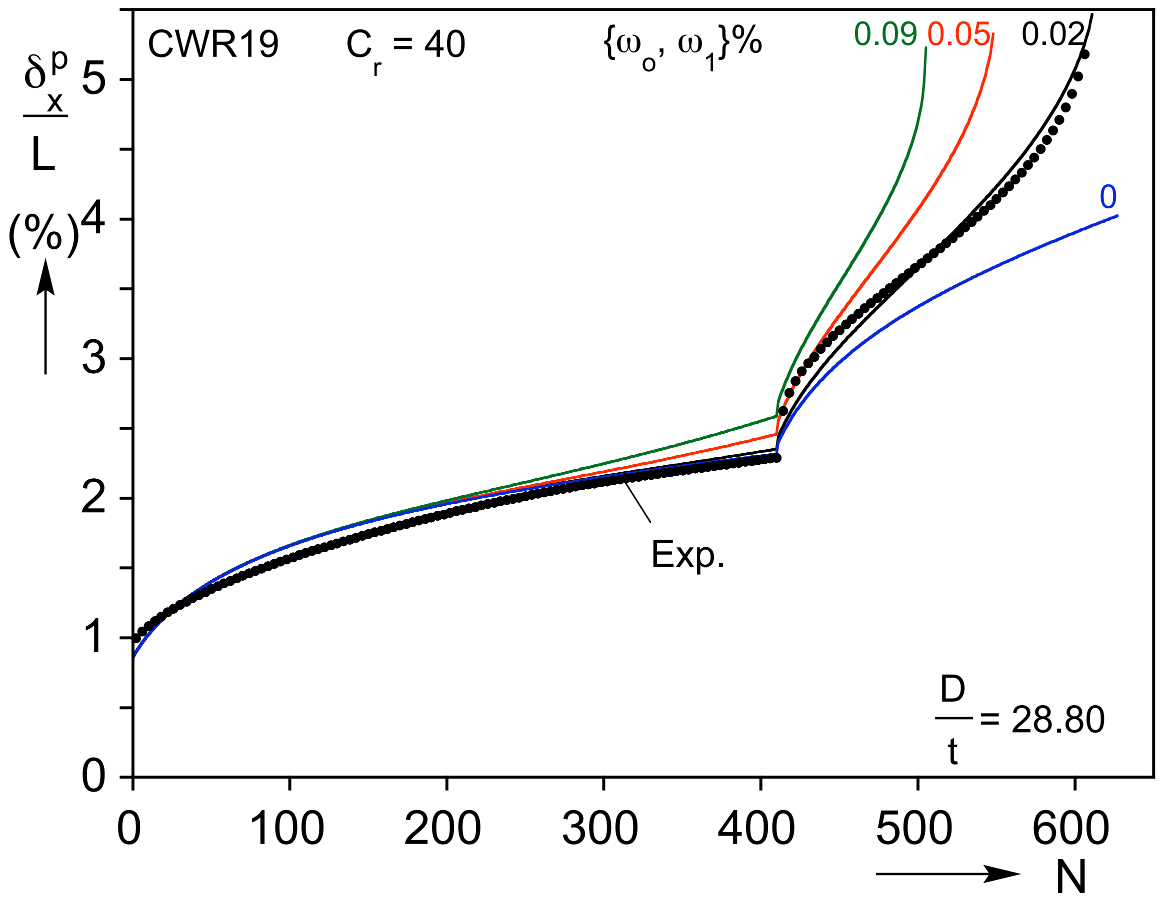

Fig. 9.5 Effect of imperfection parameters on calculated $\delta_x^p - N$ ratcheting response.

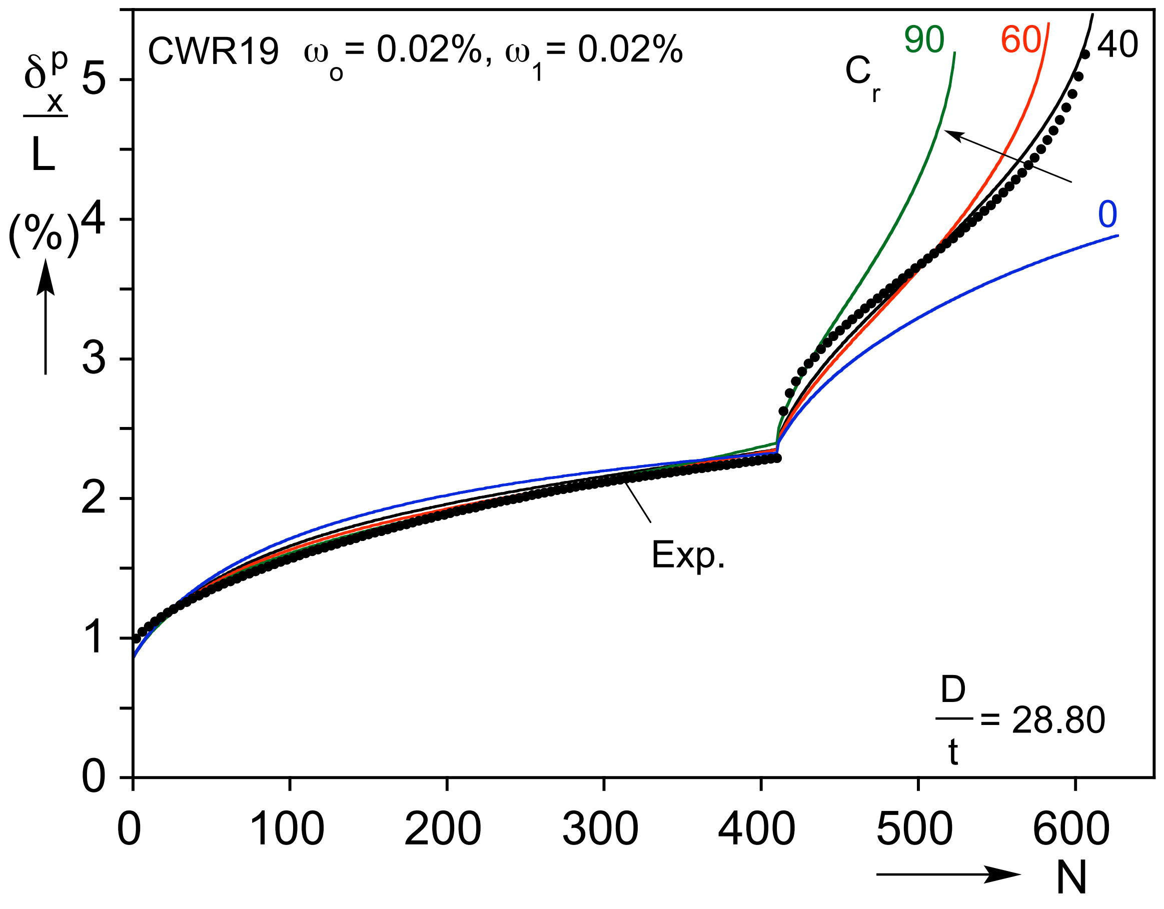

Fig. 9.6 Effect of relaxation coefficient C_r on calculated $\delta_x^p - N$ ratcheting response.

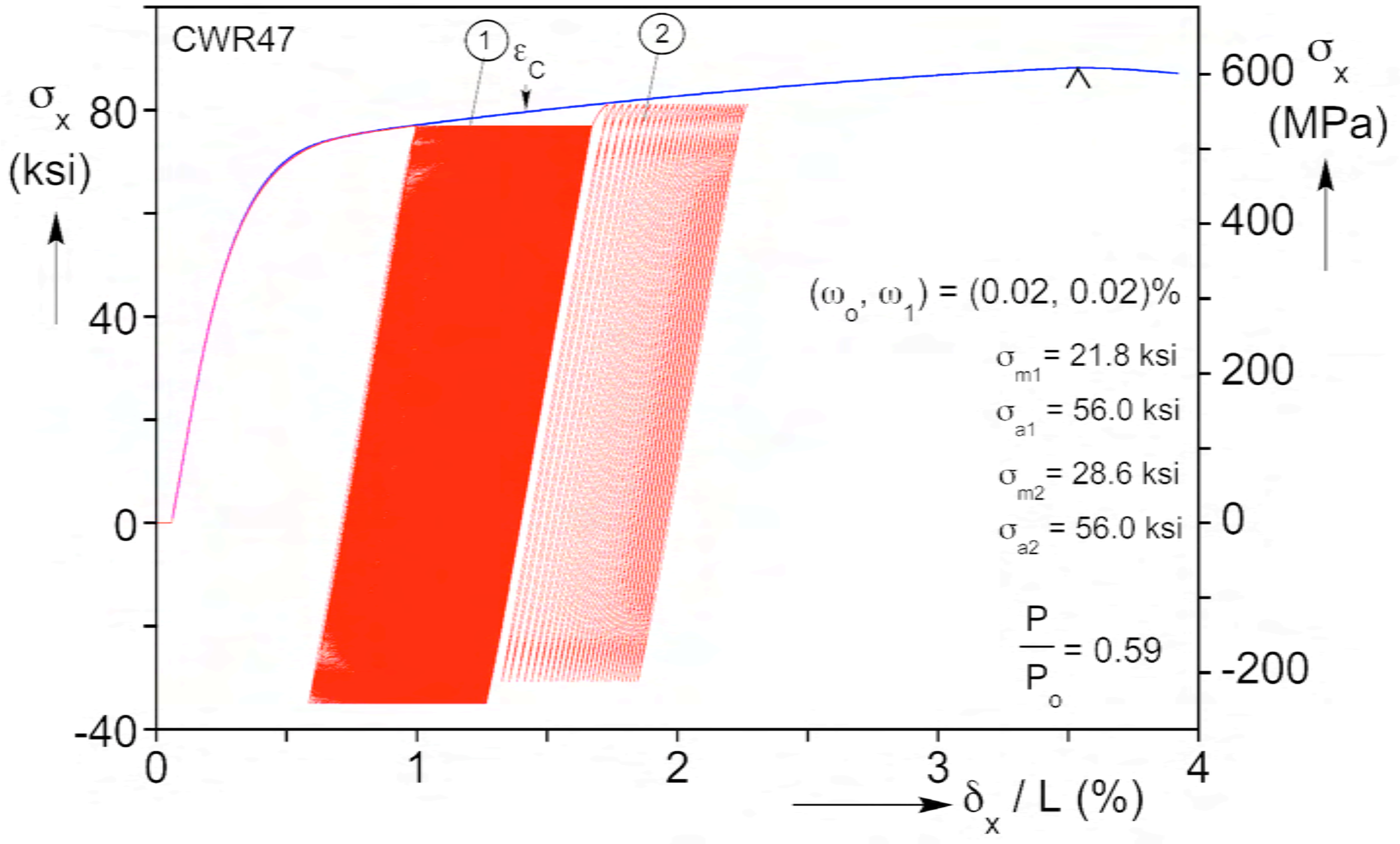

Fig. 9.7 Calculated axial stress-shortening response for CWR47 that was not pre-wrinkled.

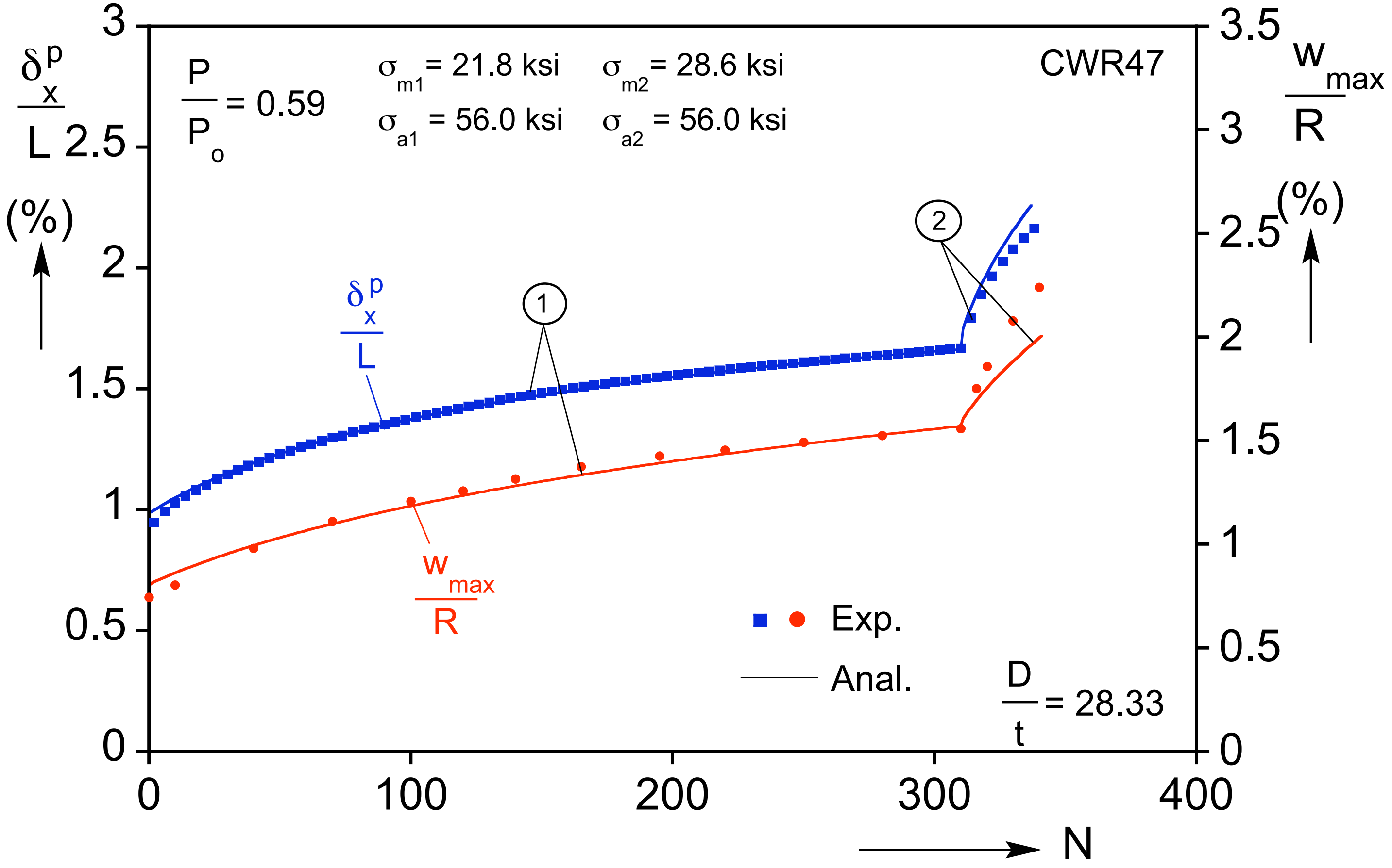

Fig. 9.8 Comparison of measured and calculated peak axial displacement and maximum radial displacement vs. *N*.

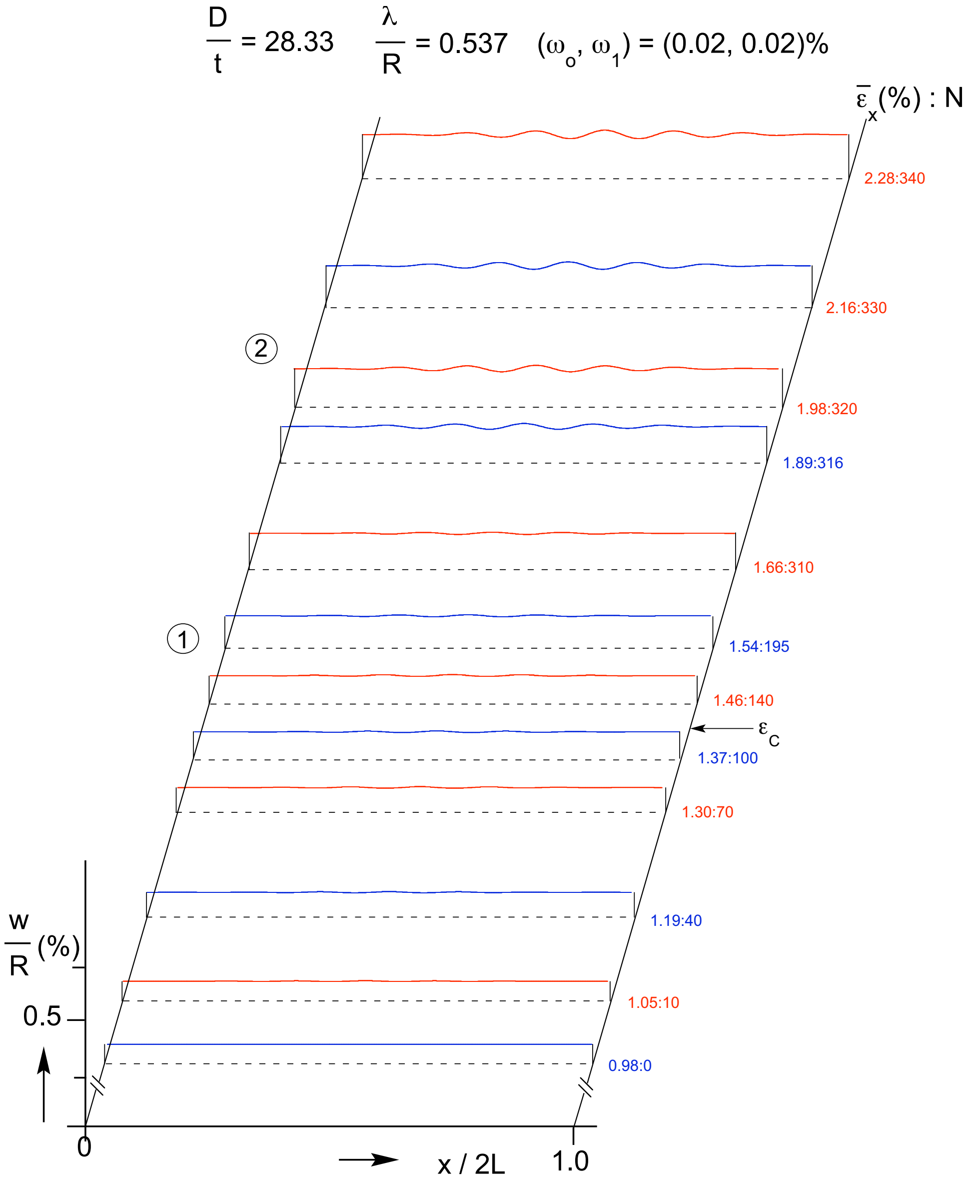

Fig. 9.9 Radial displacement axial profiles at different number of cycles showing the evolution of wrinkling.

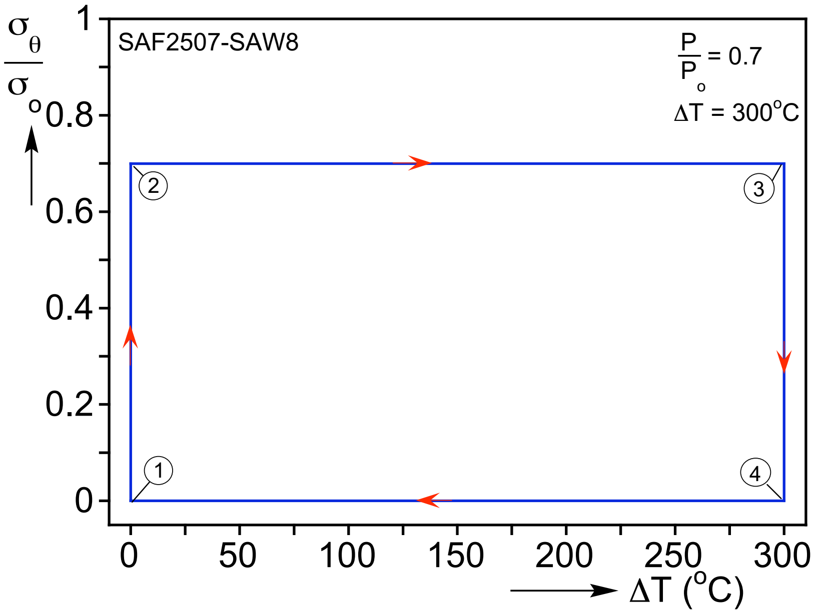

(a)

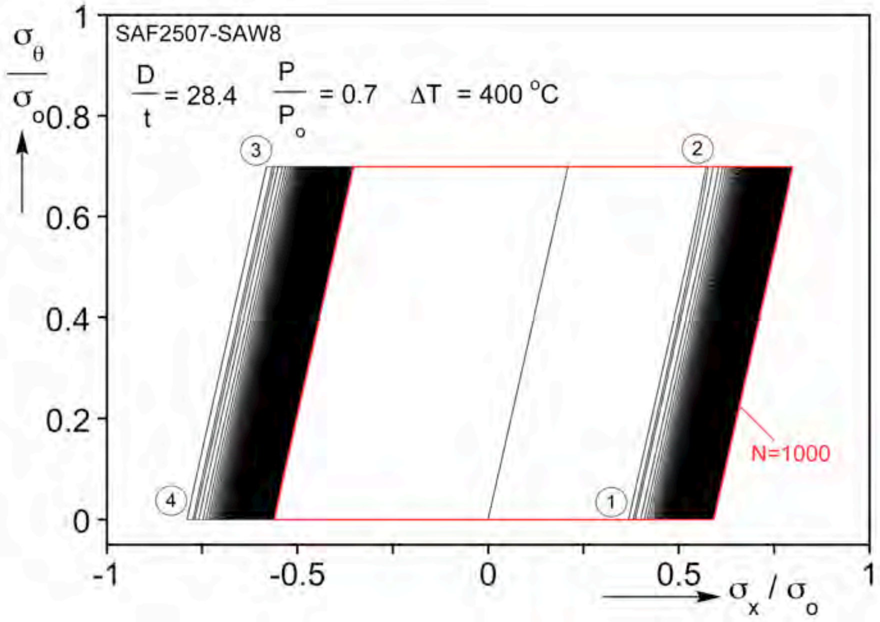

(b)

Fig. 10.1 (a) Thermal-pressure cycle that approximates startup-shutdown pipeline cycles. (b) Axial-hoop stress response induced by the pressure-temperature cycles shown in Fig. 10.1a ($N = 200$).

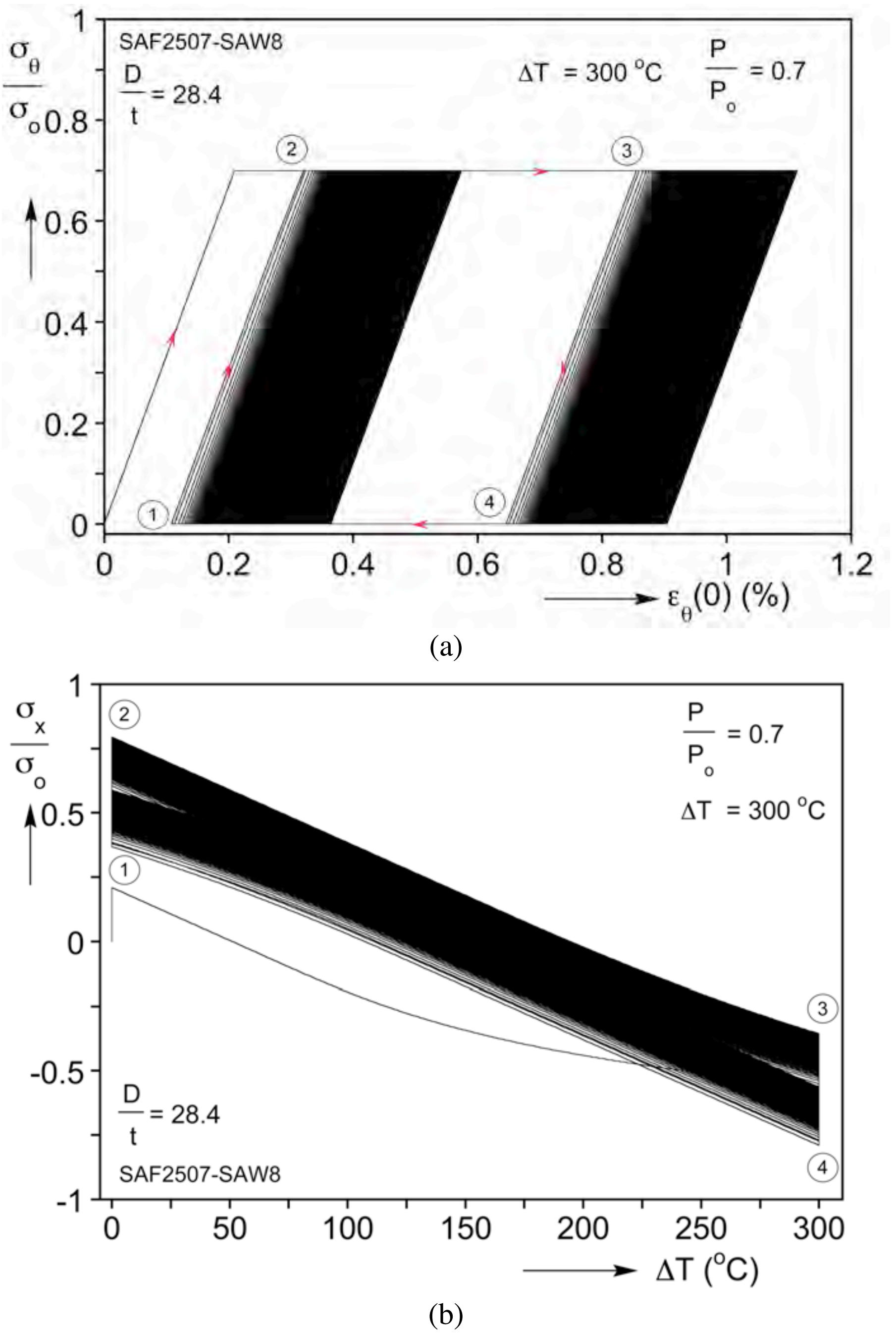

(a)

(b)

Fig. 10.2 (a) Hoop stress-strain response and (b) axial stress- ΔT response induced by the pressure-temperature cycles shown in Fig. 10.1a ($N = 200$).

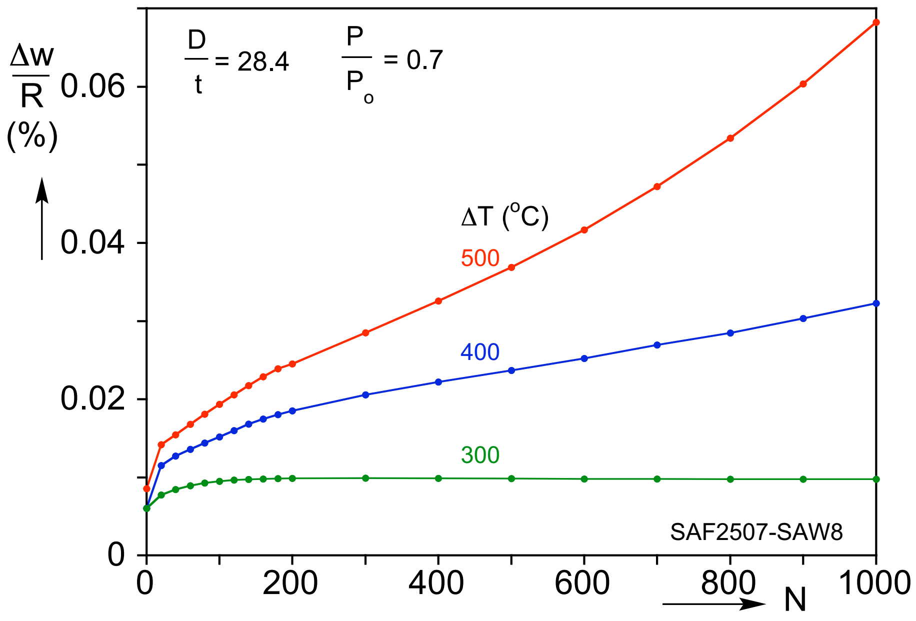

(a)

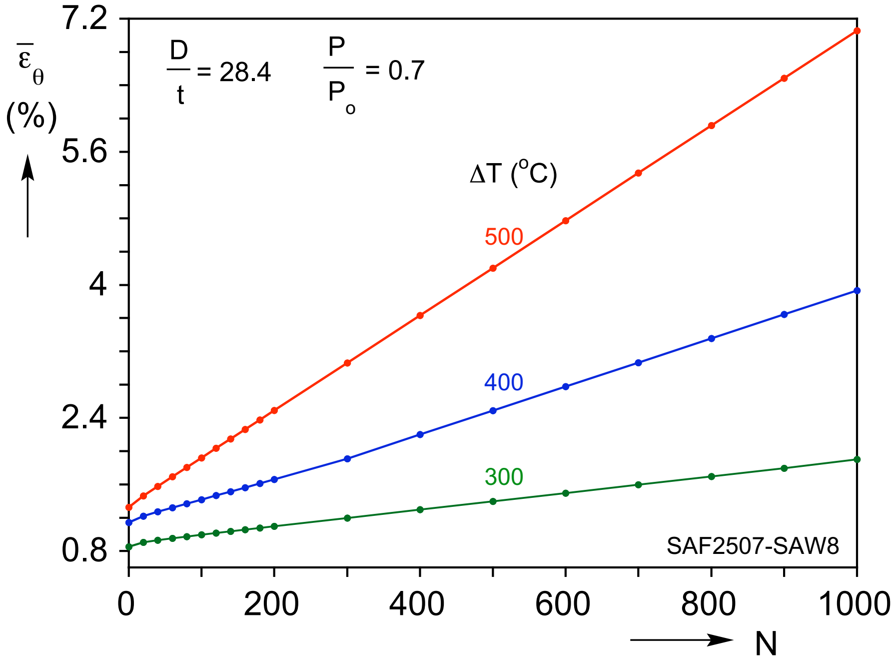

(b)

Fig. 10.3 (a) Wrinkle amplitude vs. N and (b) average hoop strain vs. N for three ΔT $(D/t = 28.4,\ P = 0.7P_o)$.

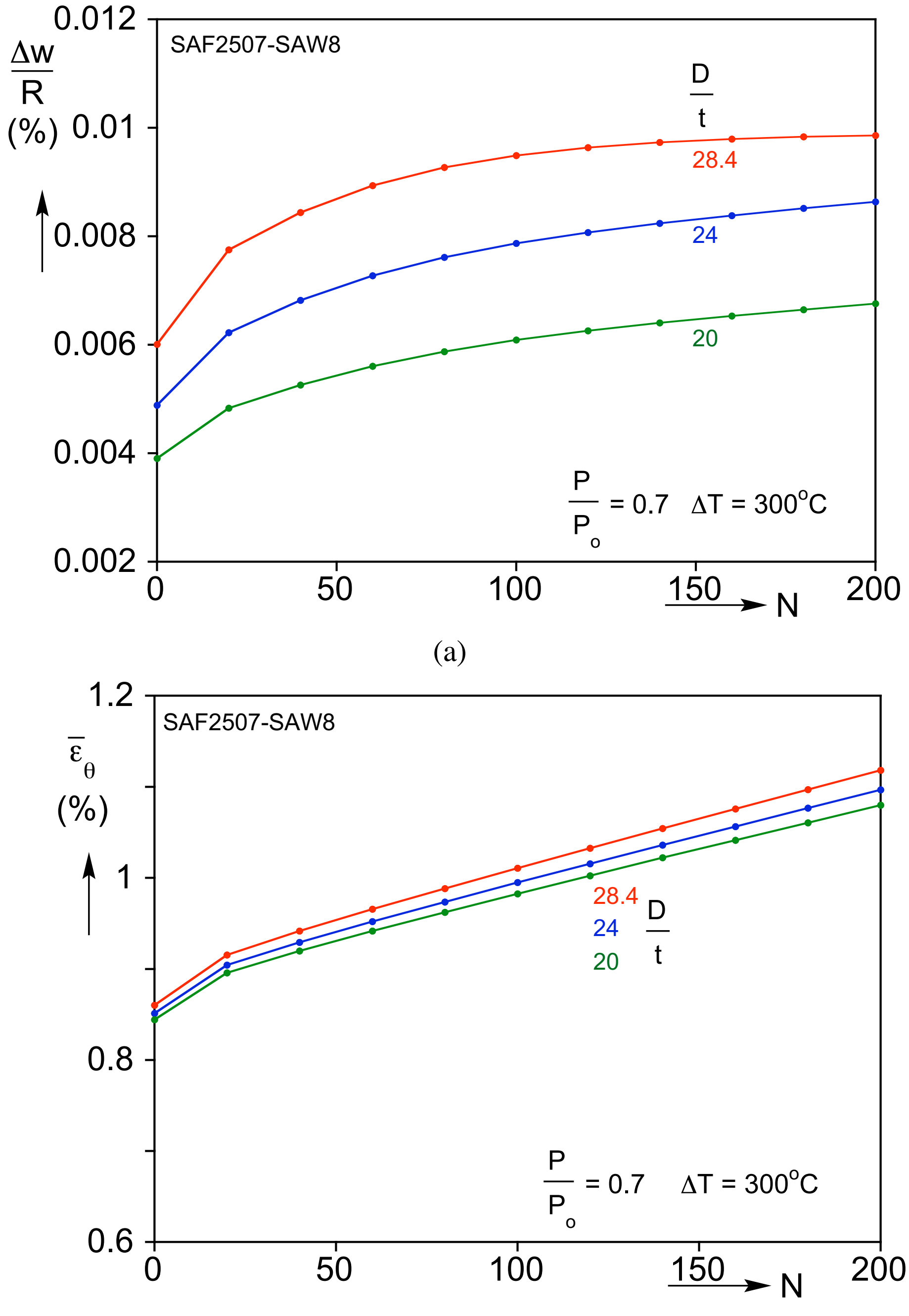

(a)

(b)

Fig. 10.4 (a) Wrinkle amplitude vs. *N* and (b) average hoop strain vs. *N* for three pipe *D*/*t* ($\Delta T = 300,\ P = 0.7 P_o$).

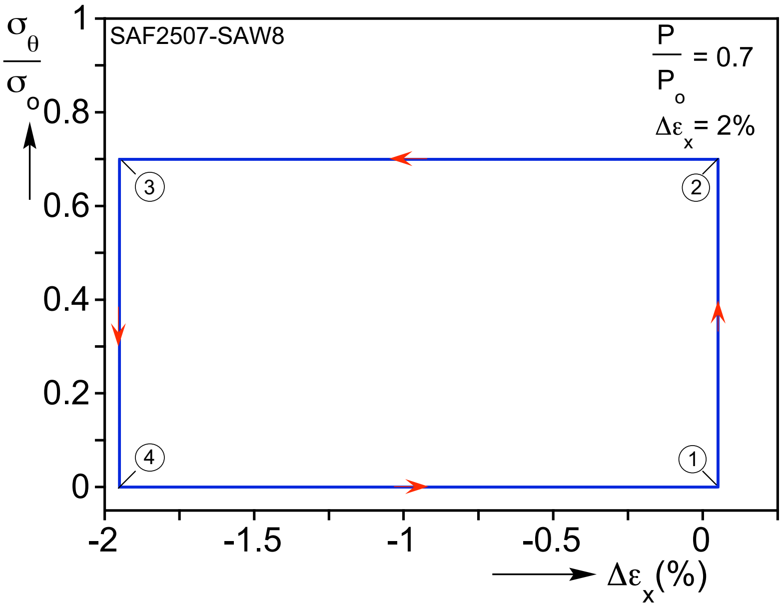

(a)

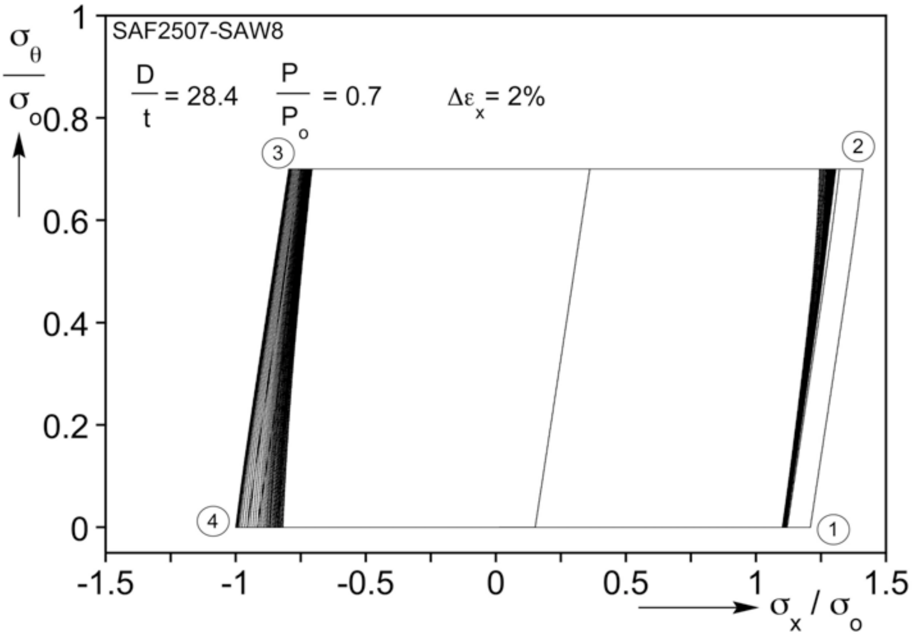

(b)

Fig. 10.5 (a) Pressure-axial strain cycle prescribed. (b) Axial-hoop stress response induced by the cycles shown in Fig. 10.5a ($N = 50$).

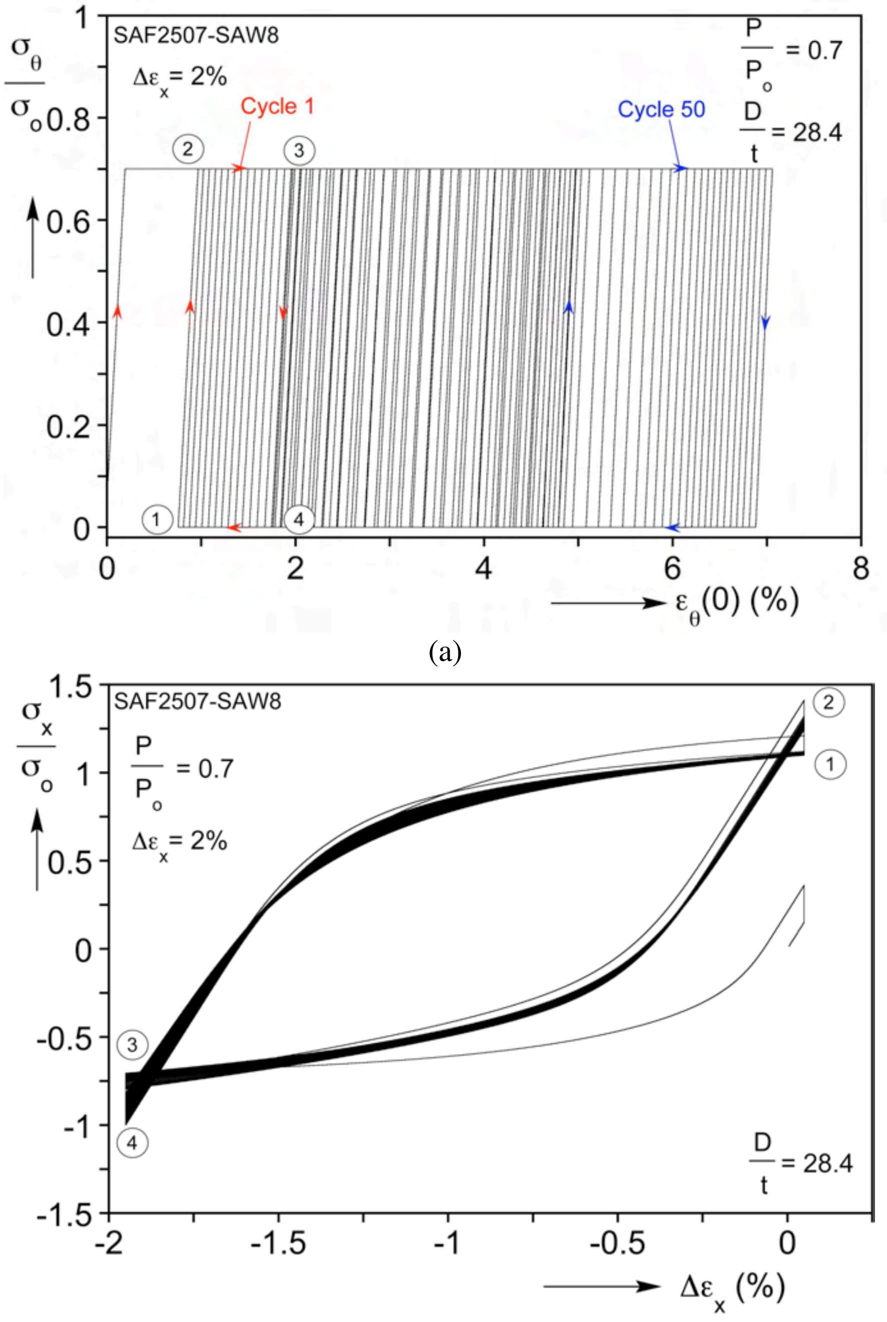

(a)

(b)

Fig. 10.6 (a) Hoop stress-strain response and (b) axial stress-$\Delta\varepsilon_x$ response induced by the cycles shown in Fig. 10.5a ($N = 50$).

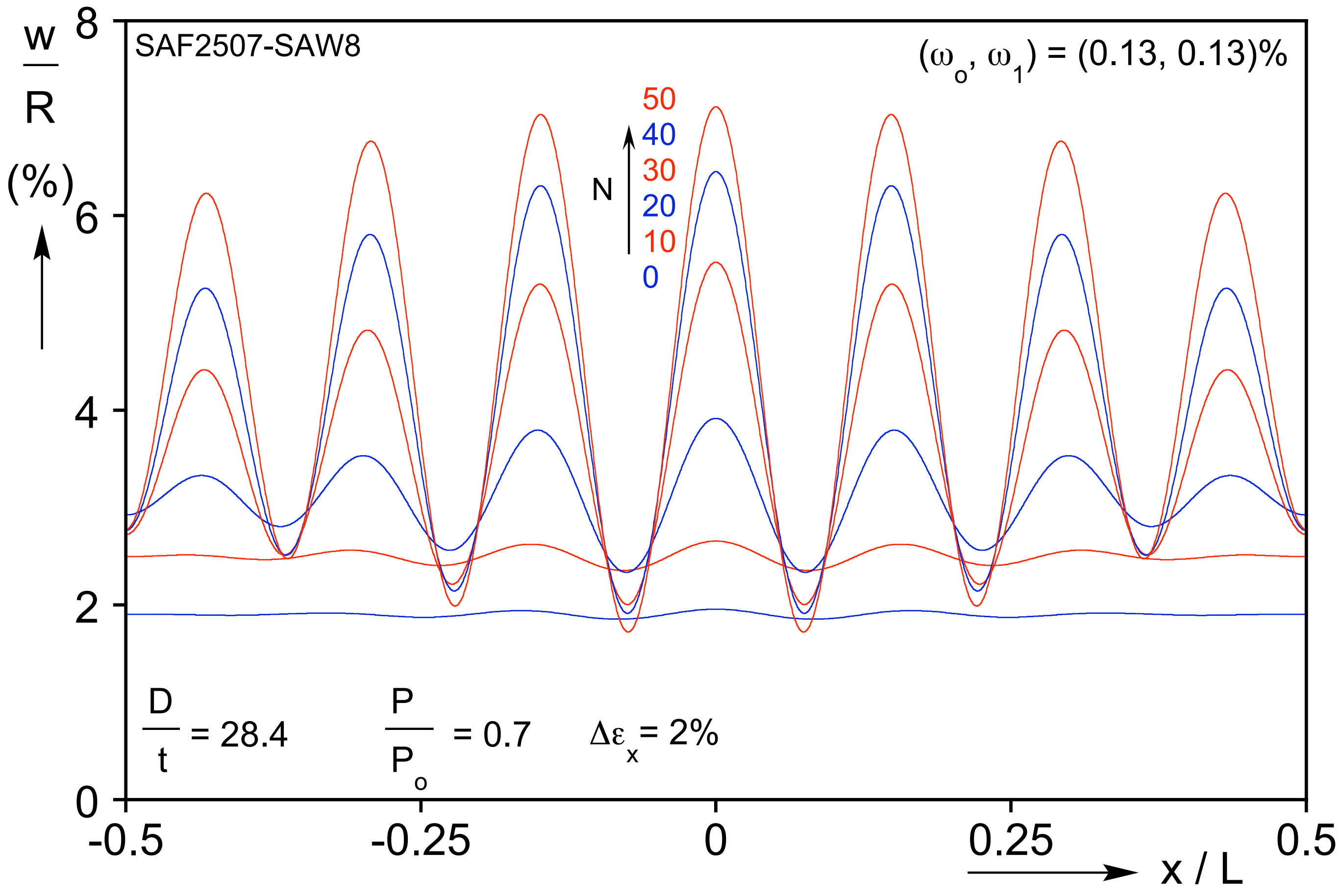

Fig. 10.7 Calculated radial displacement axial profiles after different number of cycles showing the growth of wrinkles induced by the cycles shown in Fig. 10.5a.

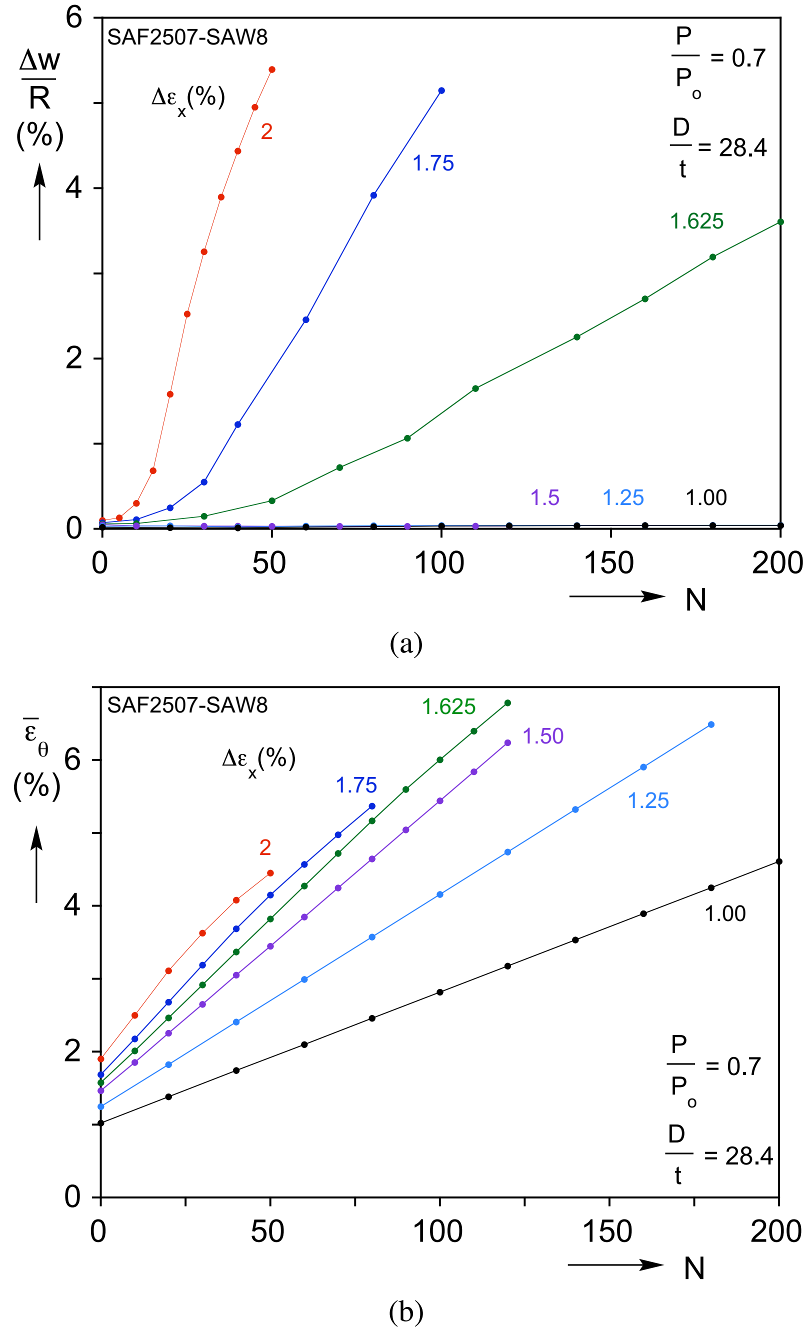

Fig. 10.8 (a) Wrinkle amplitude vs. *N* and (b) average hoop strain vs. *N* for different $\Delta\varepsilon_x$ induced by the cycles shown in Fig. 10.5a ($D/t = 28.4$ and $P = 0.7P_o$).

Appendix A: Mechanical Properties of Tubes

The tubes used in the cyclic experiments exhibit some plastic anisotropy introduced by the manufacturing process. Such anisotropy affects the mechanical behavior of the tubes including their ratcheting strains and must be accounted for in the modeling. It was found that like in other pipeline and steel tubular structures this anisotropy can be adequately represented as Hill (1948) anisotropy (see Kyriakides *et al.*, 2005; Bardi and Kyriakides, 2006; Paquette and Kyriakides, 2006). In the case of relatively thin-walled tubes under a biaxial stress state of Hill's anisotropic yield function can be written as

$$f = \left[\sigma_x^2 - \left(1 + \frac{1}{S_\theta^2} - \frac{1}{S_r^2} \right) \sigma_x \sigma_\theta + \frac{1}{S_\theta^2} \sigma_\theta^2 \right]^{1/2} = \sigma_e \qquad \text{(A.1)}$$

where $S_\theta = \dfrac{\sigma_{o\theta}}{\sigma_{ox}}$, $S_r = \dfrac{\sigma_{or}}{\sigma_{ox}}$, and $\{\sigma_{ox}, \sigma_{o\theta}, \sigma_{or}\}$ are the yield stresses in the axial, circumferential and radial directions.

The anisotropy parameters $\{S_\theta, S_r\}$ are determined following the procedure of Kyriakides and Yeh (1988) (see also Appendix B in Kyriakides and Corona, 2007). The calibration procedure involves three radial paths that are outlined below (see Fig. A.1).

A.1 UNIAXIAL TEST

The axial response and yield stress, σ_{ox}, are determined from a simple uniaxial tension test. The experiment was performed on a dog-bone shaped strip cut along the axis of the tube stock. Figure A.2 shows a drawing of the specimen.

The strips were pulled in screw-type testing machine at a constant rate of 1.34×10^{-2} in/min corresponding approximately to a constant strain rate of 10^{-4} s^{-1}. The load was measured by the testing machine load cell and the strain in the test section with a pair of strain gages as well as with a one-inch extensometer. The outputs of strain and load were recorded on a common time base using a PC based data acquisition system running LabVIEW.

Measured uniaxial stress-strain responses for SAW8 are shown in Fig A.3. Included is the response from the strain gages and the one recorded using the extensometer. The first, which comes from the average of the two strain gages, is used to evaluate the elastic modulus (E) and the yield stress at a strain offset of 0.2% (σ_{ox}). Figure A.3 also shows the material response up to 10% based on the extensometer output. This will become the basic stress-strain response of the material.

A.2 LATERAL PRESSURE TEST

The lateral pressure test involves a tube pressurized in a way that produces a purely circumferential state of stress. In other words the tube is free axially (see Appendix B of Kyriakides and Corona, 2007). The test setup used is shown schematically in Fig. A.4). The tests were conducted on a servo-hydraulic universal testing machine while pressurization was provided by the same independent pressurization system described in Chapter 2. The specimen geometry is shown in Fig. A.5.

To achieve purely circumferential state of stress, an axial compressive load was provided to balance the pressure load at the ends of the tube (PA_i). The output of the pressure transducer was amplified through an inverting amplifier and used as the command signal for the servo controller on the universal testing machine. When the internal pressure was gradually increased, the actuator moved to keep the axial force at $-PA_i$, which equilibrates the end axial due to internal pressure so the tube had the stress state of $\sigma_x = 0$ and $\sigma_\theta = PR/t$.

The axial load was recorded by the load cell on the test machine, which was calibrated to 10 V at 50 kips. Pressure was monitored by a pressure transducer that was calibrated to output 10 V at 10,000 psi. Strain gages were mounted on the test section of the specimen in the axial and transverse directions. All instruments were monitored via the same data acquisition system mentioned above. The data were stored as a text file in the PC for later processing.

A.3 HYDROSTATIC PRESSURE TEST

The hydrostatic pressure test was performed in a similar set up to that of the lateral pressure test. The specimen geometry is the same as in Fig. A.5 while the schematic of the test set up in Fig. A.4 is still applicable. The instrumentation used was similar to that described for the lateral pressure test.

To achieve hydrostatic pressure, no external command signal was needed. Rather, the machine is operated in load control and the axial load was set to zero. When the internal pressure was increased, the actuator moved to keep the machine-applied force at zero. So, in a hydrostatic pressure test, the stresses developed were $\sigma_x = PR/2t$ and $\sigma_\theta = PR/t$. These are the same that would be present if end-caps were welded to the tube and the assembly was pressurized.

A.4 ESTABLISHING THE ANISOTROPY

For the three responses to be compared it is necessary that they be converted into to equivalent stress-equivalent plastic strain. The work compatible equivalent plastic strain increment for the anisotropic equivalent stress in (A.1) is derived by requiring that $dW^p = \sigma_e d\varepsilon_e^p = \sigma_{ij} d\varepsilon_{ij}^p$. This yields

$$d\varepsilon_e^p = \sqrt{2}\left[\frac{\frac{1}{S_\theta^2}(d\varepsilon_x^p)^2 + (d\varepsilon_\theta^p)^2 + \left(1 + \frac{1}{S_\theta^2} - \frac{1}{S_r^2}\right) d\varepsilon_x^p d\varepsilon_\theta^p}{\frac{1}{S_\theta^2} + \frac{1}{S_r^2} - \frac{1}{2} - \frac{1}{2}\left(\frac{1}{S_\theta^2} - \frac{1}{S_r^2}\right)^2}\right]^{1/2} . \tag{A.2}$$

The $\sigma_e - \varepsilon_e^p$ responses with $S_\theta = S_r = 1$ for the three tests of SAW8 are shown in Fig. A.6a. Anisotropy is responsible for the extent of their difference. An approximate value of S_θ is given by the ratio $\sigma_{o\theta} / \sigma_{ox}$. A more accurate value is obtained by varying S_θ slightly until the uniaxial and lateral test responses match. Once this is achieved, the value of S_r was varied until the hydrostatic test response matched the other two as shown in Fig. A.6b. In this case $S_\theta = 1.09$ and $S_r = 0.88$.

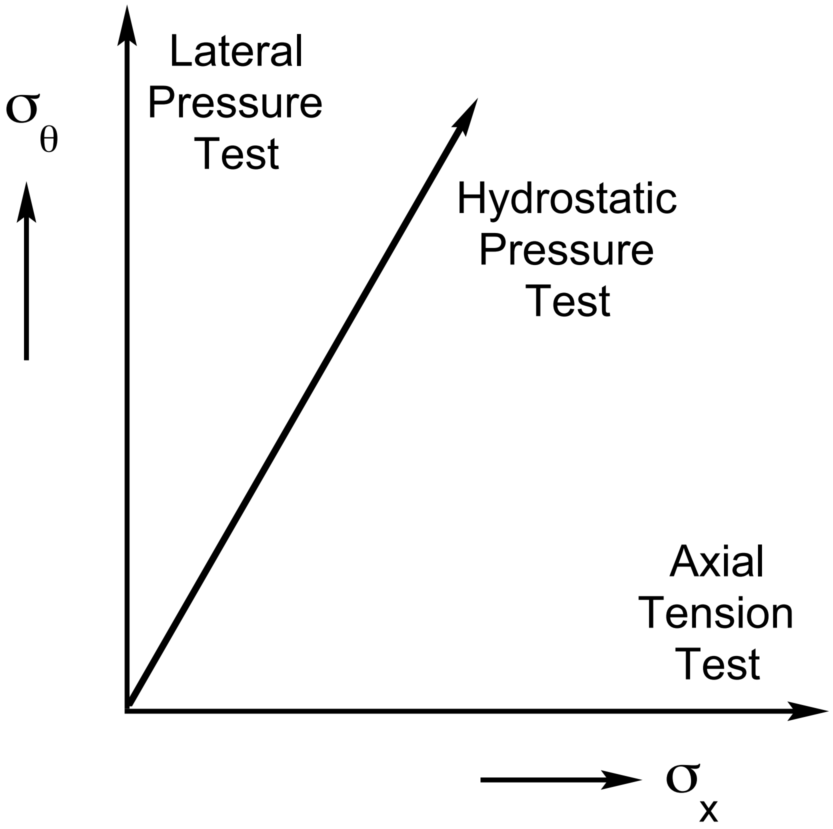

Fig. A.1 Radial stress paths used to determine plastic anisotropy in tubes (from Appendix B of Kyriakides and Corona, 2007).

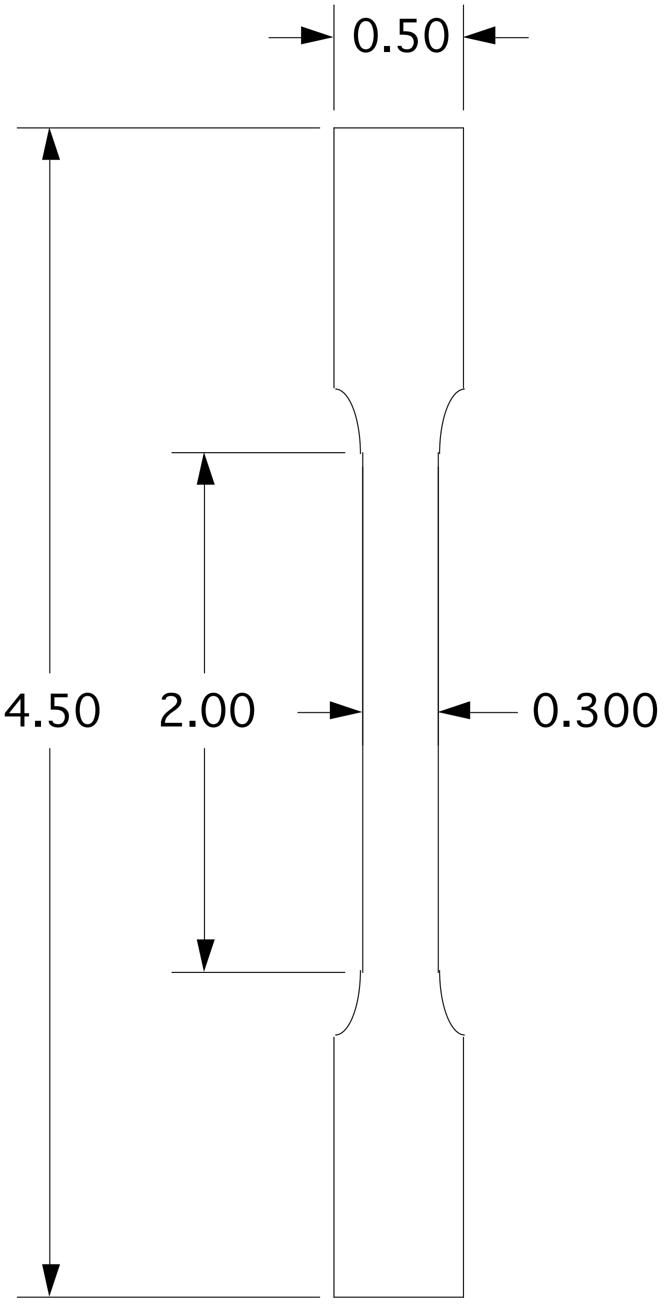

Fig. A.2 Uniaxial test specimen geometry.

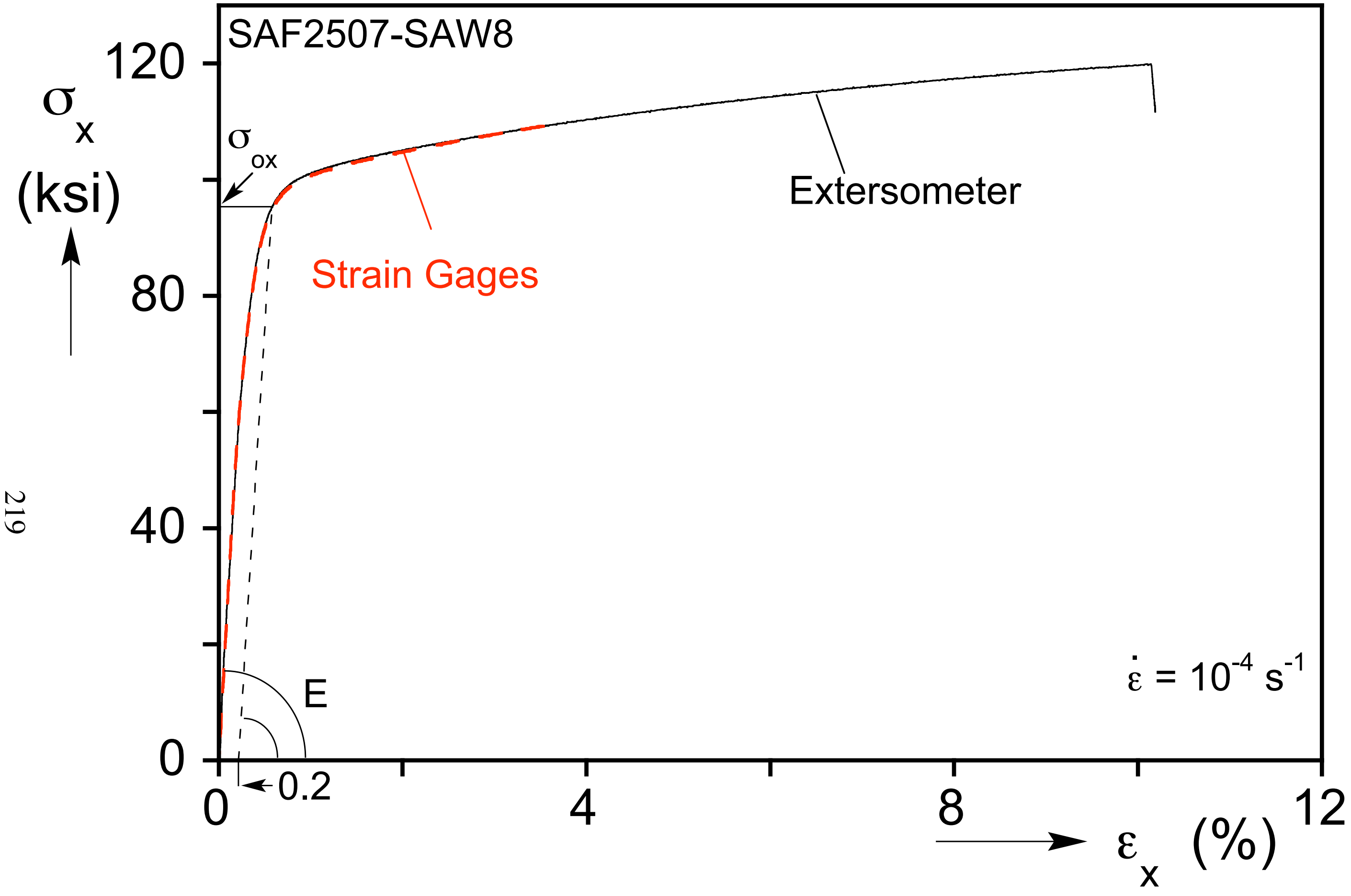

Fig. A.3 Material response of SAF 2507-SAW8 based on strain gages and extensometer.

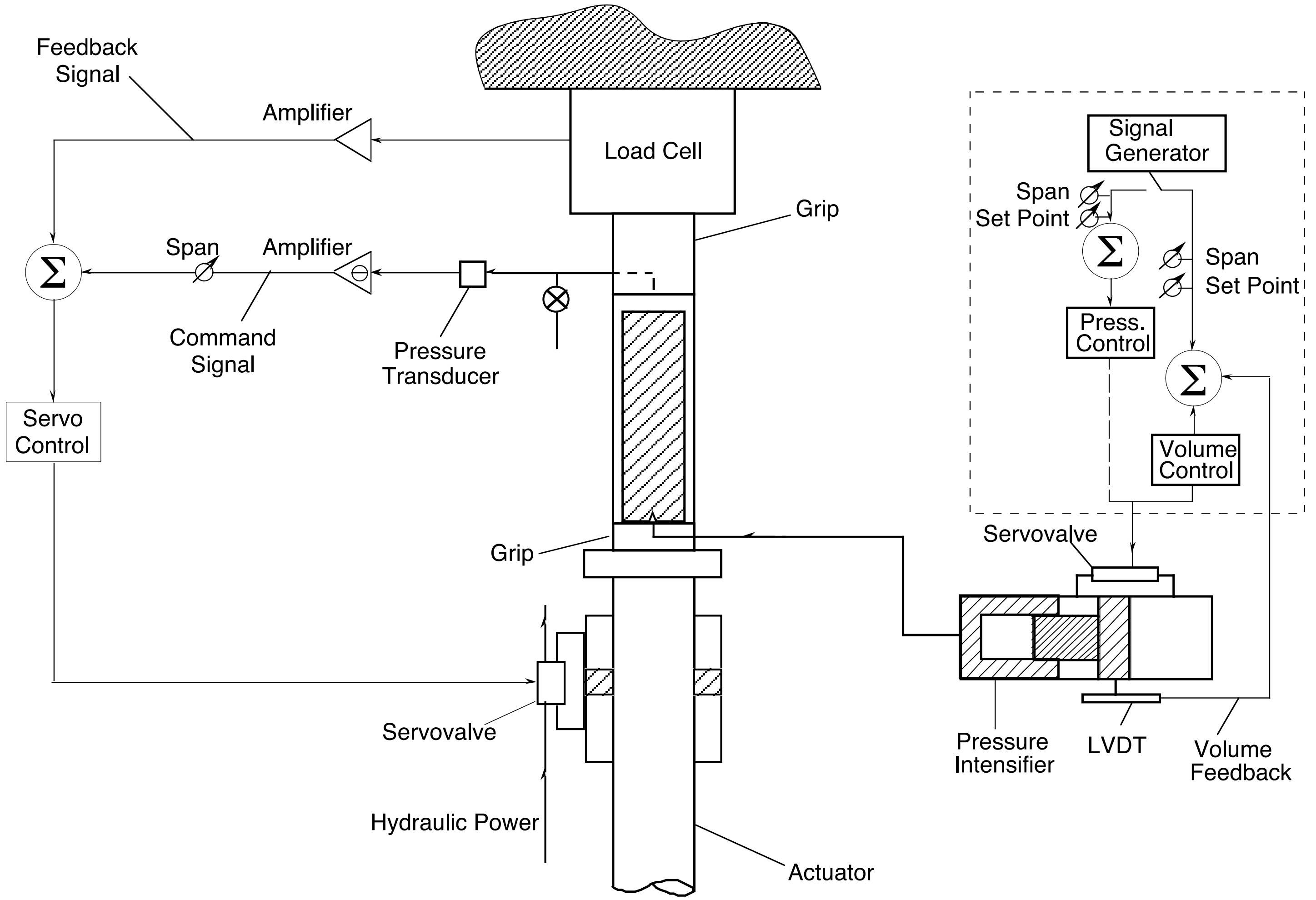

Fig. A.4 Schematic of lateral and hydrostatic pressure experimental set-up (from Kyriakides and Corona, 2007).

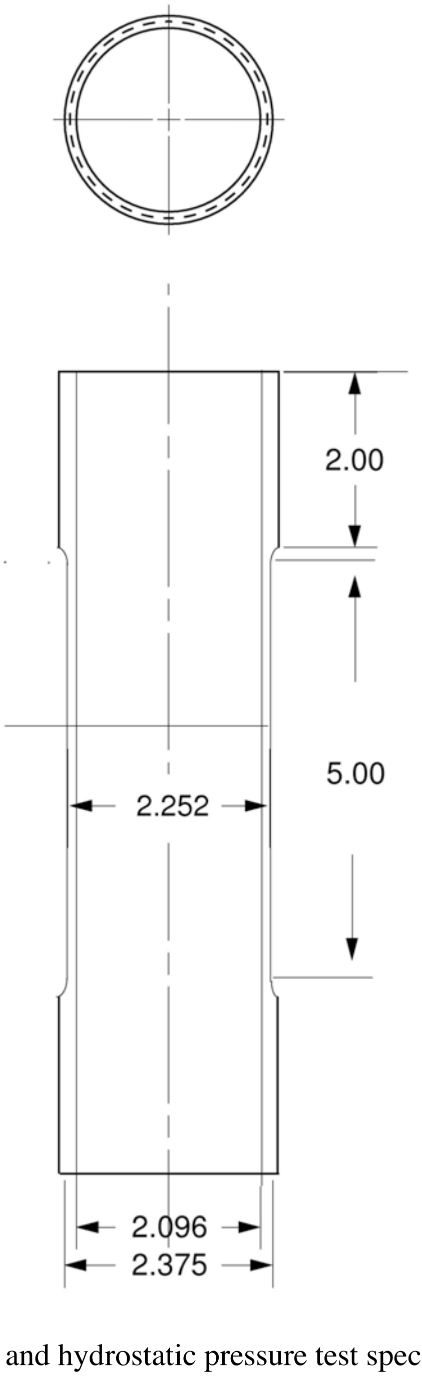

Fig. A.5 Lateral and hydrostatic pressure test specimen geometry.

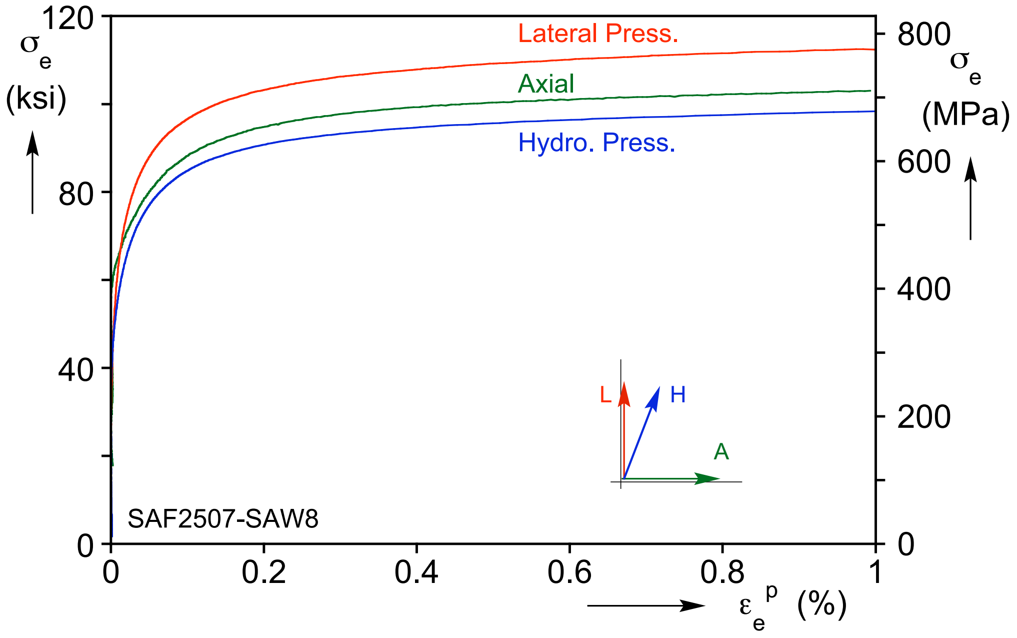

(a)

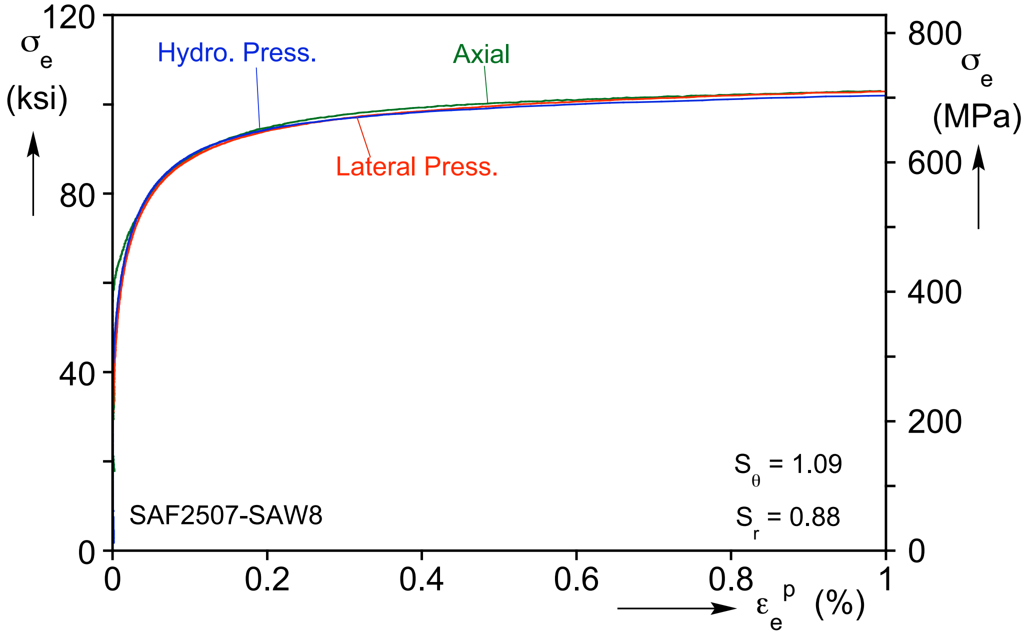

(b)

Fig. A.6 (a) Equivalent stress-plastic strain responses from three radial tests on SAF2507-SAW8 exhibiting anisotropy. (b) Coalescence of the three responses after anisotropy parameters are introduced.

Appendix B: Axisymmetric Wrinkling Bifurcation Buckling Analysis

The first plastic instability encountered in a long circular tube either loaded under pure compression or in combination with internal pressure is axisymmetric wrinkling. Such bifurcations are routinely evaluated using the J_2 deformation theory of plasticity (Batdorf, 1949; Hutchinson, 1974; Kyriakides and Corona, 2007). The tube is idealized as a long cylindrical shell with mid-surface radius (R) and wall thickness (t). Axisymmetric buckling has the following mode:

$$\tilde{u} = b \sin\frac{\pi x}{\lambda} \text{ and } \tilde{w} = a \cos\frac{\pi x}{\lambda} \tag{B.1}$$

where u and w are respectively the axial and radial displacements (e.g., see Chapters 11 and 12 of Kyriakides and Corona, 2007). The resultant critical stress (σ_C) and half-wavelength of the buckling mode (λ) are respectively:

$$\sigma_C = \left[\frac{C_{11}C_{22} - C_{12}^2}{3}\right]^{1/2}\left(\frac{t}{R}\right) \text{ and } \lambda = \pi\left[\frac{C_{11}^2}{12(C_{11}C_{22} - C_{12}^2)}\right]^{1/4}(Rt)^{1/2} \tag{B.2}$$

where $[C_{\alpha\beta}(\sigma_e)]$ are the incremental deformation theory moduli which are derived from the inverse of the following J_2 deformation theory:

$$\begin{Bmatrix} d\varepsilon_x \\ d\varepsilon_\theta \end{Bmatrix} = \frac{1}{E_s}\begin{bmatrix} 1 + q(2\sigma_x - \zeta\sigma_\theta)^2 & -\hat{\nu}_s + q(2\sigma_x - \zeta\sigma_\theta)(2\eta\sigma_\theta - \zeta\sigma_x) \\ -\hat{\nu}_s + q(2\sigma_x - \zeta\sigma_\theta)(2\eta\sigma_\theta - \zeta\sigma_x) & \eta + \frac{E_s}{E}(1-\eta) + q(2\eta\sigma_\theta - \zeta\sigma_x)^2 \end{bmatrix}\begin{Bmatrix} d\sigma_x \\ d\sigma_\theta \end{Bmatrix} \tag{B.3}$$

here

$$\sigma_e = \left[\sigma_x{}^2 - \left(1 + \frac{1}{S_\theta^2} - \frac{1}{S_r^2}\right)\sigma_x\sigma_\theta + \frac{1}{S_\theta^2}\sigma_\theta{}^2\right]^{1/2} \tag{B.4}$$

and

$$\sigma_x = \frac{-F}{2\pi Rt} \text{ and } \sigma_\theta = \frac{PR}{t} \tag{B.5}$$

where F is the net axial force and P is the internal pressure. $\{S_\theta, S_r\}$ are anisotropy parameters and they are determined as outlined in Appendix A. In addition,

$$\eta = \frac{1}{S_\theta^2},\ \zeta = \left(1 + \frac{1}{S_\theta^2} - \frac{1}{S_r^2}\right),\ q = \frac{1}{4\sigma_e^2}\left[\frac{E_s(\sigma_e)}{E_t(\sigma_e)} - 1\right],\ \hat{v}_s = \frac{\zeta}{2} + \frac{E_s}{E}\left(v - \frac{\zeta}{2}\right) \tag{B.6}$$

with E_t and E_s being respectively the tangent and secant moduli. In the present calculations E_t is evaluated using the Dafalias and Popov two-surface model calibrated to the initial monotonic stress-strain response of the material (see (6.31)).

Appendix C: Stress-Shortening Responses and Evolution of Wrinkles for Tubes Cycled Axially

This Appendix presents the stress-shortening responses and the evolution of wrinkles for 8 of the tubes tested under pure axial cycling.

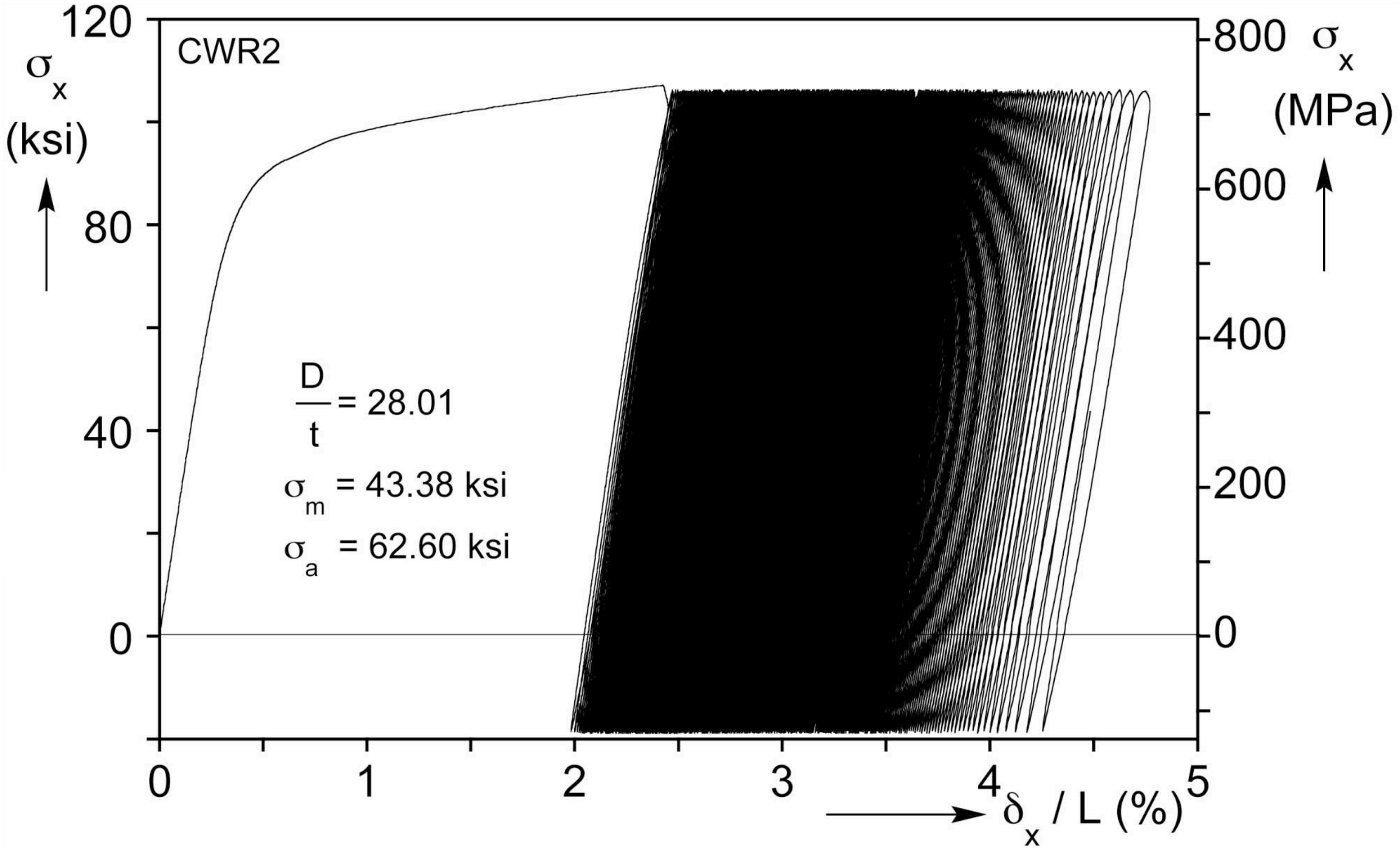

Fig. C.1a Axial stress-shortening response from cyclic loading experiment CWR2.

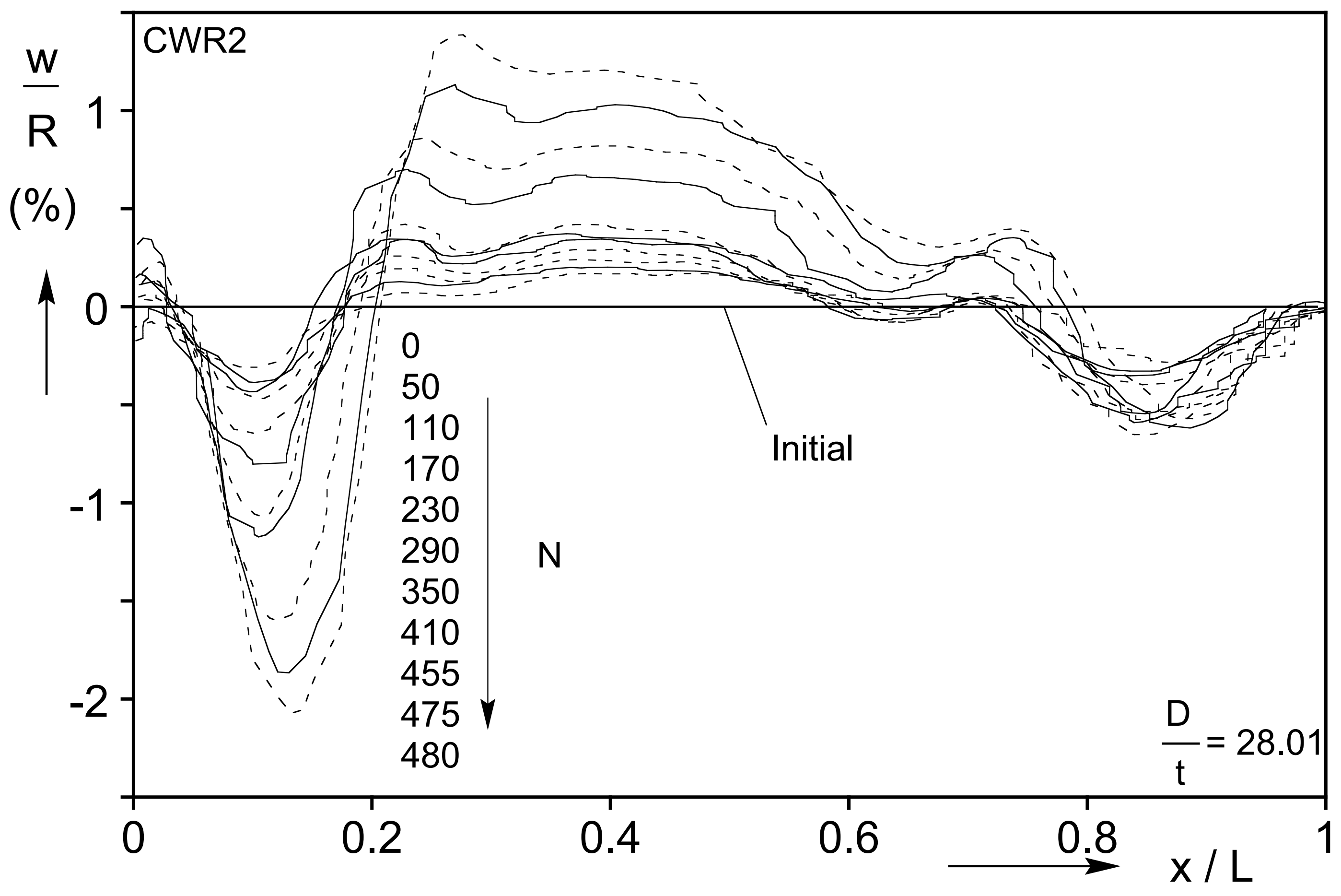

Fig. C.1b Axial scans showing evolution of wrinkles during the cycling for CWR2.

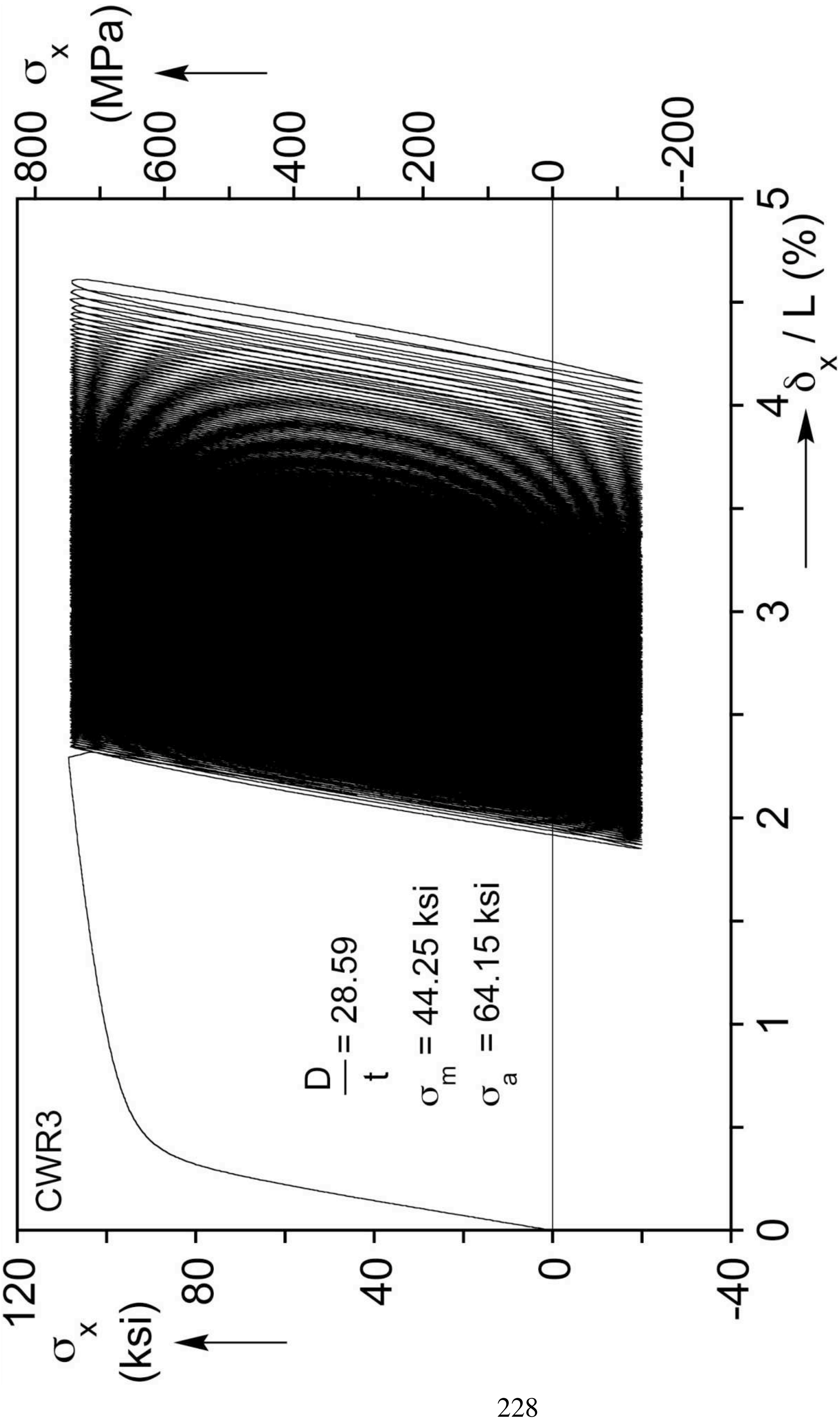

Fig. C.2a Axial stress-shortening response from cyclic loading experiment CWR3.

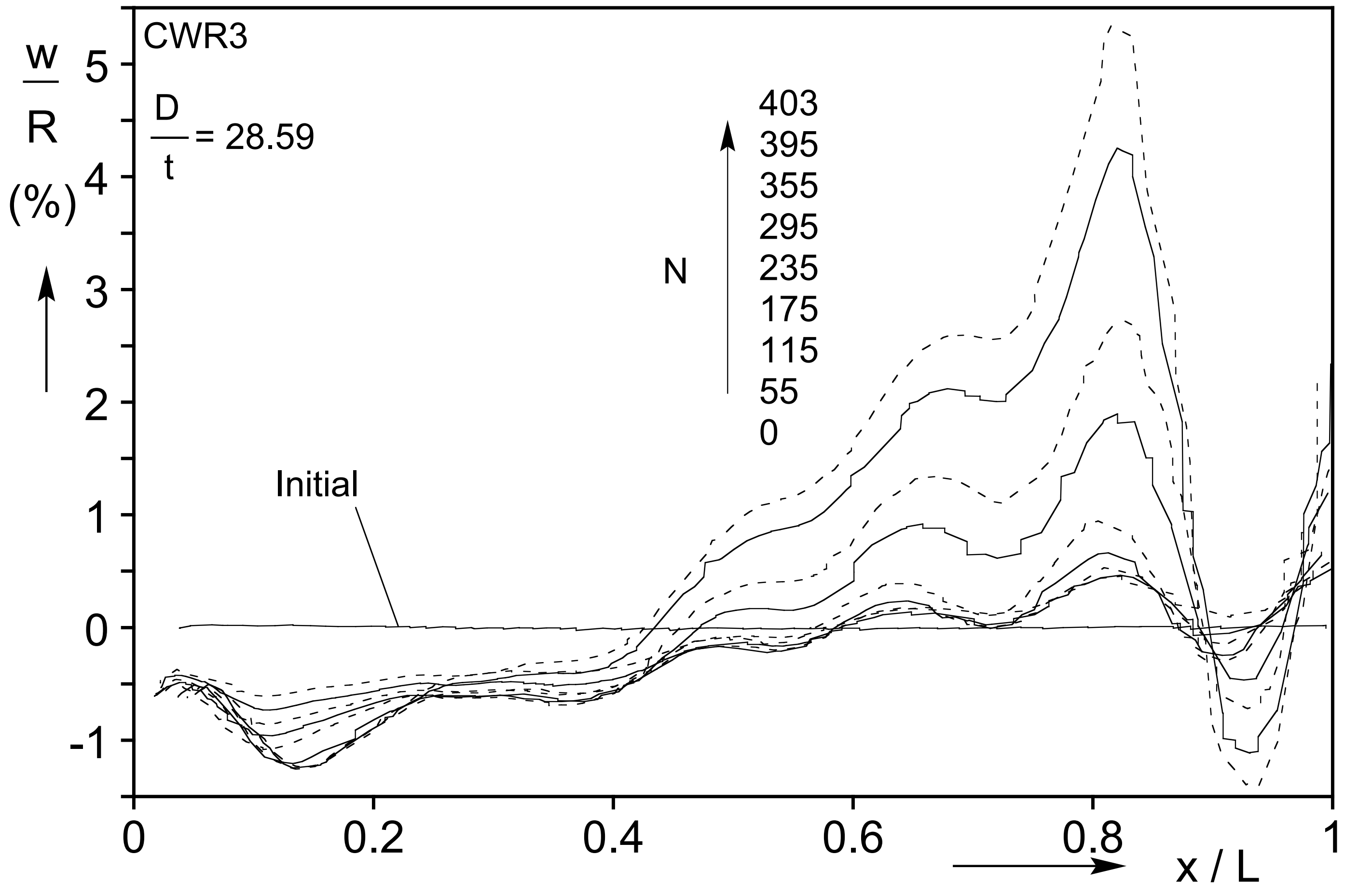

Fig. C.2b Axial scans showing evolution of wrinkles during the cycling for CWR3.

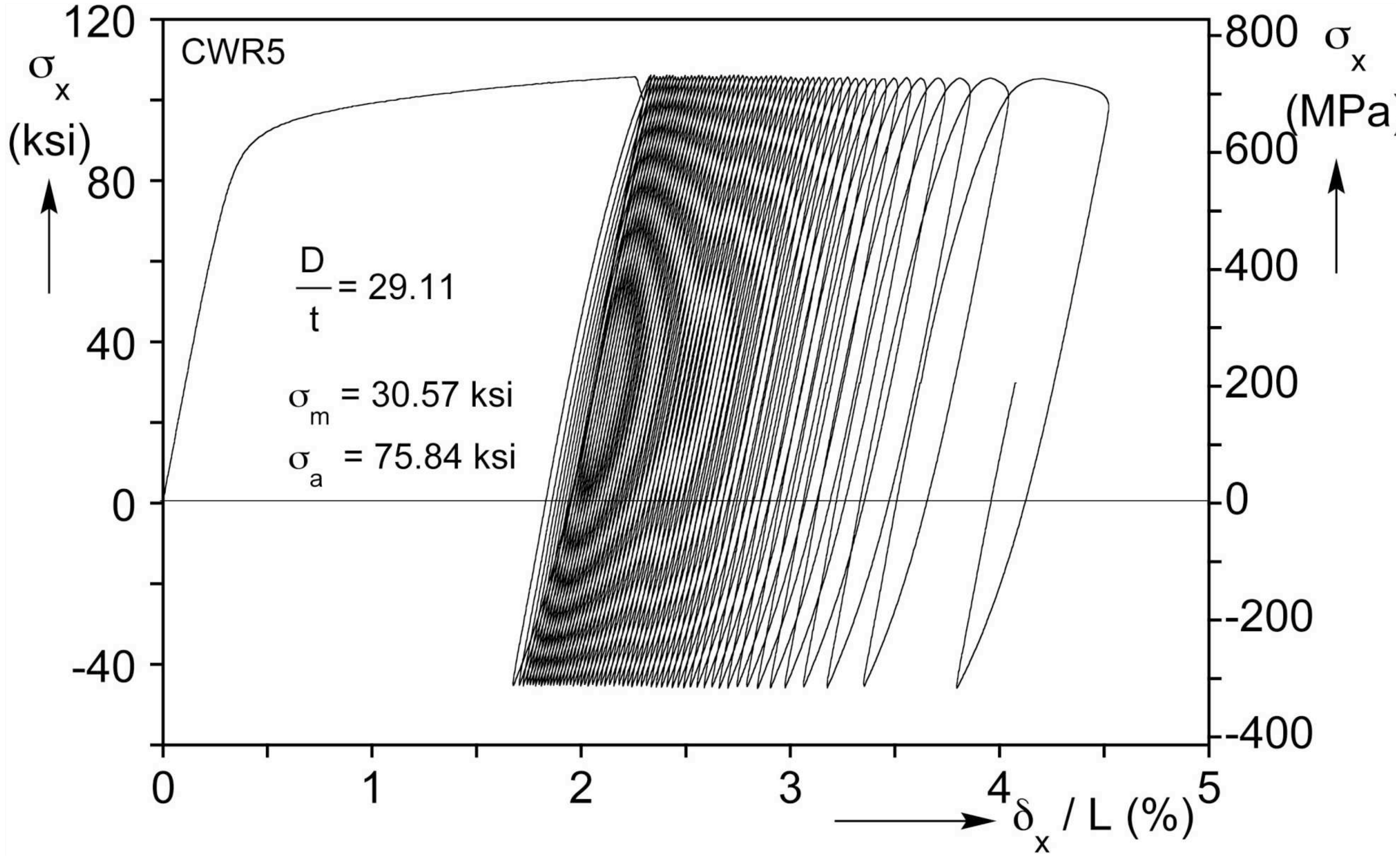

Fig. C.3a Axial stress-shortening response from cyclic loading experiment CWR5.

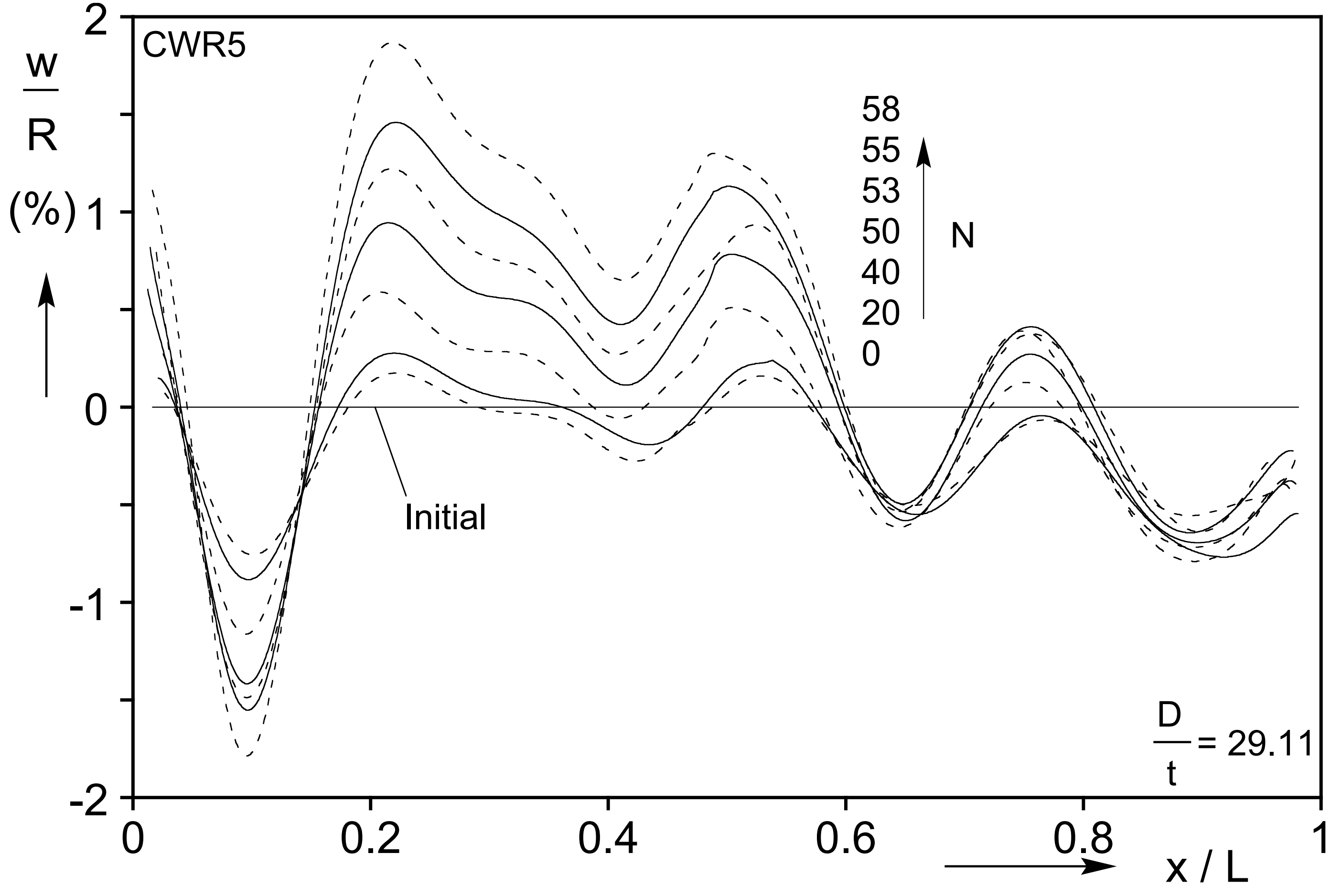

Fig. C.3b Axial scans showing evolution of wrinkles during the cycling for CWR5.

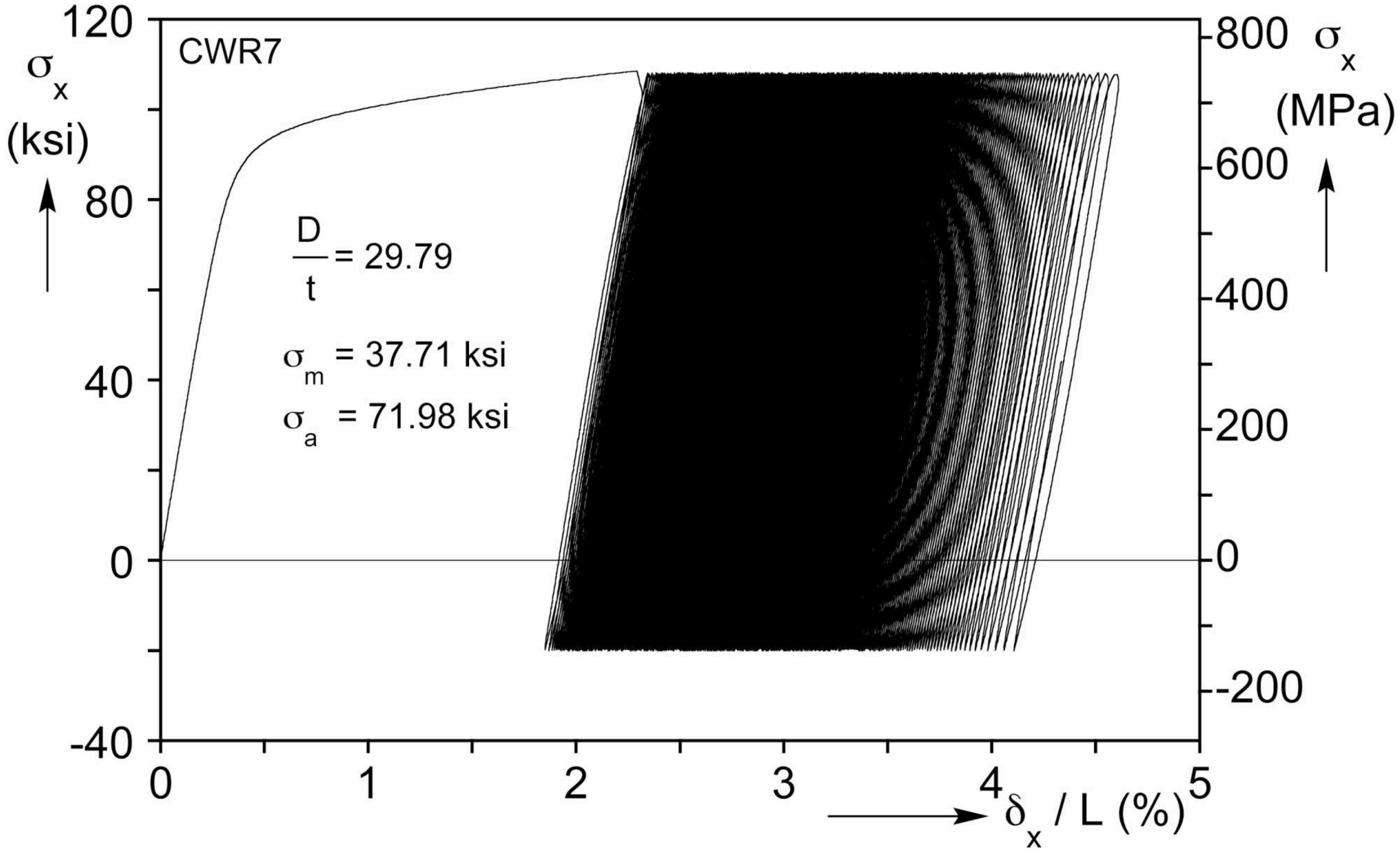

Fig. C.4a Axial stress-shortening response from cyclic loading experiment CWR7.

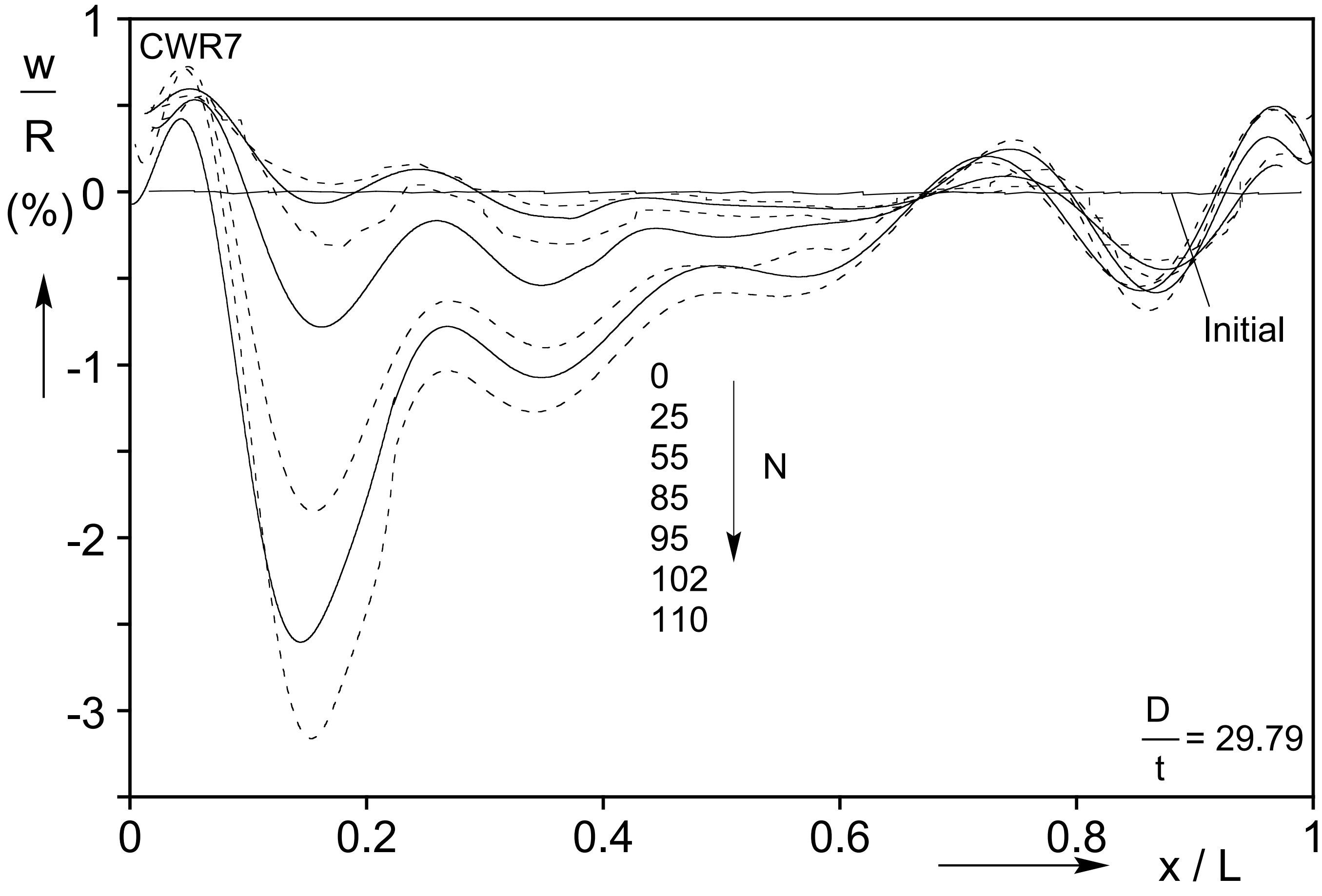

Fig. C.4b Axial scans showing evolution of wrinkles during the cycling for CWR7.

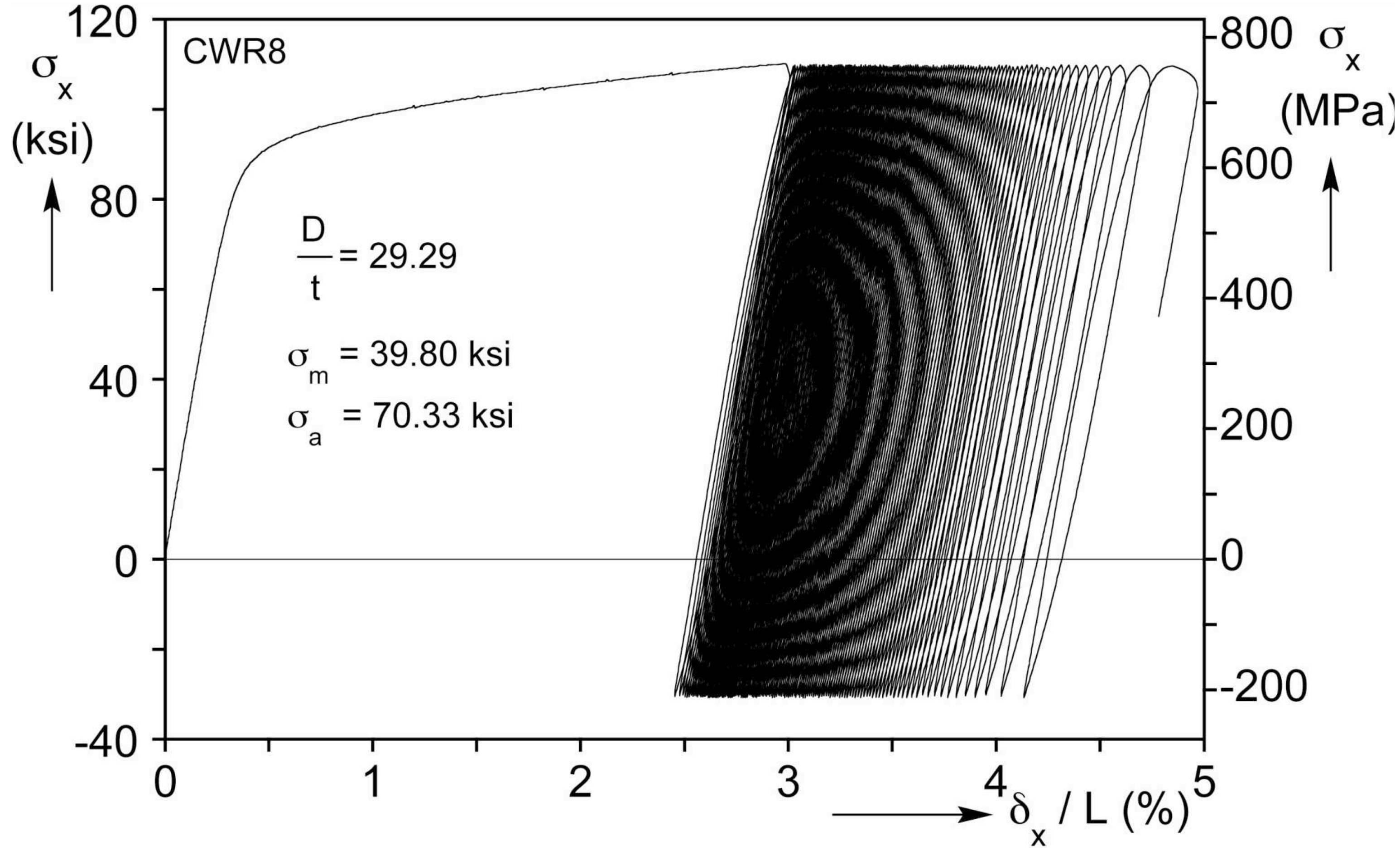

Fig. C.5a Axial stress-shortening response from cyclic loading experiment CWR8.

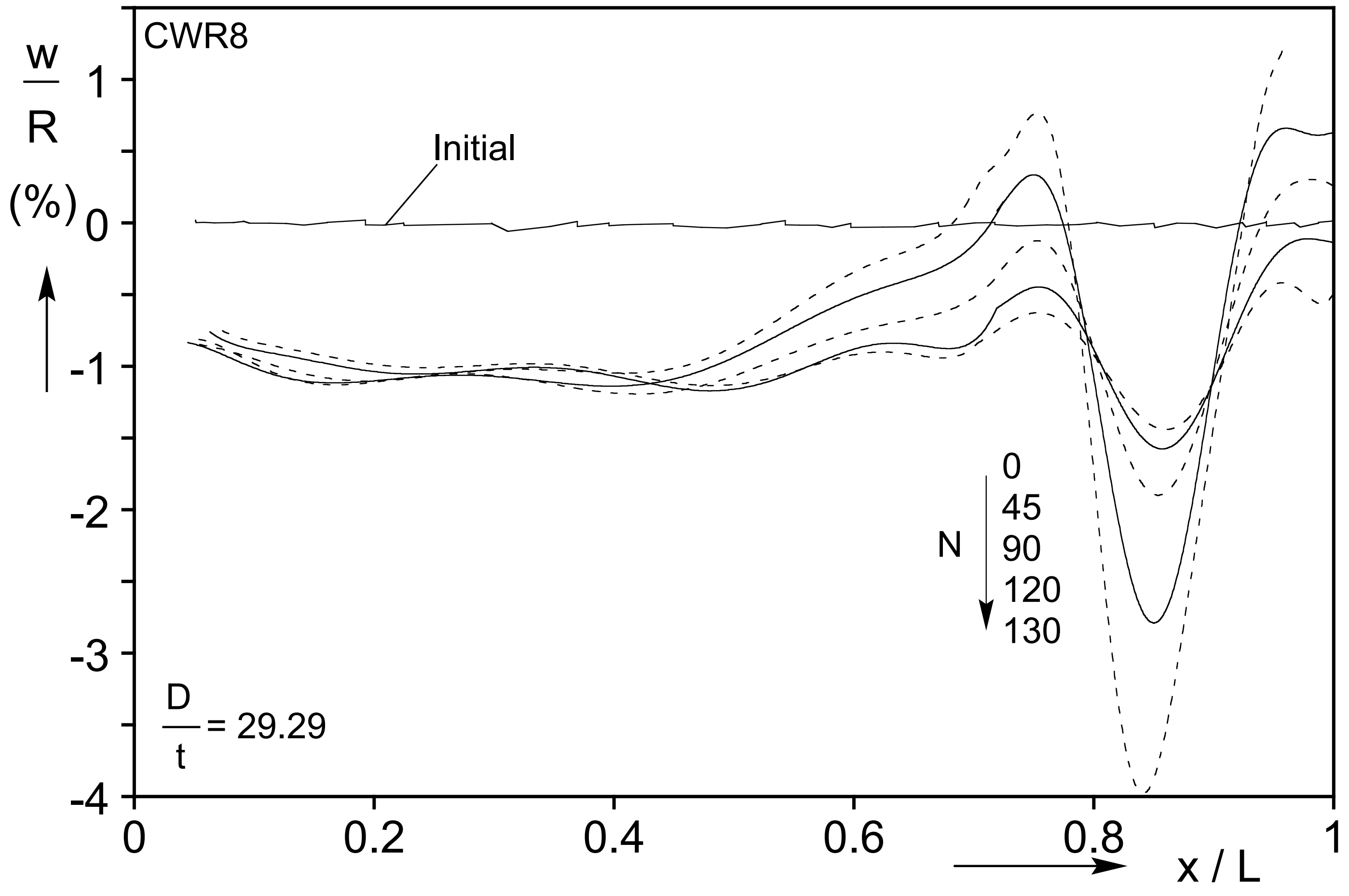

Fig. C.5b Axial scans showing evolution of wrinkles during the cycling for CWR8.

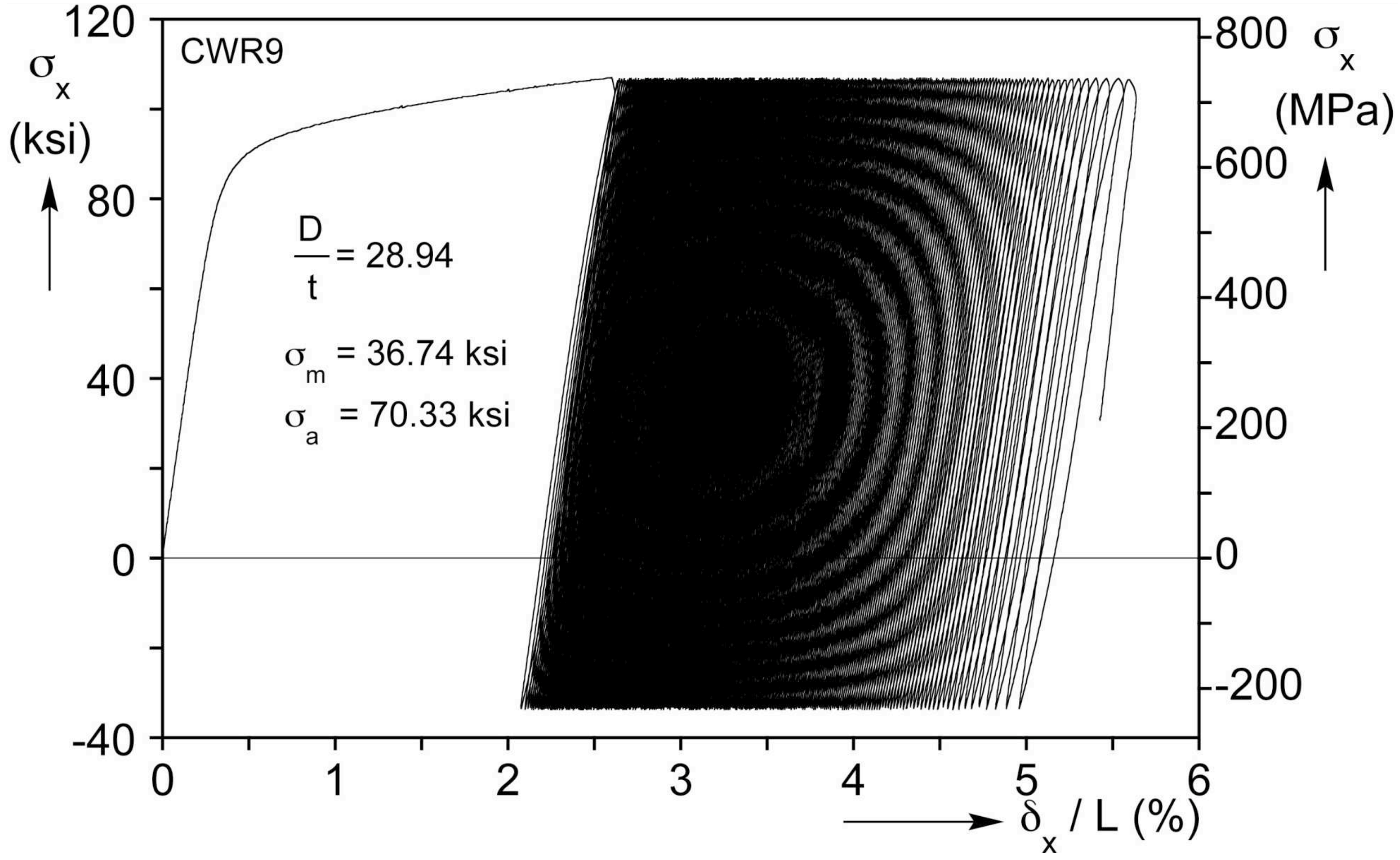

Fig. C.6a Axial stress-shortening response from cyclic loading experiment CWR9.

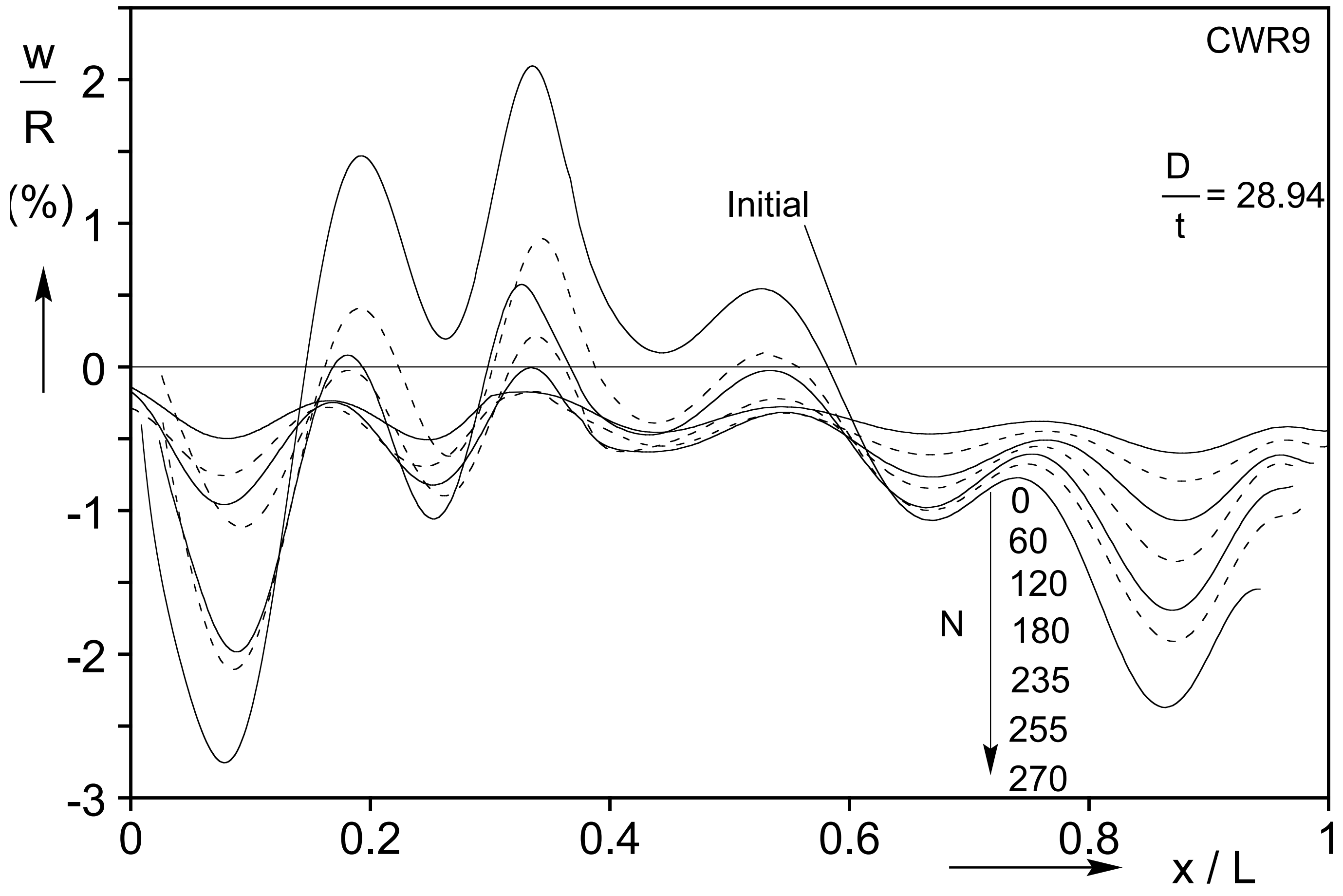

Fig. C.6b Axial scans showing evolution of wrinkles during the cycling for CWR9.

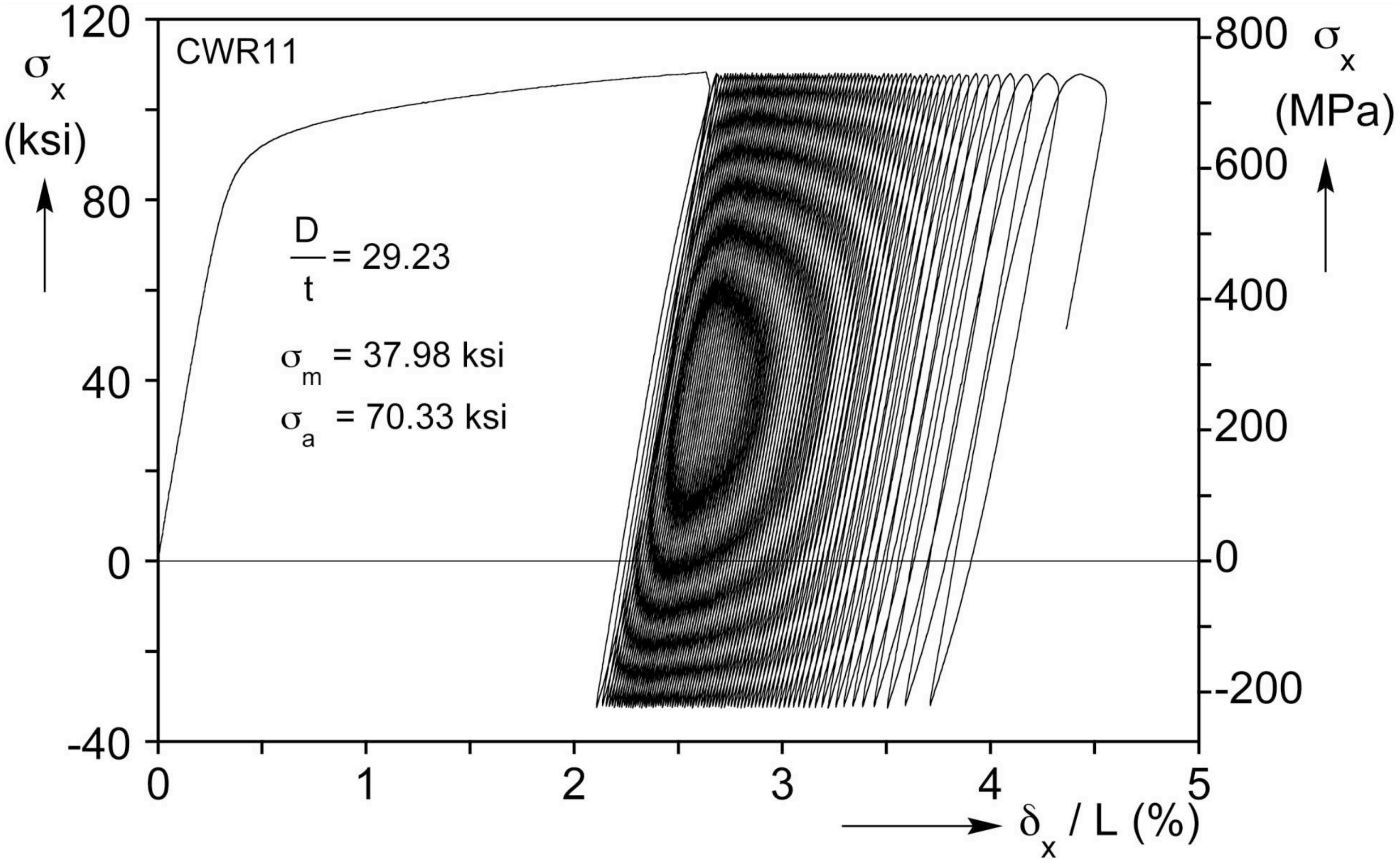

Fig. C.7a Axial stress-shortening response from cyclic loading experiment CWR11.

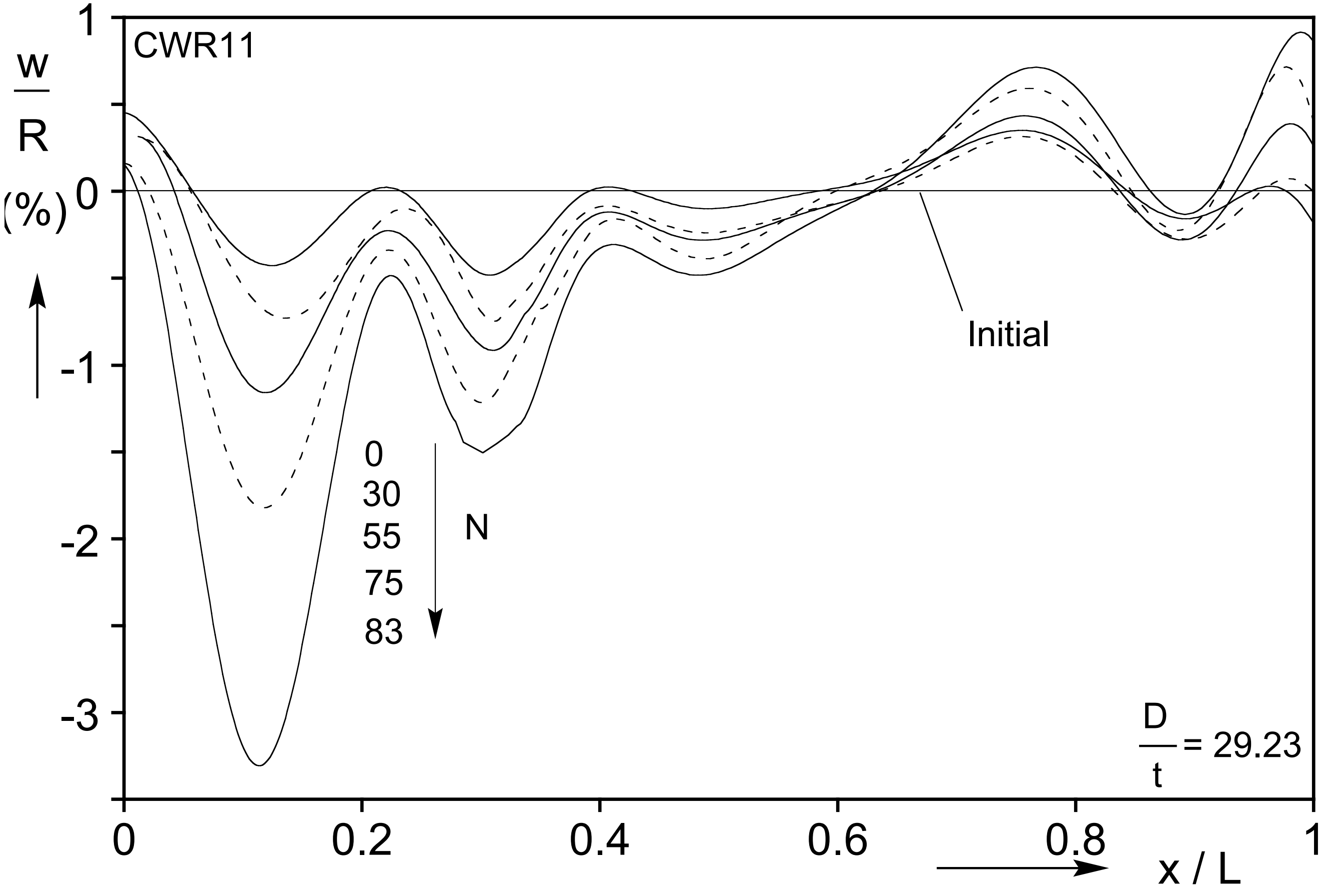

Fig. C.7b Axial scans showing evolution of wrinkles during the cycling for CWR11.

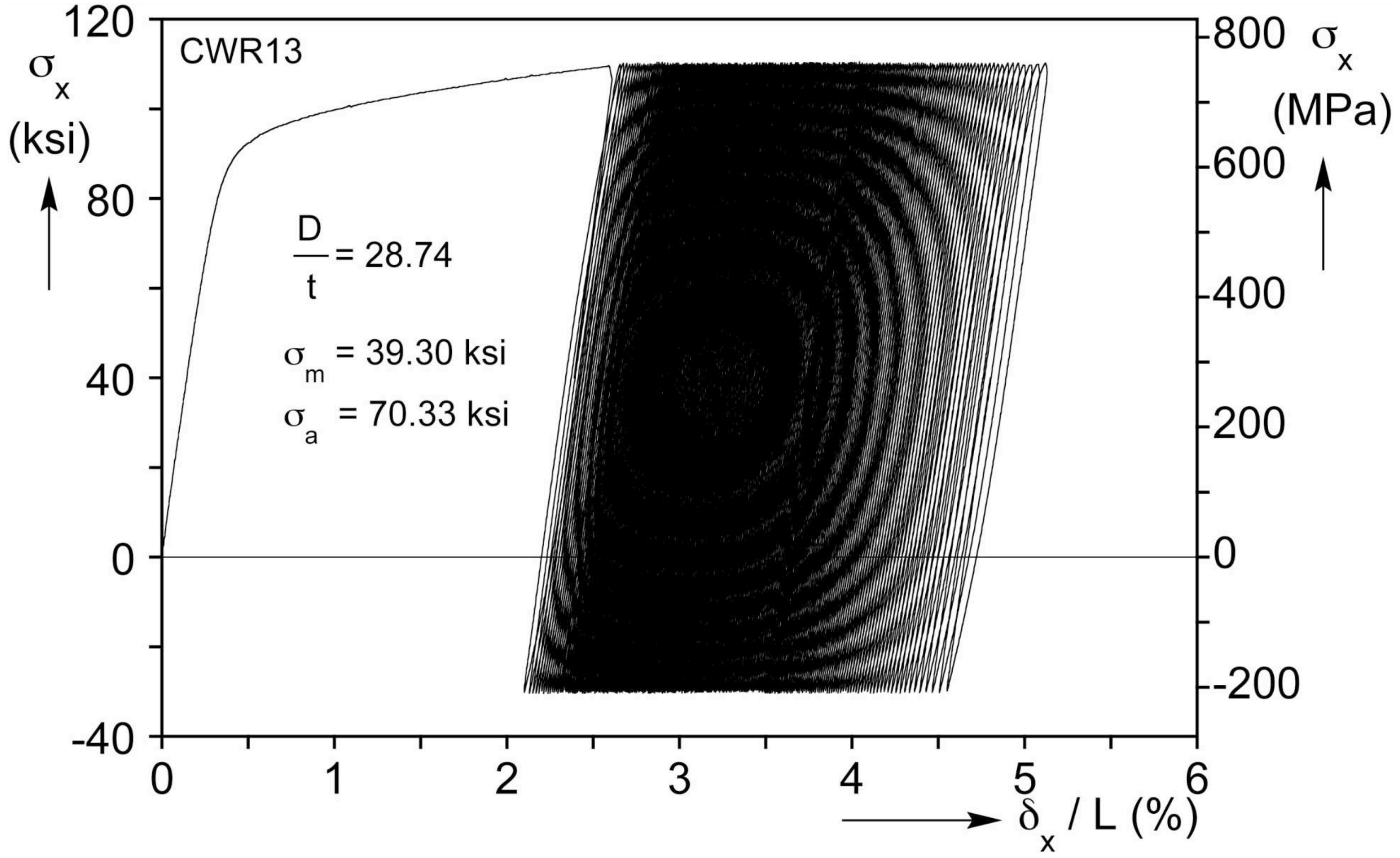

Fig. C.8a Axial stress-shortening response from cyclic loading experiment CWR13.

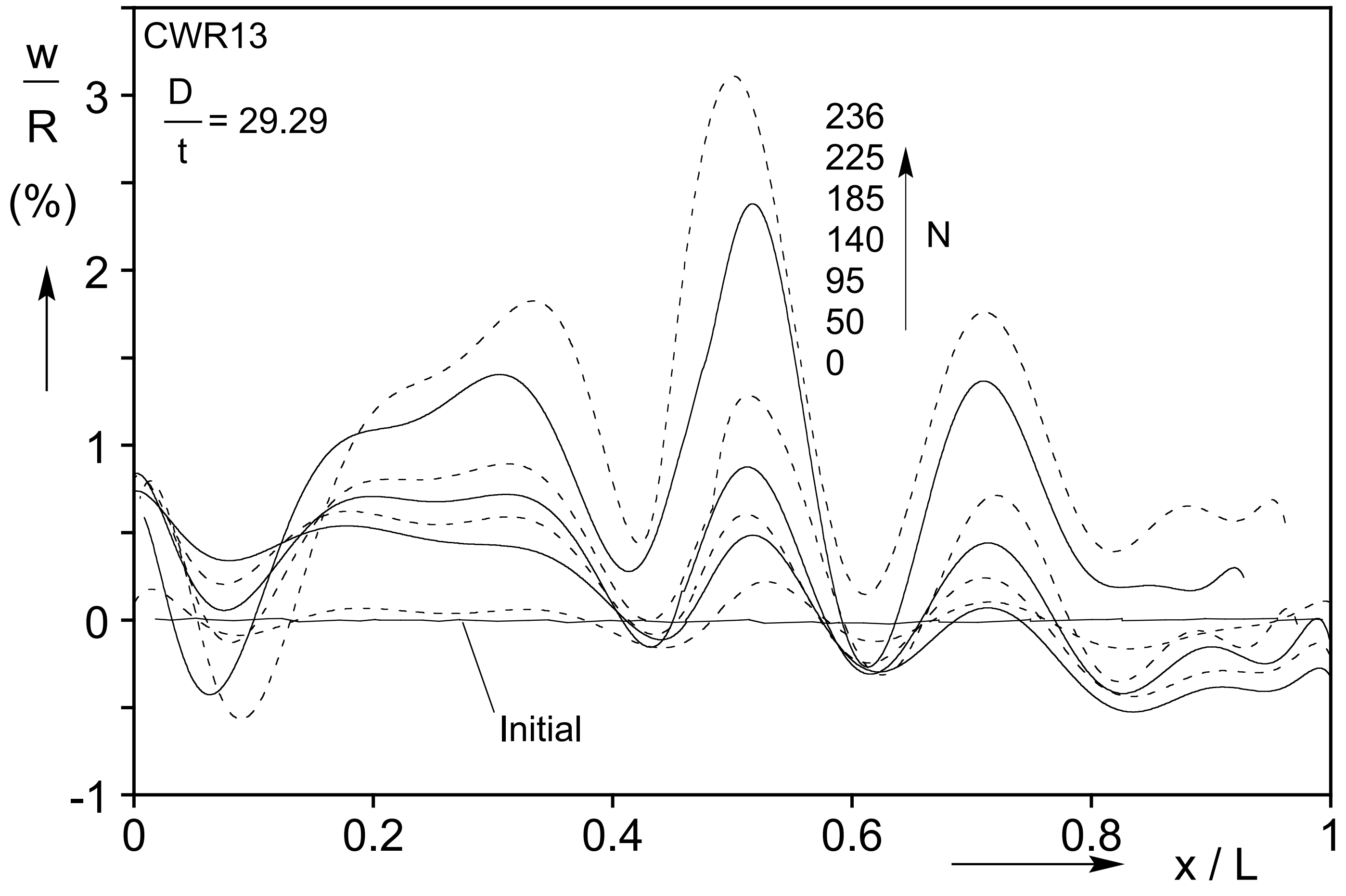

Fig. C.8b Axial scans showing evolution of wrinkles during the cycling for CWR13.

Appendix D: Stress-Shortening Responses and Evolution of Wrinkles for Tubes Cycled Axially with Internal Pressure

This Appendix presents the stress-shortening responses and the evolution of wrinkles for 12 of the tubes tested under axial cycling and constant internal pressure.

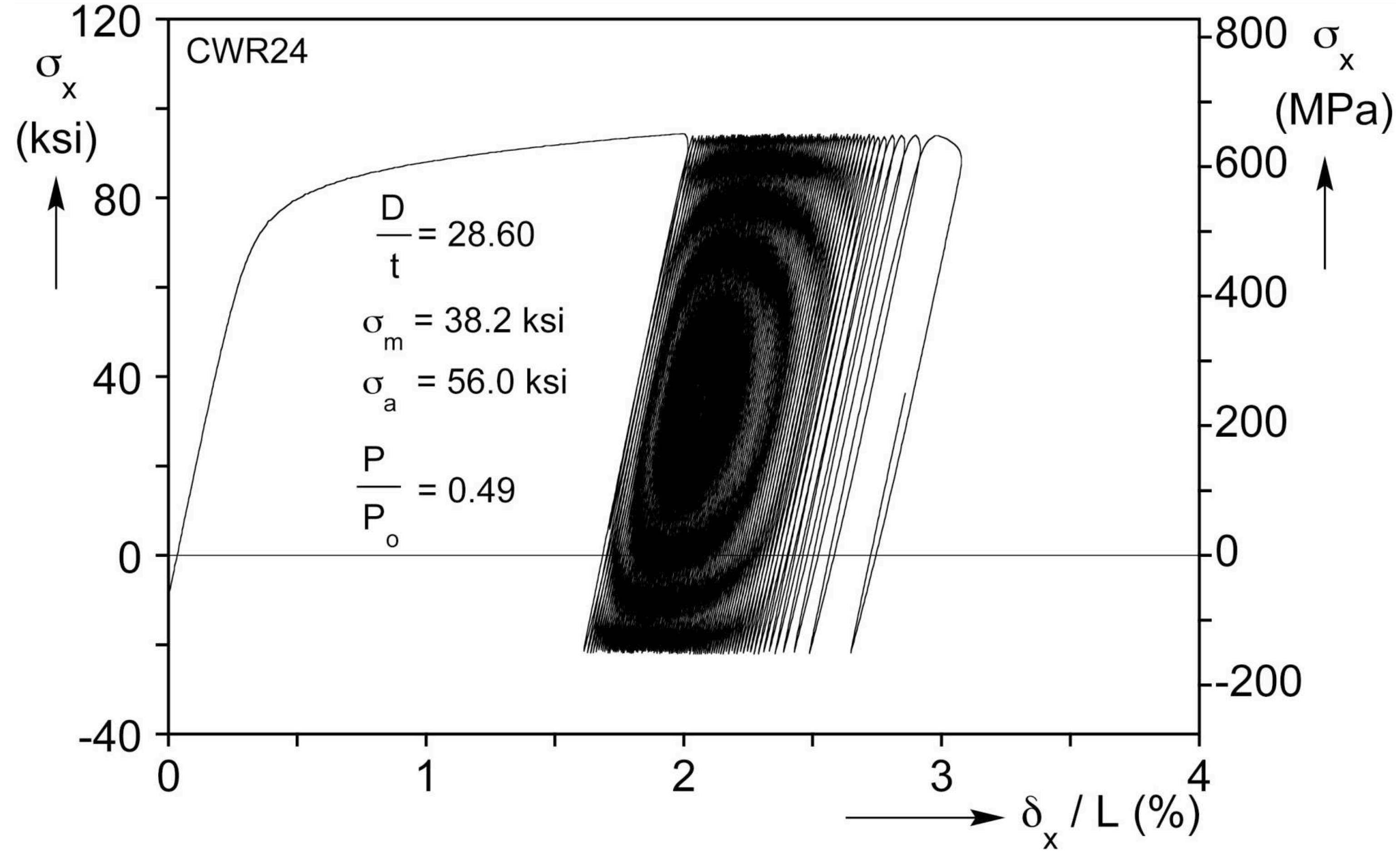

Fig. D.1a Axial stress-shortening response from cyclic loading experiment CWR24.

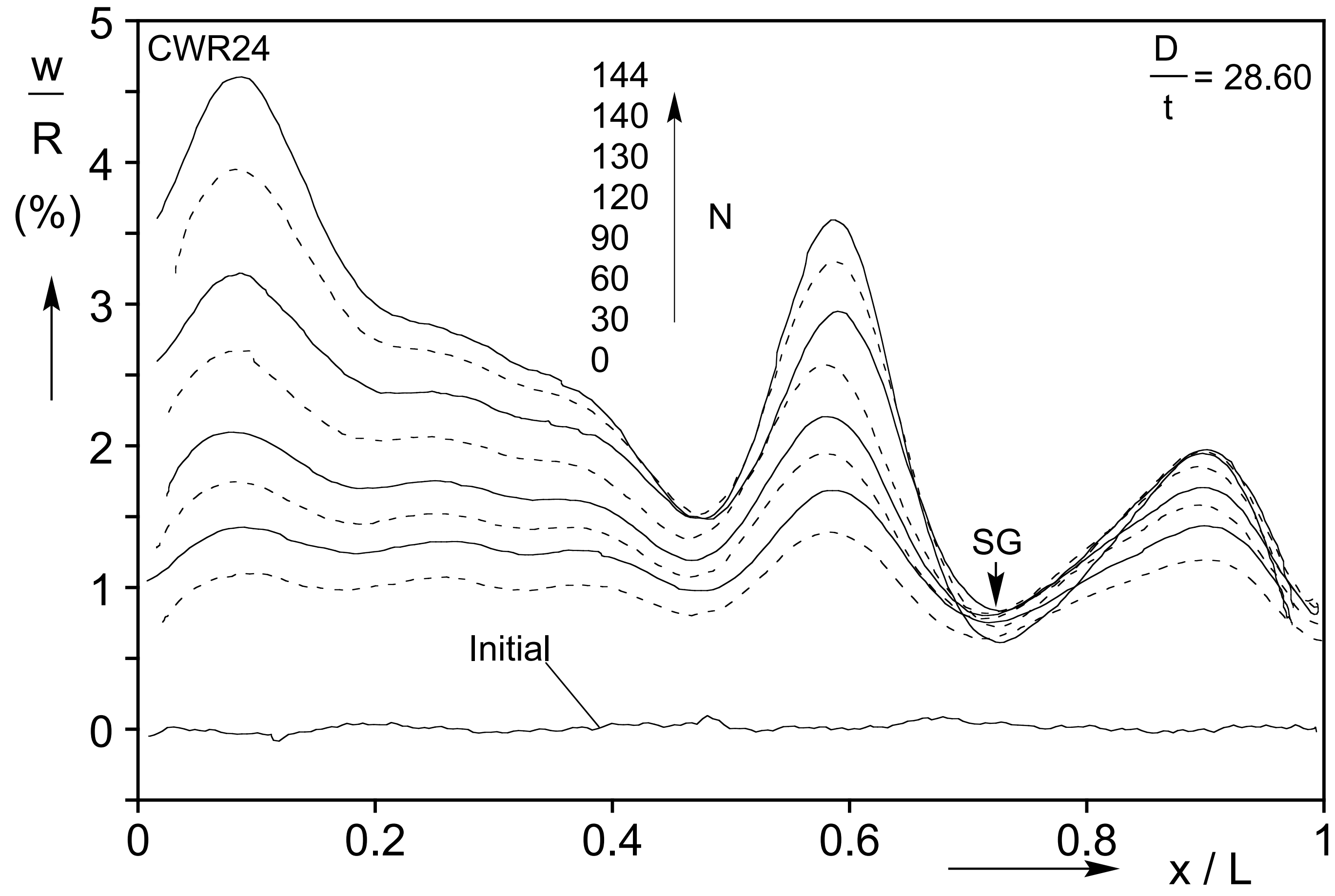

Fig. D.1b Axial scans showing evolution of wrinkles during the cycling for CWR24.

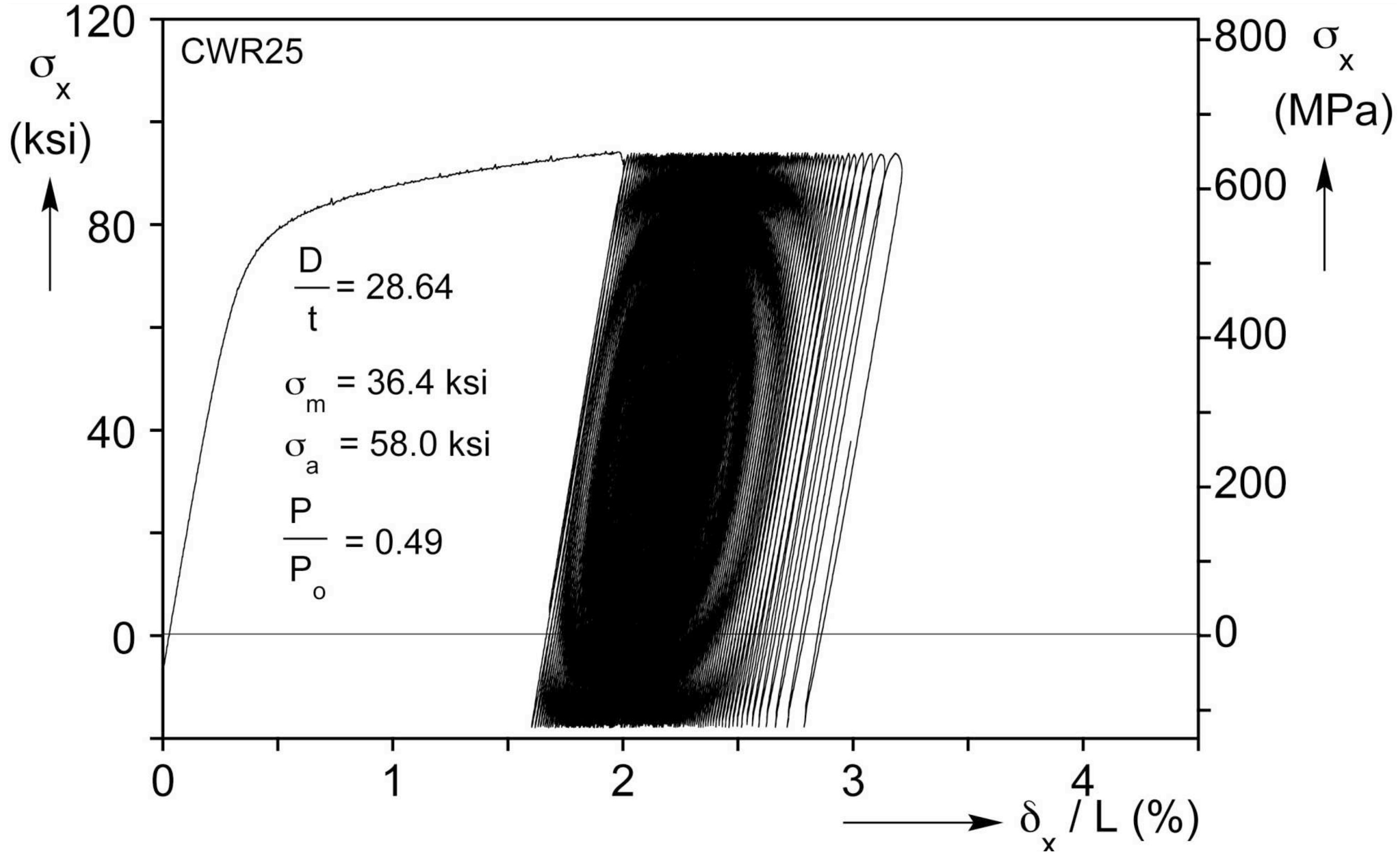

Fig. D.2a Axial scans showing evolution of wrinkles during the cycling for CWR25.

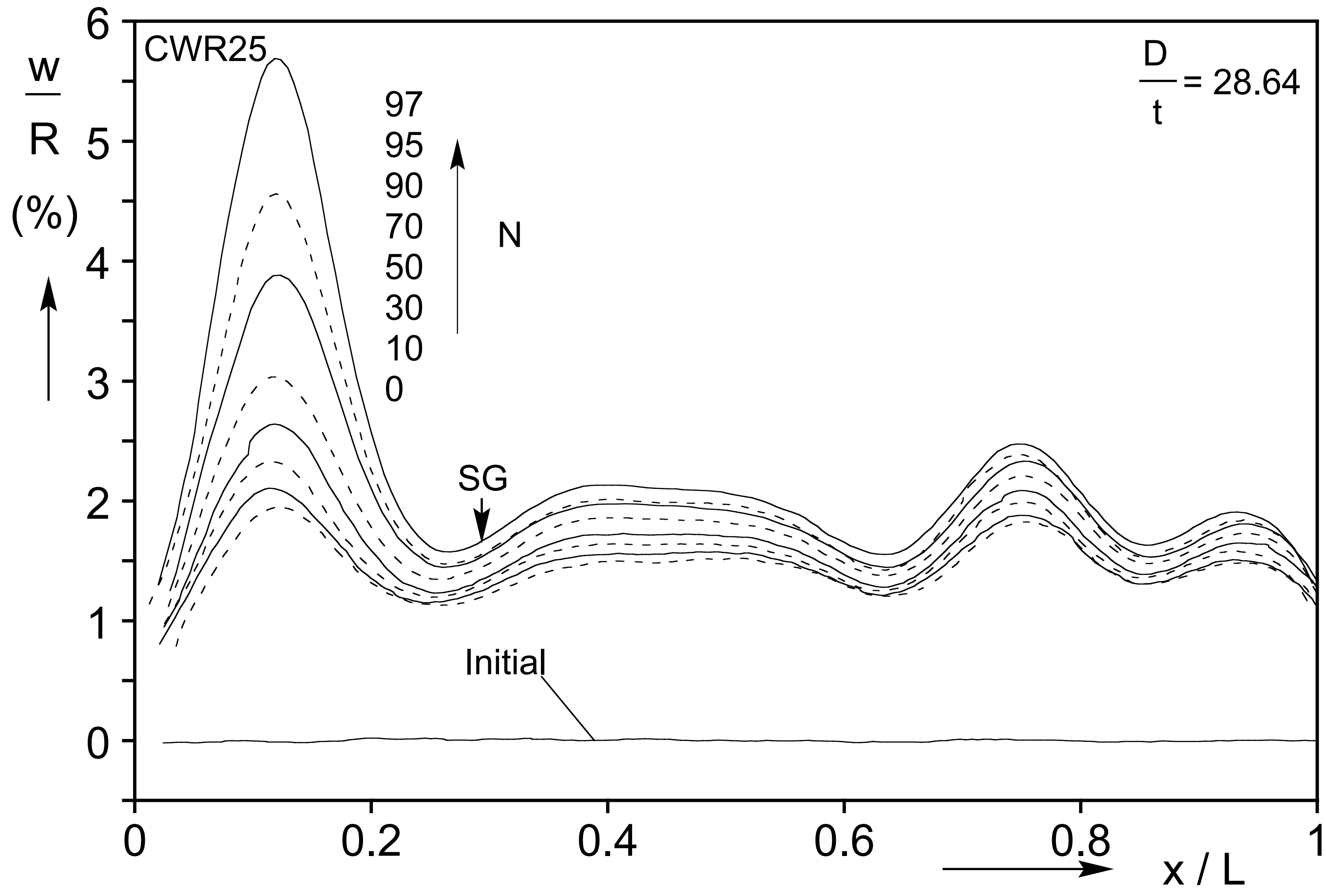

Fig. D.2b Axial scans showing evolution of wrinkles during the cycling for CWR25.

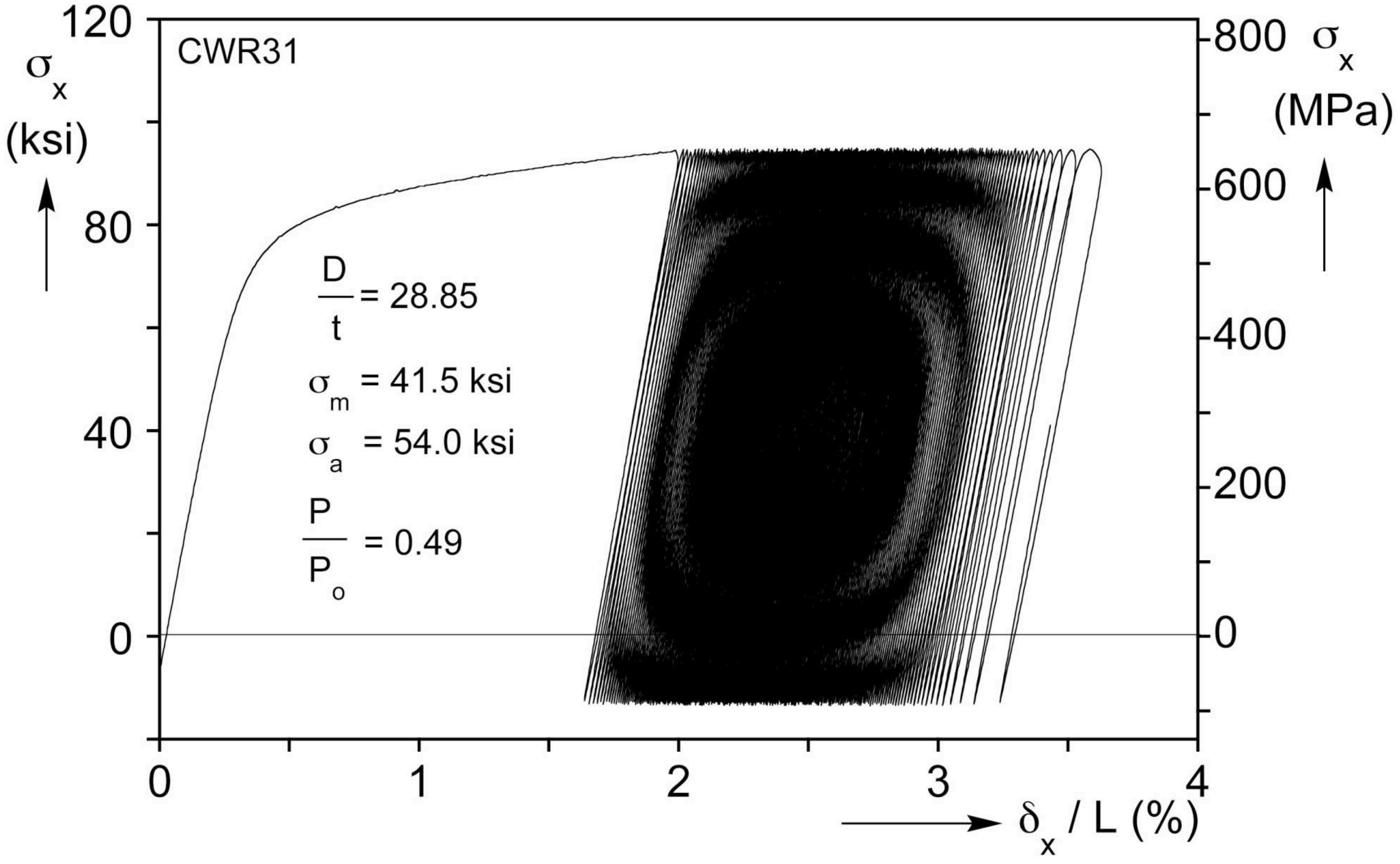

Fig. D.3a Axial stress-shortening response from cyclic loading experiment CWR31.

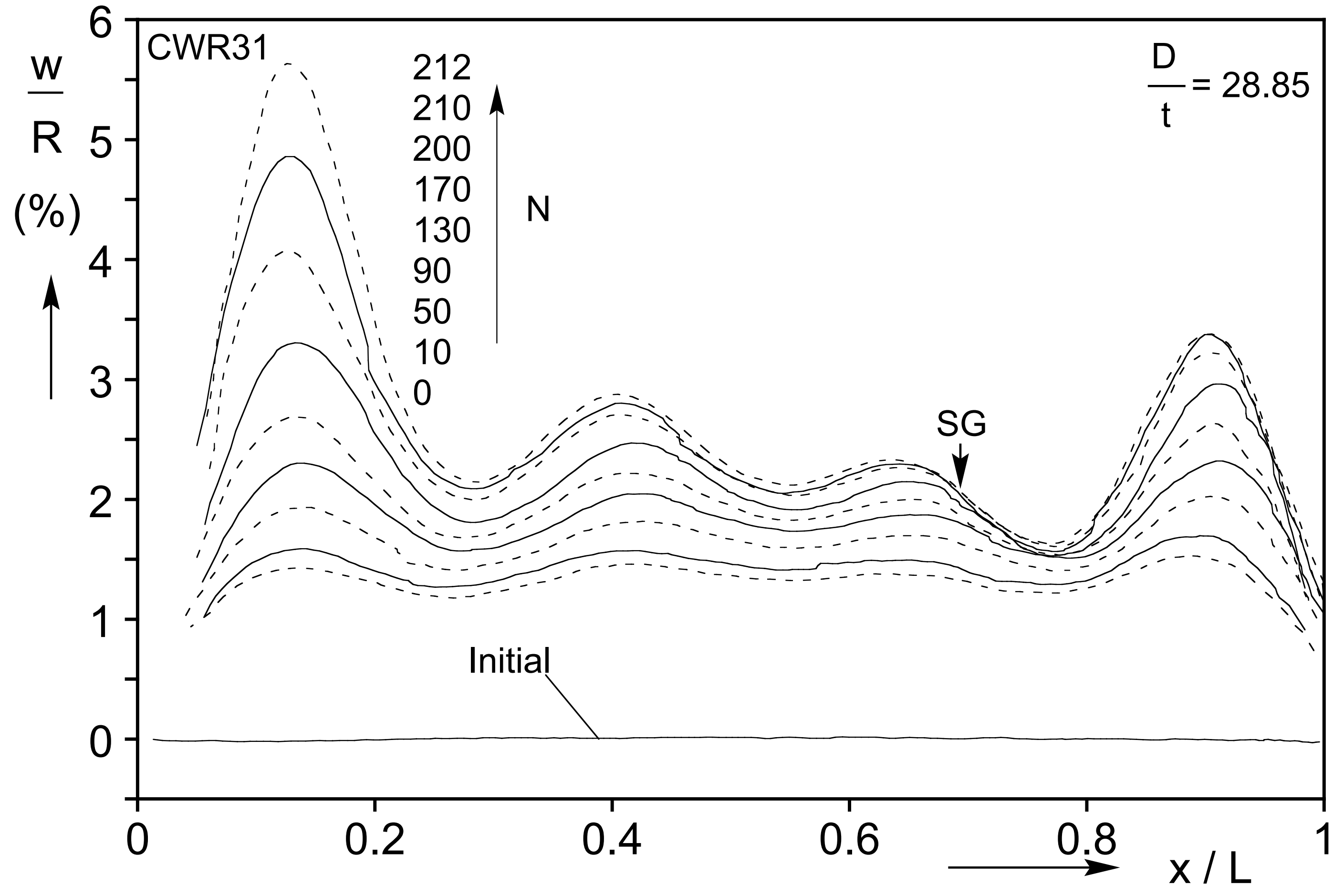

Fig. D.3b Axial scans showing evolution of wrinkles during the cycling for CWR31.

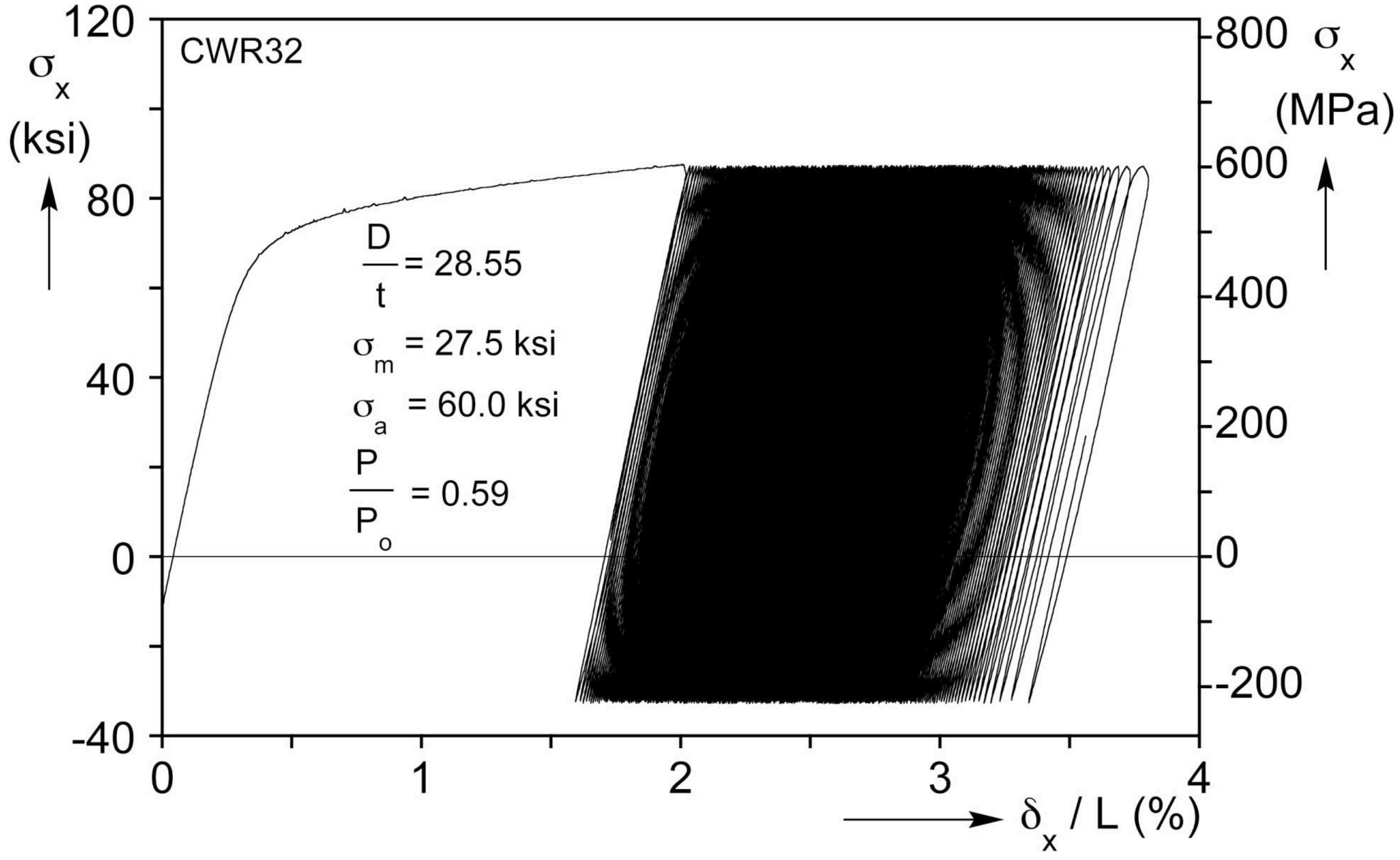

Fig. D.4a Axial stress-shortening response from cyclic loading experiment CWR32.

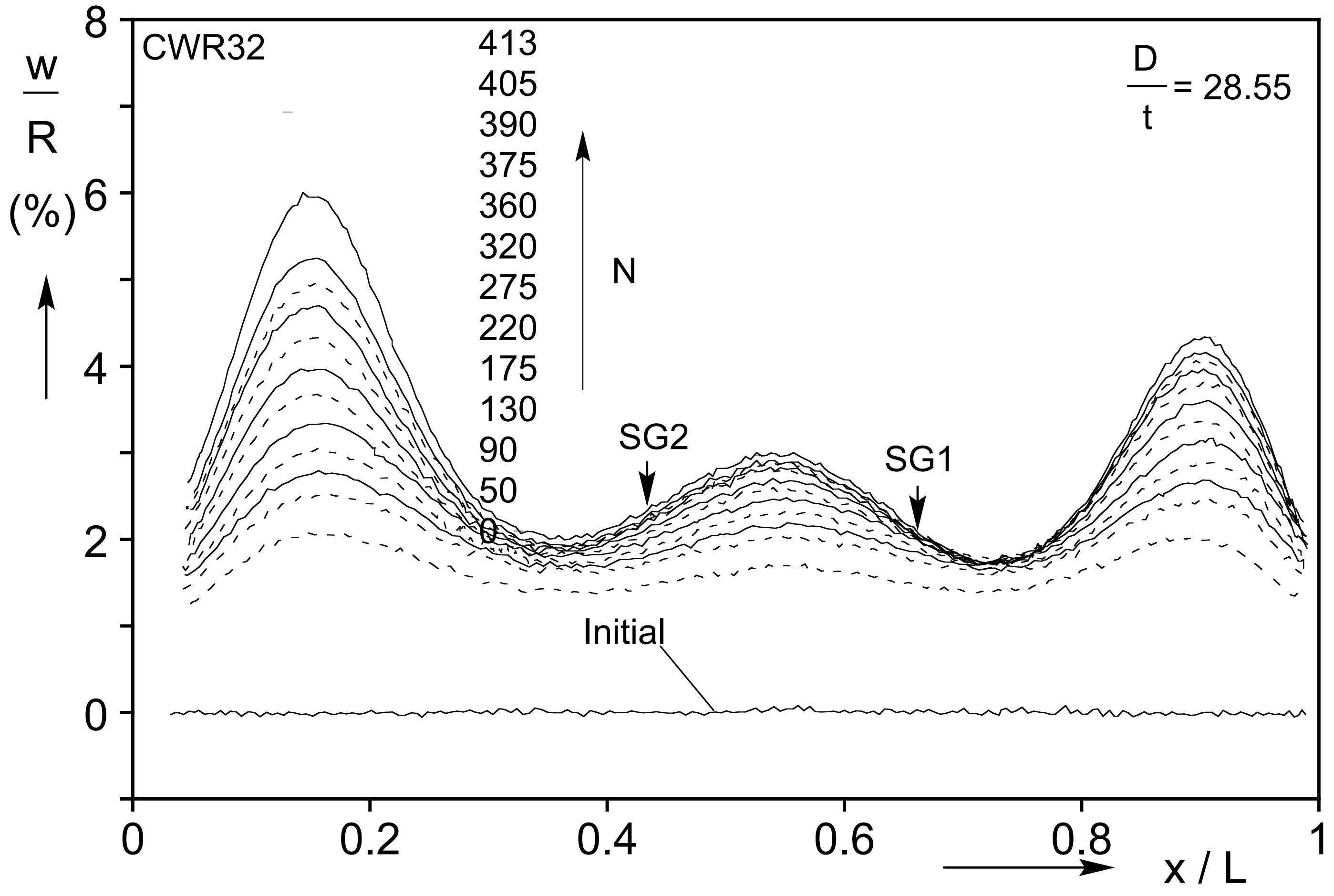

Fig. D.4b Axial scans showing evolution of wrinkles during the cycling for CWR32.

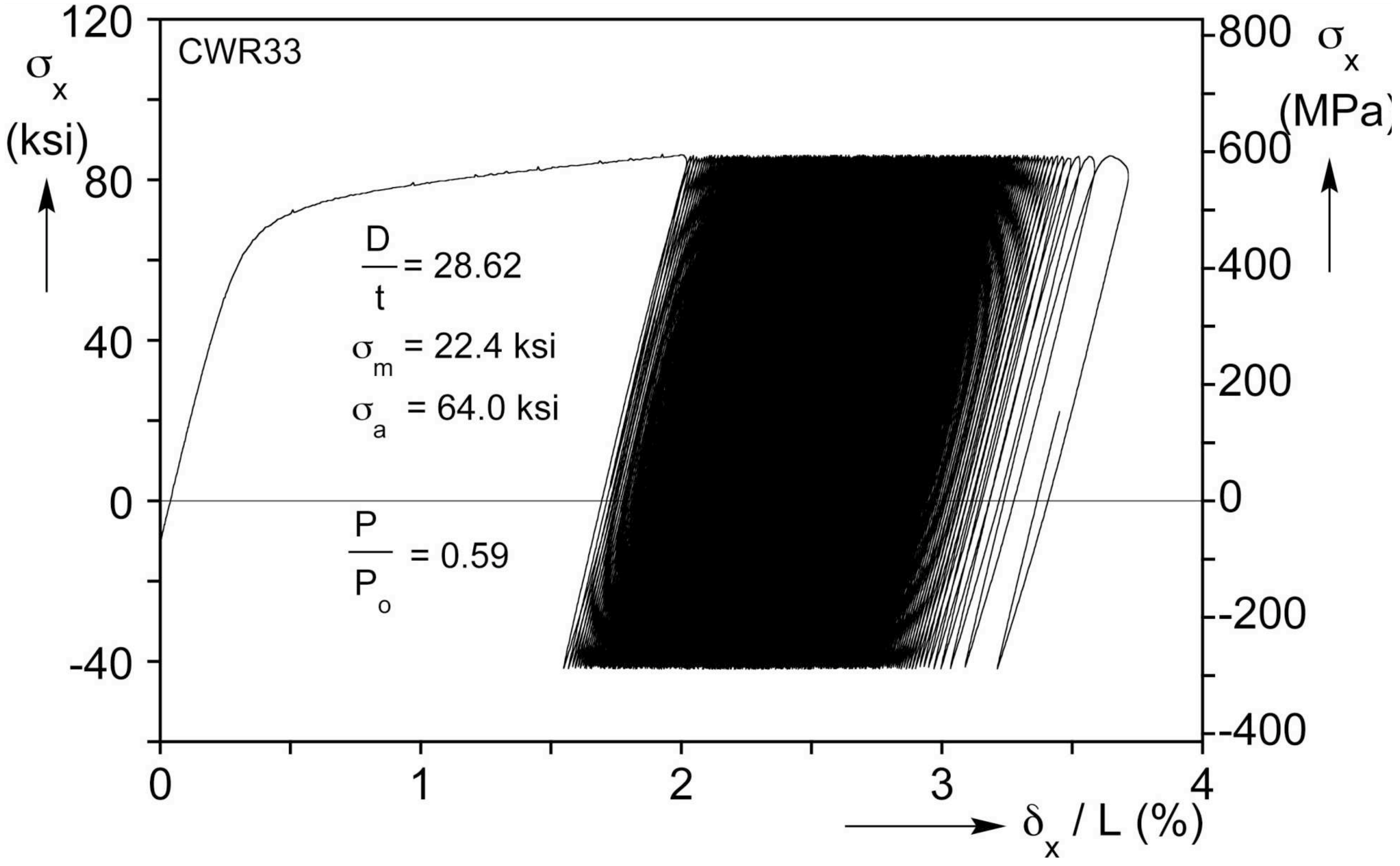

Fig. D.5a Axial stress-shortening response from cyclic loading experiment CWR33.

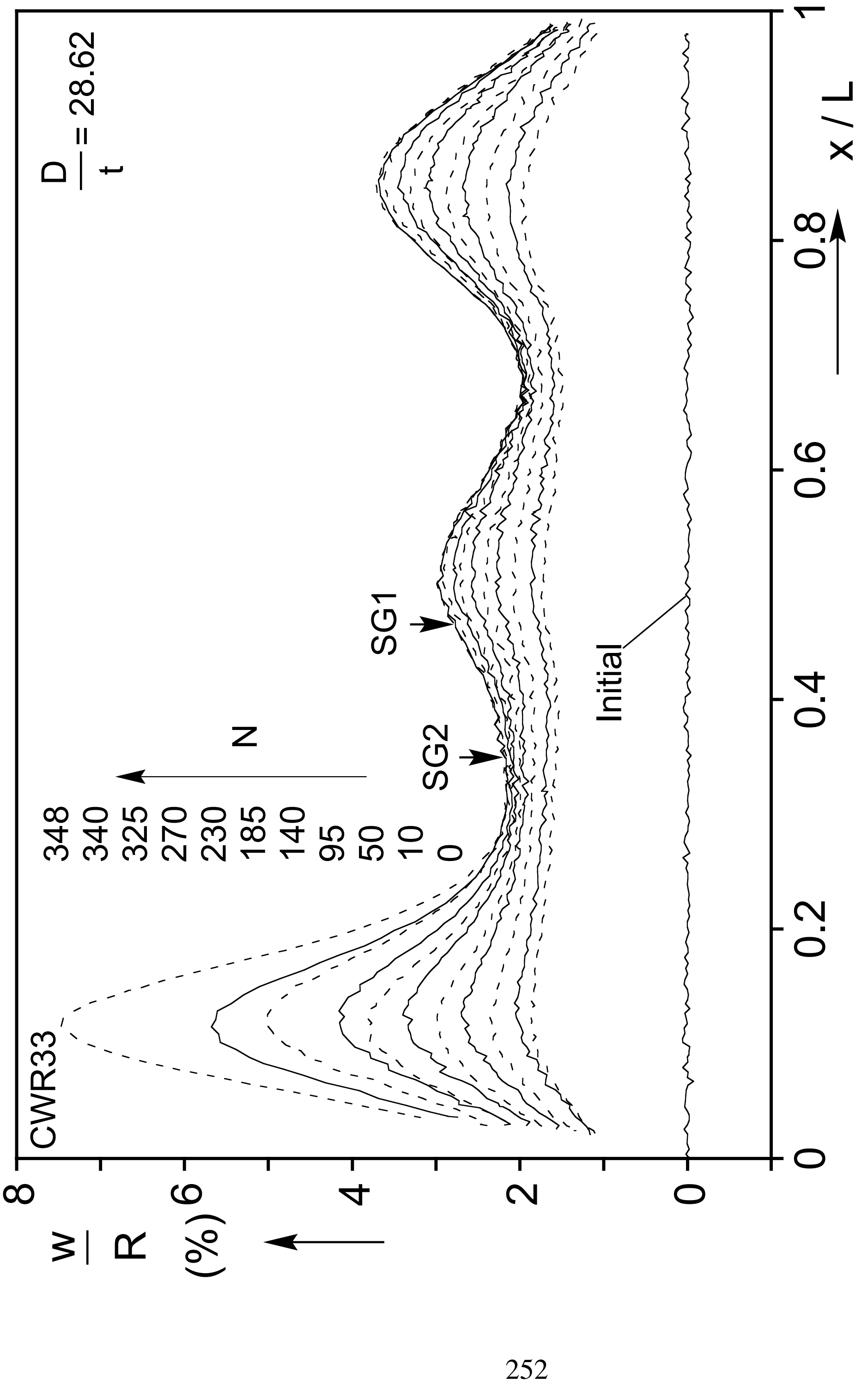

Fig. D.5b Axial scans showing evolution of wrinkles during the cycling for CWR33.

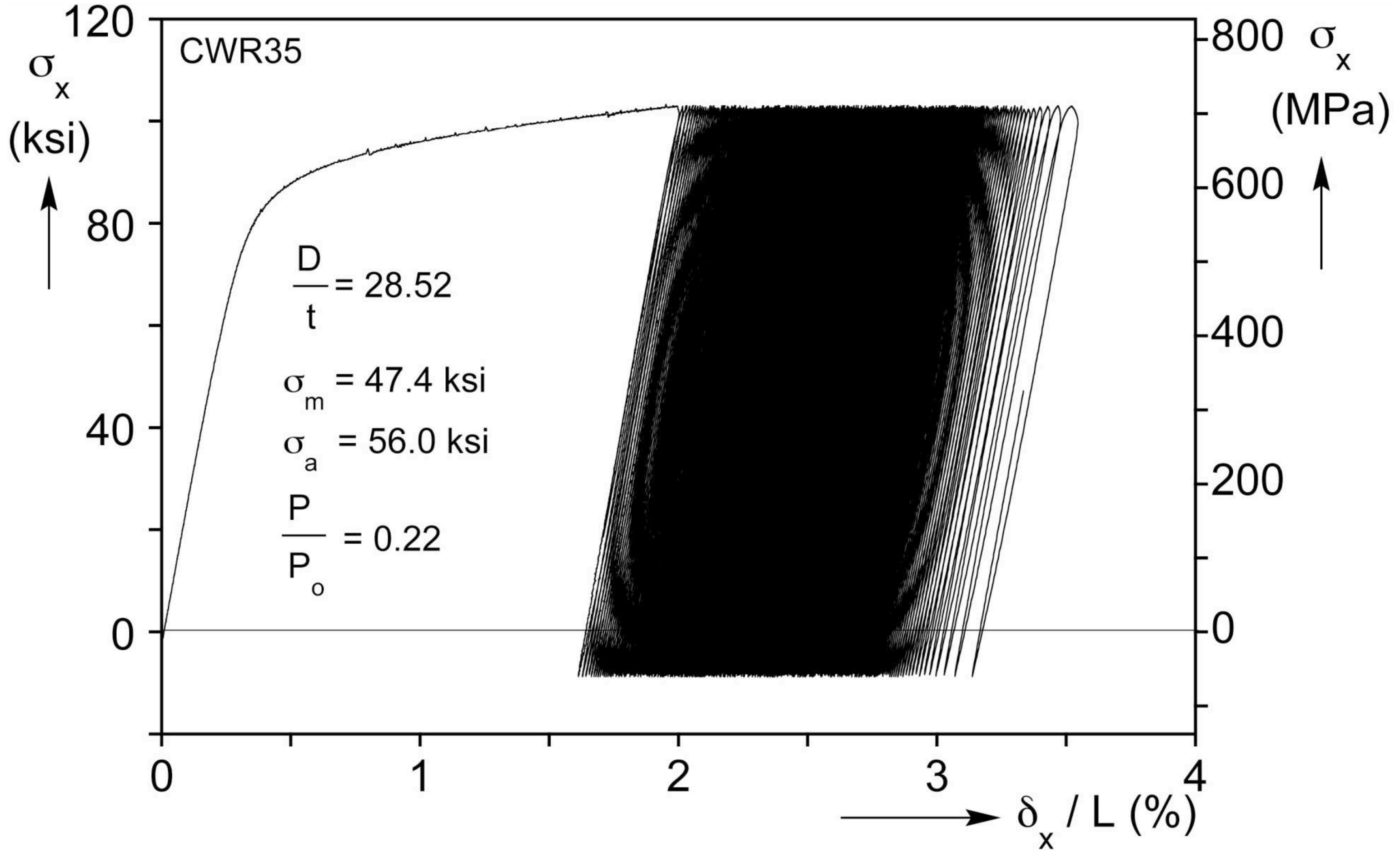

Fig. D.6a Axial stress-shortening response from cyclic loading experiment CWR35.

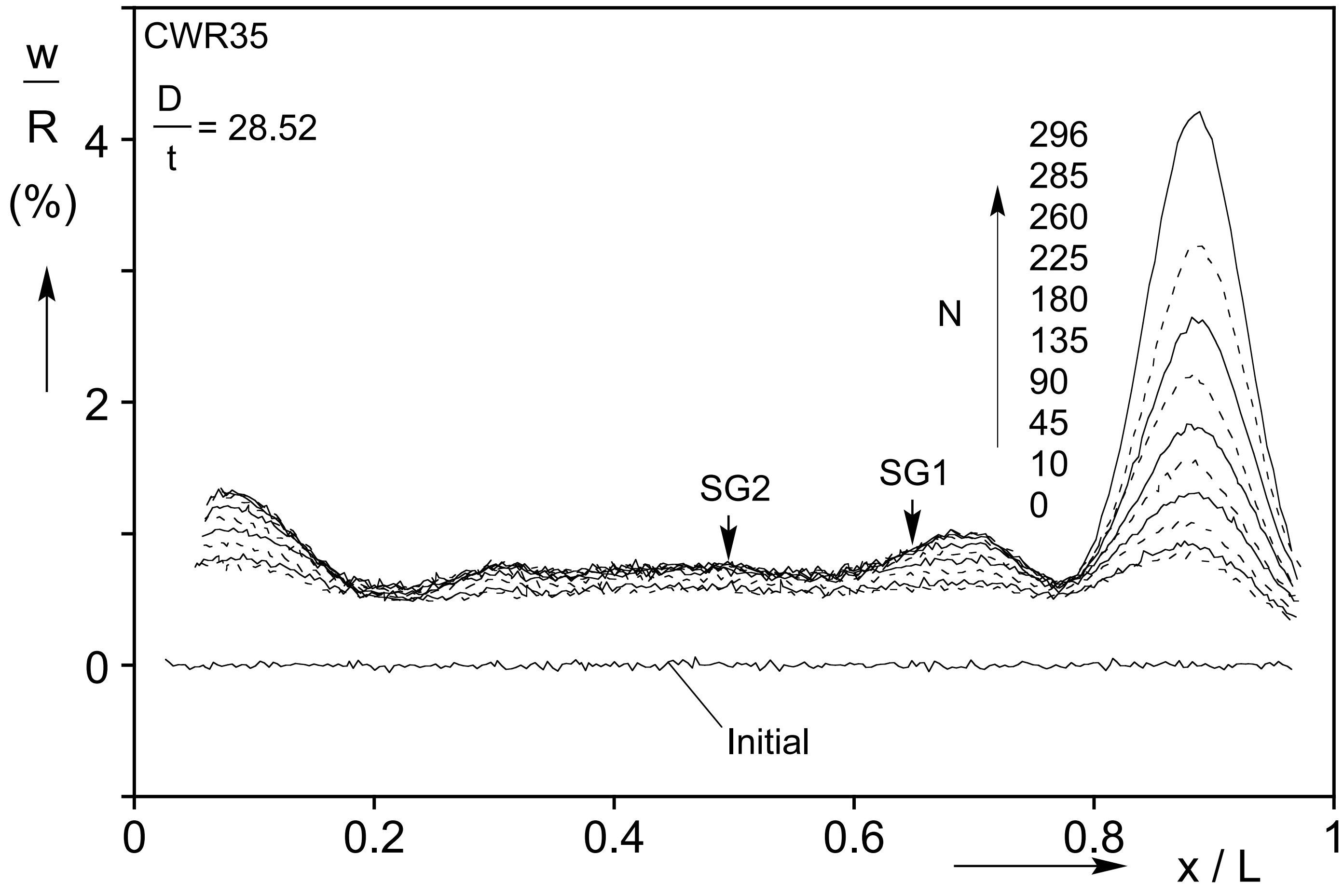

Fig. D.6b Axial scans showing evolution of wrinkles during the cycling for CWR35.

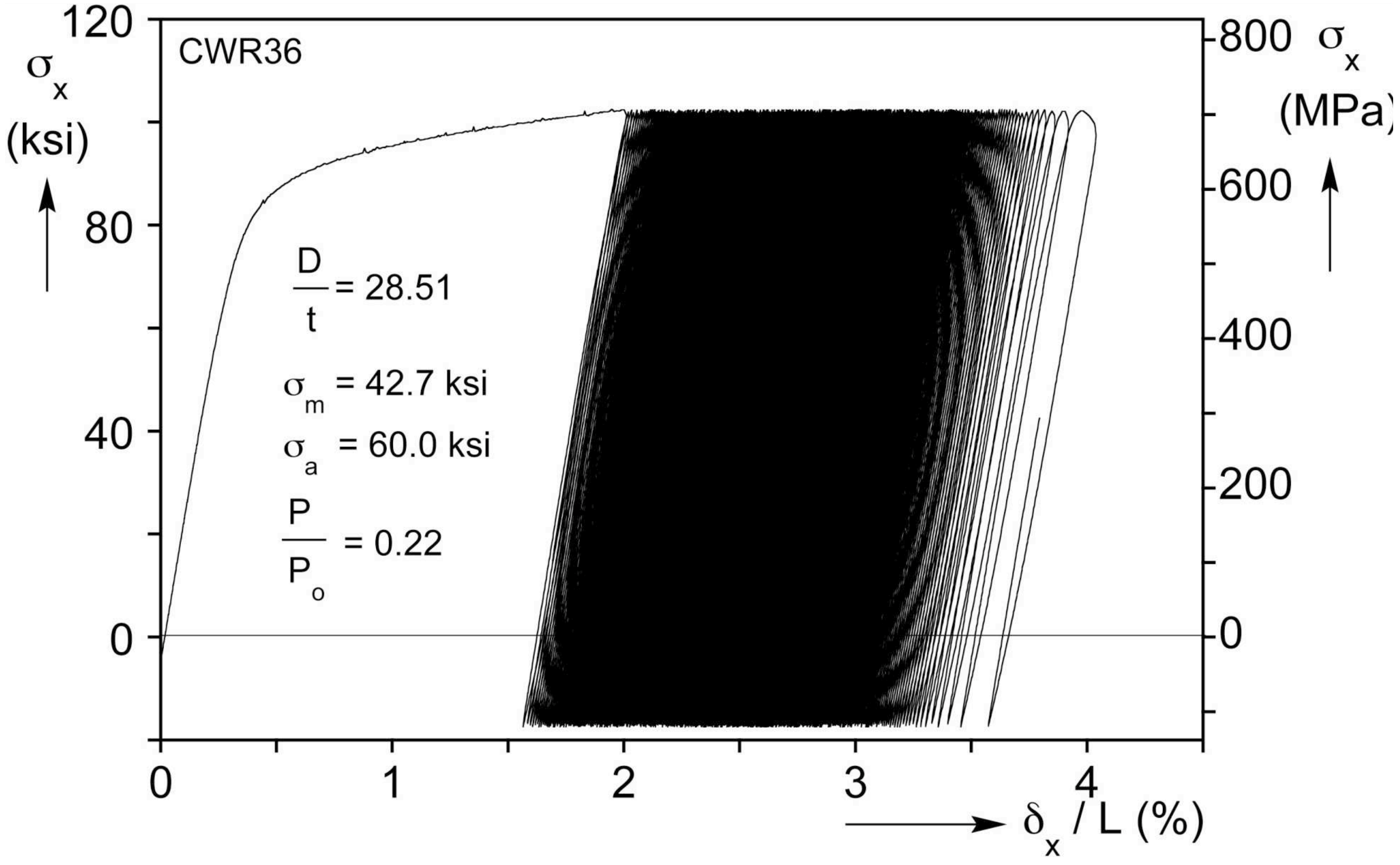

Fig. D.7a Axial stress-shortening response from cyclic loading experiment CWR36.

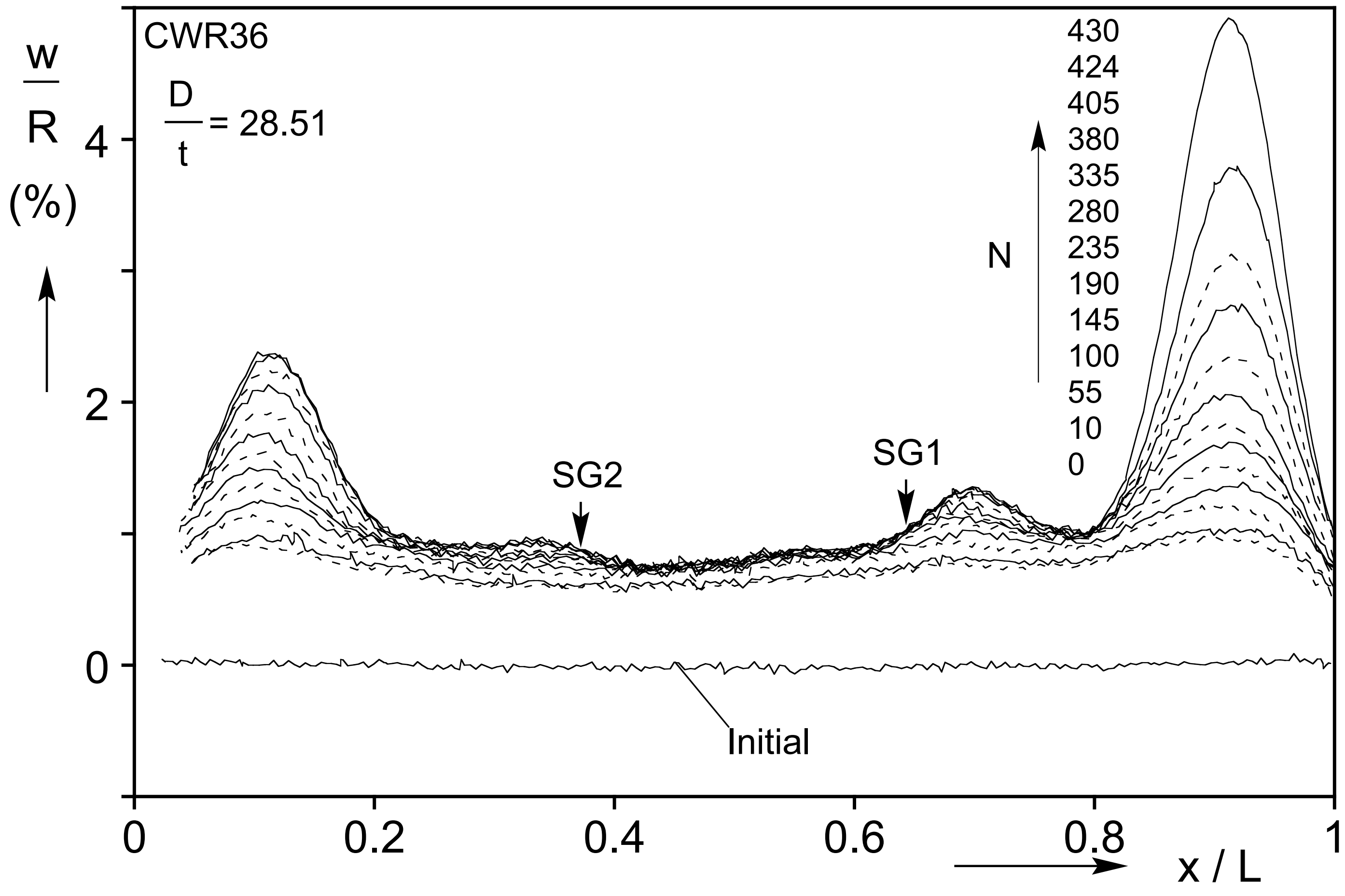

Fig. D.7b Axial scans showing evolution of wrinkles during the cycling for CWR36.

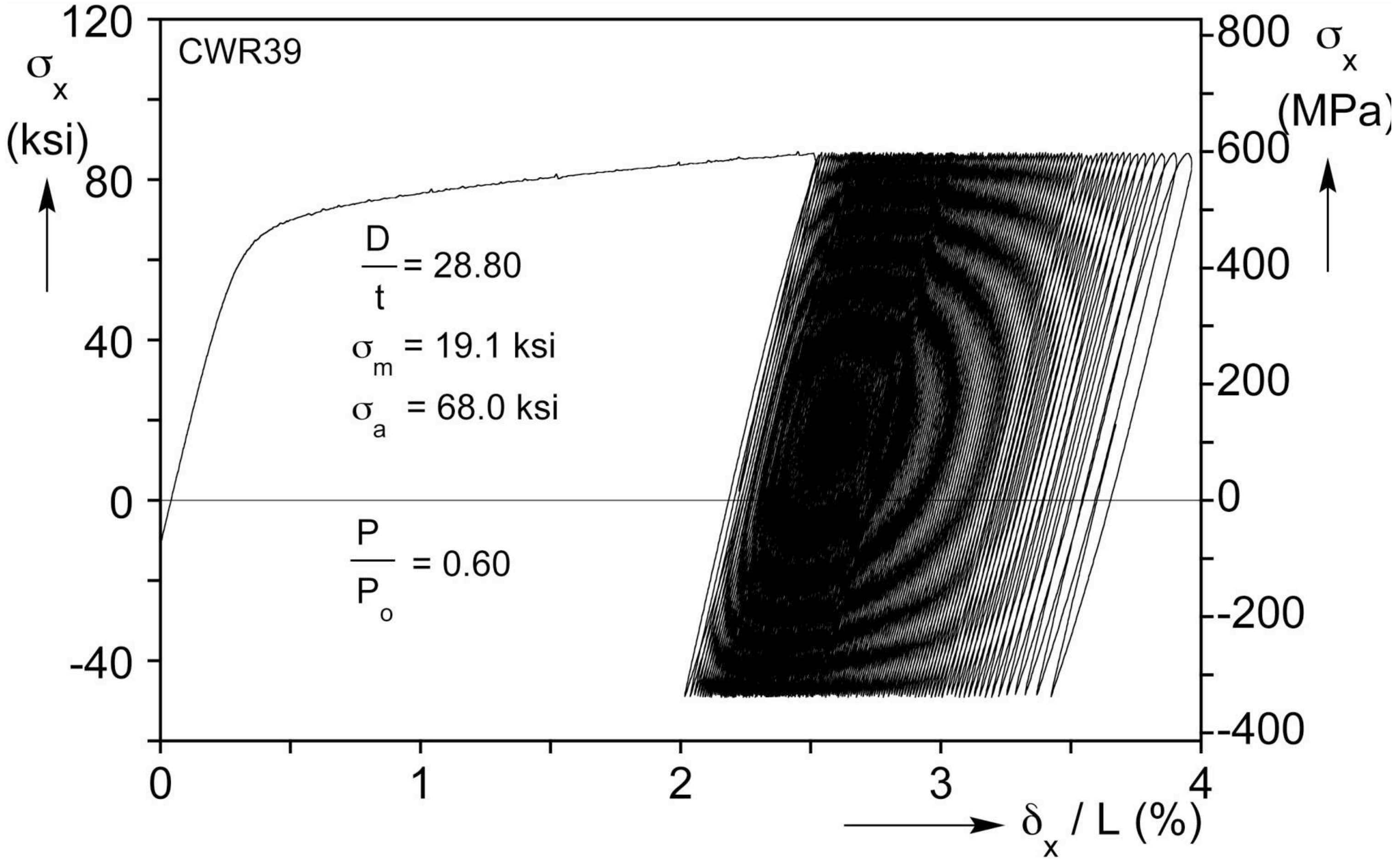

Fig. D.8a Axial stress-shortening response from cyclic loading experiment CWR39.

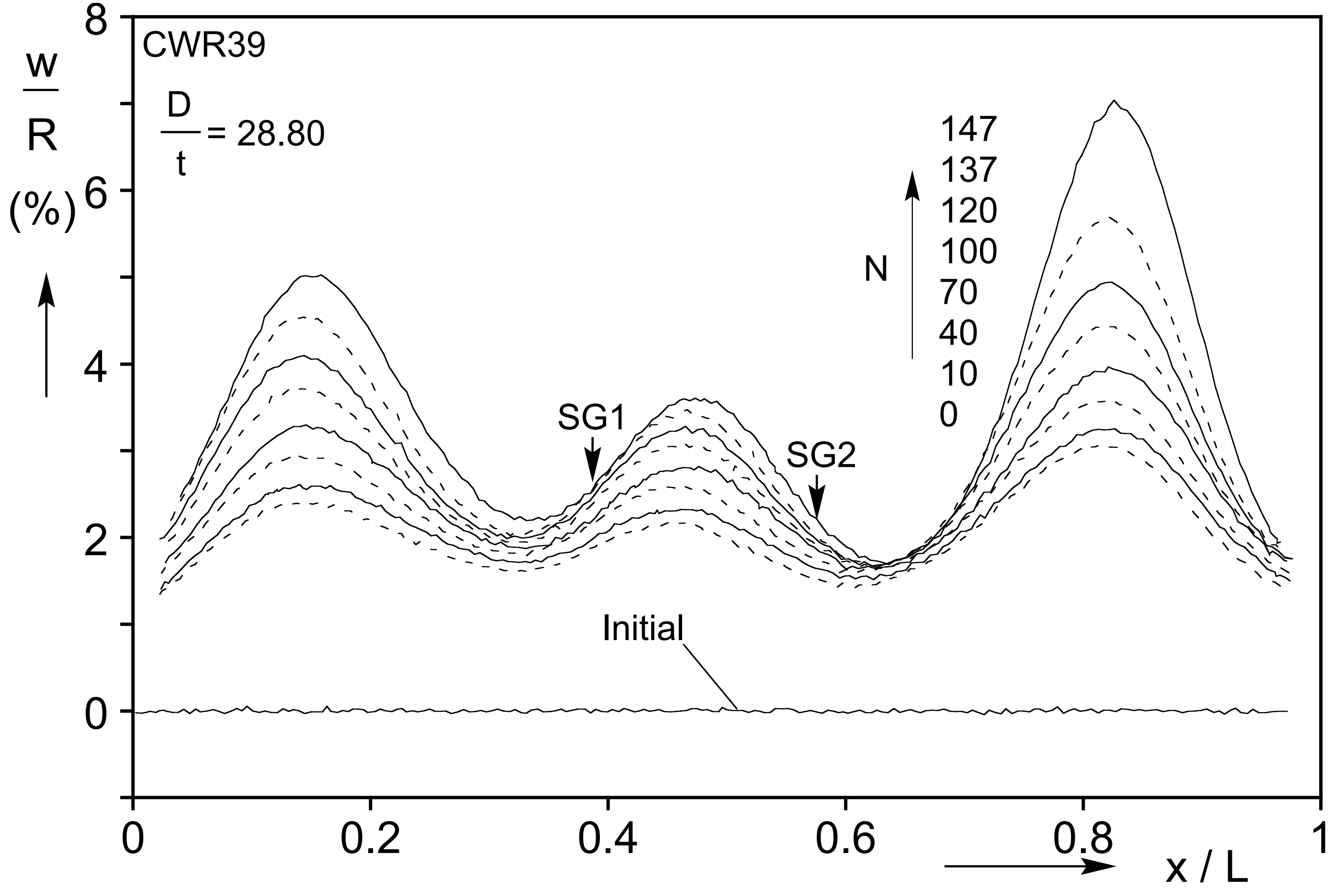

Fig. D.8b Axial scans showing evolution of wrinkles during the cycling for CWR39.

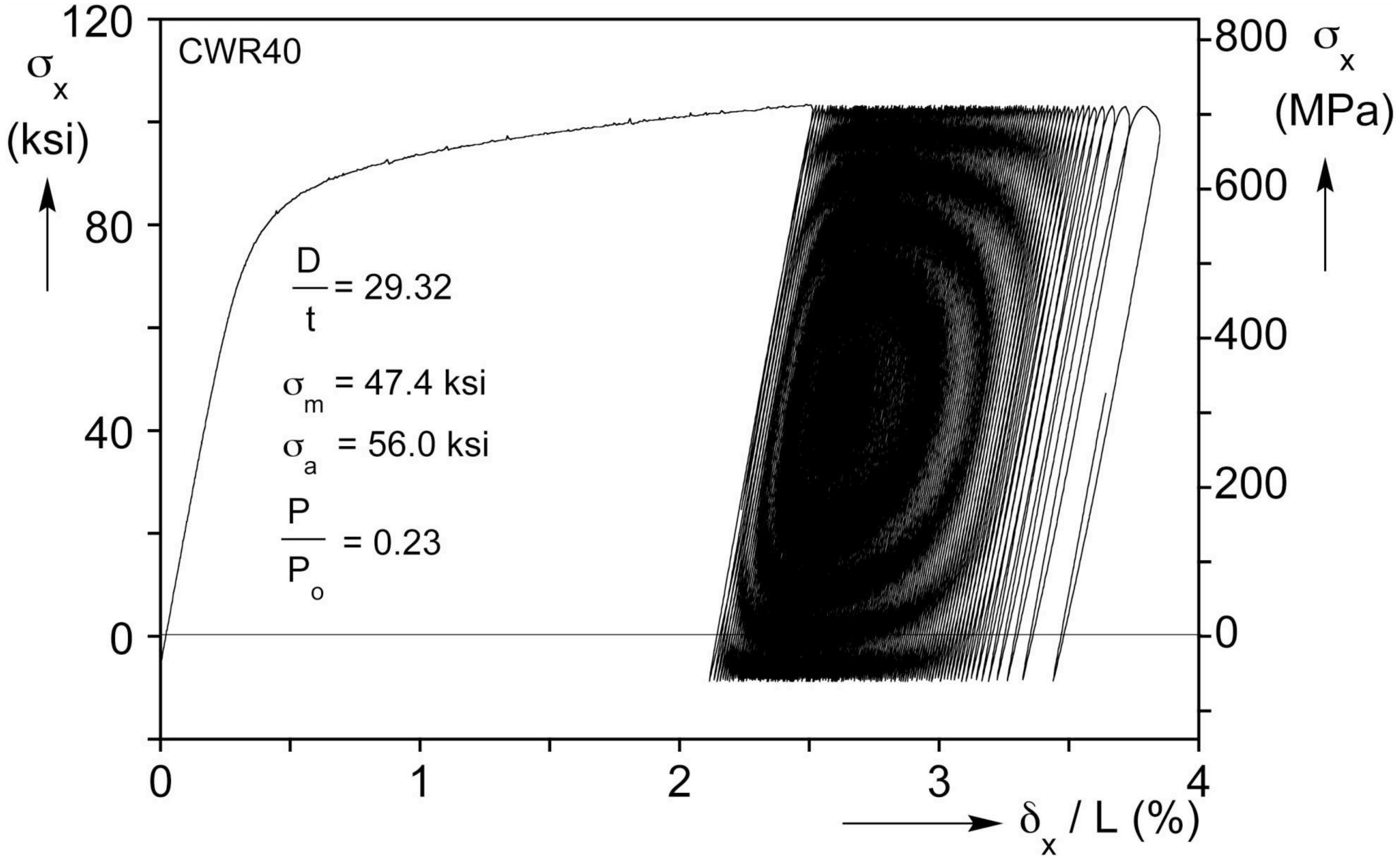

Fig. D.9a Axial stress-shortening response from cyclic loading experiment CWR40.

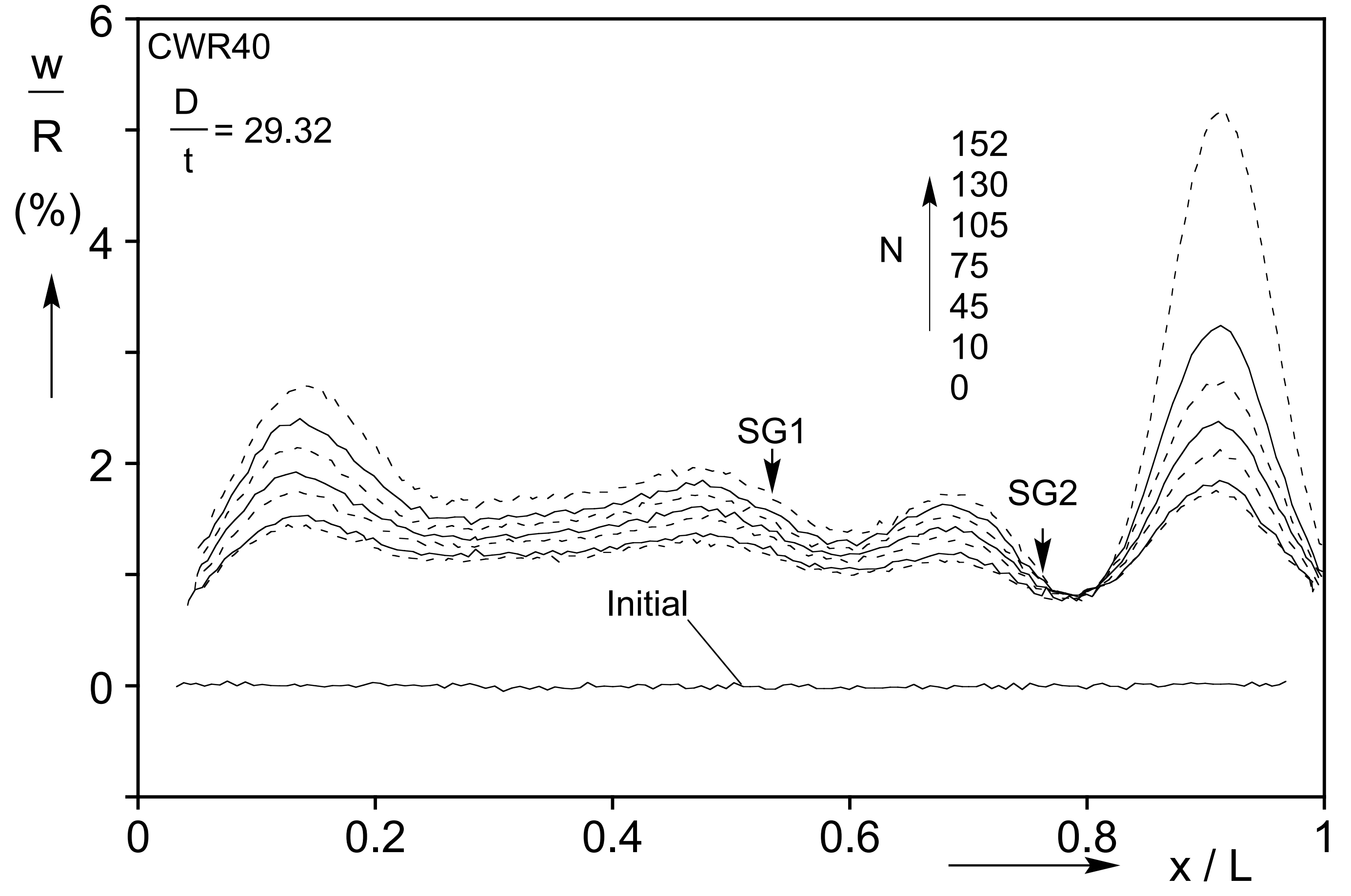

Fig. D.9b Axial scans showing evolution of wrinkles during the cycling for CWR40.

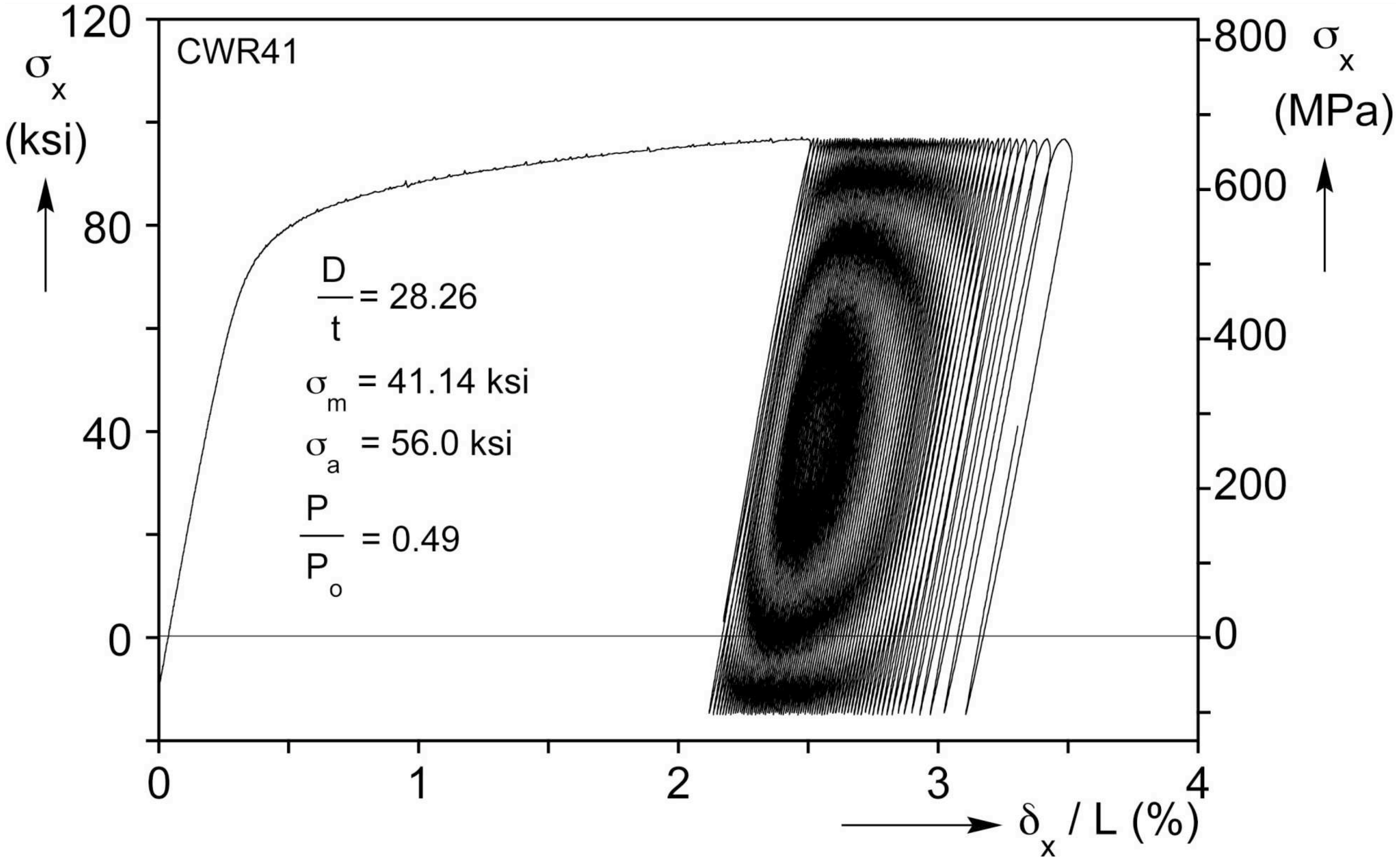

Fig. D.10a Axial stress-shortening response from cyclic loading experiment CWR41.

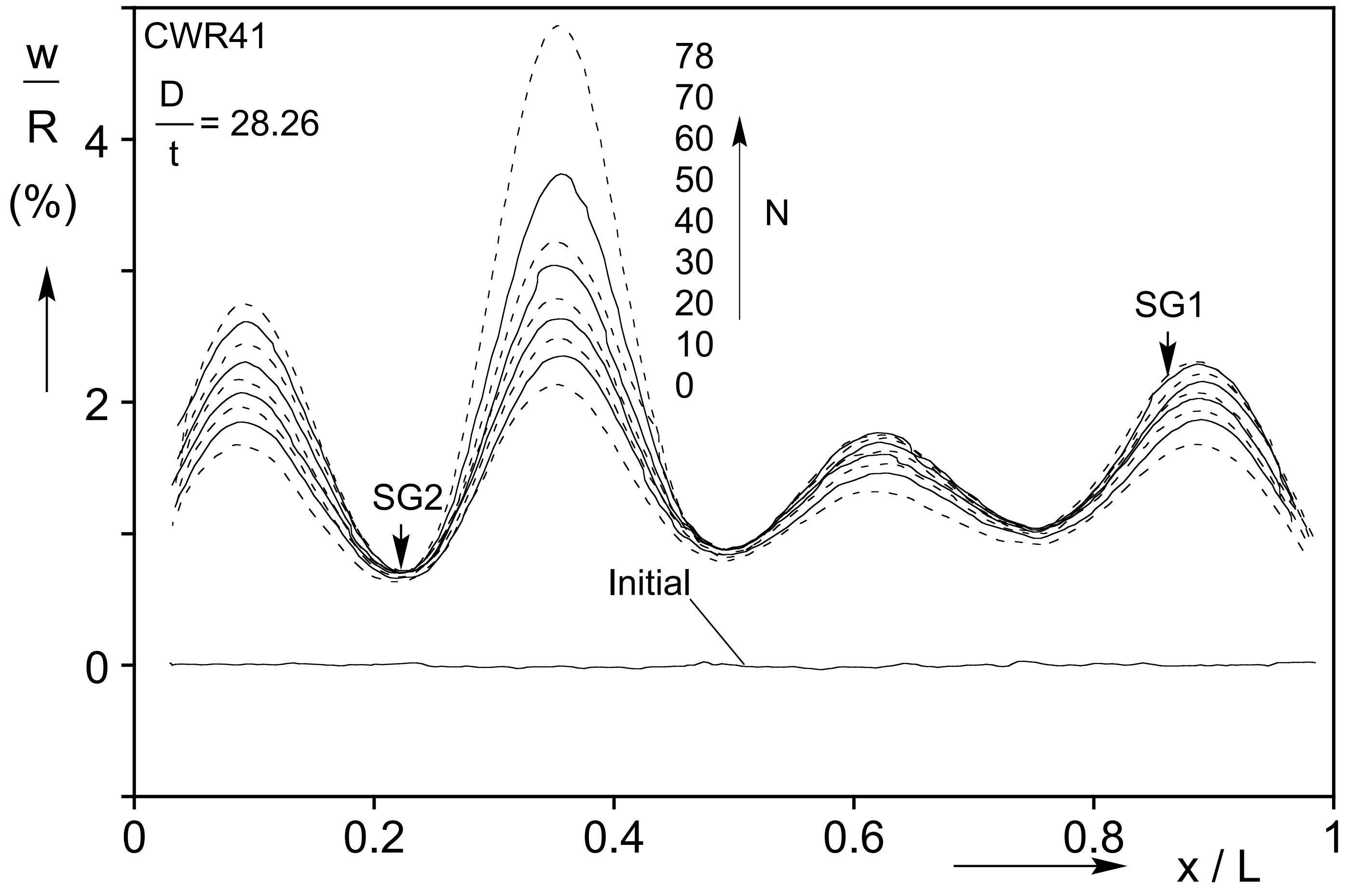

Fig. D.10b Axial scans showing evolution of wrinkles during the cycling for CWR41.

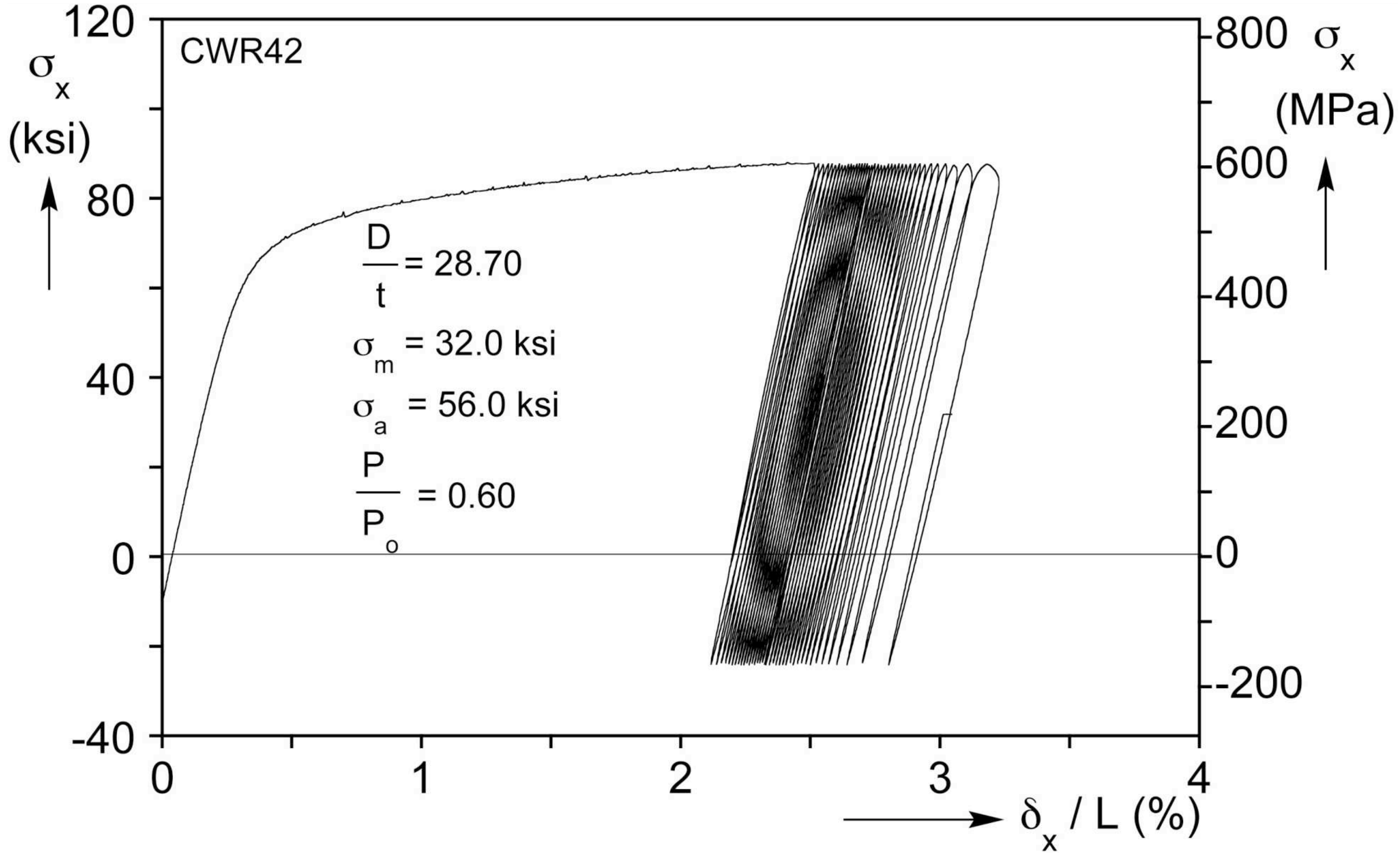

Fig. D.11a Axial stress-shortening response from cyclic loading experiment CWR42.

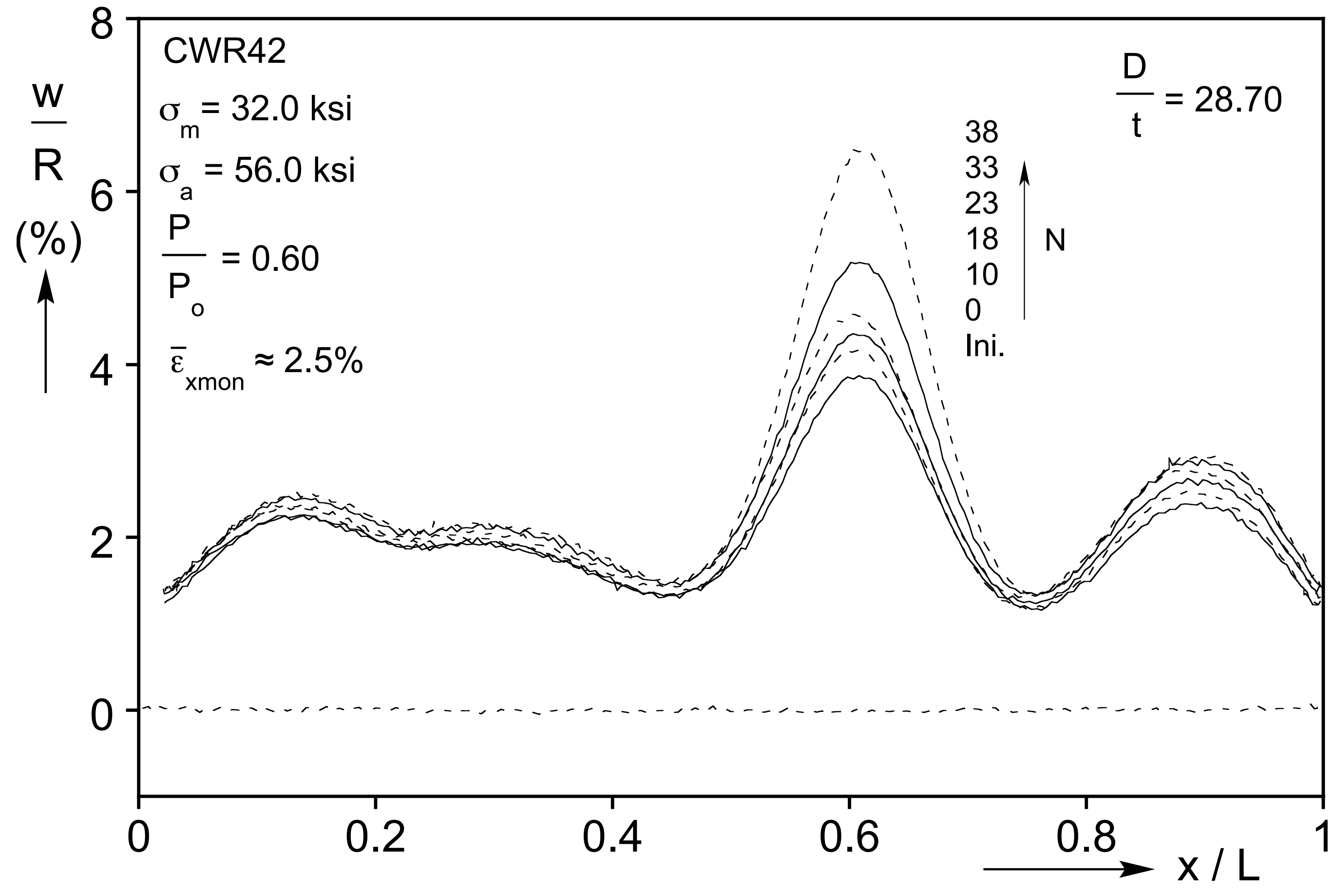

Fig. D.11b Axial scans showing evolution of wrinkles during the cycling for CWR42.

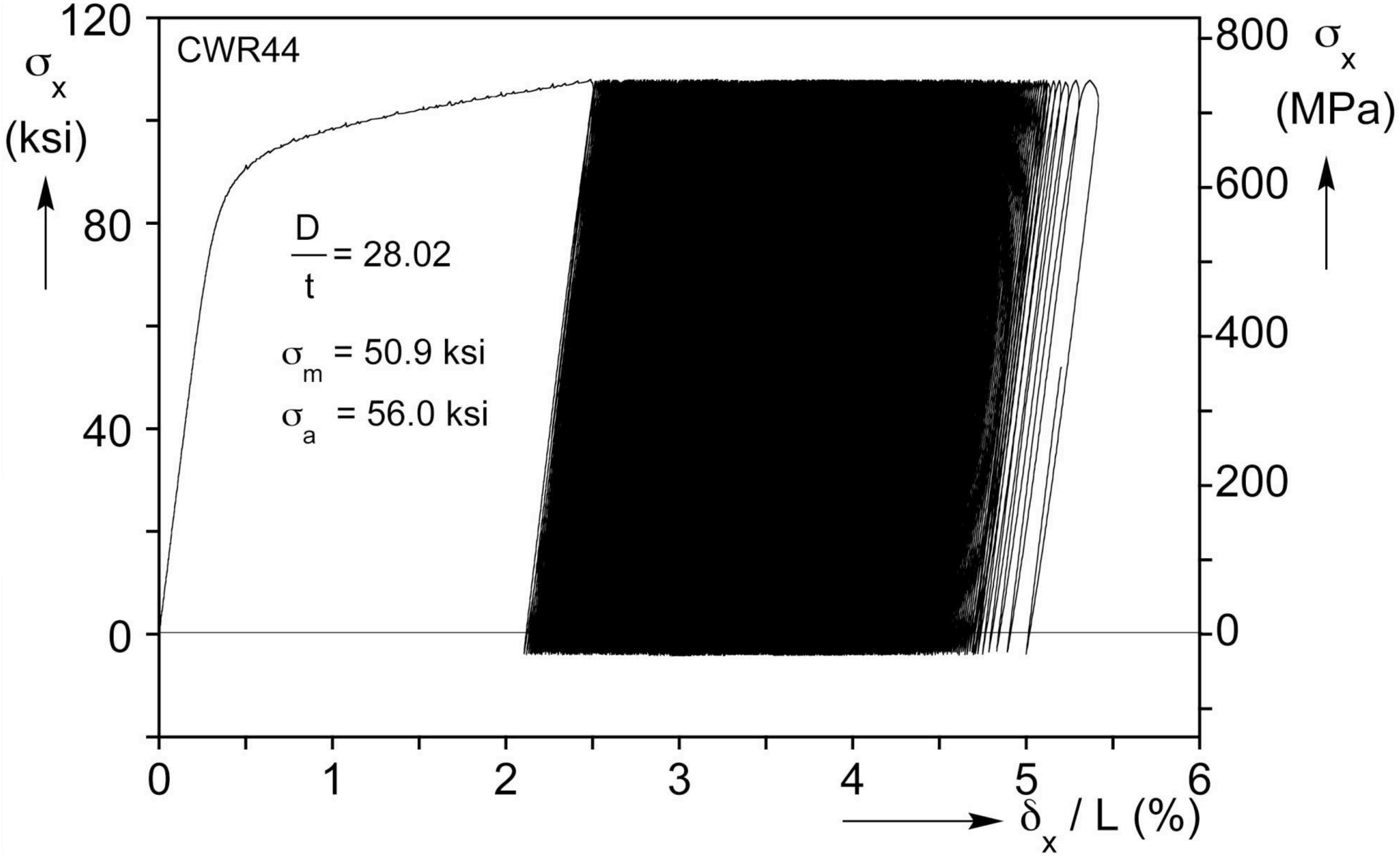

Fig. D.12a Axial stress-shortening response from cyclic loading experiment CWR44.

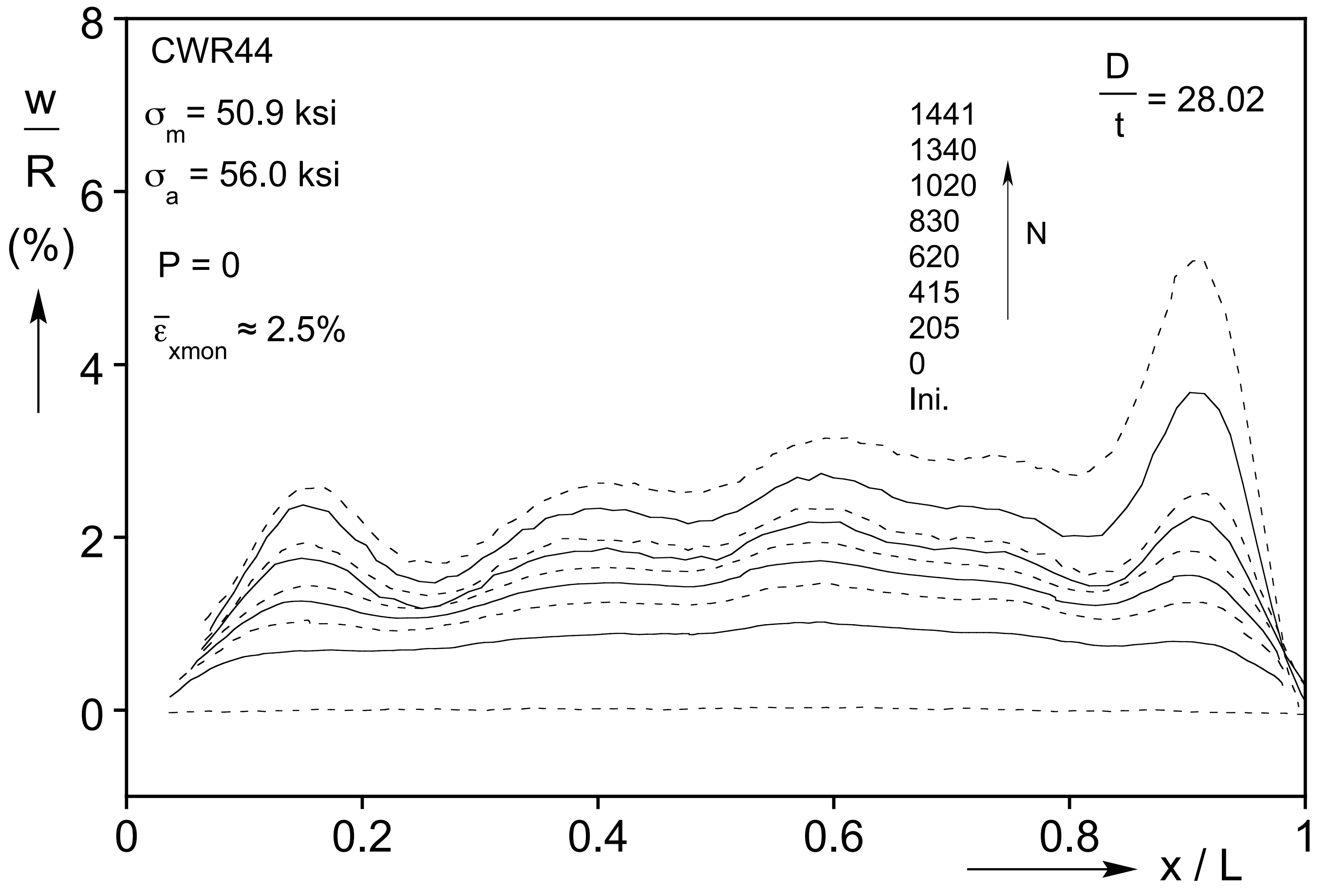

Fig. D.12b Axial scans showing evolution of wrinkles during the cycling for CWR44.

Bibliography

Abdel Karim, M. and Ohno, N. (2000). Kinematic hardening model suitable for ratcheting with steady-state. *Int'l J. Plasticity* **16**, 225-240.

Armstrong, P.J. and Frederick, C.O. (1966). A mathematical representation of the multiaxial Bauschinger effect. Berkeley Nuclear Laboratories, R & D Department, Report No. RD/B/N/731.

Bardi, F.C. (2006). Plastic buckling and collapse of circular cylinders under axial compression. PhD Dissertation, *University of Texas at Austin*, Texas, USA.

Bardi, F.C. and Kyriakides, S. (2006). Plastic buckling of circular tubes under axial compression-part I: Experiments. *Int'l J. Mechanical Sciences* **48**, 830-841.

Bardi, F.C., Kyriakides, S. and Yun, H.D. (2006). Plastic buckling of circular tubes under axial compression -part II: Analysis. *Int'l J. Mechanical Sciences* **48**, 842-854.

Bari, S. and Hassan, T. (2000). Anatomy of coupled constitutive models for ratcheting simulation. *Int'l J. Plasticity* **16**, 381-409.

Bari, S. and Hassan, T. (2001). Kinematic hardening rules in uncoupled modeling for multiaxial ratcheting simulation. *Int'l J. Plasticity* **17**, 885-905.

Bari, S. and Hassan, T. (2002). An advancement in cyclic plasticity modeling for multiaxial ratcheting simulation. *Int'l J. Plasticity* **18**, 873-894.

Batdorf, S.B. (1949). Theories of plastic buckling. *J. Aeronautical Sciences* **16**, 405-408.

Batterman, S.C. (1965). Plastic buckling of axially compressed cylindrical shells. *AIAA Journal* **3**, 316-325.

Benham, P.P. (1965). Some observations of cyclic strain-induced creep in mild steel at room temperature. *Int'l J. Mechanical Sciences* **7**, 81-86.

Chang, K.-H and Pan, W.-F. (2009). Buckling life estimation of circular tubes under cyclic bending. *Int'l J. Solids & Structures* **46**, 254-270.

Chaboche, J.L. (1986). Time-independent constitutive theories for cyclic plasticity. *Int'l J. Plasticity* **2**, 149-188.

Chaboche, J.L. (1991). On some modifications of kinematic hardening to improve the description of ratcheting effects. *Int'l J. Plasticity* **7**, 661-678.

Chen, X. and Jiao, R. (2004). Modified kinematic hardening rule for multiaxial ratcheting prediction. *Int'l J. Plasticity* **20**, 871-898.

Chen, X., Jiao, R. and Kim, K.S. (2005). On the Ohno-Wang kinematic hardening rules for multiaxial ratcheting modeling of medium carbon steel. *Int'l J. Plasticity* **21**, 161-184.

Corona, E., Hassan, T. and Kyriakides, S. (1996). On the performance of kinematic hardening rules in predicting a class of biaxial ratcheting histories. *Int'l J. Plasticity* **12**, 117-145.

Corona, E. and Kyriakides, S. (1991). Experimental investigation of the degradation and buckling of circular tubes under cyclic bending and external pressure. *Thin-Walled Structures* **12**, 229-263.

Dafalias, Y.F. and Popov, E.P. (1975). A Model of nonlinearly hardening materials for complex loading. *Acta Mechanica* **21**, 173-192.

Dafalias, Y.F. and Popov, E.P. (1976). Plastic internal variables formalism of cyclic plasticity. *ASME J. Applied Mechanics* **43**, 645-651.

Di Vito, L., Ferino J., Mannucci G., Lucci A., Vitali L., Marchesani F., Armengol M., Novelli P., Tintori F., Darcis P., Izquierdo A. and Quintanilla H. (2010). Ultra heavy wall linepine X65: ratcheting in severe cyclic straining. *Proc. 28th Int'l Conf. Ocean, Offshore & Arctic Engineering*. OMAE2010-20897.

Ellison, M.S. and Corona, E. (1998). Buckling of T-Beams under cyclic bending. *Int'l J. Mech. Scie*. **40**, 835-855.

Gellin, S. (1979). Effect of an axisymmetric imperfection on the plastic buckling of an axially compressed cylindrical shell. *ASME J. Applied Mechanics* **46**, 125-131.

Hassan, T. and Kyriakides, S. (1992). Ratcheting in cyclic plasticity-Part I: Uniaxial behavior. *Int'l J. Plasticity* **8**, 91-116.

Hassan, T., Corona, E. and Kyriakides, S. (1992). Ratcheting in cyclic plasticity- Part II: Multiaxial behavior. *Int'l Journal of Plasticity* **8**, 117-146.

Hassan, T. and Kyriakides, S. (1994a). Ratcheting of cyclically hardening and softening materials: I. Uniaxial behavior. *Int'l J. Plasticity* **10**, 149-184.

Hassan, T. and Kyriakides, S. (1994b). Ratcheting of cyclically hardening and softening materials: II. Multiaxial behavior. *Int'l J. Plasticity* **10**, 185-212.

Hassan, T. and Rahman, S.M. (2009). Simulation of ratcheting responses of elbow piping components. *Proc. of ASME 2009 Pressure Vessels and Piping*. PVP2009-77819.

Hill, R. (1948). A theory of yielding and plastic flow of anisotropic metals. *Proc. Roy. Soc.* **A193**, 281-297.

Hobbs, R. (1984). In-service buckling of heated pipelines. *Journal of Transportation Engineering*, **110**, 175-189.

Hutchinson, J.W. (1974). Plastic Buckling. In *Advances in Applied Mechanics* **14**, Ed. C. S. Yih, Academic Press, NY, pp. 67-144.

Jiang, Y.Y. and Sehitoglu, H. (1996a). Modeling of cyclic ratcheting plasticity, part I: Development of constitutive relations. *ASME J. Applied Mechanics* **63**, 720-725.

Jiang, Y.Y. and Sehitoglu, H. (1996b). Modeling of cyclic ratcheting plasticity, part II: Comparison of model simulations with experiments. *ASME J. Applied Mechanics* **63**, 726-733.

Jiao, R. and Kyriakides, S. (2009). Ratcheting, wrinkling and collapse of tubes under axial cycling. *Int'l J. Solids & Structures* **46**, 2856-2870.

Jiao, R. and Kyriakides, S. (2010). Wrinkling of tubes by axial cycling. *ASME J. Applied Mechanics* **77**, 1-11.

Kim, J.W. and Park, C.Y. (2006). Experimental investigation of the failure behavior of notched wall-thinned pipes. *Nuclear Engineering Design* **236**, 1838-1846.

Ju, G.T. and Kyriakides, S. (1988). Thermal buckling of offshore pipelines. *Journal of Offshore Mechanics and Arctic Engineering* **110**, n4, 355-364.

Klever, F.J., Palmer, A.C. and Kyriakides, S. (1994). Limit-state design of high-temperature pipelines. In, Proc. *13th International Conference on Offshore Mechanics and Arctic Engineering*, Houston, TX, Feb. 1994, Vol. V, pp. 77-92.

Kyriakides, S. and Shaw, P. K. (1987). Inelastic buckling of tubes under cyclic bending. *ASME J. Press. Vess. Techn.* **109**, 169-178.

Kyriakides, S., Bardi, F.C. and Paquette, J.A. (2005). Wrinkling of circular tubes under axial compression: Effect of anisotropy. *ASME J. Applied Mechanics* **72**, 301-305.

Kyriakides, S. and Corona, E. (2007). *Mechanics of Offshore Pipelines: Volume 1 Buckling and Collapse*. Elsevier, Oxford, UK and Burlington, Massachusetts.

Kyriakides, S. and Yeh, M.-K. (1988). Plastic anisotropy in drawn metal tubes. *ASME J. Eng. Ind.* **110**, 303-307.

Landgraf, R.W. (1970). The resistance of metals to cyclic deformation. *ASTM STP* **467**, 3-36.

Lee, L.H.N. (1962). Inelastic buckling of initially imperfect cylindrical shells subject to axial compression. *J. Aeronautical Sciences* **29**, 87-95.

McDowell, D.L. (1995). Stress state dependence of cyclic ratcheting behavior of two rail steels. *Int'l J. Plasticity* **11**, 397-421.

Morrow, J.D. (1965). Cyclic plastic strain energy and fatigue of metals. *ASTM STP* **378**, 45-87.

Moyar, G.J. and Sinclair, G.M. (1963). Cyclic strain accumulation under complex multiaxial loading. *Proc. of the Joint International Conference on Creep*, Institution of Mechanical Engineers, London, 2-47.

Murray, D.W. (1997). Local buckling, strain localization, wrinkling and postbuckling response of a line pipe. *Engineering Structures* **19**, 360-371.

Oh, C.S., Kim, Y.J. and Park, C.Y. (2008). Shakedown limit loads for elbows under internal pressure and cyclic in-plane bending. *Int'l J. Pressure Vessels and Piping* **85**, 394-405.

Ohno, N. and Wang, J.D. (1993a). Kinematic hardening rules with critical state of dynamic recovery, part I: Formulations and basic features for ratcheting behavior. *Int'l J. Plasticity* **9**, 375-390.

Ohno, N. and Wang, J.D. (1993b). Kinematic hardening rules with critical state of dynamic recovery, Part II: Application to experiments of ratcheting behavior. *Int'l J. Plasticity* **9**, 391-403.

Paquette, J.A. and Kyriakides, S. (2006). Plastic buckling of tubes under axial compression and internal pressure. *Int'l J. Mechanical Sciences* **48**, 855-867.

Rahman, S.M., Hassan, T. and Corona, E. (2008). Evaluation of cyclic plasticity models in ratcheting simulation of straight pipes under cyclic bending and steady internal pressure. *Int'l J. Plasticity* **24**, 1756-1791.

Sanders, J.L., Jr. (1963). Nonlinear theories for thin shells. *Quarterly Applied Mathematics* **21**, 21-36.

Sandvik, (2008). Sandvik SAF 2507 data sheet. *http://www.sandvik.com/*

Shaw, P.K. and Kyriakides, S. (1985). Inelastic analysis of thin-walled tubes under cyclic bending. *Int'l J. Solids & Structures* **21**, 1073-1100.

Shiratori, E., Ikegami, K. and Yoshida, F. (1979). Analysis of stress-strain relations by use of an anisotropic hardening plastic potential. *J. Mech. Phys. Solids* **27**, 213-229.

Vaze, S. and Corona E. (1998). Degradation and collapse of square tubes under cyclic bending. *Thin-Walled Structures* **31**, 325-341.

Wilkie, S.A., Dobranko, R.M. and Fladager, S.J. (2000). Case history of local wrinkling of a pipeline. *Proc. ASME International Pipeline Conference*, Calgary, Alberta, Canada, October 1-5, 2000, Vol.2, 917-922.

Yin, S., Corona, E. and Ellison, M. (2004). Degradation and buckling of I-beams under cyclic pure bending. *ASCE J. Engineering Mechanics Division* **130**, 809-817.

Yoosef-Ghodsi, Cheng, J.J.R., Murray, D.W., Doblanko, R. and Wilkie, S. (2000). Analytical Simulation and Field Measurements for a Wrinkle on the Norman Wells Pipeline. *Proc. ASME International Pipeline Conference*, Calgary, Alberta, Canada, October 1-5, 2000, Vol.2, 931-938.

Yun, H.D. and Kyriakides, S. (1990). On the beam and shell modes of buckling of buried pipelines. *Soil Dynamics and Earthquake Engineering* **9**, 179-193.

Vita

Rong Jiao was born in Jiangdu, Jiangsu province, China on June 18, 1978, the son of Zhong-Hua Jiao, and Mei Kong. After completing his high school education at Jiangdu High School of Jiangsu Province in 1996, he entered Tianjin University, and received the degree of Bachelor of Science in Chemical Engineering in July, 2000. In March 2003, he received a Master of Science degree in Chemical Process Machinery at the same University. He worked as a Mechanical Engineer in National Peiyang Distillation Engineering Company of China from April 2003 and March 2004. After that, he worked as a Visiting Scholar in Pohang University of Science and Technology in South Korea. In January 2006, he joined the Engineering Mechanics graduate program at The University of Texas at Austin pursuing a Ph.D. degree. He has co-authored the following papers:

Jiao, R. and Kyriakides, S. (2011a). Ratcheting and wrinkling of tubes due to axial cycling under internal pressure: part I experiments. *Int'l J. Solids & Structures* **48**, 2814-2826.

Jiao, R. and Kyriakides, S. (2011b). Ratcheting and wrinkling of tubes due to axial cycling under internal pressure: part II analysis. *Int'l J. Solids & Structures* **48**, 2827-2836.

Jiao, R. and Kyriakides, S. (20011c). Ratcheting, wrinkling and collapse of tubes induced by axial cycling under internal pressure. *Proc. 30th Int'l Conf. Ocean, Offshore & Arctic Engineering*. OMAE2011.

Jiao, R. and Kyriakides, S. (2010). Wrinkling of tubes by axial cycling. *ASME J. Applied Mechanics* **77**, 1-11.

Jiao, R. and Kyriakides, S. (2009a). Ratcheting, wrinkling and collapse of tubes under axial cycling. *Int'l J. Solids & Structures* **46**, 2856-2870.

Jiao, R. and Kyriakides, S. (2009b). Progressive wrinkling and collapse of pipes due to axial cycling. *Proc. 28th Int'l Conf. Ocean, Offshore & Arctic Engineering*. OMAE2009-79754.

Permanent address: Xinmin Village, Jiangdu, Jiangsu Province, China 225233.

This dissertation was typed by the author.